Modélisation en fonctionnelle de la densité atomique des transformations de phases dans le système Fe-C à basse température

Mykola Lavrskyi

Normandie Université

THÈSE

Pour obtenir le diplôme de doctorat

Spécialité Physique

Préparée au sein de Université de Rouen Normandie

Modélisation en fonctionelle de la densité atomique des transformations de phases dans le système Fe-C à basse température

Présentée et soutenue par
Mykola LAVRSKYI

Thèse soutenue publiquement le 17 Janvier 2017 devant le jury composé de		
M. Yurij HOLOVATCH	Professeur / ICMP, Lviv, Ukraine	Rapporteur
M. Philippe MAUGIS	Professeur / IM2NP, Aix-Marseille Université	Rapporteur
Mme. Florence BARAS	Chargé de recherche / ICB, Université de Bourgogne Franche-Comté	Examinateur
Mme. Sophie CAZOTTES	Maître de conférences / MATEIS, INSA de Lyon	Examinateur
Mme. Helena ZAPOLSKY	Professeur / GPM, Université de Rouen Normandie	Directeur de thèse
M. Frédéric DANOIX	Chargé de recherche / GPM, Université de Rouen Normandie	Co-encadrant de thèse

Thèse dirigée par Helena ZAPOLSKY et co-encadrée par Frédéric Danoix,
Groupe de Physique des Matériaux, UMR CNRS 6634
Université de Rouen Normandie

UNIVERSITÉ DE ROUEN NORMANDIE

SPMI ECOLE DOCTORALE

GPM Groupe de Physique des Matériaux

Acknowledgements

Firstly, I would like to express my sincere gratitude to my advisors Prof. Helena Zapolsky and Dr. Frédéric Danoix for their continuous support of my Ph.D study and related research, for his patience, motivation, and immense knowledge. Their guidance helped me in all the time of research and writing of this thesis. I appreciate all their contributions of time, ideas, and funding to make my Ph.D. experience productive and stimulating. Many thanks also to Renaud Patte for his invaluable assistance in the development of computational code, for his patience and knowledge.

Besides my advisor, I would like to thank the rest of my thesis committee: Prof. Yurij Holovatch, Prof. Philippe Maugis, Dr. Florence Baras, Dr. Sophie Cazottes, for serving as my committee members even at hardship. I also want to thank you for letting my defense be an enjoyable moment, and for your brilliant comments and suggestions, thanks to you.

Also, I thank ANR SPIDERMAN project for funding my Ph.D. thesis.

My sincere thanks also goes to GPM laboratory staff for all the administrative help and also for creating such a wonderful working atmosphere.

My time at GPM was made enjoyable in large part due to the many friends and groups that became a part of my life. I am indebted to all my laboratory colleagues, Manon, Claire, Antoine, Romain, Alexander, Edy, Yana in for the stimulating discussions, for the hard days we were working together before deadlines, and for all the fun we have had in the last four years. I am grateful for time spent with them.

A very special thanks to my friends Noshin, Isabelle, Mohit, Alfia, Begoña for providing support and friendship that I needed.

Last but not the least, I would like to thank my family: Inna, Ihor, Oleh, Nastia and Sviatoslav for supporting me spiritually throughout writing this thesis and my my life in general.

Contents

List of Figures

List of Tables

Abbreviations

ADF	**A**tomic **D**ensity **F**unction
AFT	**A**tomic **F**ragment **T**heory
APFIM	**A**tom-**P**robe **F**ield-**I**on **M**icroscopy
APT	**A**tom **P**robe **T**omography
bcc	**b**ody-**c**entered **c**ubic
BG	**B**ain **g**roup
DF	**D**ark **F**ield
DNA	**D**eoxyribo**n**ucleic **a**cid
EBSD	**E**lectron **b**acks**c**atter **d**iffraction
fcc	**f**ace-**c**entered **c**ubic
FT	**F**ourier **T**ransform
GPM	**G**roupe (de) **P**hysique (des) **M**atériaux
GT	**G**reninger-**T**roiano
IF	**I**nterstitial-**f**ree
KS	**K**urdjumov-**S**achs
MC	**M**onte **C**arlo
MD	**M**olecular **D**ynamic
MT	**M**artensite **T**ransformation
NW	**N**ishiyama-**W**assermann
OR	**O**rientation **r**elationship
PFC	**P**hase **F**ield **C**rystal
PFM	**P**hase **F**ield **M**icroelasticity
PTMC	**P**henomenological **T**heory (of) **M**artensite **C**rystallography
SAD	**S**elected **a**rea **d**iffraction
SEM	**S**canning **E**lectron **M**icroscope
TEM	**T**ransmission **E**lectron **M**icroscopy

For Kama

Introduction

One of the most powerful means of microstructure formation and, consequently, properties improvements of ferrous alloys are phase transformations. The complexity of the phase transformation reactions and the wide spectrum of microstructures requires a fully understanding of phase transition mechanisms at atomic scale. Detailed description of such phenomena in iron alloys permits the emergence of new steels with enhanced engineering properties.

All types of phase transformations can be divided into two different groups: diffusional and diffusionless [24]. The chemical composition of the new phase and the parent phase are not identical in the case of the first type of transformation. A new phase is formed by a long-range diffusion of atoms. The second type of phase transformations, diffusionless, does not involve a change in chemical composition of the parent phase but rather its crystal structure. We will consider both types of transformations.

The aim of the present work is to describe martensite transformation and carbon diffusion in martensite using atomistic approach for modeling phase transitions at atomic scale, in particular, the martensite transformation and the following aging processes in martensite.

This thesis consists of five chapters. The outline of this work is as follows.

In the first chapter, the main aspect of martensite transformation, the mechanism of martensite formation, the martensite morphology and influence of carbon content are considered. Then, the experimental studies of the preliminary stage of aging of martensite are presented. The main objectives and choice of computational method to model martensite transformation and carbon diffusion in martensite phase are discussed.

The second chapter is dedicated to description of computational methods used in this work. First, the Atomic Density Function (ADF) theory on constrain Ising lattice is introduced. Then, a new approach, called the Atomic Fragment Theory (AFT), is described in details. The stability condition which can be applied to study the stability of alloys with respect to concentration fluctuations is presented. The interaction potentials used in the AFT are discussed.

In the third chapter, to show the versatility and efficiency of the AFT the self-assembling dynamics of initially disordering system with increasing topological complexity is tested. In particular, the self-assembly of non-ideal gas/liquid, diamond and zinc-blend structures, single-strand and double-stranded helixes are considered.

In the fourth chapter, the AFT is used to describe the martensite transformation from austenite phase. A detailed description of the initial conditions, choice of interaction potential and computational parameters are given. The obtained simulation results are analyzed in real and reciprocal space. The diffraction patterns and pole figures of the final configurations are constructed. The comparison of the simulation results with experimental studies is given in section discussion.

In chapter five, the ADF theory on constrained Ising lattice is used to describe the redistribution of carbon atoms during aging processes in martensite. In considered model elastic and chemical interatomic interactions are taken into account. The first part of this chapter is dedicated to detail description of the interaction potential, method of calculation of the scattering intensities and the choice of computational parameters. Using ADF approach two diffusion kinetics of carbon atoms in martensite phase are considered. The system with the tetragonality factor $t_1 = -0.1$ which can be associated to bcc Fe-C alloys and the system with $t_1 = -0.27$ which corresponds to Fe-Ni-C alloys. The discussion of the obtained results is given in the last section of this chapter.

The main results are summarized in the conclusions and some future prospects are proposed. Some mathematical calculations and details of methodology used in our work are presented in the appendixes at the end of this manuscript.

Chapter 1

Literature review: martensitic transformations and aging of martensite

1.1 Martensite transformations

The martensite transformation (MT) is a diffusionless transformation when cooperative movements of atoms in crystal lattice induce a phase change in crystal structure. The new phase, which forms from the parent phase, is called *martensite* or α'-phase. During this transformation the parent phase maintains metastable and in carbon steels is called austenite or γ-phase. The MT accompanied by the formation of rich microstructure and its morphology is strongly depended on alloy composition. In general, the MT is observed in different materials, such as nonferrous alloys, pure metals, ceramics, minerals, inorganic compounds, solidified gases and polymers [25].

The process of martensite formation is carried out by quenching. This procedure provides a diffusionless character of transformation. Before transformation, steel is only consist of γ-phase at temperature above the A_3 temperature or the eutectoid temperature, A_1, according to carbon content (see the iron-carbon (Fe-C) diagram in Figure 1.1). When austenite is cooled below A_3 or A_1 temperatures the transformation of crystal lattice occurs. Figure 1.2 schematically shows the free energy temperature dependence for two phases. At temperatures above T_0 the free energy of γ-phase is lower then that of α'-phase. Therefore γ-phase is stable. T_0 is a metastable equilibrium temperature, which corresponds to coexistence of two phases. At temperatures below T_0 the free energy of martensite phase becomes smaller than of austenite one and phase transformation begins. Because the crystal lattices of product and parent phases are different, the growth of new phase induces the elastic strain. Thus, the kinetic barrier for a growth of new phase occurs. If the driving force magnitude is not enough large to overcome the kinetic barrier, then the transformation can be blocked at any stage. To overcome this kinetic barrier and to

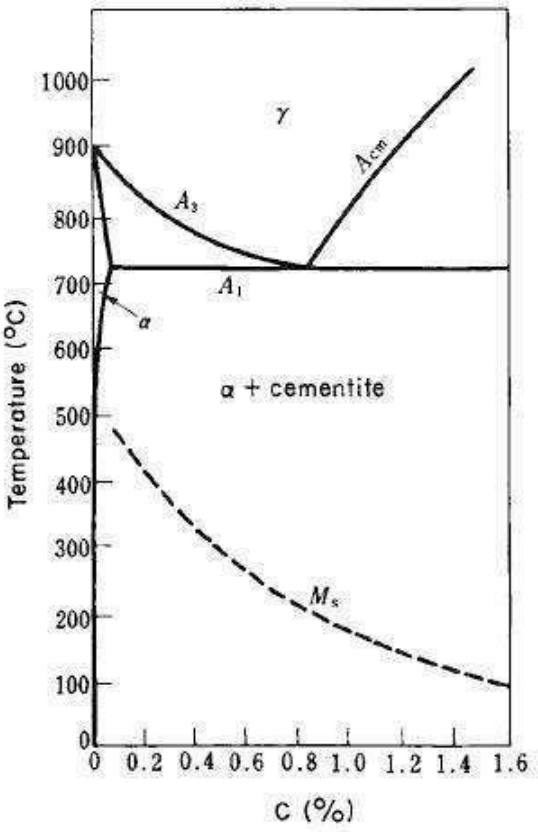

FIGURE 1.1: Phase diagram of Fe-C system shows which phases are to be expected at metastable equilibrium for different combinations of temperature and carbon content [1]. Martensite start, M_s, temperatures as a function of carbon content in Fe-C alloys are shown.

start a martensitic transformation, the system is cooling to the temperature which is known as martensite-start temperature M_s. In Fe-C system the temperature M_s depends of the carbon concentration. It is important to note, that to obtain martensite phase the quenching velocity should be high. Otherwise, during slow cooling, the diffusion of atoms takes place (in particular the carbon atoms diffusion) and as result two phases form: ferrite (α-Fe) and cementite (Fe_3C). In the case of rapid cooling the atoms don't have a time to diffuse. When the temperature M_s is reached, the very rapid growth of the α'-phase starts with a speed close to the speed of sound in metal (~ 1100 ms^{-1} in steel). The martensite transformation is completed at temperature M_f. The experimental measurements show that chemical composition of martensite and austenite is the same. It indicates that martensite transformation is a diffusionless transition.

The γ-phase has a face-centered cubic (fcc) lattice structure with the lattice parameter about $a^{fcc} = 0.356$ nm. Carbon atoms are dissolved in fcc iron matrix. The highest content of carbon in austenite is 2.11 wt.% at 1148 °C. The decreasing of a temperature decreases a carbon solubility and forms the new phase: cemetite or iron carbide (see Fig.1.1). The α iron has less solubility then the γ, about 0.02 wt.% at 727 °C. The crystal lattice of ferrite corresponds to body-centered cubic (bcc) lattice with the lattice parameter $a^{bcc} = 0.286$ nm at

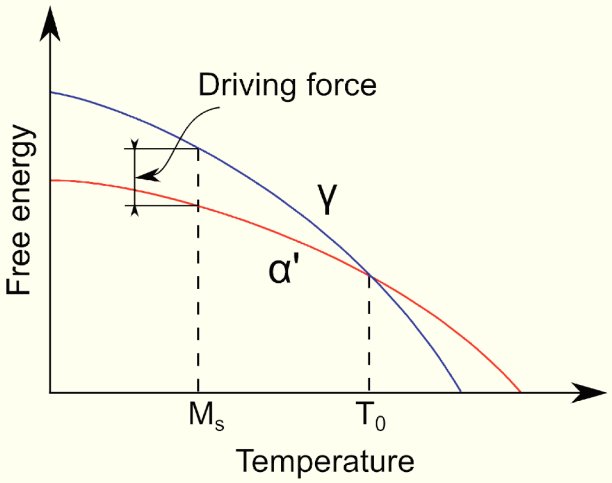

FIGURE 1.2: The schematic plots of the free energy for γ and α' phases, in blue and red, respectively

room temperature.

The location of carbon atoms in the austenite and martensite lattices gives a key to the understanding of the mechanism of phase transformation. In fcc and bcc lattices there are two types of interstitial voids, which can be occupied by carbon atoms: octahedral and tetrahedral interstitial sites (Fig. 1.3, 1.4). The radius of a carbon atom is $r_C = 0.07$ nm. The octahedral

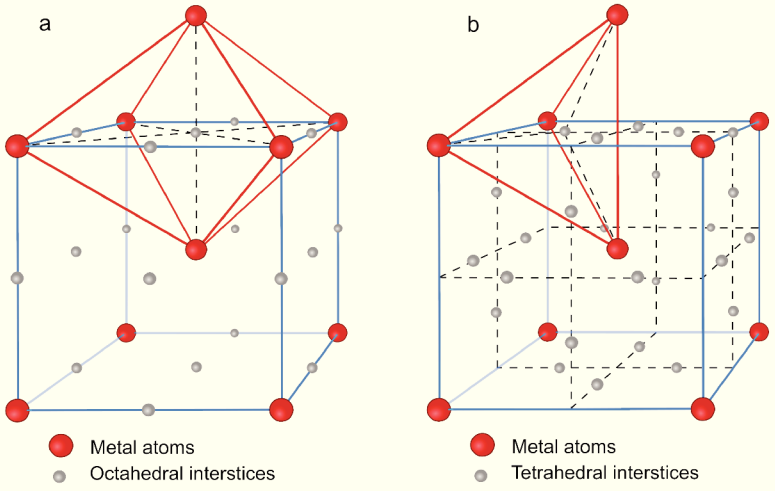

FIGURE 1.3: (a) Octahedral and (b) tetrahedral interstitial voids in bcc structure

interstitial sites of austenite can accommodate the atom of radius about $r_{oct}^{fcc} = 0.052$ nm. The size of tetrahedral voids is smaller: $r_{tetra}^{fcc} = 0.028$ nm. Of course, the octahedral sites are more favorable for carbon atoms, but some lattice expansion is required. The voids in bcc ferrite lattice can accommodate atoms of radii $r_{oct}^{bcc} = 0.019$ nm and $r_{tetra}^{bcc} = 0.035$ nm, that corresponds to octahedral and tetrahedral interstitial voids, respectively. Small sizes of interstitial voids in ferrite explain its very small solubility of carbon.

Thus, carbon atoms in austenite are distributed over the octahedral interstitial sites in fcc lattice. During rapid diffusionless transformation they are trapped in octahedral sites of a bcc

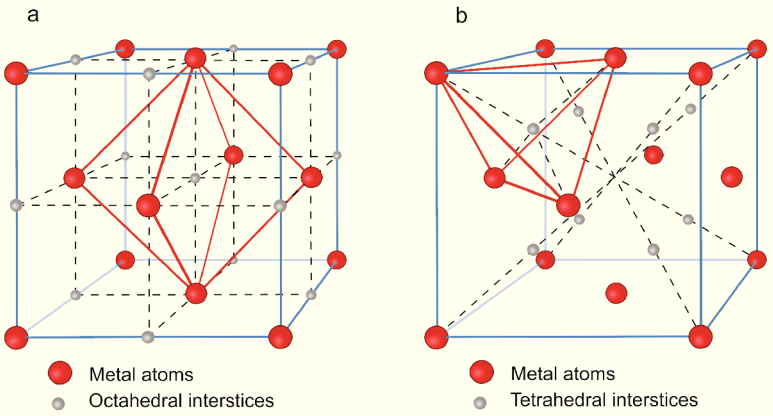

FIGURE 1.4: (a) Octahedral and (b) tetrahedral interstitial voids in fcc structure

lattice (Fig.1.3(a)). Octahedral interstitial sites in bcc lattice are divided between three bcc sublattices (Fig.1.5). The sites of each sublattice are located between two iron atoms in one of

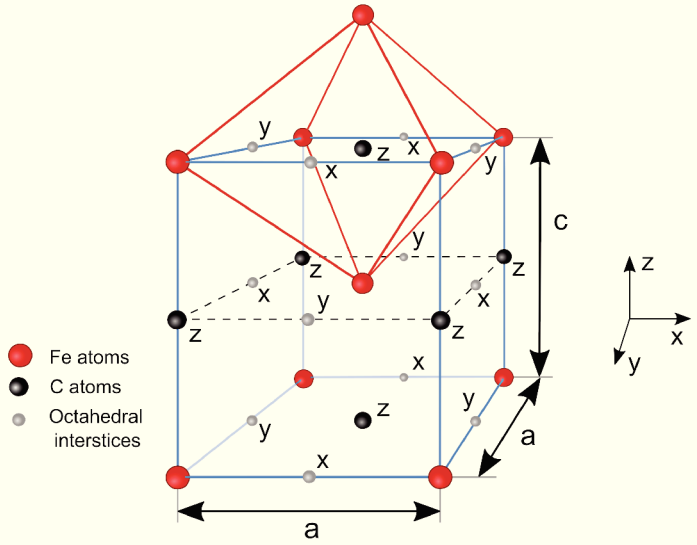

FIGURE 1.5: Martensite body-centered tetragonal crystal structure in Fe-C alloys. The third, O_z, sublattice of octahedral interstitial voids is occupied by carbon atom. Other two sublattices are carbon free

three directions $[100]_{bcc}$, $[010]_{bcc}$ and $[001]_{bcc}$ of the host bcc lattice, which correspond to the first, O_x, second, O_y, and third, O_z, sublattices. After MT carbon atoms occupy mainly only one of them. The octahedral sites in bcc lattice are not symmetrical and each carbon atom displace neighboring iron atoms situated at a distance $a/2$ more that at a distance $a/\sqrt{2}$. If carbon atoms occupied O_z sublattice there is an expansion in $[001]_{bcc}$ direction and a compression in $[100]_{bcc}$ and $[010]_{bcc}$ directions. As a result, the cubic body-centered lattice becames tetragonal (bct). The lattice parameter c of the tetragonal cell is bigger that of other two parameters a. With increasing of the carbon content in the martensite, the axial ratio c/a also increases. The experimental investigations show almost linear axial ratio dependence of the

carbon concentration (Fig.1.6):

$$c/a = 1.000 + 0.046\rho \text{ [26]}, \tag{1.1}$$

where ρ is the carbon concentration in wt.%.

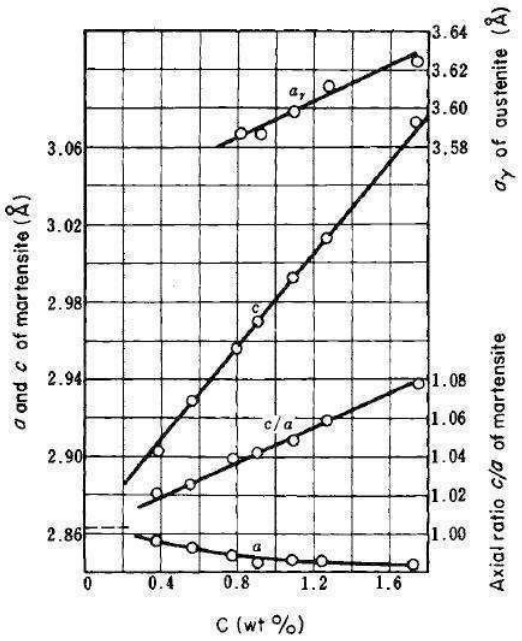

FIGURE 1.6: Lattice constants of tetragonal martensite and austenite in Fe-C steels [1]

The distortion of iron lattice induces the barriers for the dislocation movements and, as a result, big hardness of martensite is observed. Figure 1.7 shows that hardness of martensite grows with increasing of carbon content. Also, martensite steels can acquire some technologically important properties, such as shape memory effect, superelasticity, superplasticity, and high mechanical damping [27].

It is well accepted that mechanical properties of steel are strongly depend on their microstructure. That is why, the understanding and prediction of microstructure formation in steels is a fundamental question for their future development and design. Present understanding of martensite transformations is based on the phenomenological theory of martensite crystallography (PTMC) [25, 28, 29]. This theory is formulated in pure geometrical terms. The basic assumption of the PTMC is the invariance of the planar interface between austenite and martensite phases under the transformations. The change of the crystal structure during martensite transformation induces the macroscopic change of the parent crystal shape and consequently generates a big internal stress inside a material (Figure 1.9(b)). This stress can't be minimized only by the lattice deformation. Thus the lattice invariant transformation occurs and involves deformation of the martensite. PTMC allows to deduce an invariant plane strain deformation from choosing a pure shear lattice invariant deformation and a lattice correspondence between the parent and product phases. To minimize the strain energy, the interfaces between austenite and martensite

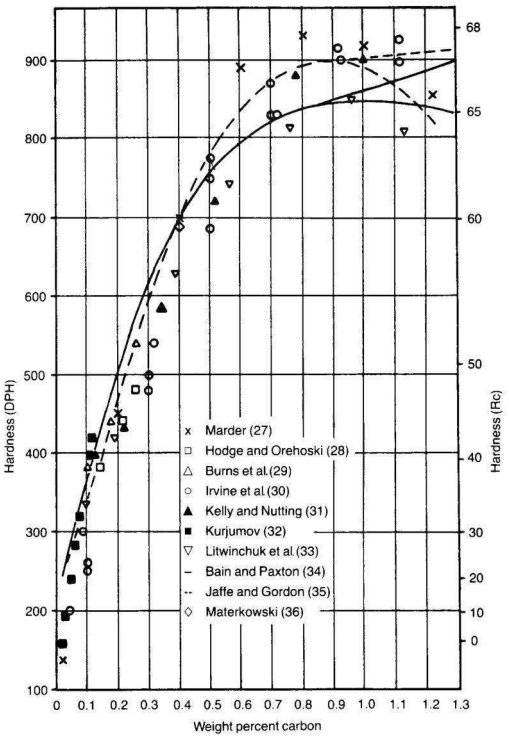

FIGURE 1.7: Hardness of martensite as a function of carbon concentration in steels [2]

should be invariant under the transformation: it should be unrotated and undistorted. This interface is called *habit plane*. Figure 1.8 schematically shows the interface between two phases and the surface tilting which is induced by the shape change. It is worth noting that usually the habit plane is not completely flat and have some curvature. This fact is conditioned by surroundings which constrained the transformation [25] (Figure 1.10(e)).

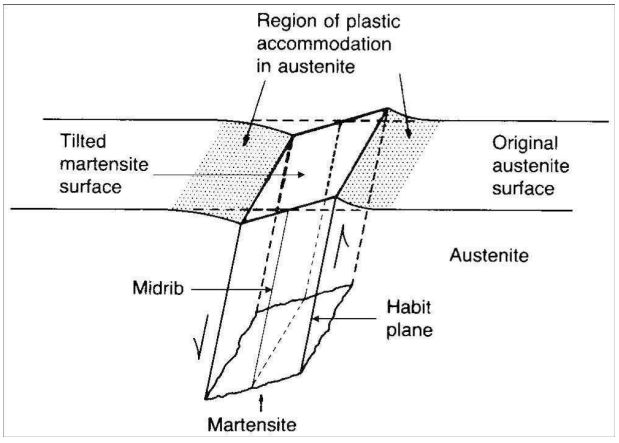

FIGURE 1.8: The schematic representation of the plate martensite and its habit plane

There are two mechanisms of the lattice invariant transformation: slip and twinning. Slip mechanism involves the sliding of the crystal blocks over one other along the definite crystallographic planes. These close-packed planes are called slip planes (Figure 1.9(c)). Slip is generated by the movement of the perfect dislocations. The partial dislocations induce twinning. A twin

structure in a crystalline solid occurs between two adjacent regions of the same crystal lattice, where one of the regions is related to other by a simple shear (Figure 1.9(d)). Figure 1.9 sche-

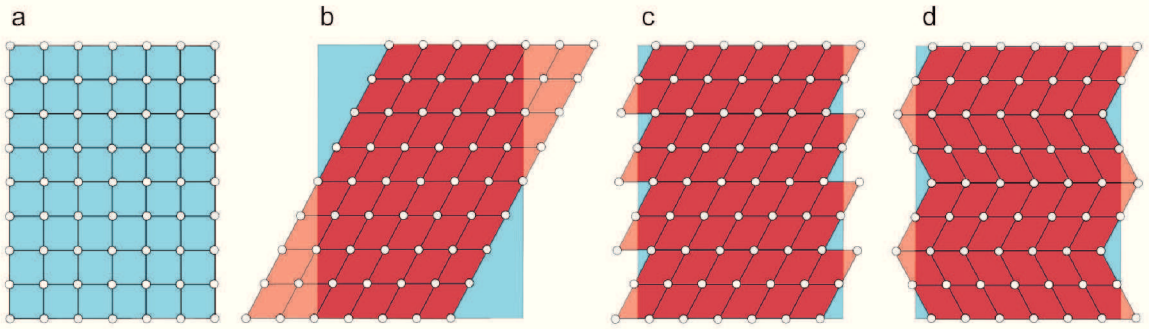

FIGURE 1.9: Schematic representation of the different mechanisms of martensite transformation:(a) undeformed parent crystal; martensite produced by (b) lattice deformation, and by lattice deformation and lattice invariant shear: (c) slip and (d) twinning. The blue rectangle show the position of the parent crystal block

matically shows the lattice-invariant shear which reduces the internal stresses in the material. The habit plane on this figure is presented by the vertical dashed lines. It can be seen that the lattice invariant deformation (by slip or twinning) keep the habit plane unrotated and undistorted [1, 2, 29]. It should be noted that the PTMC is a phenomenological theory that relates the crystallographic features of phases before and after martensite transformation. However, this approach does not consider a movement of individual atoms.

The more general theory of martensite inclusions and the direction of the habit plane between austenite and martensite phases has been propose in [17, 30]. In particular, in these works is predicted that martensite inclusion in austenite matrix should have a thin plate shape aligned along to invariant plane.

1.1.0.1 The characterization of martensite microstructure

The complex microstructure of martensitic steels can be divided into two major types, namely, lath- and plate martensite [1, 2]. In Fig.1.10 the optical micrographs of martensite with a different morphology according to the martensite carbon content are presented. Less commonly, the morphologies named butterfly, thin plate and lenticular martensite [31, 32] have been also observed afterward.

The microstructure of lath martensite is characterized by certain hierarchy (Fig.1.11(a)) [3, 12, 33, 34]: parent austenite grain–packet–block–sub-block–individual lath. The first level of hierarchy is the elementary crystallite, *lath*. Lath is a needle-like morphological unit of martensite, its length is a few microns and less than a micron of a thickness. The laths of martensite are oriented to the austenite prior grain in one of 24 Kurdjumow-Sachs (KS) relationships, which are called KS variants marked as V1, V2,...,V24. All variants can be divided into four groups: V1-V6, V7-V12, V13-V18, V19-V24. Each of these groups have common parallel relationship of close-packed planes of austenite. Laths of the same group form a well-defined *packet*. A prior

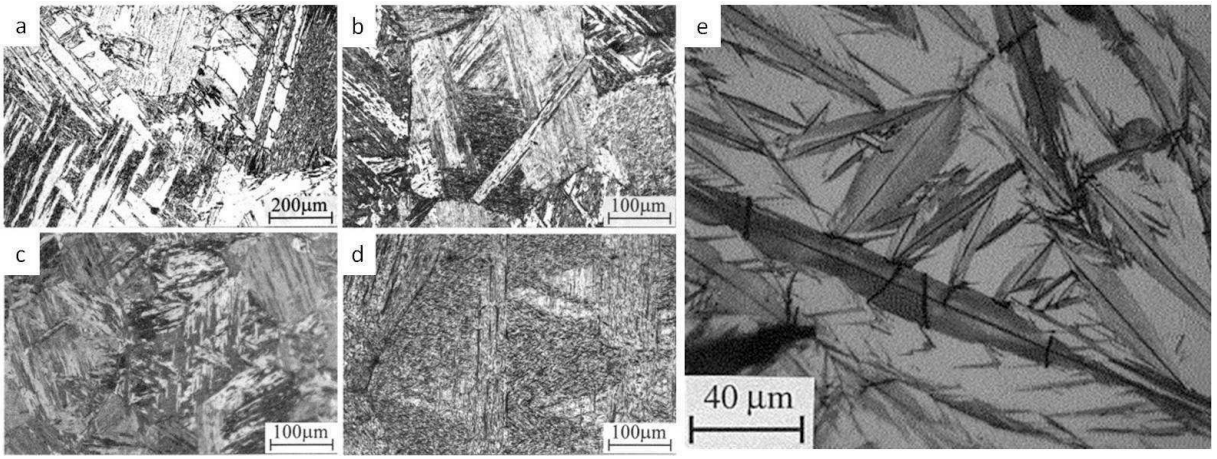

FIGURE 1.10: The optical micrographs of the martensite with different carbon content: (a) Fe-0.0026C, (b) Fe-0.18C, (c) Fe-0.38C, (d) Fe-0.61C alloys with lath microstructure [3] and (e) Fe-1.86C alloy with plate microstructure [4]

austenite grain consists of packets of all four kinds. Within the packet laths form plates, named *blocks*, of three types: B1, B2 and B3. Boundaries between blocks are roughly planar. Each block consists of laths of a single variant or it is a composite of laths of two variants with a small misorientation of 10.53°. For example, in the V1-V6 packet there are three kind of such pairs: V1/V4, V2/V5 and V3/V6, which correspond to B1, B2 and B3 blocks, respectively. Several individual laths of the same variant in a bivariant block form *sub-blocks*, with irregular boundaries. Adjacent blocks in a given packet can contain combinations of variants with three misorientations: 60.0° (V1/V3, V1/V5, V2/V4, V2/V6 and V4/V6), 49.5° (V1/V6, V2/V3 and V4/V5) and 70.5° (V1/V2, V3/V4 and V5/V6). All these variant combinations are interrelated by misorientation angle around $[011]_\alpha$ rotation axis.

There is an interrelation of a variant selection in a packet with a carbon content in the martensite. In the interstitial free (IF) steels the pairing with small misorientation, for example V1/V4, is dominant. The increasing of carbon concentration in steel shifts the dominance of variant pairing from V1/V4 to V1/V2 [5], see Fig.1.11(b-c). At the same time, the size of blocks and packets decreases with increasing of carbon content [3]. For steels with a high carbon content the V1/V16 variant pair is typical, see Fig.1.11(d).

The mechanism, that provides the martensite formation, depends of the carbon content in iron-carbon alloys (Figure 1.10). In low carbon steels with the concentration of carbon < 0.6 wt.% and where the concentration of dislocations is quite high the slip mechanism is more favorable to provide the lattice invariant deformation. In these steels, the slip mechanism produces the lath martensite (Figure 1.10(a-d)) with the habit plane close to $\{111\}_\gamma$ (in the case of twin-free martensite) or $\{557\}_\gamma$ relatively to the austenite phase [1]. Since the carbon atoms block the dislocations and complicate its movements across the crystal the twinning mechanism becomes dominant in high carbon steels [17]. The resulting microstructure of twinning martensite contains the plates with several internal twins and midrib (Figure 1.10(e)). The increasing of

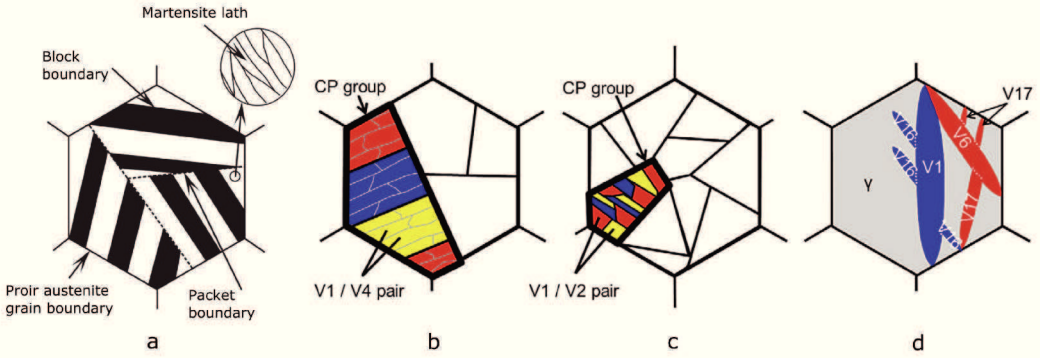

FIGURE 1.11: (a) Schematic representation of the characteristic morphology of lath martensite in an austenite grain; schematic diagram showing a change in microstructure of lath martensite in (b) interstitial-free (IF) steel, (c) 0.75C alloy, (d) 1.8C alloy. The same color in packet (close-packed (CP) group) represents variants of the same Bain group [5].

the carbon content increases the fraction of plate martensite and at concentration of carbon of about 1 wt.% the plate shape is favorable (Fig.1.12). The observed habit planes in high-carbon

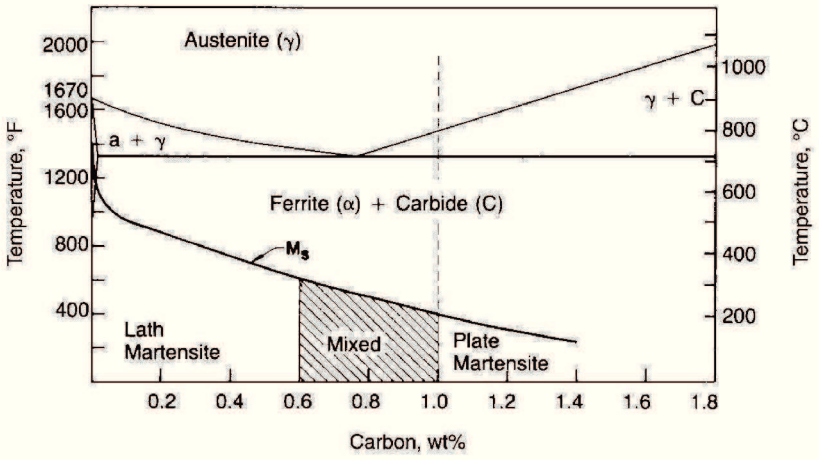

FIGURE 1.12: The transition from lath to plate martensite with increasing carbon content [2]

steels are $\{225\}_\gamma$ or $\{259\}_\gamma$ [1].

The $\{259\}_\gamma$ habit plane is more favorable at low temperature of martensite transformation and the product phase has GT or NW relations with austenite. But the martensite with the $\{225\}_\gamma$ habit plane has KS ORs with parent phase [2].

1.1.0.2 The nucleation and growth of martensite

The consideration of the strain energy minimization is not enough to understand the morphology of martensite and its formation. To describe the formation and growth of martensite nucleus the transformation dynamics should be understood.

The strain energy contribution to the nucleation barrier of a single variant martensitic particle is too high to overcome by thermal fluctuations, this is why it was suggested that there are pre-existing martensitic embryos around a dislocation defect. A detailed review of the

general mechanism of martensitic nucleation, that is assisted by crystal defects, can be found in [35–37]. These embryons are a complex nanoscale assemblages of martensitic microdomains rather than a homogeneous single-domain particle. The developing of a model of the MT, which describes the formation of a complex microstructure, seems to be too complicated problem to solve it analytically. This is why a better insight into the development of martensite structure could be given by numerical methods.

In 1990s computer simulations of the MT dynamics has been performed using the Monte Carlo (MC) simulation [38] (in 2D), the molecular dynamic (MD) method [39] (in 3D at the microscopic scale), the phase field microelasticity (PFM) approach [40]. Recently the Phase Field method was used [14] to investigate a MT. In particular, it was shown in order to growth a martensite nuclei are transformed into multivariant cluster.

1.2 Aging of the martensite

The product phase of the martensite transformation is unstable with respect to increasing temperature after quenching (here, the temperatures below the temperature of austenite formation are considered). The heating of martensite is called tempering or aging. Commonly, the tempering is used to increase toughness, ductility, fracture resistance of steel, but at the same time the tempering is accompanied by reduction of strength[41] and hardness in the material. These changes of properties in steels are caused by the structural changes in martensite due to its instability at tempering. The supersaturation of carbon atoms in the crystal lattice of martensite, the retained austenite, the high density of dislocations are driving forces that induce carbide formation and the ferrite matrix growth [2, 4]. The earlier stages of tempering at the temperature range slightly above and below the room temperature (from -40 to 100°C) are separately allocated in tempering. It is termed the room-temperature aging or the zeroth stage of tempering. The aging corresponds to the stage when changes in martensite structure are not accompanied by the carbide formation. The carbide-forming stages are classified as tempering.

Further, we will focus on the structural changes taking place in the aging processes in steels at room temperature. There are many experimental investigations of martensite aging that used the numerous techniques: X-ray [42] and neutron diffraction, transmission electron microscopy (TEM)[6–9, 43, 44], atom-probe field-ion microscopy (APFIM)[7, 45–47], Mössbauer spectroscopy. In particular, it has been shown that aging kinetics are controlled by carbon atoms diffusion [48].

Olson and Cohen [49] distinguished two stages of aging. At the first stage (A1) carbon-rich clusters are formed, then at the second stage (A2) a fine modulated tweed microstructure appears, that contains elastically distorted carbon-deficient regions. Carbon atom clusters occur between 270 and 370 K. Nagakura and coworkers [6, 8] associated diffuse spikes around the fundamental spots on the diffraction pattern with clustering of carbon atoms. The diffusion spikes are elongated very close to [102] direction. The exact direction of carbon clusters can

be defined from the angle θ between c-axis and diffusion spikes, Fig.1.13. With increasing of

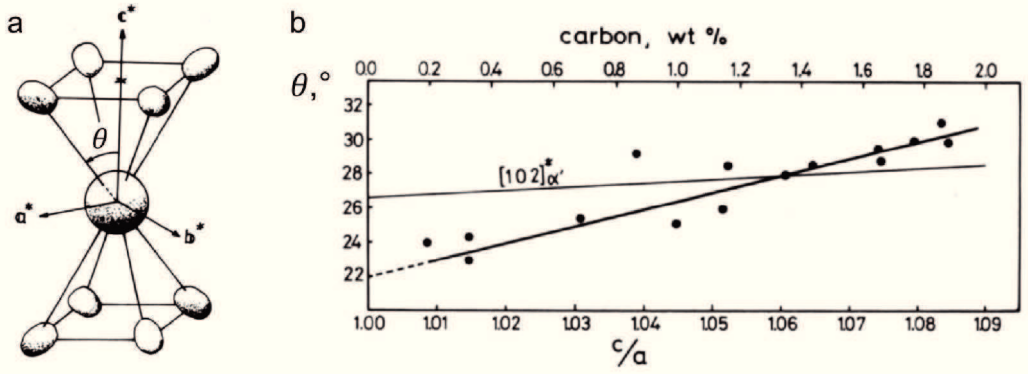

FIGURE 1.13: (a) Schematic representation of satellite spots intensity distribution. Vectors $\mathbf{a}^*$, $\mathbf{b}^*$, $\mathbf{c}^*$ are unit translations in reciprocal space. (b) Dependence of the angle θ between the direction of the spike of diffraction spot and the $\mathbf{c}^*$ axis, against the axial ratio $\frac{c}{a}$. Thin line corresponds to the angle between $[102]_{\alpha'}$ and the $\mathbf{c}^*$ axis [6].

carbon content the angle θ grows. A model for the modulated structure is shown in Fig.1.14.

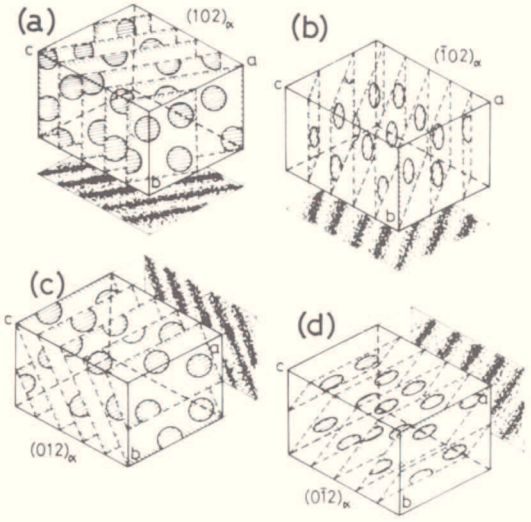

FIGURE 1.14: Cluster model of the modulated structure [6] with four possible directions (a), (b), (c), (d) of the structural modulation in martensite. The carbon concentration fluctuations are shown by the projection along the a and b axes.

In the Fe-Ni-C alloys the direction of diffuse spikes elongation is close to [023] direction [7]. The change of carbon content also leads to the change in angle θ, as it is shown in Fig.1.15. Also it should be noted that diffuse spikes become more intense with increasing of the carbon content in martensite.

The elongation of diffuse spikes only in $\langle 023 \rangle$ directions, that can be seen in Fig.1.15, but not in $\langle 203 \rangle$ or $\langle 230 \rangle$ directions, indicates that only one octahedral sublattice is occupied by the carbon atoms in the iron lattice therefore martensite is tetragonal. The preferential selection of only one of octahedral sublattices can be treated as a kinematical effect that occurs after displacive transformation, as it was described above, or it can be interpreted as a result of

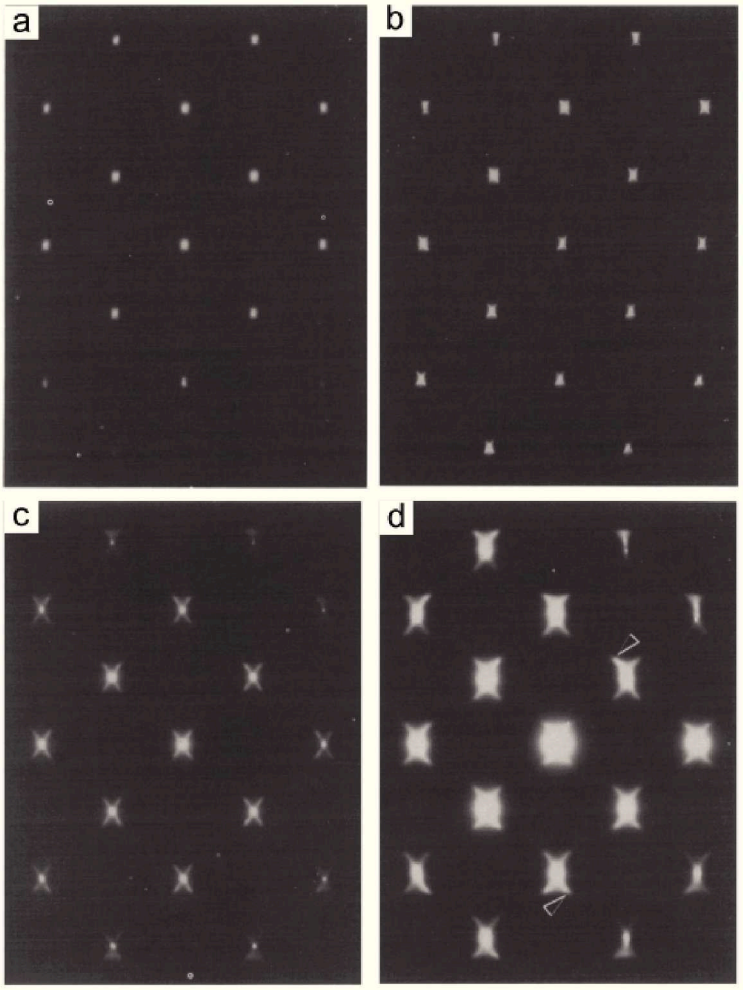

FIGURE 1.15: [100] diffraction patterns from martensites (a) Fe-25Ni-0.2C aged for 2 days, (b) Fe-25Ni-0.4C aged for 2 hours, (c) Fe-15Ni-1C aged for 26 minutes, (d) Fe-1.8Mn-1.8C aged for 8 days [7].

orientational ordering. Thus, the random occupation of all three sublattices by carbon atoms is considered as disordered state, in this case the lattice of iron is cubic. The phenomenological model describing the orientational ordering, first, was proposed by Zener in 1948 [16]. This model is called as *Zener ordering* model and the tetragonal martensite is referred as *Zener-ordered* martensite.

According to Zener model, the Zener-ordering is driven by the elastic interactions between carbon impurity atoms. Later, Kurdjumov and Khachaturyan [17, 50] proposed more fundamental approach based on the static concentration waves method [17] and microscopic elasticity theory [17, 51–53]. It has been shown that repulsive carbon-carbon chemical interactions should be taken into account in the description of the order/disorder transition. In both models, of Zener and Khachaturyan, a composition-depended critical temperatures for carbon ordering are predicted. The critical carbon concentration at room temperature in Zener model is 0.25 wt.%, while according to the model of Khachaturyan the critical concentration is much smaller 0.03

wt%. The experimental study [42] of the cubic/tetragonal transition of martensite at room temperature gives the value of carbon critical concentration about 0.18 wt%.

In the aged martensite at temperatures somewhat higher then room temperature (60-80°C) a long-period phase was identified by analyzing of superlattice spots in electron diffraction patterns [9, 54]. The determined structure is orthorhombic, elongated along to the c-axis of martensite with lattice parameters $a = b = \sqrt{2}a_0$ and $c = 12c_0$, where a_0 and c_0 are the lattice parameters of martensite. This long-period ordered phase has the composition Fe_4C. Fig.1.16 shows possible structures of this long-period ordered phase.

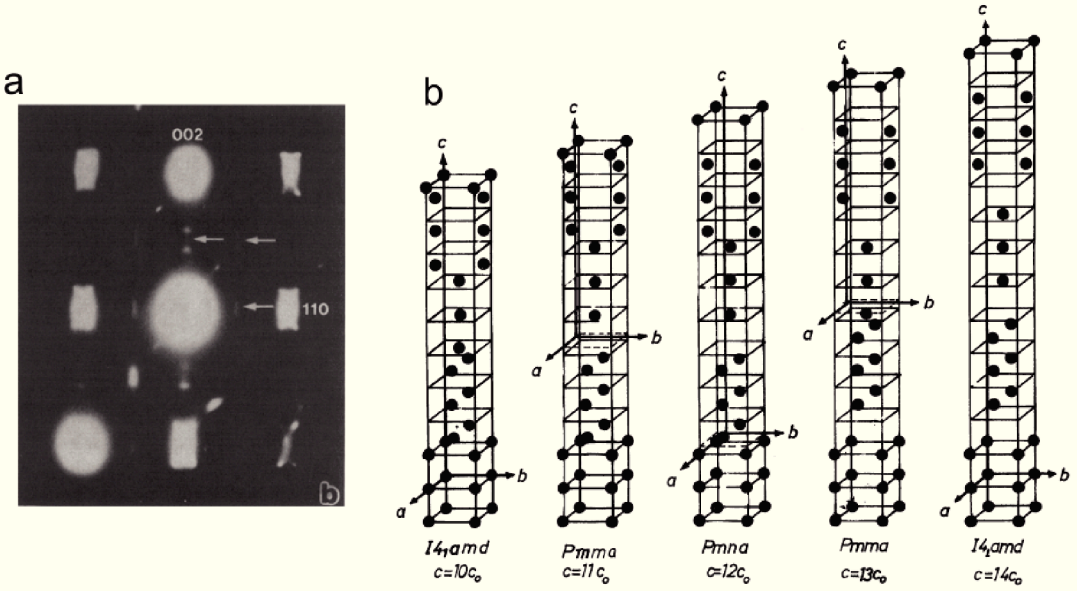

FIGURE 1.16: (a) $[1\bar{1}0]$ diffraction pattern from Fe-1.62C martensite [8]. (b) Possible crystal structures of long-period ordered phase with super periods $c = 10c_0$, $c = 11c_0$, $c = 12c_0$, $c = 13c_0$ and $c = 14c_0$ from left to right [9]. Black circles represent positions of carbon atoms.

To study the compositional fluctuations in martensite that occur during earlier stages of aging the atom-probe analysis was also used. In particular, it has been shown that in carbon-rich regions the carbon content is lower than would be expected for Fe_4C. The maximum carbon concentration at the earlier stages of aging at room temperature was of the order of 11at% C for the Fe-15Ni-1C martensite [46] and 10at% C for the Fe-23Ni-0.42C [45]. More recent 3D atom-probe studies [47] have confirmed that the concentration of the high-carbon regions at around 10at% is typical for room temperature aging of the Fe-Ni-C martensite. The composition fluctuations of the high-carbon regions continuously increase and gradually attain its equilibrium (or metastable equilibrium) value. To explain the continuous increase in compositional amplitude with time during aging and occurrence of the modulated structure the decomposition by a spinodal mechanism has been suggested [7, 17, 55].

The carbon concentration of 10-11 at.% corresponds to approximately Fe_8C or $Fe_{16}C_2$ stoichiometry. For such a concentration the carbon-rich regions can be described as a structure,

that is isostructural to the nitride $Fe_{16}N_2$ (α''-phase). Although the α''-phase experimentally was never been observed, it can be obtained from the γ'-Fe_4C phase received from Mössbauer spectroscopy and X-ray diffraction. Fig.1.17 illustrating that systematic removal of half of the carbon atoms from Fe_4C gives $Fe_{16}C_2$ structure. Later, Sinclair and coworkers [56] using mole-

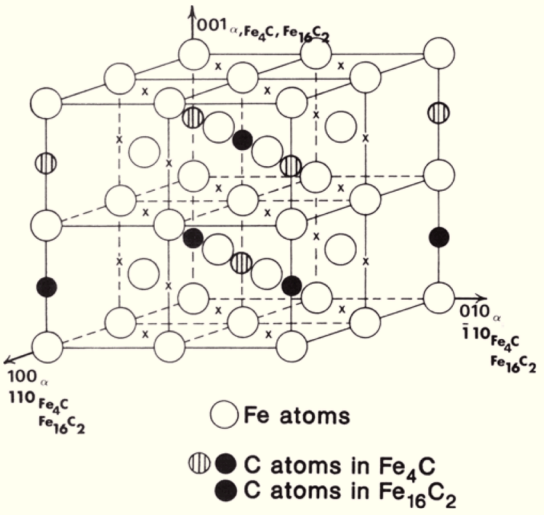

FIGURE 1.17: Schematic representation of Fe_4C and $Fe_{16}C_2$ structures [7].

cular dynamics study confirmed the possibility of formation of the α''-$Fe_{16}C_2$ phase. But there are no diffraction evidence for $Fe_{16}C_2$ structure, it can not be assumed that high-carbon regions are fully ordered in this structure.

The aim of our study is to understand at atomic scale the different steps of the martensitic transition and following redistribution of carbon atoms in martensite.

1.3 Modeling methods

In the last 25 years, a significant progress has been done in description of kinetics in multi-components systems at atomic scale using MD and Monte carlo simulations. These methods supplement each other. The MD, is a straightforward approach to a numerical solution of equations of motions for 6N dynamic variables where N is the number of atoms. However, a sheer number of variable limits the size of studied systems to $N \sim 10^5$ and time of its evolution to $t \sim 10^{-8}$ s. Recent modifications of MD by coarse graining improve the addressable time but at expense of the lost spatial resolution. However, the MD is still not well-suited to study slow evolving systems with the typical diffusion time scale. The MC alternative complements the MD since it can be applicable to the diffusional time scale. A stochastic sampling in the MC dynamics requires a generation of a Markov chain that takes a significant time because it requires a search and update of databases, time scale separation and one process-at-a time execution. To model microstructure evolution with complex morphologies we need powerful method that would allow to investigate long-time evolution of systems at atomic scale.

Such a method was developed by Khachaturyan [17, 57, 58]. It is based on kinetic theory formulated in terms of the crystal lattice site diffusion in a solid solution. The investigations of the kinetic evolution in this method are provided by solving Onsager microscopic diffusion equations. This theory is also named as atomic density function (ADF) theory on constrained Ising lattice. It can be applied to model solid-solid isostructural transformations as ordering, decomposition, coarsening etc.

In 2002, Elder propose a phase field crystal method (PFC) [59, 60] to model long temporal evolution of materials at the atomic length scale. The phase field in this model has been interpreted as an atomic density function in the continuum space. There are a lot of applications of PFC in modeling crystallization, elastic deformations in materials, formation of dislocations.

Later in [61] Jin and Khachaturyan developed more general ADF theory. They showed that the phenomenological PFC theory is a particular case of ADF approach.

However, there are still significant difficulties of atomic scale prototyping of a slow diffusional self-organisation of atoms in complex structures. This is especially the case if the evolution is in the continuum space, the system consists of comparatively large number of atoms, and evolution time is long, ranging from a fraction of seconds to years.

In [62, 63] we propose such an approach that may be supplemental to MD and MC and addresses their aforementioned limitations in computationally very effective way. This development turned out to be possible because we (1) introduced a characterisation of a multi-atomic system in terms of quasiparticles named fratons, (2) proposed a new simple form of phenomenological model potentials describing a directionality, length and strength of atom-atom bonding and (3) used the kinetic equations of the atomic density field (ADF) theory describing the atomic scale diffusion. In this work we will show that proposed approach is able to successfully simulate a self-assembly of high-complexity structures and we will apply this approach to model a martensite transformation.

Chapter 2

Atomic Fragment Theory in Self-Assembly of Atoms

Properties of material at macroscale are often determined by its structure at microscale. Recently, phase field crystal method (PFC) has been proposed to model a temporal evolution of materials at atomic length scale [59, 60]. More general formulation of this approach, Atomic Density Function (ADF), has been proposed in [61]. In ADF theory the atoms are associated to a periodic field of the atomic densities which considered as the occupation probabilities.

It was shown that the ADF theory is capable to correctly reproduce the elastic and plastic deformations of crystals, diffusion of defects, liquid-solid transition, structural transformations [57, 61, 64]. In general case this dynamic is taken place at time range that can be spread from a fraction of seconds to years. However, at present, there are still significant difficulties to prototype the evolution of complex structure at atomic scale with large number of atoms, especially, if it starts from initially disordered distribution of atoms. In this chapter the Atomic Fragment Theory (AFT) [62, 63] will be introduced and some example of its applications will be done.

2.1 ADF on constrained lattice

At first, we will present the ADF approach on the constrained Ising lattice proposed by Khachaturyan in [17]. This approach can be used to model isostructural phase transformation and order/disorder phase transition. Since we will use ADF approach for studying of processes in Fe-C system, where carbon atoms occupy interstices of the host iron lattice, the following description of the method is applied only to interstitial solid solutions. In general case, the atomic configuration can be described by random variable $c(\mathbf{r})$ which can take 1 or 0 values:

$$c(\mathbf{r}) = \begin{cases} 1, & \text{if site } \mathbf{r} \text{ is occupied by atom,} \\ 0, & \text{otherwise.} \end{cases} \tag{2.1}$$

In this approach, the atomic configuration is described by a single-site occupation probability function $n(\mathbf{r},t) = \langle c(\mathbf{r})\rangle_t, \quad 0 \leq \langle c(\mathbf{r})\rangle_t \leq 1$. Where symbol $\langle \ldots \rangle_t$ means averaging over the time-dependent ensemble of occupation numbers $c(\mathbf{r})$The function $n(\mathbf{r},t)$ defines of probability of finding atom in site $\mathbf{r}$. The vector $\mathbf{r}$ indicates a site of the computational grid, which is playing a role of the underlying Ising lattice. All sites of Ising lattice are crystallographically equivalent. In multi-component system with different kind of atoms, several occupation probabilities $n_\alpha(\mathbf{r},t)$ should be defined, where index $\alpha = 1,2,\ldots,m$ corresponds to different kind of atoms.

2.1.1 Free Energy Functional

The occupation probabilities, $n_\alpha(\mathbf{r})$, have similarity to the Fermi-Dirac functions (see for example [65]), hence each site can be occupied or not by one atom of kind α, the occupation probabilities, $n_\alpha(\mathbf{r})$, can be assimilated to the Fermi-Dirac distribution function:

$$n_\alpha(\mathbf{r}) = \left[\exp\left(\frac{-\mu_\alpha + \Phi_\alpha(\mathbf{r})}{k_B T}\right) + 1\right]^{-1}, \tag{2.2}$$

where k_B is Boltzmann constant, T is the temperature, μ_α is the chemical potential, $\Phi_\alpha(\mathbf{r})$ is a mean field potential. In the case of conservative system, the conservation condition is:

$$\sum_{\mathbf{r}} n_\alpha(\mathbf{r}) = \sum_{\mathbf{r}} \left[\exp\left(\frac{-\mu_\alpha + \Phi_\alpha(\mathbf{r})}{k_B T}\right) + 1\right]^{-1} = N_\alpha. \tag{2.3}$$

In mean field approximation $\Phi_\alpha(\mathbf{r})$ can be expressed as:

$$\Phi_\alpha(\mathbf{r}) = \sum_{\beta=1}^{m} \sum_{\mathbf{r}'} w_{\alpha\beta}(\mathbf{r}-\mathbf{r}') n_\alpha(\mathbf{r}'), \tag{2.4}$$

where $w_{\alpha\beta}(\mathbf{r}-\mathbf{r}')$ is the pairwise interaction energy of α-β pair of atoms situated at $\mathbf{r}$ and $\mathbf{r}'$, respectively. Summation over $\mathbf{r}'$ and β in Eq.(2.4) is carried out over all N_0 sites of the computational grid lattice and over all kinds of atoms ($\beta = 1,2,\ldots,m$), respectively. Substituting (2.4) in Eq.(2.2) yields:

$$n_\alpha(\mathbf{r}) = \left[\exp\left(\frac{-\mu_\alpha + \sum_\beta \sum_{\mathbf{r}'} w_{\alpha\beta}(\mathbf{r}-\mathbf{r}') n_\alpha(\mathbf{r}')}{k_B T}\right) + 1\right]^{-1}. \tag{2.5}$$

In the ADF approach the free energy functional can be written as:

$$F = F(\{n_\alpha(\mathbf{r})\}, T) = U - TS - \sum_{\mathbf{r}} \sum_{\alpha=1}^{m} \mu_\alpha n_\alpha(\mathbf{r}). \tag{2.6}$$

Here U is internal energy of system and S is entropy. The entropy can be written as:

$$S = -k_B \sum_{\mathbf{r}} \left[\sum_{\alpha=1}^{m} n_\alpha(\mathbf{r}) \ln n_\alpha(\mathbf{r}) + \left(1 - \sum_{\alpha=1}^{m} n_\alpha(\mathbf{r})\right) \ln \left(1 - \sum_{\alpha=1}^{m} n_\alpha(\mathbf{r})\right) \right]. \tag{2.7}$$

The model Hamiltonian is given by

$$H = \frac{1}{2} \sum_{\mathbf{r},\mathbf{r}'} \sum_{\alpha=1}^{m} \sum_{\beta=1}^{m} w_{\alpha\beta}(\mathbf{r} - \mathbf{r}') n_\alpha(\mathbf{r}) n_\beta(\mathbf{r}'). \tag{2.8}$$

In this expression, the summation over $\mathbf{r}$ and $\mathbf{r}'$ and on the all kinds atoms in Eq.(2.8) is carried out over all N_0 sites of the computational grid lattice.

Then using Eqs.(2.6), (2.7), (2.8) Helmholtz free energy can be presented in mean field approximation [17] as

$$\begin{aligned} F(\{n_\alpha(\mathbf{r})\}, T) &= \frac{1}{2} \sum_{\mathbf{r},\mathbf{r}'} \sum_{\alpha=1}^{m} \sum_{\beta=1}^{m} w_{\alpha\beta}(\mathbf{r} - \mathbf{r}') n_\alpha(\mathbf{r}) n_\beta(\mathbf{r}') + \\ &+ k_B T \sum_{\mathbf{r}} \left[\sum_{\alpha=1}^{m} n_\alpha(\mathbf{r}) \ln n_\alpha(\mathbf{r}) + \left(1 - \sum_{\alpha=1}^{m} n_\alpha(\mathbf{r})\right) \ln \left(1 - \sum_{\alpha=1}^{m} n_\alpha(\mathbf{r})\right) \right] - \\ &- \sum_{\mathbf{r}} \sum_{\alpha=1}^{m} \mu_\alpha n_\alpha(\mathbf{r}). \end{aligned} \tag{2.9}$$

Then the minimization of this energy will define the equilibrium state of this system.

2.2 Atomic Fragment Theory(AFT)

Since the ADF theory on constrained lattice is a discrete model, it cannot be applied to model phase transitions, which induce displacements of atoms. For example, this approach cannot be applied for the description of diffusionless transformations, where structural transition occur by displacements of atoms. Also, the discrete model cannot describe the atomic configuration near grain boundaries, solid-liquid transition, self-assembly phenomena of austenite-martensite transformation. To describe all these phenomena continuous models should be developed.

In our work the continuous version of the ADF model was developed. We called this new approach the Atomic Fragment Theory (AFT). In this method two novel concepts have been introduced: the atomic pseudoparticles and a new form of the model Hamiltonian. In the AFT is assumed that each atom is a sphere comprised of its finite elements, which are atomic fragments, and treat these fragments as pseudo-particles. These pseudo-particles are named fratons. The fratons are considered as interacting pseudo-particles occupying sites of the computational grid playing a role of the underlying Ising lattice. In the proposed fraton model, the configurational degrees of freedom are occupation numbers, $c(\mathbf{r})$, where the vector $\mathbf{r}$ describes a site of the computational grid lattice. The function $c(\mathbf{r})$ is equal to either 1 if the site at $\mathbf{r}$ is occupied by

a fraton or 0 if it is vacant.

$$c(\mathbf{r}) = \begin{cases} 1, & \text{if site } \mathbf{r} \text{ is occupied by fraton,} \\ 0, & \text{otherwise.} \end{cases} \tag{2.10}$$

At finite temperature, T, the system is described by averaging over the time-dependent ensemble. The averaging gives the occupation probability, $\rho(\mathbf{r},t) = \langle c(\mathbf{r})\rangle_t, \quad 0 \le \langle c(\mathbf{r})\rangle_t \le 1$, where the symbol $\langle \ldots \rangle_t$ implies averaging over the time-dependent ensemble and t is time. *The occupation probability, $\rho(\mathbf{r},t)$, in fact, is the probability that a point $\mathbf{r}$ is anywhere inside the volume of any sphere describing an atom at the moment t.*

In the multi-component systems, the number of types of fratons is equal to the number of different atomic components of the system.

2.2.1 Model Potential

In the AFT the Helmholtz energy, F, is determined by the Eq.(2.9), where F is a functional of the occupation probabilities $\{\rho_\alpha(\mathbf{r})\}$.

The proper choice of a model Hamiltonian describing the interaction of fratons should result in both their "condensation" into atomic spheres and the movement of the spheres into the desirable equilibrium atomic configuration driven by the spontaneous minimization of the free energy. The model Hamiltonian (2.8) uses the Connolly-Williams approximation [66, 67] mapping in this case the fraton-fraton interaction into the interaction of their pairs. The chosen fraton-fraton interaction model potential $w_{\alpha\beta}(\mathbf{r}-\mathbf{r}')$ should guarantee the self-assembly of initially randomly distributed fratons into a desirable structure. The Fourier transform (FT) of such a potential is:

$$\widetilde{w}_{\alpha\beta}(\mathbf{k}) = \frac{1}{N_0}\sum_{\mathbf{r}} w_{\alpha\beta}(\mathbf{r}) e^{-i\mathbf{kr}}, \tag{2.11}$$

where the summation is carried out over all sites of the Ising lattice (grid), and the wave vector, $\mathbf{k}$, is defined at all quasi-continuum points of the first Brillouin zone of the computational grid, that is, at all N_0 the points in the k-space permitted by the periodical boundary conditions.

To model the spontaneous self-assembly of a disordered atomic distribution into chosen in advance 3D atomic structures of arbitrary geometric complexity we introduced a new approach in a formulation of model potential based on the concepts of structural clusters and cluster amplitudes.

A structural cluster is defined as a minimum size group of geometric points (cluster) whose size is just sufficient to fully reproduce the topological features of the desirable final configuration of the α-atoms. An amplitude of structural cluster of the kind α and is defined as:

$$\Psi_\alpha^{clstr}(\mathbf{k}) = \sum_{j_\alpha} w_j(\alpha,\mathbf{k}) e^{-i\mathbf{kr}_{j_\alpha}}, \tag{2.12}$$

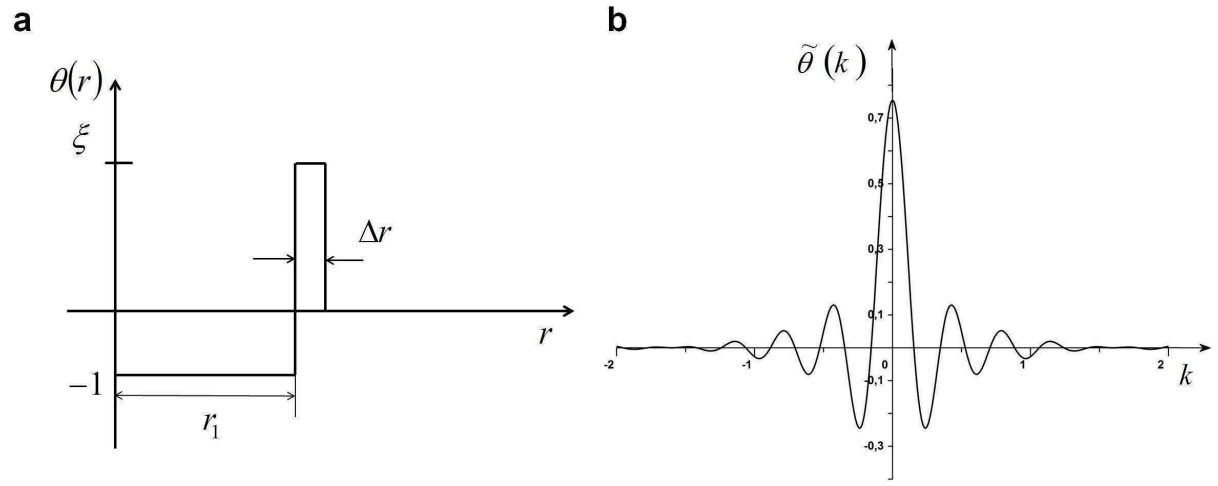

FIGURE 2.1: (a)Schematic representation of short-range potential $\theta(r)$. (b)Example of FT of $\theta(r)$ with the following input parameters: $\xi = 4$, $\Delta\hat{r} = 0.25$.

where summation is carried out over all points of the α-kind cluster, the index j_α numbers these points, and $w_j(\alpha, \mathbf{k})$ is the weight of the contribution of each point of the cluster to its amplitude. The constants $w_j(\alpha, \mathbf{k})$ are chosen to reproduce the desirable thermodynamic and mechanical properties of the simulated atomic aggregate.

With these definitions, we present the Fourier Transform of the model potential as sum of what we call the short-range and long-range interactions:

$$\widetilde{w}_{\alpha\beta}(\mathbf{k}) = \lambda_1 \tilde{\theta}_\alpha(\mathbf{k})\delta_{\alpha\beta} + \lambda_2 \Psi_\alpha^{clstr}(\mathbf{k})\Psi_\beta^{clstr}(\mathbf{k})^*. \tag{2.13}$$

Here $\delta_{\alpha\beta}$ is the Kronecker delta function. The function $\theta_\alpha(\mathbf{r})$ and its Fourier Transform $\tilde{\theta}_\alpha(\mathbf{k})$ are the spherically symmetric functions describes the short-range fraton-fraton pair interaction. It is responsible for the spontaneous "condensation" of fratons into atomic spheres. λ_1 is a constant which determines the strength of the short-range atomic repulsion. The second term of Eq.(2.13) describes the long-range part of the fraton-fraton pair interaction responsible for the mutual arrangement of atoms in the final desired configuration. It is presented as a bilinear expansion in cluster amplitudes, $\Psi_\alpha^{clstr}(\mathbf{k})$. λ_2 in (2.13) is a fitting parameter determining a strength of the long-range interaction.

The simplest choice of the short range part of the interaction potential $\theta(\mathbf{r})$ is a step function, which is shown in Fig.2.1(a). The Fourier Transform of the function, $\widetilde{\theta}(\mathbf{k})$, schematically shown in Fig.2.1, and can be written as

$$\begin{aligned}\widetilde{\theta}(\mathbf{k}) &= \frac{4\pi}{k^3}\left(-\left(\sin\left(kr_1\right) - kr_1\cos\left(kr_1\right)\right)\right) \\ &+ \frac{4\pi}{k^3}\xi\left(\left(\sin\left(k\left(r_1+\Delta r\right)\right) - k\left(r_1+\Delta r\right)\cos\left(k\left(r_1+\Delta r\right)\right)\right) - \left(\sin\left(kr_1\right) - kr_1\cos\left(kr_1\right)\right)\right),\end{aligned} \tag{2.14}$$

where the constant r_1 is the radius of attractive part of short range interaction potential, r_1 being a length parameter determining atomic radius, Δr is the width of its repulsive part and $\xi = \frac{|\theta_{max}(\mathbf{r})|}{|\theta_{min}(\mathbf{r})|}$ is the ratio between the modules of minimum and maximum value of the shape function presented in Fig.2.1.

It should be mentioned, that the smooth dependencies of the function $\theta(\mathbf{r})$ on $\mathbf{r}$ are also possible if they have similar topological features, and ensure attractive and repulsive parts of the short range interaction.

The free energy (2.9), corresponding to the mean field approximation [17], is asymptotically accurate at low and high temperatures, and its accuracy asymptotically increases if the interaction radius is much greater than the distance between interacting particles. The last condition is automatically satisfied in our case because the continuous movement of atoms can be satisfactory described only if the computational grid increment playing the role of the spacing of the Ising lattice is much smaller than the atomic radius.

2.3 Response Function and instability of homogeneous state with respect to infinitesimal fluctuations

To consider the stability of system with respect to fluctuations next development can be done. In this subsection the stability condition will be establish based on the introduction of the response function. The approach used in this section can be applyed in both cases: the ADF theory and the AFT. At temperature near the temperature of the phase transition, the occupation probabilities can be written as

$$n_\alpha(\mathbf{r}) = \bar{n}_\alpha + \Delta n_\alpha(\mathbf{r}), \tag{2.15}$$

where $\bar{n}_\alpha$ is the average atomic fraction of α-atoms in the solution, and $\Delta n_\alpha(\mathbf{r})$ are the periodic fluctuations of $n_\alpha(\mathbf{r})$.

Then, the variation of free energy, $\Delta F = F\left(\{\bar{n}_\alpha + \Delta\bar{n}_\alpha(\mathbf{r})\}\right) - F\left(\{n_\alpha(\mathbf{r})\}\right)$, can be expanded in Taylor series with respect to these fluctuations:

$$\begin{aligned}\Delta F &= \sum_{\mathbf{r}}\sum_{\alpha} A_\alpha(\mathbf{r})\Delta n_\alpha(\mathbf{r}) + \frac{1}{2}\sum_{\mathbf{r},\mathbf{r}'}\sum_{\alpha\beta} B_{\alpha\beta}(\mathbf{r},\mathbf{r}')\Delta n_\alpha(\mathbf{r})\Delta n_\beta(\mathbf{r}') \\ &+ \frac{1}{3!}\sum_{\mathbf{r},\mathbf{r}',\mathbf{r}''}\sum_{\alpha\beta\gamma} C_{\alpha\beta\gamma}(\mathbf{r},\mathbf{r}',\mathbf{r}'')\Delta n_\alpha(\mathbf{r})\Delta n_\beta(\mathbf{r}')\Delta n_\gamma(\mathbf{r}'') + \ldots,\end{aligned} \tag{2.16}$$

where

$$A_\alpha(\mathbf{r}) = \left.\frac{\partial F\left(\{\Delta n_\alpha(\mathbf{r})\}, T\right)}{\partial \Delta n_\alpha(\mathbf{r})}\right|_{n_\alpha(\mathbf{r})=\bar{n}_\alpha},$$

$$B_{\alpha\beta}(\mathbf{r},\mathbf{r}') = \left.\frac{\partial^2 F\left(\{\Delta n_\alpha(\mathbf{r})\},T\right)}{\partial\Delta n_\alpha(\mathbf{r})\partial\Delta n_\beta(\mathbf{r}')}\right|_{n_\alpha(\mathbf{r})=\bar{n}_\alpha, n_\beta(\mathbf{r}')=\bar{n}_\beta},$$

$$C_{\alpha\beta\gamma}(\mathbf{r},\mathbf{r}',\mathbf{r}'') = \left.\frac{\partial^3 F\left(\{\Delta n_\alpha(\mathbf{r})\},T\right)}{\partial\Delta n_\alpha(\mathbf{r})\partial\Delta n_\beta(\mathbf{r}')\partial\Delta n_\gamma(\mathbf{r}'')}\right|_{n_\alpha(\mathbf{r})=\bar{n}_\alpha, n_\beta(\mathbf{r}')=\bar{n}_\beta, n_\gamma(\mathbf{r}'')=\bar{n}_\gamma}$$

are the expansion coefficients calculated in the homogeneous state. In the disordered homogeneous state all sites are crystallographically equivalent, thus $A_\alpha(\mathbf{r}) = A_\alpha = const$. Considering that the number of the atoms of each kind is a constant value we can write:

$$\sum_{\mathbf{r}} \Delta n_\alpha(\mathbf{r}) = 0. \tag{2.17}$$

Therefore, the second term in expansion (2.16) is equal zero:

$$\sum_{\mathbf{r}}\sum_{\alpha} A_\alpha(\mathbf{r})\Delta n_\alpha(\mathbf{r}) = \sum_{\alpha} A_\alpha \sum_{\mathbf{r}} \Delta n_\alpha(\mathbf{r}) = 0. \tag{2.18}$$

Then the variation of free energy can be written as:

$$\begin{aligned}\Delta F &= \frac{1}{2}\sum_{\mathbf{r},\mathbf{r}'}\sum_{\alpha\beta} B_{\alpha\beta}(\mathbf{r},\mathbf{r}')\Delta n_\alpha(\mathbf{r})\Delta n_\beta(\mathbf{r}') \\ &\quad + \frac{1}{3!}\sum_{\mathbf{r},\mathbf{r}',\mathbf{r}''}\sum_{\alpha\beta\gamma} C_{\alpha\beta\gamma}(\mathbf{r},\mathbf{r}',\mathbf{r}'')\Delta n_\alpha(\mathbf{r})\Delta n_\beta(\mathbf{r}')\Delta n_\gamma(\mathbf{r}'') + \ldots\end{aligned} \tag{2.19}$$

Here we consider only the infinitesimal fluctuations of occupational probabilities $\Delta n_\alpha(\mathbf{r})$. Thus, only the first non vanishing term in Eq.(2.19) can be considered:

$$\Delta F = \frac{1}{2}\sum_{\mathbf{r},\mathbf{r}'}\sum_{\alpha\beta} B_{\alpha\beta}(\mathbf{r},\mathbf{r}')\Delta n_\alpha(\mathbf{r})\Delta n_\beta(\mathbf{r}'). \tag{2.20}$$

Using (2.9) the Eq.(2.20) gives

$$\Delta F = \frac{1}{2}\sum_{\mathbf{r},\mathbf{r}'}\sum_{\alpha\beta}\left[w_{\alpha\beta}(\mathbf{r}-\mathbf{r}') + \frac{\partial^2 f(\{\bar{n}_\alpha\})}{\partial\bar{n}_\alpha\partial\bar{n}_\beta}\right]\Delta n_\alpha(\mathbf{r})\Delta n_\beta(\mathbf{r}'). \tag{2.21}$$

As it was proposed in [17], the fluctuations of the occupation probabilities can be expressed using the static concentration wave representation:

$$n_\alpha(\mathbf{r}) = \bar{n}_\alpha + \sum_{\mathbf{k}} \widetilde{\Delta n}_\alpha(\mathbf{k}) e^{i\mathbf{k}\mathbf{r}}, \tag{2.22}$$

where $\widetilde{\Delta n}_\alpha(\mathbf{k}) = \sum_{\mathbf{r}} \Delta n_\alpha(\mathbf{r}) e^{-i\mathbf{kr}}$ is the Fourier amplitude of static concentration waves of the component α with the wave vector $\mathbf{k}$. In this representation the free energy change (2.21) yield

$$\Delta F = \frac{1}{2} \sum_{\mathbf{k}} \sum_{\alpha\beta} D_{\alpha\beta}(\mathbf{k}, T, \{\bar{n}_\alpha\}) \widetilde{\Delta n}_\alpha(\mathbf{k}) \widetilde{\Delta n}^*_\beta(\mathbf{k}). \tag{2.23}$$

Here

$$D_{\alpha\beta}(\mathbf{k}, T, \{\bar{n}_\alpha\}) = \widetilde{w}_{\alpha\beta}(\mathbf{k}) + \frac{\partial^2 f(\{\bar{n}_\alpha\})}{\partial \bar{n}_\alpha \partial \bar{n}_\beta}. \tag{2.24}$$

$D_{\alpha\beta}(\mathbf{k}, T, \{\bar{n}_\alpha\})$ is a response function which describes the characteristic properties of homogeneous solution at temperature T. This function is defined in (2.24) as an element of the $m \times m$ matrix, where m is the number of the independent components in solution. Since the interaction energies, $\widetilde{w}_{\alpha\beta}(\mathbf{k})$, and the second derivatives of a local free energy, $\frac{\partial^2 f(\{\bar{n}_\alpha\})}{\partial \bar{n}_\alpha \partial \bar{n}_\beta}$, are the real values and symmetrical with respect to permutations of indexes α and β, the matrix $D_{\alpha\beta}(\mathbf{k}, T, \{\bar{n}_\alpha\})$ is Hermitian and symmetric and can be written as:

$$\hat{D} = \begin{pmatrix} D_{11} & D_{12} & \dots & D_{1m} \\ D_{12} & D_{22} & \dots & D_{2m} \\ \vdots & \vdots & \ddots & \vdots \\ D_{1m} & D_{2m} & \dots & D_{mm} \end{pmatrix}. \tag{2.25}$$

Then with definition (2.24) we can rewrite the Eq.(2.23) as

$$\Delta F = \frac{1}{2} \sum_{\mathbf{k}} \sum_{\alpha\beta} D_{\alpha\beta}(\mathbf{k}, T, \{\bar{n}_\alpha\}) \widetilde{\Delta n}_\alpha(\mathbf{k}) \widetilde{\Delta n}^*_\beta(\mathbf{k}). \tag{2.26}$$

Expression (2.26) can be diagonalized by using normal mode representation of static concentration waves. In this representation, the occupation probability fluctuations $\Delta n_\alpha(\mathbf{r})$ can be written as a linear superposition of normal static concentration waves $\Psi_\alpha^{(s;\mathbf{k})}(\mathbf{r})$:

$$\Delta n_\alpha(\mathbf{r}) = \sum_{\mathbf{k}} \sum_{s=1}^{m} Q_s(\mathbf{k}) \Psi_\alpha^{(s;\mathbf{k})}(\mathbf{r}), \tag{2.27}$$

where $Q_s(\mathbf{k})$ are amplitudes of normal concentration waves $\Psi_\alpha^{(s;\mathbf{k})}(\mathbf{r})$, the index s indicates a normal mode of a normal static concentration wave ($s = 1, 2, \dots, m$). These normal modes characterize relative vibrations of the atoms of different sublattices formed by atoms of different kinds. $\Psi_\alpha^{(s;\mathbf{k})}(\mathbf{r})$ can be expressed in the form of Bloch functions:

$$\Psi_\alpha^{(s;\mathbf{k})}(\mathbf{r}) = v_\alpha(s;\mathbf{k}) e^{i\mathbf{kr}}. \tag{2.28}$$

Let the vectors $\Psi_\alpha^{(s;\mathbf{k})}(\mathbf{r})$ be the eigenvectors of the matrix $D_{\alpha\beta}(\mathbf{k},T,\{\bar{n}_\alpha\})$ and $v_\alpha(s;\mathbf{k})$ are the "polarization vectors". Then $\Psi_\alpha^{(s;\mathbf{k})}(\mathbf{r})$ satisfy the eigenvalue equation:

$$\sum_\beta \sum_{\mathbf{r}'} D_{\alpha\beta}((\mathbf{r}-\mathbf{r}'),T,\{\bar{n}_\alpha\})\Psi_\beta^{(s;\mathbf{k})}(\mathbf{r}') = \lambda_s(\mathbf{k},T)\Psi_\alpha^{(s;\mathbf{k})}(\mathbf{r}), \tag{2.29}$$

where

$$D_{\alpha\beta}((\mathbf{r}-\mathbf{r}'),T,\{\bar{n}_\alpha\}) = \sum_{\mathbf{k}} D_{\alpha\beta}(\mathbf{k},T,\{\bar{n}_\alpha\})e^{i\mathbf{kr}}.$$

In Eq.(2.29) $\{\lambda_s(\mathbf{k},T)\} = (\lambda_1(\mathbf{k},T),\lambda_2(\mathbf{k},T),\ldots,\lambda_m(\mathbf{k},T))$ are eigenvalues of the matrix $D_{\alpha\beta}(\mathbf{k},T,\{\bar{n}_\alpha\})$. Substituting (2.28) in (2.29) gives the next secular equation

$$\sum_\beta D_{\alpha\beta}(\mathbf{k},T,\{\bar{n}_\alpha\})v_\beta(s;\mathbf{k}) = \lambda_s(\mathbf{k},T)v_\alpha(s;\mathbf{k}). \tag{2.30}$$

This equation has a non-trivial solution if

$$\det\left|\left|\hat{D}(\mathbf{k},T,\{\bar{n}_\alpha\}) - \lambda_s(\mathbf{k},T)\hat{I}\right|\right| = 0. \tag{2.31}$$

The equation (2.31) is a characteristic equation and allows to find the eigenvalues $\lambda_s(\mathbf{k},T)$. Since the matrix $\hat{D}(\mathbf{k},T,\{\bar{n}_\alpha\})$ is Hermitian, all eigenvalues $\lambda_s(\mathbf{k},T)$ are real values and all eigenvectors are orthogonal to each other

$$\sum_\alpha v_\alpha(s;\mathbf{k})v_\alpha(s';\mathbf{k}) = \delta_{ss'}. \tag{2.32}$$

Using previous consideration the amplitude of static concentration waves $\widetilde{\Delta n}_\alpha(\mathbf{k})$ can be expressed as:

$$\widetilde{\Delta n}_\alpha(\mathbf{k}) = \sum_{s=1}^{m} Q_s(\mathbf{k})v_\alpha(s;\mathbf{k}). \tag{2.33}$$

Substituting Eq.(2.33) in (2.26) gives

$$\Delta F = \frac{1}{2}\sum_{\mathbf{k}}\sum_{\alpha\beta}\sum_{ss'} D_{\alpha\beta}(\mathbf{k},T,\{\bar{n}_\alpha\})Q_s(\mathbf{k})Q_{s'}^*(-\mathbf{k})v_\alpha(s;\mathbf{k})v_\beta^*(s';-\mathbf{k}).$$

Using (2.30) and (2.32) the expression for the free energy change (2.26) can be rewritten in the quadratic form:

$$\Delta F = \frac{1}{2}\sum_{\mathbf{k}}\sum_{s} \lambda_s(\mathbf{k},T)\left|Q_s(\mathbf{k})\right|^2. \tag{2.34}$$

Then the sign of the free energy change ΔF will determine whether the homogeneous solution

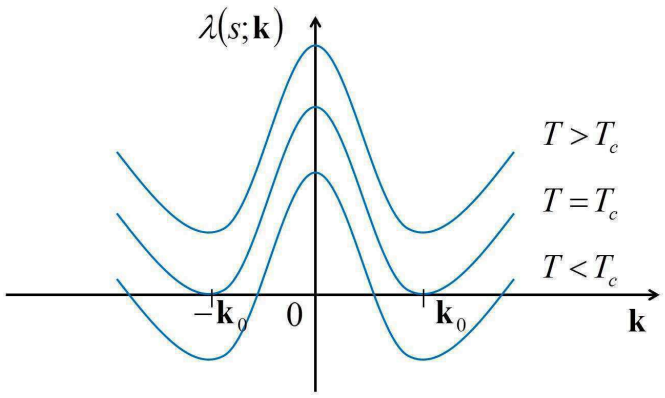

FIGURE 2.2: The plots of the lowest branch of the spectrum $\lambda_{s_0}(\mathbf{k}, T)$ for different temperatures. All functions $\lambda_{s_0}(\mathbf{k}, T)$ reach the minimum at $\mathbf{k}_0$. For simplification on this graph vector $\mathbf{k}$ is a one-dimensional vector.

is stable or unstable with respect to fluctuations. In Eq.(2.34) the factor $|Q_s(\mathbf{k})|^2$ is always positive. Thus, if all eigenvalues $\{\lambda_s(\mathbf{k}, T)\}$ are positively defined for all wave vectors $\mathbf{k}$ any fluctuations $Q_s(\mathbf{k})$ will increase the free energy. In this case the homogeneous state is stable with respect to the infinitesimal fluctuations.

If for some wave vector $\mathbf{k} = \mathbf{k}_0$ the eigenvalue $\lambda_s(\mathbf{k}, T)$ reaches 0 or became less then zero, $\lambda_{s_0}(\mathbf{k}_0, T) \leq 0$, then any infinitesimal fluctuation with amplitude $Q_{s_0}(\mathbf{k}_0)$ with vector $\mathbf{k}_0$ will grow and involve instability of homogeneous state. The system becomes unstable with respect to fluctuation at $\mathbf{k} = \mathbf{k}_0 \neq 0$ and spatially periodic heterogeneous structure appears. This case is called "ordering". If $\mathbf{k}_0 = 0$ then the instability results the formation of the mixture of two homogeneous phases with different mean atomic concentration. The last case is called "decomposition".

The temperature T, at which system becomes unstable with respect to infinitesimally small fluctuations, is called absolute instability temperature T_c. The homogeneous solution is stable (or metastable) above this temperature ($T > T_c$). At $T = T_c$ the lowest branch of the spectrum $\lambda_{s_0}(\mathbf{k}, T)$ reached zero at $\mathbf{k} = \mathbf{k}_0$ (Fig.2.2) and system loses its stability with respect to the periodic structure with the period $\mathbf{k}_0$. In Fig.2.2 we present the eigenvalues of the response function as function of T.

The same consideration can be done in the case of AFT. In the case of continuum model the state of the system (liquid, gas or solid) depends on the temperature T and average density $\bar{\rho}_\alpha$. At high temperatures atoms are randomly distributed and can be described by homogeneous densities $\{\bar{\rho}_\alpha\} = (\bar{\rho}_1, \bar{\rho}_2, \ldots, \bar{\rho}_n)$. In this disordered state all sites on the computational grid are characterized by the same occupation probabilities

$$\rho_\alpha(\mathbf{r}) = \bar{\rho}_\alpha. \tag{2.35}$$

This case corresponds to the gas or liquid state. The difference between these states is only in value of density ($\bar{\rho}_{liquid} \gg \bar{\rho}_{gas}$).

With decreasing of temperature T the system becomes unstable with respect to the periodic modulation of atomic density and crystallisation takes place. In the case of a solidification that is a first order phase transition, there is the temperature range $T_c < T < T_0$ where a homogeneous solution is in a metastable state. Where T_0 is the equilibrium first-order transition temperature in which the free energy functional are equal for liquid (disordered) and solid (ordered) phases and the temperature T_c is called the absolute instability temperature. In the metastable state the homogeneous solution is stable with respect to infinitesimal fluctuations of the density. When the amplitude of the fluctuations increases the system becomes unstable to some value of an amplitude. This means that there is a local minimum of the free energy functional in which system remains stable to small fluctuations of homogeneous distribution. The fluctuations with the highest amplitude allow to overcome the nucleation barrier and the solidification process start. When $T < T_c$ the solidification occurs without nucleation. The homogeneous solution becomes unstable with respect to infinitesimal fluctuations

$$\Delta\rho_\alpha(\mathbf{r}) = \rho_\alpha(\mathbf{r}) - \bar{\rho}_\alpha. \tag{2.36}$$

Thus it is possible to write the stability conditions of homogeneous state:

$$\left.\frac{\partial\lambda_{s_0}(\mathbf{k}, T_c)}{\partial\mathbf{k}}\right|_{\mathbf{k}=\mathbf{k}_0} = 0, \tag{2.37}$$

$$\lambda_{s_0}(\mathbf{k}_0, T_c) = 0. \tag{2.38}$$

The first equation (2.37) is a condition for $\lambda_{s_0}(\mathbf{k}, T_c)$ to have minimum at $\mathbf{k} = \mathbf{k}_0$. The second one (2.38) gives the condition for the function $\lambda_{s_0}(\mathbf{k}_0, T_c)$ to reach the low bound of the metastabilty range at $T = T_c$. Usually the function $\lambda_{s_0}(\mathbf{k}, T_c)$ reaches the minimum not only at one point $\mathbf{k}_0$ but in some interval $\mathbf{k}_0 \pm \Delta\mathbf{k}$. Therefore the uniform solution becomes unstable with respect to the fluctuations at all these wave vectors $\{\mathbf{k}_0 + \Delta\mathbf{k}\}$. However, the wave with $\mathbf{k}_0$ growth more rapid then others one. It should be noted, to obtain the stability condition in the case of the large fluctuations the high-order terms in Taylor expansion in Eq.(2.19) should be considered.

To illustrate the definition of the response function and eigenvectors for single- and two-components systems will be considered. For a single-component system ($m = 1$) the matrix $\hat{D}$ consists only of one element. Then the eigenvalue $\lambda(\mathbf{k}, T)$ is

$$\lambda(\mathbf{k}, T) = D(\mathbf{k}, T, \bar{n}) = \widetilde{w}(\mathbf{k}) + \frac{\partial^2 f(\bar{n})}{\partial\bar{n}^2}. \tag{2.39}$$

The second derivative of the local free energy functional can be found from Eqs. (2.7) and (2.6). Finally the eigenvalue is

$$\lambda(\mathbf{k}, T) = \widetilde{w}(\mathbf{k}) + \frac{k_B T}{\bar{\rho}(1-\bar{\rho})}. \tag{2.40}$$

Here the first term determines the minima $\{\mathbf{k}_0\}$ at which the system becomes unstable and the second one defines the temperature of the absolute instability T_c. Using Eqs. (2.37) and (2.38) the stability conditions are defined as

$$\min\left(\lambda(\mathbf{k}, T_c)\right) = \min\left(\widetilde{w}(\mathbf{k}) + \frac{k_B T_c}{\bar{n}(1-\bar{n})}\right) = 0. \tag{2.41}$$

Finding the stability conditions for the two-components ($m = 2$) system is more complex. In this case the matrix of the response functions is

$$\hat{D} = \begin{pmatrix} D_{11} & D_{12} \\ D_{12} & D_{22} \end{pmatrix}. \tag{2.42}$$

The components of the matrix (2.42) could be obtained from Eqs.(2.24), (2.7) and (2.6):

$$\begin{aligned} D_{11}(\mathbf{k}, T, \{\bar{n}_\alpha\}) &= \widetilde{w}_{11}(\mathbf{k}) + k_B T\left(1-\bar{n}_2\right)/\left(\bar{n}_1(1-\bar{n}_1-\bar{n}_2)\right), \\ D_{22}(\mathbf{k}, T, \{\bar{n}_\alpha\}) &= \widetilde{w}_{22}(\mathbf{k}) + k_B T\left(1-\bar{n}_1\right)/\left(\bar{n}_2(1-\bar{n}_1-\bar{n}_2)\right), \\ D_{12}(\mathbf{k}, T, \{\bar{n}_\alpha\}) &= \widetilde{w}_{12}(\mathbf{k}) + k_B T/(1-\bar{n}_1-\bar{n}_2). \end{aligned}$$

In this case, the system will loose its stability at the temperature where the eigenvalues of the matrix $\hat{D}$ become negative. The eigenvalues $\lambda_s(\mathbf{k}, T)$ $(s = 1, 2)$ could be found from characteristic equation (2.31):

$$\begin{vmatrix} D_{11}-\lambda & D_{12} \\ D_{12} & D_{22}-\lambda \end{vmatrix} = 0. \tag{2.43}$$

There are two solutions of the equation (2.43):

$$\lambda_{1,2}(\mathbf{k}, T) = \frac{D_{11} + D_{22} \pm \sqrt{\left(D_{11}-D_{22}\right)^2 + 4D_{12}^2}}{2}. \tag{2.44}$$

Since the third term in (2.44) is always positively defined or equal zero, the lowest branch $\lambda_2(\mathbf{k}, T)$ (with "$-$" in the right part) is

$$\lambda_2(\mathbf{k}, T) = \frac{D_{11} + D_{22} - \sqrt{\left(D_{11}-D_{22}\right)^2 + 4D_{12}^2}}{2}. \tag{2.45}$$

Then the temperature of order-disorder transition is describing by the condition: $\min\left(\lambda_2(\mathbf{k}, T_c)\right) = 0$.

2.4 Kinetic equation

The temporal evolution of the density function, $\{\rho_\alpha(\mathbf{r}, t)\}$, or occupation probabilities, $\{n_\alpha(\mathbf{r}, t)\}$, of the multi-component system can be described by a microscopic Onsager equations [61]:

$$\frac{dn_\alpha(\mathbf{r}, t)}{dt} = \sum_{\mathbf{r}'} \sum_{\beta=1}^{m} \frac{L_{\alpha\beta}(\mathbf{r} - \mathbf{r}')}{k_B T} \frac{\delta F}{\delta n_\beta(\mathbf{r}', t)}. \tag{2.46}$$

In Eq.(2.46), a linear proportionality between the flux of probabilities, $\frac{dn_\alpha(\mathbf{r},t)}{dt}$, and the thermodynamic driving force, $\frac{\delta F}{\delta n_\beta(\mathbf{r}',t)}$, is assumed. $L(\mathbf{r})_{\alpha\beta}$ is the matrix of kinetic coefficients, k_B is the Boltzmann constant, T is temperature.

The sum of occupation probabilities over all the lattice sites is equal to the total number of solute atoms in the system

$$\sum_{\mathbf{r}} n_\alpha(\mathbf{r}, t) = N_\alpha. \tag{2.47}$$

Then the summation of Eq.(2.46) over all sites yields

$$\sum_{\mathbf{r}} \frac{dn_\alpha(\mathbf{r}, t)}{dt} = \sum_{\mathbf{r}} \left(\sum_{\mathbf{r}'} \sum_{\beta=1}^{m} \frac{L_{\alpha\beta}(\mathbf{r} - \mathbf{r}')}{k_B T} \frac{\delta F}{\delta n_\beta(\mathbf{r}', t)} \right) = 0,$$

this equation can be also written in the next form

$$\sum_{\mathbf{r}} \frac{dn_\alpha(\mathbf{r}, t)}{dt} = \frac{1}{k_B T} \sum_{\mathbf{r}'} \sum_{\beta=1}^{m} \frac{\delta F}{\delta n_\beta(\mathbf{r}', t)} \sum_{\mathbf{r}} L_{\alpha\beta}(\mathbf{r} - \mathbf{r}') = 0. \tag{2.48}$$

In general case:

$$\sum_{\mathbf{r}'} \sum_{\beta=1}^{m} \frac{\delta F}{\delta n_\beta(\mathbf{r}', t)} \neq 0.$$

Therefore, to satisfy the condition the matrix of kinetic coefficients should satisfy next equation:

$$\sum_{\mathbf{r}} L_{\alpha\beta}(\mathbf{r} - \mathbf{r}') = 0. \tag{2.49}$$

In k space this condition becomes $\widetilde{L}_{\alpha\beta}(\mathbf{k}) = 0$. In the case of continuum model, Eq.(2.49) satisfies the conservation condition of the total number of fratons of each kind (and thus the conservation of the total volume of all corresponding atoms).

As the elements of matrix of kinetics coefficients is constant then the Fourier transform of these coefficients can be expressed as a function of distance:

$$\widetilde{L}_{\alpha\beta}(\mathbf{k}) = \sum_{\mathbf{r}} L_{\alpha\beta}(\mathbf{r}) e^{-i\mathbf{kr}}.$$

In the long-wave approximation, for large distances $\mathbf{r}-\mathbf{r}'$, which correspond to small $\mathbf{k}$, we can expand $\widetilde{L}_{\alpha\beta}(\mathbf{k})$ in Taylor series around $\mathbf{k}=0$:

$$\widetilde{L}_{\alpha\beta}(\mathbf{k}) = \widetilde{L}_{\alpha\beta}(0) + \left.\frac{\partial \widetilde{L}_{\alpha\beta}(\mathbf{k})}{\partial k}\right|_{\mathbf{k}=0} k + \left.\frac{\partial^2 \widetilde{L}_{\alpha\beta}(\mathbf{k})}{\partial k^2}\right|_{\mathbf{k}=0} k^2 + \dots$$

Taking into account condition (2.49) and spherical symmetry of function $\widetilde{L}_{\alpha\beta}(\mathbf{k})$, $\widetilde{L}_{\alpha\beta}(\mathbf{k}) = \widetilde{L}_{\alpha\beta}(-\mathbf{k})$, the first nonvanishing term in Taylor series is

$$\widetilde{L}_{\alpha\beta}(\mathbf{k}) \approx -L^0_{\alpha\beta} k^2, \tag{2.50}$$

where $L^0_{\alpha\beta} \equiv -\left.\frac{\partial^2 \widetilde{L}_{\alpha\beta}(\mathbf{k})}{\partial k^2}\right|_{\mathbf{k}=0}$ is the mobility coefficients matrix. This mobility is proportional to the jump probability between a pair of atoms (or fratons) α and β at nearest-neighbor sites per unit time.

Then the k-representation of the kinetic equation (2.46) is

$$\frac{d\widetilde{n}_\alpha(\mathbf{k},t)}{dt} = -\sum_{\beta=1}^{m} \widetilde{L}_{\alpha\beta}(\mathbf{k}) \left(\widetilde{w}_{\alpha\beta}(\mathbf{k}) \widetilde{n}_\beta(\mathbf{k},t) + \left\{ \ln \frac{n_\beta(\mathbf{r},t)}{n_l(\mathbf{r},t)} \right\}_{\mathbf{k}} \right), \tag{2.51}$$

where

$$\begin{aligned}
\widetilde{L}_{\alpha\beta}(\mathbf{k}) &= \sum_{\mathbf{r}} L_{\alpha\beta}(\mathbf{r}) e^{-i\mathbf{kr}}, \\
\widetilde{w}_{\alpha\beta}(\mathbf{k}) &= \sum_{\mathbf{r}} w_{\alpha\beta}(\mathbf{r}) e^{-i\mathbf{kr}}, \\
\widetilde{\rho}_\alpha(\mathbf{k},t) &= \sum_{\mathbf{r}} \rho_\alpha(\mathbf{r}) e^{-i\mathbf{kr}}, \\
\left\{ \ln \frac{n_\alpha(\mathbf{r},t)}{n_m(\mathbf{r},t)} \right\}_{\mathbf{k}} &= \sum_{\mathbf{r}} \ln \frac{n_\alpha(\mathbf{r},t)}{n_m(\mathbf{r},t)} e^{-i\mathbf{kr}}
\end{aligned}$$

are the Fourier Transforms of the corresponding functions defined on the computational grid sites. Since for the multicomponent system $n_l(\mathbf{r},t) = 1 - n_1(\mathbf{r},t) - n_2(\mathbf{r},t) - \dots n_{m-1}(\mathbf{r},t)$ only $m-1$ independent kinetic equations for the atoms (or fratons) should be solved.

2.5 Conclusions

In this chapter first, the ADF approach has been described. This approach can be applied to model the decomposition and ordering on the constrain Ising lattice. It was shown the relation between eigenvalues of the response function, $D(\mathbf{k}, T)$, and the temperature of the phase transition. The stability condition obtained in this work allows to get the absolute instability temperature T_c, below which the homogeneous solution loses its stability with respect to infinitesimal fluctuations. It will be shown in Chapter5 that this approach can be used to study the carbon diffusion in Fe-C system during aging at room temperature.

New development of ADF theory in the the case on the nonconstrained Ising lattice was proposed. The proposed fraton theory rests on two novel conceptual premises: (a) the introduction of interacting pseudoparticles that we call fratons that described two configurational states of each point of continuum space. One is an event in which the point is inside the atomic sphere of any atom and the other is an event in which the point is outside of atomic sphere; the fratons are considered as a non-ideal gas whose 'condensation' describes a diffusional self-assembling of atomic system, and (b) a concept of a structural cluster function describing the directions, length and strength of interatomic bonds. The latter allows us to formulate a new and simple model Hamiltonian that is proportional to a bilinear expansion in these cluster functions. This model Hamiltonian provides the formation of a predetermined atomic structure and has a sufficient flexibility to describe the desired mechanic and thermodynamic properties of this structure.

In the next chapters the applications of the ADF and AFT approaches will be present.

Chapter 3

Application of the AFT to the modelling of self-assembly of complex structures

To illustrate the versatility and efficiency of the AFT, we tested its application to the modelling of the self-assembly of three groups of 3D structures of increasing complexity. They are non-ideal gas/liquid, single-component crystals, two-component crystals, and polymers with a helix and a double helix structure mimicking biological macromolecules. The modelling was carried out by numerical solution of the FT representation of the kinetic equation type (2.46) and in the case of fratons it becomes :

$$\frac{d\widetilde{\rho}_\alpha(\mathbf{k},t)}{dt} = -\sum_{\beta=1}^{m} \widetilde{L}_{\alpha\beta}(\mathbf{k}) \left(\widetilde{w}_{\alpha\beta}(\mathbf{k})\widetilde{\rho}_\beta(\mathbf{k},t) + \left\{ \ln \frac{\rho_\beta(\mathbf{r},t)}{\rho_l(\mathbf{r},t)} \right\}_{\mathbf{k}} \right). \tag{3.1}$$

Here $\widetilde{L}(\mathbf{k})_{\alpha\beta}$ is the FT of matrix of kinetic coefficients, k_B is the Boltzmann constant. Indices, α and β, label fratons describing different kinds of atoms ($\alpha = 1, 2, \ldots, m$), $\widetilde{w}_{\alpha\beta}(\mathbf{k})$ is the fraton-fraton interaction. Eq.(3.1) was solved using the semi-implicit Fourier spectral method proposed in [68].

An additional characterization of atomic configurations is their diffraction pattern. The diffraction pattern, which is a distribution of intensity of scattered radiation in the 3D reciprocal space of the wave vectors, $\mathbf{k} = (k_x\, k_y\, k_z)$, was determined as the squared modulus of the Fourier Transform of the density function $\rho(r)$:

$$I(\mathbf{k}) = |\widetilde{\rho}(\mathbf{k})|^2 = \left| \sum_{\mathbf{r}} \rho(\mathbf{r}) e^{-i\mathbf{kr}} \right|^2, \tag{3.2}$$

where $I(\mathbf{k})$ is proportional to the intensity distribution of a diffuse scattering. And for the multicomponent system it gives:

$$I(\mathbf{k}) = \sum_{\alpha\beta} \widetilde{\rho}_{\alpha}(\mathbf{k})\widetilde{\rho}^{*}_{\beta}(\mathbf{k}). \tag{3.3}$$

In our modeling reduced parameters have been used. The average density is defined as $\hat{\bar{\rho}}_{\alpha} = \rho^{at}_{\alpha}\frac{4\pi R^3_{\alpha}}{3}$ where $\rho^{at}_{\alpha} = \frac{N_{\alpha}}{V}$ is the density of α atoms in the ground state, N_{α} is number of the atoms of sort α, V is the total volume of the system, and R_{α} is the atomic radius. According to this definition, the reduced density, $\hat{\bar{\rho}}_{\alpha}$, is also a fraction of all computational grids sites occupied by fratons of the kind α. The input parameter ξ in the short range interaction, $\theta_{\alpha}(\mathbf{r})$, is measured in the units of $k_B T_0$ (see Fig.2.1(a)), where T_0 is the solidification temperature. The lengths are measured in units of r_1, which is very close to the atomic radius; the grid lattice increment, $\hat{l}$ (the spacing of the underlying Ising lattice), is defined as a fraction of the atomic radius. The temperature $\hat{T}$ is also measured in units of T_0. The reduced time, $\hat{t}$, is measured in units of typical atomic migration time, τ_0. The reduced kinetic coefficients, $\hat{L}(\mathbf{r})$, are measured in units of τ_0^{-1}.

3.1 Non-ideal gas

The first example is a modeling of a condensation of a disordered distribution of fratons into the atomic spheres followed by their rearrangement during the equilibration process. In the case of a single-component system, we will omit the symbol α. The initial disordered configuration was described by a sum of a homogeneous fratons density, $\hat{\bar{\rho}}$ with stochastically generated "infinitesimally small" noise.

The model potential (2.13) for a single-component system is:

$$\widetilde{w}(\mathbf{k}) = \lambda_1 \tilde{\theta}(\mathbf{k}) + \lambda_2 \left|\Psi^{clstr}(\mathbf{k})\right|^2. \tag{3.4}$$

In this modeling, we considered only a short-range interaction described by only the first term of this model potential ($\lambda_2 = 0$).

Fig.3.1 shows the results of the numerical solution of Eq.(3.1) describing a spontaneous "condensation" of fratons with the average density $\hat{\bar{\rho}} = 0.1$ into higher density clusters visualizing the atoms. Fig.3.1(a) presents the density of fratons, $\hat{\bar{\rho}}$, in the initial disordered configuration with a small static inhomogeneity, $|\Delta\rho_{max}| = 1.5 \cdot 10^{-3}$. As follows from Figs.3.1(b-d), the fratons form randomly distributed sphere-like clusters describing a disordered distribution of atoms. This configuration can be associated with a liquid or amorphous state.

The same kind of modeling but with different initial concentrations was also done. Figures 3.2(a)–(d) show the final configurations of fratons with different reduced densities, $\hat{\bar{\rho}}$, equal to 0.01 (Fig.3.2(a)), 0.05 (Fig.3.2(b)), 0.1 (Fig.3.2(c)), and 0.3 (Fig.3.2(d)). Other parameters

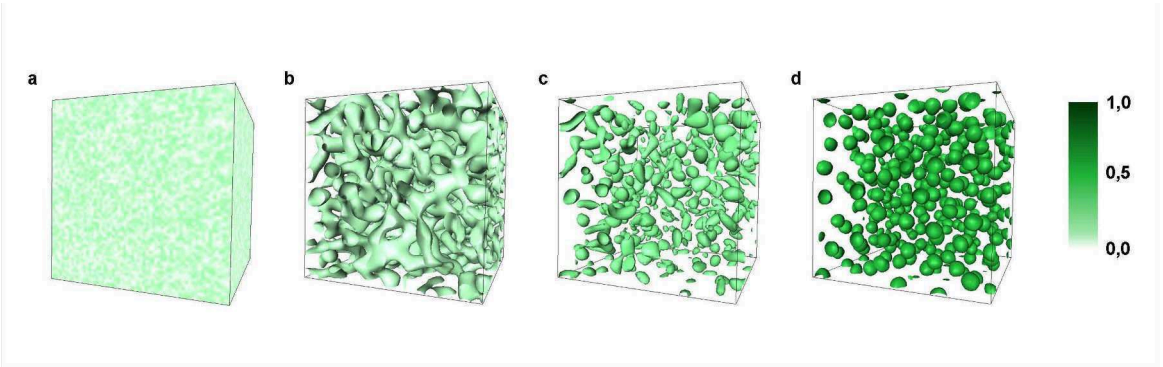

FIGURE 3.1: Temporal evolution of the fraton density corresponding to the times (a) $\hat{t} = 0$, (b) $\hat{t} = 1000$, (c) $\hat{t} = 2000$ and (d) $\hat{t} = 4000$. In (a), green colour corresponds to the value of the fratons' density function $\hat{\rho}(\mathbf{r})$ at a given point $\mathbf{r}$. The parameters in these simulations are $\hat{\lambda}_1 = 45.5$, $\xi = 4$, $\hat{D} = 1$, $\hat{\bar{\rho}} = 0.1$, $\hat{l} = 0.25$, $\Delta\hat{r} = 0.25$ and $\hat{T} = 0.886$. The size of the simulation box is $64 \times 64 \times 64$. The initial configuration is the layer in the middle of the simulation box where small inhomogeneities ($|\Delta\rho_{max}| = 1.5 \cdot 10^{-3}$) at the sites of the fcc lattice have been introduced.

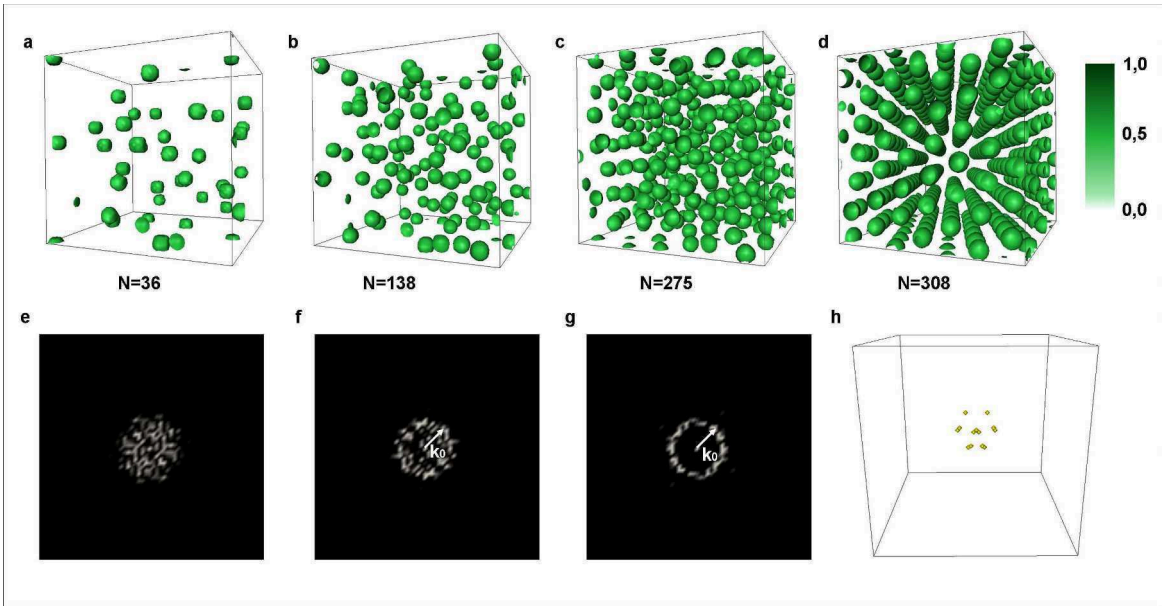

FIGURE 3.2: Equilibrium configurations of atomic fratons with different reduced densities self-assembled by short range interaction (first term in Eq.(3.4)) from disordered state (a,b,c,d). The corresponding diffraction patterns of atomic configurations formed by fratons are shown on the (e,f,g,h). Images (e,f,g) are (100)-plane section of the reciprocal space of their simulated diffraction patterns of the configuration on the (a, b, c) which are calculated via Eqs. (3.2–3.3); (h) 3D image of a simulated intensity distribution in the k-space from the configuration presented on (d).

corresponding to these simulations are $\xi = 4$, $\hat{D} = 1$, $\hat{l} = 0.25$, $\Delta\hat{r} = 0.25$; for the case with $\hat{\bar{\rho}} = 0.01$: $\hat{\lambda}_1 = 408$ and $\hat{T} = 0.857$; for $\hat{\bar{\rho}} = 0.05$: $\hat{\lambda}_1 = 87$ and $\hat{T} = 0.913$; for $\hat{\bar{\rho}} = 0.1$: $\hat{\lambda}_1 = 45.5$ and $\hat{T} = 0.886$; for $\hat{\bar{\rho}} = 0.3$: $\hat{\lambda}_1 = 21.5$, and $\hat{T} = 0.968$. The size of the simulation box is $64 \times 64 \times 64$.

In all these examples, the final structures obtained by self-assembling of fratons can be interpreted as a co-existence of two states, the liquid-like gas of atoms with high short-range

order and the gas with no or very little correlation. This is expected state for the considered low density systems with the conserved number of fratons and, thus, conserved number of atoms. "Liquid" is visualized by atomic spheres distributed with the significantly short-range order while the gas is described by a disordered distribution of fratons. The obtained difference in the number of atoms with the increase of atomic density is a result of a changing of a ratio between equilibrium volume fractions of these two coexisting states, liquid and gas, under the atomic conservation condition. The simulated diffraction patterns obtained for these structures using Eqs. (3.2–3.3) are presented in the Fig.3.2(e)–(h).

The Fig.3.2 also shows, that the increase of density of fratons, $\hat{\overline{\rho}}$, (and thus the increase of atomic density), results in different equilibrium structures; the structure became more ordered with the increase of the density, $\hat{\overline{\rho}}$. It is reflected in increasing of the intensity of spherical layer of intensity distribution on the diffraction patterns. The last is typical for a liquid state (Figs.3.2(a,e) and (b,f)). However, at $\hat{\overline{\rho}} = 0.3$, the structure looks more like either imperfect crystal with the hcp or fcc close packed structure (Fig.3.2(d,h)) or as a two phase (hcp+fcc) state consisting of imperfect close-packed crystalline regions and liquid with high correlation. The diffraction pattern of this configuration, shown in Fig.3.2(d), confirm that this structure has a topological long range order.

Therefore, the chosen short-range interaction model Hamiltonian in the fraton theory, as is expected, correctly provides a transition from the liquid/gas state to the crystalline state upon the isothermal increase of atomic density from $\hat{\overline{\rho}} = 0.01$ to $\hat{\overline{\rho}} = 0.3$. It also indicates that the short-range interaction (interaction radius is commensurate with the atomic diameter) reflecting the weak short-range attraction and strong repulsion of atomic cores leads to the formation of the close packed crystalline state.

Since the average atomic density and temperature are the external thermodynamic parameters of our system, the model also correctly reproduces the required change of the equilibrium state upon isothermal increase of atomic density in a single component system. This density increase results in a transition across the liquid-solid line on the T-ρ phase diagram and produces the corresponding crystallization.

To better prototype the crystallization, we have to take into account the following. As it is well known, the solidification always produces a polycrystalline state if special efforts to prevent this outcome are not made. An underlying reason for that is an isotropy of the space resulting in a degeneration of the energy of the crystalline phase with respect to any rigid-body rotation and translation. Under these circumstance, a single crystal state is achieved only if we lift this degeneration either by introducing a substrate or the external symmetry-lifting field. In our modelling, to lift this degeneration, we used the same approach to a computational prototyping of a single crystal "growth" as well: we introduced into the initial disordered distribution of fratons a layer of width $4r_1$ with the small deviations of the atomic fratons density ($\Delta\hat{\rho} = 0.0015$) and symmetry of the fcc lattice (see Fig.3.3(a)). This layer mimics a role of a substrate.

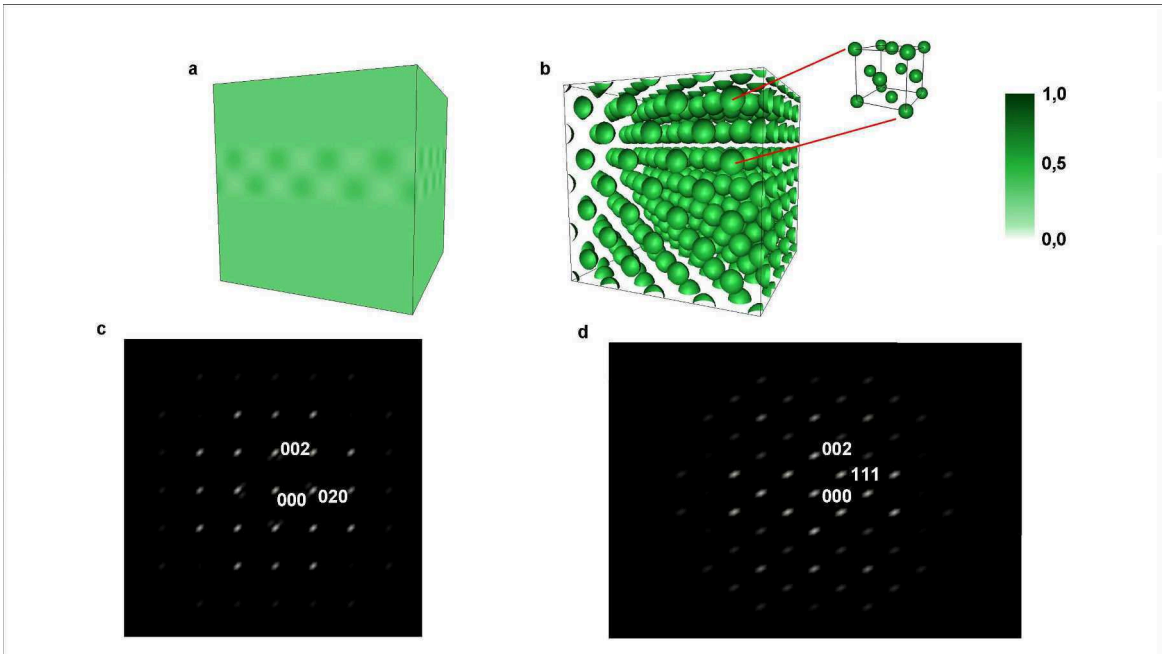

FIGURE 3.3: Initial (a) and final (b) configurations of fratons. The unit cell of the final structure is also shown in (b) and can be easily identified as the unit cell of the final fcc structure. The parameters in these simulations are $\hat{\lambda}_1 = 21.74$, $\xi = 4$, $\hat{D} = 1$, $\hat{\bar{\rho}} = 0.25$, $\hat{l} = 0.182$, $\Delta\hat{r} = 0.25$ and $\hat{T} = 0.924$. The size of the simulation box is $64 \times 64 \times 64$. The initial configuration is the layer in the middle of the simulation box where small inhomogeneities ($|\Delta\rho_{max}| = 1.5 \cdot 10^{-3}$) at the site of the fcc lattice have been introduced. In this simulation, only short-range interaction has been taken into account. The simulated diffraction pattern indicates the fcc symmetry of the atomic arrangement. The intensity distribution in the final configuration in the (100) and (111) reciprocal lattice planes are presented in (c) and (d), respectively.

Being "infinitesimal", these heterogeneities of the density field are too small to trigger the evolution to the "wrong" structure. However, they are sufficient to lift the translational and orientational isotropy of the continuum space, and thus to suppress the formation of a polycrystalline state. The average density in this simulation was set to be $\hat{\bar{\rho}} = 0.25$.

Fig.3.3(b) shows the final equilibrium configuration of the atoms that is easily recognizes as the fcc structure. The similar conclusion can be reached analysing the diffraction patterns of this structure shown in Fig.3.3(c) and Fig.3.3(d). The reflections (002), (111), (220), which characterise the fcc structure, are clearly seen.

3.2 Diamond structure

The next level of complexity is the self-assembly of a single-component crystal with several atoms in a Bravais lattice unit cell. As an example, we have chosen a crystal with the diamond structure. Such a structure is characteristic for Si and Ge semiconductor materials.

In this case, besides the short-range interaction used in the previous examples, the long-range interaction, described by the second term in Eq.(3.4), has been included. A chosen structural

cluster in this case is a cubic unit cell of the diamond lattice: it consists of eight points in the positions of the atoms in this unit cell, as shown in Fig.3.4(a).

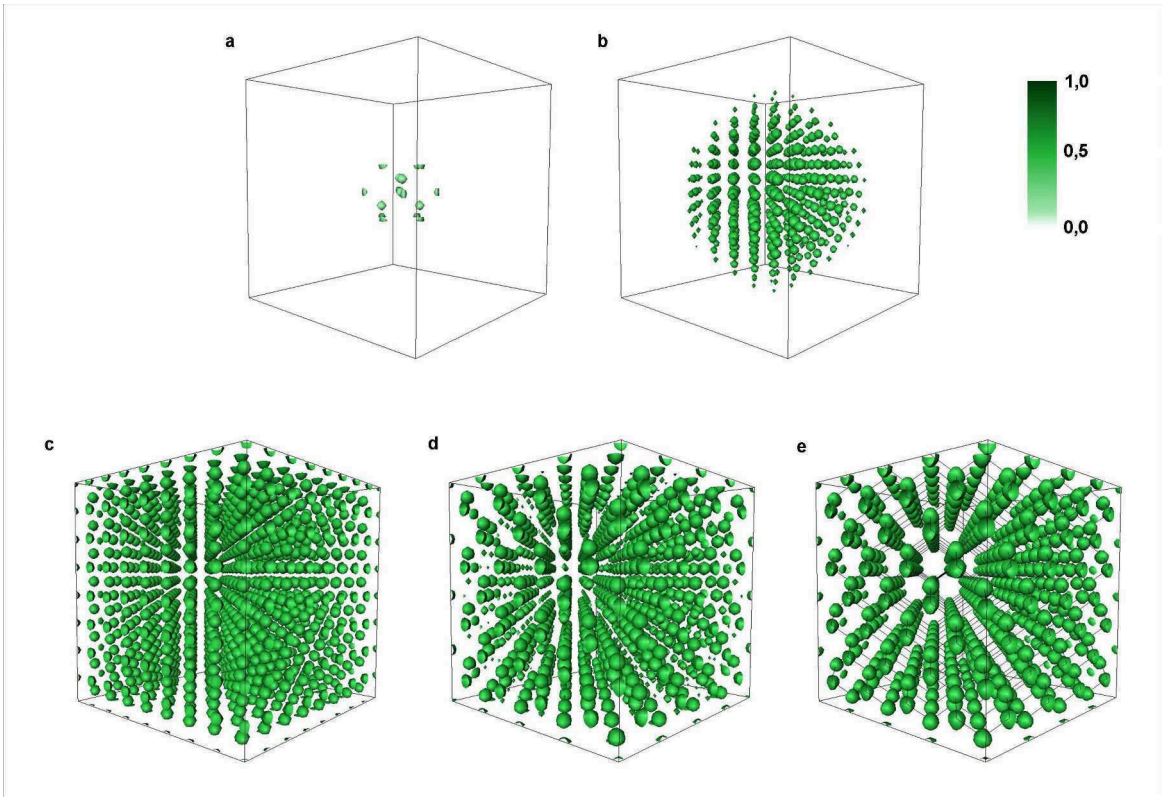

FIGURE 3.4: Example of a self-assembly of fratons into diamond structure at reduced times $\hat{t}$ of (a) $\hat{t}=0$, (b) $\hat{t}=600$, (c) $\hat{t}=1000$, (d) $\hat{t}=2800$, and (e) $\hat{t}=3000$. The parameters in this simulations are $\hat{\lambda}_1=14.085$, $\hat{\lambda}_2=-7.042$, $a=4.57$, $\xi=2$, $\hat{D}=1$, $\hat{\overline{\rho}}=0.07$, $\hat{l}=0.286$, $\Delta\hat{r}=0.17$ and $\hat{T}=0.732$. The initial configuration was an embryo consisting of the small variation of the fratons' density at the sites of the structural cluster of diamond structure embedded in the gas of disordered fratons. This initial configuration is the atomic cluster of the diamond structure placed in the centre of the simulation box. The size of the simulation box is $64\times64\times64$.

The diamond lattice has the fcc Bravais lattice with a two-atom basis, the atoms of the basis being displaced by the vector, $a\left(\frac{1}{4}\frac{1}{4}\frac{1}{4}\right)$, where a is the crystal lattice parameter; the coordinates are given as fractions of the crystal lattice parameter along the cube sides [69]. A chosen structural cluster in this case is a cubic unit cell of the diamond lattice: it consists of eight points in the positions of the atoms in this unit cell, as shown in Fig.3.4(a). The four points forming a fcc lattice cubic cell ((000), $a\left(\frac{1}{2}\frac{1}{2}0\right)$, $a\left(0\frac{1}{2}\frac{1}{2}\right)$, $a\left(\frac{1}{2}0\frac{1}{2}\right)$) and additional four points obtained from them forgoing by the basis shift, $a\left[\frac{1}{4}\frac{1}{4}\frac{1}{4}\right]$.

The function $\Psi^{clstr}(\mathbf{k})$ was constructed by using its definition (2.12) and the coordinates of the chosen structural cluster points:

$$\Psi^{clstr}(\mathbf{k})=\left(1+e^{-i\frac{a}{4}(k_x+k_y+k_z)}\right)\left(1+e^{-i\frac{a}{2}(k_x+k_y)}+e^{-i\frac{a}{2}(k_x+k_z)}+e^{-i\frac{a}{2}(k_y+k_z)}\right), \tag{3.5}$$

where a is a lattice constant of diamond structure, $k_i = \frac{2\pi m_i}{aN}$ (where $i = x, y$ or z, $m_i = 1 \dots N$, N is the number of simulation grid in a given direction). With this definition, the Fourier transform of the long range interaction, $\widetilde{w}_{LR}(\mathbf{k})$, can be written as:

$$\widetilde{w}_{LR}(\mathbf{k}) = \lambda_2(\mathbf{k})\widetilde{\Omega}_D(\mathbf{k}), \tag{3.6}$$

where

$$\begin{aligned}\widetilde{\Omega}_D(\mathbf{k}) &= \Psi^{clstr}(\mathbf{k})\left(\Psi^{clstr}(\mathbf{k})\right)^* = \\ &= \left(1 + e^{-i\frac{a}{4}(k_x+k_y+k_z)}\right)\left(1 + e^{-i\frac{a}{2}(k_x+k_y)} + e^{-i\frac{a}{2}(k_x+k_z)} + e^{-i\frac{a}{2}(k_y+k_z)}\right).\end{aligned} \tag{3.7}$$

Then, the Fourier transform of the total fraton-fraton potentials is:

$$\widetilde{w}(\mathbf{k}) = \lambda_1\widetilde{\theta}(\mathbf{k}) + \lambda_2(\mathbf{k})\widetilde{\Omega}_D(\mathbf{k}), \tag{3.8}$$

where the first term describes the short range interaction. The functions $\widetilde{\Omega}_D(\mathbf{k})$ and $\widetilde{\theta}(\mathbf{k})$, were normalized by the absolute value of a difference between the maximum and minima values of these functions, respectively. The chosen parameters are $\hat{\lambda}_1 = 14.085$, $\hat{\lambda}_2 = -7.042$, $a = 4.57$, $\xi = 2$, $\hat{D} = 1$, $\hat{\bar{\rho}} = 0.07$, $\hat{l} = 0.286$, $\Delta\hat{r} = 0.17$ and $\hat{T} = 0.732$. The initial state is described by the randomly distributed fratons. Translational and rotational degeneracy is lifted by introducing a small static inhomogeneity, $\hat{\rho}(\mathbf{r}) = 0.03$ (it is a deviation of fraton density, $\hat{\rho}(\mathbf{r})$, from $\hat{\bar{\rho}} = 0.07$, at the points of a unit cell sites of a single unit cell of the diamond lattice), placed in the centre of the simulation box.

The spontaneous self-organization of fratons into the diamond structure is shown in Fig.3.4. The intermediate structure in the pattern formation dynamics at the reduced time $\hat{t} = 60000$ is shown in Fig.3.4(b). A very interesting aspect of this self-assembling of the diamond crystal passes through is the development of the transient cubic body centered (bcc) structure (Fig.3.4(c)) at the early stages of evolution. The lattice parameter of this bcc structure is half that of the diamond structure. This transient state gradually transformed to the diamond structure by the gradual disappearance of some atoms in the bcc structure and the formation of the diamond structure. To better visualize the final structure, presented in Fig.3.4(e), the unit cell as well as the links between the first neighbours are shown.

The final diamond structure and its diffraction pattern are shown in Fig.3.5 where Fig.3.5(b) shows the simulated intensity distribution in the (110) section of the reciprocal space generated by the structure shown in Fig.3.5(a). This diffraction pattern is typical for the diamond structure: the most strong calculated diffraction peaks (220), (111), (311) and (400), are the strongest peaks of the diamond lattice as well. The peaks {200}, which are forbidden by the extinction rule for the diamond lattice, are also absent on the calculated diffraction pattern of the simulated structure. As is well known, the extinction rule for the diamond structure forbids

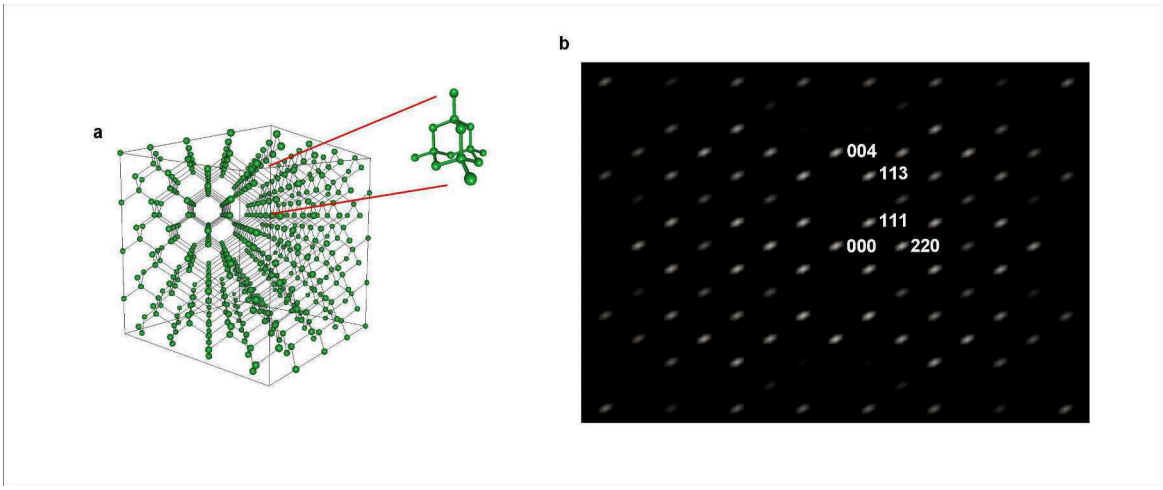

FIGURE 3.5: Simulated diamond structure: (a) Distribution of fratons at $\hat{t} = 3000000$. To clarify the structure, the links between first neighbours are drawn. (b) The diffraction pattern in the (110)-plane of the reciprocal k-space. The main diffraction peaks of the diamond structure are indicated: (111), (220), (113), and (400).

reflections whose indexes are either meeting the conditions: h, k, l are mixed odd and even; or all are even with the condition $h + k + l \neq 4n$.

3.3 Zinc-blende structure

Continuing our test of potentiality of the fraton theory, we gradually increased complexity of the modeled structure. As example, we considered the formation of a two-component crystalline phase with the zinc-blende atomic structure. The zinc-blende structure is observed in GaAs, InP, InAs, GaP, ZnO, ZnS alloys [70]. Semiconductor materials, such as GaAs, InP, GaSb, have increasing technological importance because of their use in solar cells [71], lasers [72], photodetectors [73].

A two-component systems atomic arrangement is formed by a "condensation" of two kinds of fratons, belonging to type A and B. This condensation should produce atoms A and B, respectively. The spontaneous arrangement caused by an equilibration of a disordered distribution of the fratons is described by the kinetic equations Eq.(3.1). For a two-component system,

Eq.(3.1) in the reciprocal space is reduced to two equations:

$$\frac{\partial\widetilde{\rho}_A(\mathbf{k},t)}{\partial t} = \widetilde{L}_{AA}(\mathbf{k})\left[\widetilde{w}_{AA}(\mathbf{k})\widetilde{\rho}_A(\mathbf{k},t) + \widetilde{w}_{AB}(\mathbf{k})\widetilde{\rho}_B(\mathbf{k},t) + \left(\ln\frac{\rho_A(\mathbf{r}',t)}{1-\rho_A(\mathbf{r}',t)-\rho_B(\mathbf{r}',t)}\right)_{\mathbf{k}}\right] + \widetilde{L}_{AB}(\mathbf{k})\left[\widetilde{w}_{AB}(\mathbf{k})\widetilde{\rho}_A(\mathbf{k},t) + \widetilde{w}_{BB}(\mathbf{k})\widetilde{\rho}_B(\mathbf{k},t) + \left(\ln\frac{\rho_B(\mathbf{r}',t)}{1-\rho_A(\mathbf{r}',t)-\rho_B(\mathbf{r}',t)}\right)_{\mathbf{k}}\right], \tag{3.9a}$$

$$\frac{\partial\widetilde{\rho}_B(\mathbf{k},t)}{\partial t} = \widetilde{L}_{AB}(\mathbf{k})\left[\widetilde{w}_{AA}(\mathbf{k})\widetilde{\rho}_A(\mathbf{k},t) + \widetilde{w}_{AB}(\mathbf{k})\widetilde{\rho}_B(\mathbf{k},t) + \left(\ln\frac{\rho_A(\mathbf{r}',t)}{1-\rho_A(\mathbf{r}',t)-\rho_B(\mathbf{r}',t)}\right)_{\mathbf{k}}\right] + \widetilde{L}_{BB}(\mathbf{k})\left[\widetilde{w}_{AB}(\mathbf{k})\widetilde{\rho}_A(\mathbf{k},t) + \widetilde{w}_{BB}(\mathbf{k})\widetilde{\rho}_B(\mathbf{k},t) + \left(\ln\frac{\rho_B(\mathbf{r}',t)}{1-\rho_A(\mathbf{r}',t)-\rho_B(\mathbf{r}',t)}\right)_{\mathbf{k}}\right], \tag{3.9b}$$

where A and B designates two sorts of atoms and corresponding two sorts of fratons. The Fourier transforms of the interaction energies, $\widetilde{w}_{\alpha\beta}(\mathbf{k})$ determined by Eq.(6), are:

$$\widetilde{w}_{AA}(\mathbf{k}) = \lambda_1^A\widetilde{\theta}_A(\mathbf{k}) + \lambda_2^A(\mathbf{k})\widetilde{\Omega}_{zb}^{AA}(\mathbf{k}), \tag{3.10a}$$

$$\widetilde{w}_{BB}(\mathbf{k}) = \lambda_1^B\widetilde{\theta}_B(\mathbf{k}) + \lambda_2^B(\mathbf{k})\widetilde{\Omega}_{zb}^{BB}(\mathbf{k}), \tag{3.10b}$$

$$\widetilde{w}_{BB}(\mathbf{k}) = \lambda_2^{AB}(\mathbf{k})\widetilde{\Omega}_{zb}^{AB}(\mathbf{k}), \tag{3.10c}$$

where $\widetilde{\Omega}_{zb}^{\alpha\beta}(\mathbf{k}) = \Psi_\alpha^{clstr}(\mathbf{k})\left(\Psi_\alpha^{clstr}(\mathbf{k})\right)^*$.

The zinc-blende structure has two atoms, A and B in a primitive unit cell of the fcc Bravais lattice with positions (000) and $a\left(\frac{1}{4}\frac{1}{4}\frac{1}{4}\right)$, correspondingly. To describe the model Hamiltonian providing evolution of this two-component structure, we needed two structural clusters, viz., the clusters of type A and B. The cluster A consists of four points: the point (000) and the points of its nearest neighbors in the fcc lattice, $a\left(\frac{1}{2}\frac{1}{2}0\right)$, $a\left(0\frac{1}{2}\frac{1}{2}\right)$, $a\left(\frac{1}{2}0\frac{1}{2}\right)$ The cluster B also consists of four points. They are obtained from the four points of the cluster A by the shift, $a\left[\frac{1}{4}\frac{1}{4}\frac{1}{4}\right]$. The points of both clusters for the A and B fratons are shown in Fig.3.6 by green and red colors. With this definition, the cluster Ψ-functions for the two structural clusters are:

$$\Psi_A^{clstr}(\mathbf{k}) = 1 + e^{-i\frac{a}{2}(k_x+k_y)} + e^{-i\frac{a}{2}(k_x+k_z)} + e^{-i\frac{a}{2}(k_y+k_z)}, \tag{3.11a}$$

$$\Psi_B^{clstr}(\mathbf{k}) = e^{-i\frac{a}{4}(k_x+k_y+k_z)}\left(1 + e^{-i\frac{a}{2}(k_x+k_y)} + e^{-i\frac{a}{2}(k_x+k_z)} + e^{-i\frac{a}{2}(k_y+k_z)}\right). \tag{3.11b}$$

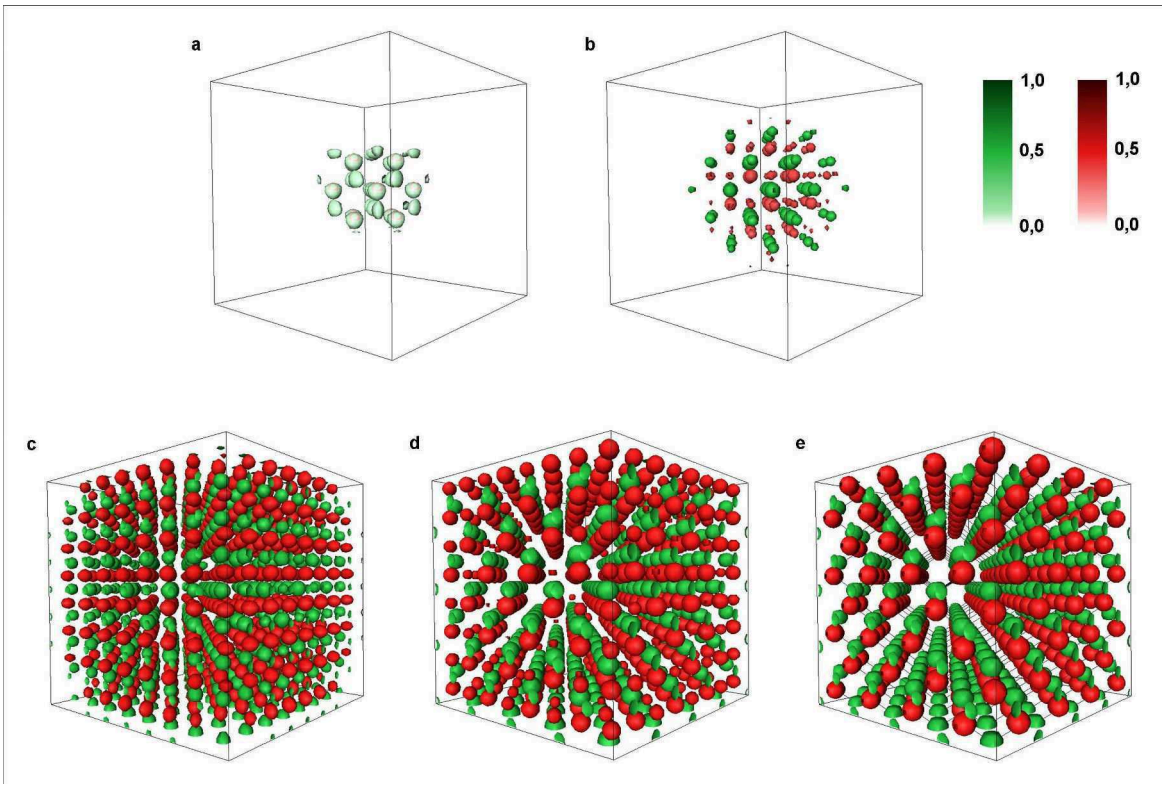

FIGURE 3.6: Example of a self-assembly of fratons into zinc-blende structure at reduced times $\hat{t}$ of (a) $\hat{t}=0$, (b) $\hat{t}=1600$, (c) $\hat{t}=1900$, (d) $\hat{t}=2800$, and (e) $\hat{t}=30000$. The parameters in this simulation are $\hat{\lambda}_1^A=3.77$, $\hat{\lambda}_1^B=5.84$, $\hat{\lambda}_2^A=-1.88$, $\hat{\lambda}_2^B=-2.92$, $\hat{\lambda}_2^{AB}=-2.26$, $\hat{D}_{AA}=\hat{D}_{BB}=1$, $\hat{D}_{AB}=-0.5$, $\hat{\bar{\rho}}_A=0.07$, $\hat{\bar{\rho}}_B=0.045$, $\hat{l}=0.25$, $r_1^A=1.143r_1^B$, $\xi=2$, $\Delta\hat{r}=0.17$, $\hat{a}=4.0$ and $\hat{T}=0.235$. The initial configuration is the atomic cluster of a diamond structure placed in the centre of the simulation box. The size of the simulation box is $64\times64\times64$. Two sorts of atoms with different atomic sizes are indicated in red and green.

Using these definitions the functions $\widetilde{\Omega}_{zb}^{\alpha\beta}(\mathbf{k})$ in the Eq.(3.10a–3.10c) can be written as:

$$\Omega_{zb}^{AA}(\mathbf{k})=\Omega_{zb}^{AA}(\mathbf{k})= \\ =4+4\left(\cos\left(\frac{k_xa}{2}\right)\cos\left(\frac{k_ya}{2}\right)+\cos\left(\frac{k_xa}{2}\right)\cos\left(\frac{k_za}{2}\right)+\cos\left(\frac{k_ya}{2}\right)\cos\left(\frac{k_za}{2}\right)\right), \tag{3.12a}$$

$$\Omega_{zb}^{BB}(\mathbf{k})=2\cos\left(\frac{a}{4}(k_x+k_y+k_z)\right)\times \\ \times\left[4+4\left(\cos\left(\frac{k_xa}{2}\right)\cos\left(\frac{k_ya}{2}\right)+\cos\left(\frac{k_xa}{2}\right)\cos\left(\frac{k_za}{2}\right)+\cos\left(\frac{k_ya}{2}\right)\cos\left(\frac{k_za}{2}\right)\right)\right]. \tag{3.12b}$$

The difference in size of different species of atoms has been taken into account in the short range potential. In these simulations the ratio of two atomic radii was chosen 0.875. The size of the simulation grid, $\hat{l}=0.25$, was measured in the units of r_1^A. Therefore, the value of r_1^B was chosen equal to $3.5\hat{l}$. For the zinc-blende structure we used the following set of input parameters: $\hat{\lambda}_1^A=3.77$, $\hat{\lambda}_1^B=5.84$, $\hat{\lambda}_2^A=-1.88$, $\hat{\lambda}_2^B=-2.92$, $\hat{\lambda}_2^{AB}=-2.26$, $\hat{D}_{AA}=\hat{D}_{BB}=1$, $\hat{D}_{AB}=-0.5$,

$\hat{\bar{\rho}}_A = 0.07$, $\hat{\bar{\rho}}_B = 0.045$, $\hat{l} = 0.25$, $r_1^A = 1.143 r_1^B$, $\xi = 2$, $\Delta\hat{r} = 0.17$, $\hat{a} = 4.0$ and $\hat{T} = 0.235$. The initial configuration was a single unit cell embryo of the diamond embedded into the two-component gas consisting of disordered fratons of two kinds. The temporal evolution of densities of the fratons obtained by the solution of two kinetic equations (3.9a) and (3.9a) for two species of fratons ($\alpha = A, B$) is shown in Fig.3.6. As follows from Fig.3.6(e), the evolution eventually leads to the formation of the zinc-blende crystal. To better visualize the zinc-blende structure, we draw the links between the first neighbours that are also shown in Fig.3.6(e). In Fig.3.6, green and red atoms represent the two sorts of atoms, for example Zn and S, respectively. A difference with the diamond structure is that the positions of two identical atoms in the basis of the diamond structure are occupied by different atoms in the zinc-blend structure. Each sort of atoms forms the fcc lattice with the period of the fcc Bravais lattice a. As is expected, these two fcc lattices are shifted with respect to each other by the distance, $a\left(\frac{1}{4}\frac{1}{4}\frac{1}{4}\right)$.

The (110) section of the simulated diffraction pattern of the configuration shown in Fig.3.7(a) is presented in Fig.3.7(b). The first strongest diffraction peaks are (200), (111), (220) and (311).

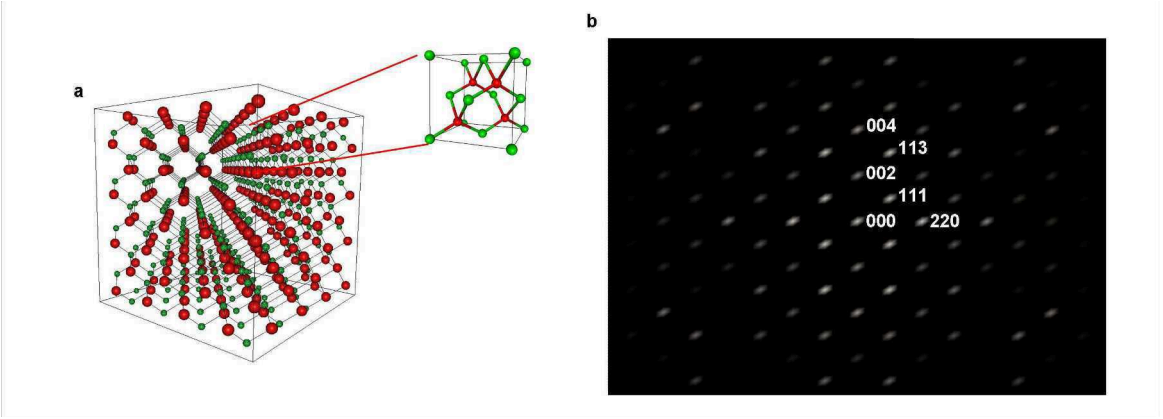

FIGURE 3.7: (a) Simulated configuration of fratons obtained by a spontaneous "condensation" of fratons into the atomic structure at $\hat{t} = 3000000$. The spherical clusters of fratons of type A and B which describe atoms A and B are shown in different colors. The unit cell clarifying links between the nearest neighbours are indicated. (b) The (110) section of the reciprocal **k**-space. The main peaks of the zinc-blende structure are indicated: (002), (111), (311) and (400).

The positions and intensity of these peaks are in agreement with the extinction rule: reflections from the zinc-blend structure: with mixed odd and even h,k,l indices are forbidden.

3.4 Helix and Double-helix structure

Molecules with a helix architecture are observed in organic materials [74–76], helix-shaped graphite nanotubes [77, 78], liquid crystal[79, 80], proteins, and, of course, DNA and RNA polymeric molecules [81–83]. Then, the most challenging test of the potency of the fraton theory would be its ability to describe a spontaneous self-assembly for the most interesting case relevant to biology, that is, the self-assembly of a double helix polymer from "soup" of

randomly distributed of fratons. We chosen this system because, as far as we know, a self-assembly of randomly distributed monomers into double-tread helix polymers was a too complex phenomenon to prototype by the existing methods.

3.4.1 Modeling of helix structure

To model a self-assembly of helix structure, fraton-fraton potential producing a helix structure should be directional and have a built-in chirality. The geometrical parameters of the configuration of the structural cluster are the pitch length, P, the number of coils per pitch, $n_0 = 6$, the distance between coils in z-direction, h, and the radius of the coil, u (see Fig.3.8).

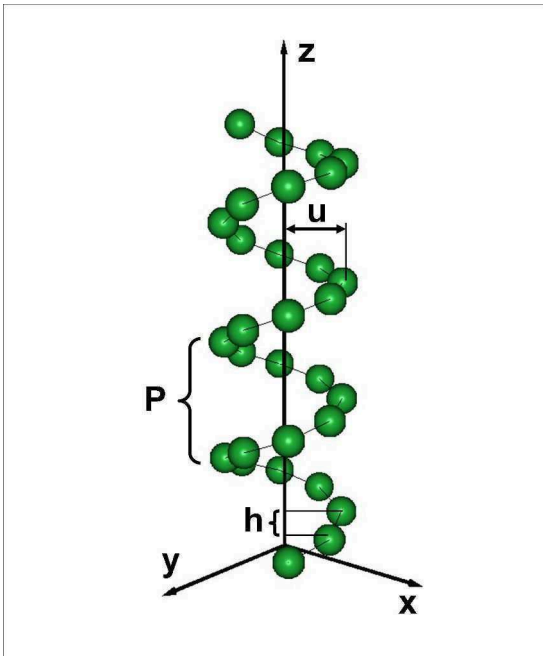

FIGURE 3.8: Illustration of the geometrical parameters of the helical structure: P is a pitch, h is a distance between the nearest coils along the z axis and helix radius u.

Then the coordinates of points of the helix occupied by molecules are:

$$\mathbf{r}_s = \left(u\cos\left(\tfrac{2\pi}{n_0}s\right) \quad u\sin\left(\tfrac{2\pi}{n_0}s\right) \quad hs \right), \tag{3.13}$$

where s runs from 0 to $n_0 - 1$, n_0 is the number of coils in the pitch.

Our chosen structural cluster consists of two pitches. The second-pitch segment of the cluster is needed to introduce a chirality into the long-range part of the model potential. The size of the structural cluster would be drastically reduced if the chirality were built-in in the short-range part of the fraton-fraton interaction. This can be done by a straightforward modification of the short-range interaction.

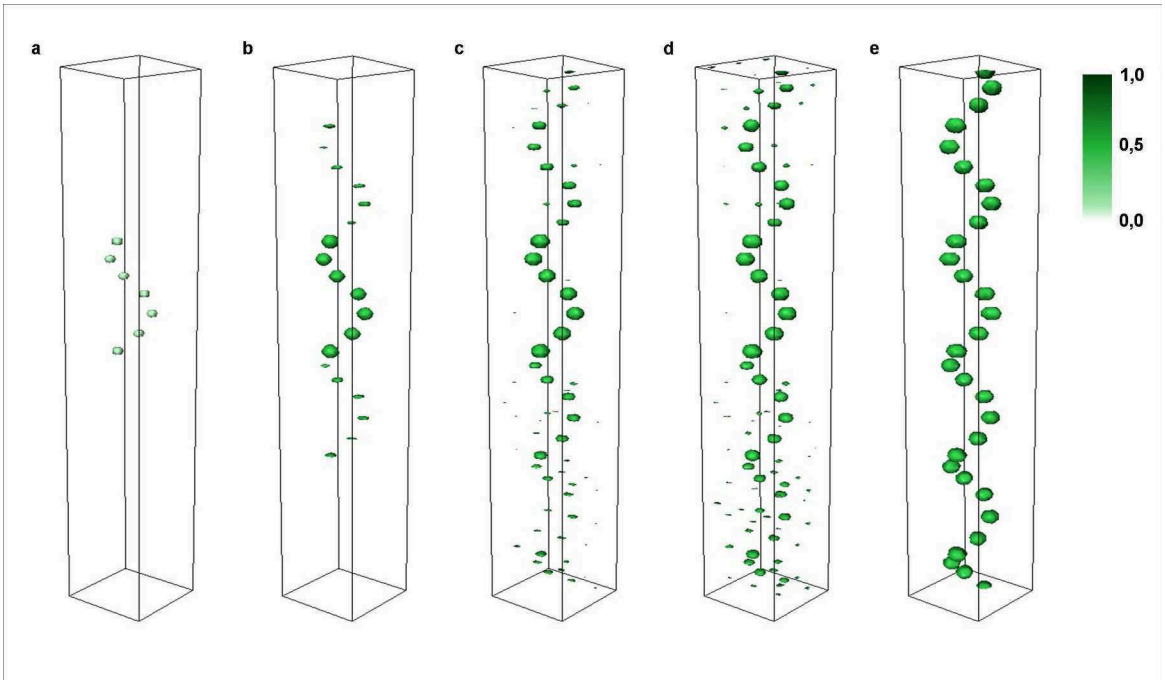

FIGURE 3.9: Example of self-assembly of the fratons into the helix structure at reduced time of (a) $\hat{t} = 0$, (b) $\hat{t} = 2000$, (c) $\hat{t} = 2500$, (d) $\hat{t} = 3000$, and (e) $\hat{t} = 7000$. The input parameters in this simulation are: $\hat{\lambda}_1 = 61.14$, $\hat{\lambda}_2 = -69.87$, $\hat{h} = \hat{u} = 1.56$, $n_0 = 6$, $\xi = 2$, $\hat{D} = 1$, $\hat{\bar{\rho}} = 0.0096$, $\hat{l} = 0.22$, $\Delta\hat{r} = 0.17$ and $\hat{T} = 0.568$. The size of the simulation box is $32 \times 32 \times 210$. The initial configuration shown in (a) is $n_0 + 1$ coils in the helix structure.

Using this definition of cluster for the formulation of the function $\Psi(\mathbf{k})$ for the helical structure, presented in Fig.3.8 gives:

$$\Psi^{clstr}(\mathbf{k}) = \left(1 + e^{-in_0hk_z}\right) \sum_{s=0}^{n_0-1} e^{-i\mathbf{k}\mathbf{r}_s}. \tag{3.14}$$

Then function $\widetilde{\Omega}_H(\mathbf{k})$ is:

$$\widetilde{\Omega}_H(\mathbf{k}) = (2 + 2\cos(n_0hk_z)) \left(6 + 2 \sum_{n>m=0}^{n_0-1} \cos\phi(n,m)\right), \tag{3.15}$$

where

$$\phi(n,m) = k_x u \left(\cos\frac{2\pi n}{n_0} - \cos\frac{2\pi m}{n_0}\right) + k_y u \left(\sin\frac{2\pi n}{n_0} - \sin\frac{2\pi m}{n_0}\right) + k_z h(n-m). \tag{3.16}$$

In this simulation the following parameters were used: $\hat{D} = 1$, $\hat{\lambda}_1 = 61.14$, $\hat{\lambda}_2 = -69.87$, $\hat{l} = 0.22$, $\hat{h} = \hat{u} = 1.56$, $n_0 = 6$, $\xi = 2$, $\hat{\bar{\rho}} = 0.0096$ and $\hat{T} = 0.568$. The parameters of the $\theta(\mathbf{k})$ function were chosen the same as for the diamond structure. The size of the simulation box was $210 \times 32 \times 32$. The initial embryo lifting the spatial and rotational energy degeneration was a one pitch inhomogeneity introduced in the centre of the simulation box. In the first step, we considered a random distribution of fratons of one kind. We also assumed that the desired helix

has a single spherical monomer in each coil and approximate these monomers by a spherical shape. The latter is not a critical assumption for the theory. It is just a simplification that reduces the computational time.

The solution of Eq.(3.1) with the model potential given by Eqs.(3.15),(3.16) in this case describes an evolution that eventually produces the single-stranded helix shown in Fig.3.9.

The simulated diffraction pattern obtained for helix structures presented in the Fig.3.10(a) in (010) plane.

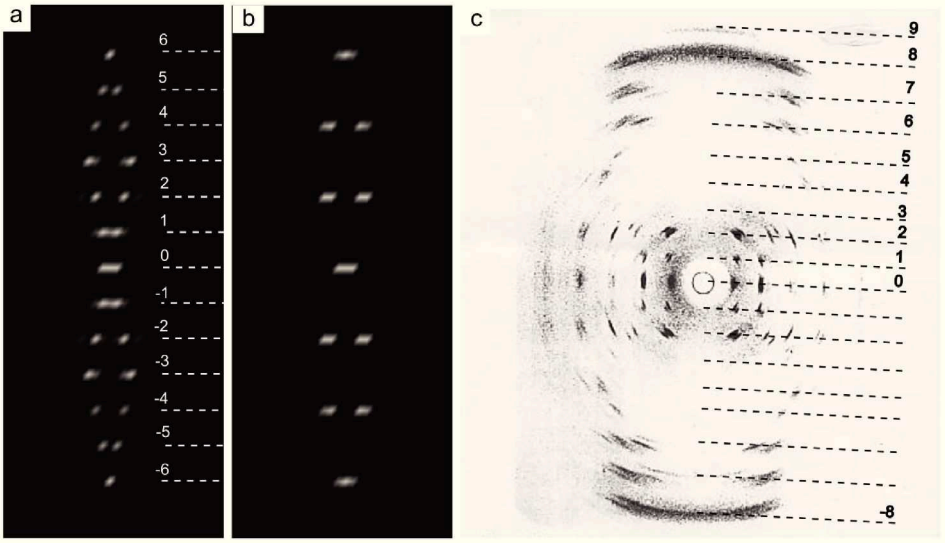

FIGURE 3.10: Diffraction pattern of the final stage of simulation of (a) helix structure in (010) plane, (b) double-helix structure in (100) plane. The layer-planes are numbered 0-6. (c) The X-ray diffraction pattern of an A-DNA fibre in near normal incidence. The layer-planes are numbered 0-9. Note the deformation of the layer-planes and the movement of the diffraction features towards asymmetric positions on the north and south layer-planes [10]. The layer-planes are perpendicular to the plane of the picture.

The allowed values of the wave vector $\mathbf{k}$ of the scattered waves in helical structures laying on the horizontal planes given as equation $k_z = 2\pi/h$. These planes are called layer-planes.

3.4.2 Modeling of double-helix structure

The last example of our simulation is related to the growth of the double helix structure. This structure consists of two complimentary strands. To model a spontaneous self-assembling the double stranded helix, we had to introduce (as for the zinc-blend structure) complimentary fratons of two types, A and B. Their "condensation" should form monomers of the complementary helix strands. The introduction of the second kind of fratons, which is complementary to the first kind, results in their self-assembly of a complementary strand and the formation of a double-helix molecule. The complementarity of the species is taken into consideration introducing in the model Hamiltonian a term describing the interaction of complementary fratons. We used the same type of the structural clusters for the fratons of the kind A and B. Each of them consists of two pitches of helix structure. However, the clusters are rotated with respect to each

other about axis z by $\varphi = \pi$. Then, using the definition of the functions $\Psi_\alpha(\mathbf{k})$ by Eq.(2.12) for $\alpha = A, B$, gives:

$$\Psi_A^{clstr}(\mathbf{k}) = \left(1 + e^{-in_0hk_z}\right) \sum_{s=0}^{n_0-1} e^{-i\mathbf{k}\mathbf{r}_s}, \tag{3.17a}$$

$$\Psi_A^{clstr}(\mathbf{k}) = e^{-i\frac{n_0h}{2}k_z} \left(1 + e^{-in_0hk_z}\right) \sum_{s=0}^{n_0-1} e^{-i\mathbf{k}\mathbf{r}_s}. \tag{3.17b}$$

We assume that $\widetilde{\Omega}_{DH}^{AA}(\mathbf{k}) = \widetilde{\Omega}_{DH}^{BB}(\mathbf{k}) = \widetilde{\Omega}_H(\mathbf{k})$, where $\widetilde{\Omega}_H(\mathbf{k})$ is defined by Eq.(3.15). Then the function $\widetilde{\Omega}_{DH}^{AB}(\mathbf{k})$ is:

$$\widetilde{\Omega}_{DH}^{AB}(\mathbf{k}) = 2\cos\left(\frac{n_0h}{2}k_z\right)\left(2 + 2\cos\left(n_0hk_z\right)\right)\left(6 + 2\sum_{n>m=0}^{n_0-1}\cos\phi(n,m)\right). \tag{3.18}$$

The simulation box size and input parameters for two kinds of complimentary fratons were chosen the same as for a single-thread helix and the interaction between helix is defined by $\hat{\lambda}_2^{AB} = -1.78$, $\hat{T} = 0.033$.

In spite of all these oversimplifications, this model describes some generic features relevant

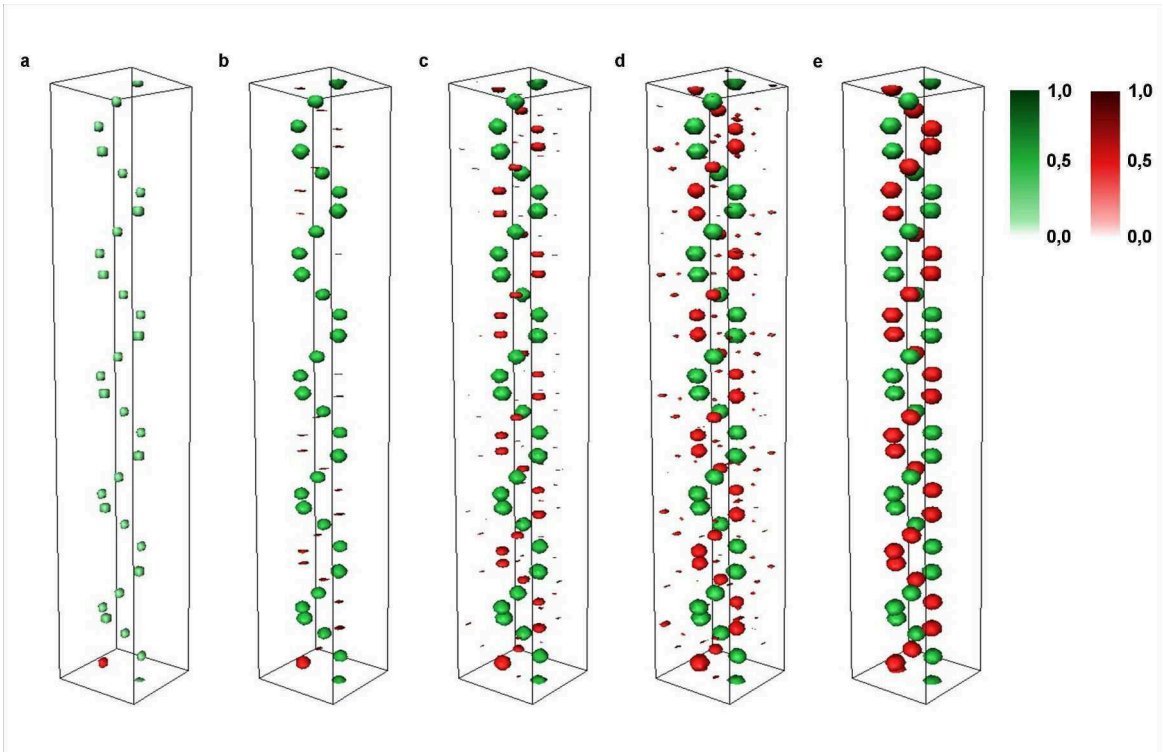

FIGURE 3.11: Self-assembly of the fratons into a double helix structure at reduced time of (a) $\hat{t} = 0$, (b) $\hat{t} = 1500$, (c) $\hat{t} = 2000$, (d) $\hat{t} = 3000$, and (e) $\hat{t} = 15000$. The input parameters in this simulation are $\hat{\lambda}_1^A = \hat{\lambda}_1^B = 4.07$, $\hat{\lambda}_2^A = \hat{\lambda}_2^B = -4.07$, $\hat{\lambda}_2^{AB} = -1.78$, $r_1^A = r_1^B$, $\hat{h} = \hat{u} = 1.56$, $n_0 = 6$, $\xi = 2$, $\hat{D}_{AA} = \hat{D}_{BB} = 1$, $\hat{D}_{AB} = -0.5$, $\hat{\bar{\rho}}_A = \hat{\bar{\rho}}_B = 0.0096$, $\hat{l} = 0.22$, $\Delta\hat{r} = 0.17$ and $\hat{T} = 0.033$. The size of the simulation box is $32 \times 32 \times 210$. The initial configuration shown in (a) is one helix and one coil of the second helix.

to the spontaneous formation of single-stranded polymeric molecule and the growth of the complementary strand of the monomers eventually producing a double-stranded helix configuration (see Fig. (3.11)). In this case, the first single-stranded helix is a template for the aggregation on it of complementary monomers to form a double-stranded helix. For clarity, we show the clusters of fratons (monomers) of the second strand in red.

Fig.3.10(b) shows the simulated diffraction pattern of double helix structure in (100) reciprocal plane. We can see that in comparison with the single-thread helix (Fig.3.10(a)), there is an extinction of each second layer-plane on the diffraction pattern of the double helix structure. The X-ray diffraction patterns for DNA show somewhat similar diffraction pattern [10, 84, 85]. For example, in Fig.3.10(c) is shown X-ray diffraction pattern of A-DNA with numbered layer-planes. Its real structure is formed by two right-handed polynucleotide chains that are coiled about the same axis [10].

3.5 Conclusions

In this chapter, we selected the most difficult cases of self-assembling wherein the initial system is atomically disordered so that its configuration "knows" nothing about the final atomic pattern that should be spontaneously self-assembled. This self-assembling is driven only by the chosen model Hamiltonian, and, specifically, by mutual orientation, length and strength of interatomic bonds. We considered situations wherein the self-assembling is taken place at diffusion time scale, which may range from a fraction of a second to years. A typical time of this evolution is dictated by the typical time of evolution of time-dependent ensemble rather than typical times of atomic dynamics like time of atomic vibrations. Difficulty in addressing such slow evolving systems probably was a reason why a spontaneous formation of some of them (crystals and polymers) from a liquid solution of atoms or monomers has not been modelled yet in the diffusional time scale.

The developed approach opens a way to answer numerous outstanding questions concerning the atomistic mechanisms of the formation of defects (dislocations, grain boundaries, etc.), nucleation in solid-solid transformations, the formation of polymers due to aggregation of monomers in their solution, folding and crystallisation of polymers, and their responses to external stimuli. This list can be significantly extended. Especially interesting are the modelling results describing the spontaneous self-assembly of monomers into a single-stranded polymeric helix and the formation of a double-helix structure obtained by aggregation of complementary monomers on the single-stranded helix playing the role of a template. This result may be also considered as an attempt to formulate and execute the simplest prototyping of the spontaneous formation of homopolymeric DNA from a liquid solution of monomers playing the role of nucleotides.

Finally, the use of the new model Hamiltonian formulated in terms of the structural clusters and proposed fraton model provide already a ready tool to address a general problem of spontaneous pattern formation by self-assembling of any randomly distributed building elements in

the time scale ranging from sub-seconds to years. This approach can be also straightforwardly extended for the prototyping of self-assembly of elementary building block monomers with more complex molecular structures. In the latter case, we have to generalise the concept of fratons of atoms by introducing fraton of molecules and modify accordingly the model short-range part of the model fraton-fraton Hamiltonian. Then this modification should provide a "condensation" of the molecular fratons into molecules and subsequent self-assembly of these molecules. In principle, this approach can be even used for the description of three-dimensional pattern formation by any macroscopic objects and optimisation of their properties. The "fratons" in this case being fragments of these objects are also macroscopic.

Chapter 4

Martensitic Transformations

4.1 Martensitic Transformations

In this chapter, the Quasiparticle approach based on the AFT, described in the previous Chapter2, will be applied to model MT in carbon steels.

4.1.1 Mechanism of transition

Historically, the first theory which explains a mechanism of the lattice transformation from fcc to bcc (or bct) was proposed by Bain in 1924. According to this theory the fcc lattice of austenite can be transformed into bcc ferrite lattice by compression of 20.3% along the direction $[001]_\gamma$ of austenite lattice and expansion of 12.6% in two perpendicular directions $[1\bar{1}0]_\gamma$ and $[110]_\gamma$ on $(110)_\gamma$ plane. In this case $[1\bar{1}0]_\gamma$, $[110]_\gamma$ and $[001]_\gamma$ directions fcc lattice correspond to $[100]_{\alpha'}$, $[010]_{\alpha'}$ and $[001]_{\alpha'}$ directions of the bcc lattice with a ratio $\sqrt{2}$ along $[001]_\gamma$ axis. This relationship between austenite and martensite phases is called the Bain correspondence. Fig.4.1(a) shows how the Bain correspondence enables to identify bct unit cell in the two adjacent

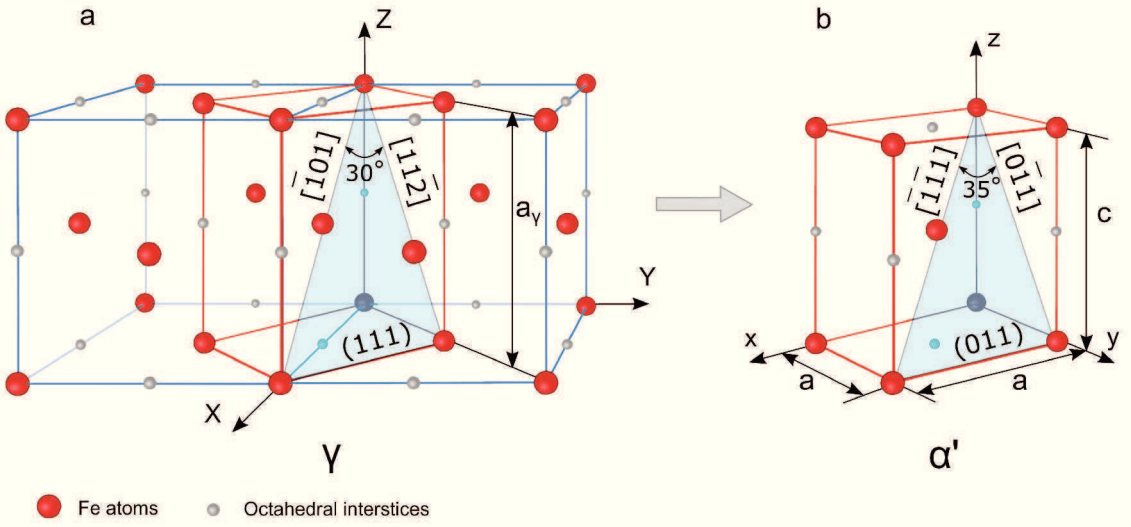

FIGURE 4.1: Bain correspondence between austenite and martensite phases [1]

fcc unit cells. The martensite bcc lattice (Fig.4.1(b)) forms by deformation of the bct (Fig.4.1(a)) lattice: compression along $[001]_\gamma$ axis and expansion along $[1\bar{1}0]_\gamma$ and $[110]_\gamma$ directions. This transformation is induced by Bain strain and requires a minimum of atomic motion. In steels the resulting martensite lattice parameters a and c correspond to a given carbon content. In earlier theories it was thought that the formation of α' phase from γ phase occurs exactly by this mechanism.

However, the Bain strain does not satisfy the conditions of the habit plane formation and could not describe the hole transformation [86]. In fact, the experimentally observed correspondence between γ and α' phases are different of proposed by Bain correspondences.

4.1.1.1 Orientation relationships

As was discussed in the introduction, the martensite transformation is diffusionless phase transition where the low temperature martensite phase with bct structure growths in the high temperature austenite fcc phase. The misfit between this two structures induces the internal elastic stress in the system. The minimisation of the total free energy of system that contains the elastic and chemical contributions, produces some special orientational relations between two phases. Experimentally different orientations between these phases has been observed: Kurdjumov-Sachs (KS), Nishiyama-Wassermann (NW), Greninger-Troiano (GT), Pitsch and Bain orientation relationships (ORs). In the plain carbon steels the most often found KS ORs. However, NW relationships have been observed in Fe-30% Ni alloys [1]. In nickel steels, the GT ORs have been found, which are intermediate between KS and NW ORs. Pitsch correspondence has been found in iron-nitrogen alloys [87]. It should be remarks, that Bain relationships have been found in Fe_3Pt and Fe_3Al-C martensites.

In our modeling we will be interested only about KS ORs. In KS ORs $\{111\}_\gamma$ close-packed planes of fcc structure are parallel to the bcc $\{011\}_{\alpha'}$ close-packed planes:

$$\{111\}_\gamma \| \{011\}_{\alpha'}. \tag{4.1}$$

There are four possible close-packed planes in the fcc structure. Each close-packed plane consists of the six different orientations of the bcc structure along close-packed directions. These orientations are called crystallographic variants. On the Figure 4.2 ([11]) the $(111)_\gamma$ plane of austenite is indicated as a triangle and six variants of martensite which can be obtained from this $(111)_\gamma$ planes are shown. The $(011)_{\alpha'}$ martensite plane is shown as a rectangle. In general case fcc structure consists of the four possible $\{111\}_\gamma$ close-packed planes: $(111)_\gamma$, $(1\bar{1}1)_\gamma$, $(\bar{1}11)_\gamma$ and $(11\bar{1})_\gamma$; there are 24 equivalent crystallographic KS ORs (variants). The ORs for all these 24 variants are presented in the table 4.1. In this table the misorientation angle between a given variant with respect to variant V1 is also done [18].

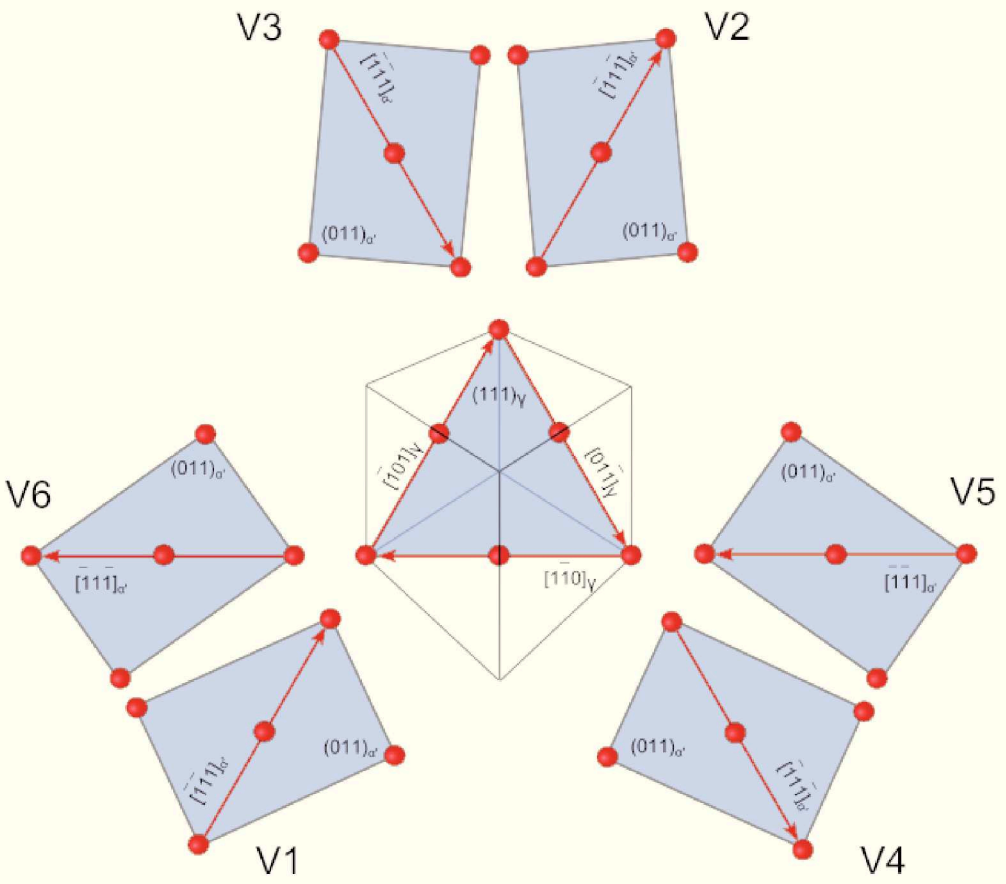

FIGURE 4.2: Schematic representation of six crystallographic variants (V1-V6) which correspond to KS ORs

4.1.1.2 The orientation transformation matrix

The coordinates of atoms in one of the KS variants of martensite can be found from the coordinates of the fcc lattice using transformation matrix ($\alpha J \gamma$). To calculate this matrix, the method presented in the book [25] was used. Thereafter one example of the calculation of this matrix for the first variant V1 of KS will be done.

The coordinates of each atom in the lattice can be described by some vector $\mathbf{u}$. The magnitude of the vector $\mathbf{u}$ and its direction with respect to other vectors can be determined by the set of the basis vectors. A basis for austenite is convenient to choose as orthogonal right-handed basis $\{\mathbf{a}_i\}$ $(i = 1, 2, 3)$ along to the three axes of the face-centered cubic unit cell with the lattice parameter, a_0^{fcc}. The basis for the martensite, $\{\mathbf{b}_i\}$ $(i = 1, 2, 3)$, is chosen in the same way: basis vectors are aligned along edges of the base-centered unit cell with the lattice parameter, a_0^{bcc}. For convenience we will denote fcc and bcc bases as "γ" and "α", respectively.

Thus the vector $\mathbf{u}$ can be written as a linear combination of the γ or α bases. In γ basis $\mathbf{u}$ can be presented as

$$\mathbf{u} = u_1\mathbf{a}_1 + u_2\mathbf{a}_2 + u_3\mathbf{a}_3,$$

or in column representation

$$[\gamma;\mathbf{u}] = \begin{pmatrix} u_1 \\ u_2 \\ u_3 \end{pmatrix}. \tag{4.2}$$

The α basis can be expressed by the matrix equation through the γ basis:

$$\begin{pmatrix} \mathbf{b}_1 \\ \mathbf{b}_2 \\ \mathbf{b}_3 \end{pmatrix} = \begin{pmatrix} M_{11} & M_{12} & M_{13} \\ M_{21} & M_{22} & M_{23} \\ M_{31} & M_{32} & M_{33} \end{pmatrix} \begin{pmatrix} \mathbf{a}_1 \\ \mathbf{a}_2 \\ \mathbf{a}_3 \end{pmatrix} \equiv (\alpha M \gamma) \begin{pmatrix} \mathbf{a}_1 \\ \mathbf{a}_2 \\ \mathbf{a}_3 \end{pmatrix}. \tag{4.3}$$

TABLE 4.1: The 24 crystallographic variants of the KS ORs. Various Bain groups (BG) and misorientation angle (θ) of variant V2 to V24 relative to V1 are given in the table [18].

Variant number	Plane parallel	Direction parallel	BG	Misorientation from V1 (θ)
1	$(111)_\gamma \| (011)_\alpha$	$[\bar{1}01]_\gamma \| [\bar{1}\bar{1}1]_\alpha$	B1	-
2		$[\bar{1}01]_\gamma \| [\bar{1}1\bar{1}]_\alpha$	B2	60°
3		$[01\bar{1}]_\gamma \| [\bar{1}\bar{1}1]_\alpha$	B3	60°
4		$[01\bar{1}]_\gamma \| [\bar{1}1\bar{1}]_\alpha$	B1	10.5°
5		$[1\bar{1}0]_\gamma \| [\bar{1}\bar{1}1]_\alpha$	B2	60°
6		$[1\bar{1}0]_\gamma \| [\bar{1}1\bar{1}]_\alpha$	B3	49.5°
7	$(1\bar{1}1)_\gamma \| (011)_\alpha$	$[10\bar{1}]_\gamma \| [\bar{1}\bar{1}1]_\alpha$	B2	49.5°
8		$[10\bar{1}]_\gamma \| [\bar{1}1\bar{1}]_\alpha$	B1	10.5°
9		$[\bar{1}\bar{1}0]_\gamma \| [\bar{1}\bar{1}1]_\alpha$	B3	50.5°
10		$[\bar{1}\bar{1}0]_\gamma \| [\bar{1}1\bar{1}]_\alpha$	B2	50.5°
11		$[011]_\gamma \| [\bar{1}\bar{1}1]_\alpha$	B1	14.9°
12		$[011]_\gamma \| [\bar{1}1\bar{1}]_\alpha$	B3	57.2°
13	$(\bar{1}11)_\gamma \| (011)_\alpha$	$[0\bar{1}1]_\gamma \| [\bar{1}\bar{1}1]_\alpha$	B1	14.9°
14		$[0\bar{1}1]_\gamma \| [\bar{1}1\bar{1}]_\alpha$	B3	50.5°
15		$[\bar{1}0\bar{1}]_\gamma \| [\bar{1}\bar{1}1]_\alpha$	B2	57.2°
16		$[\bar{1}0\bar{1}]_\gamma \| [\bar{1}1\bar{1}]_\alpha$	B1	20.6°
17		$[110]_\gamma \| [\bar{1}\bar{1}1]_\alpha$	B3	51.7°
18		$[110]_\gamma \| [\bar{1}1\bar{1}]_\alpha$	B2	47.1°
19	$(11\bar{1})_\gamma \| (011)_\alpha$	$[\bar{1}10]_\gamma \| [\bar{1}\bar{1}1]_\alpha$	B3	50.5°
20		$[\bar{1}10]_\gamma \| [\bar{1}1\bar{1}]_\alpha$	B2	57.2°
21		$[0\bar{1}\bar{1}]_\gamma \| [\bar{1}\bar{1}1]_\alpha$	B1	20.6°
22		$[0\bar{1}\bar{1}]_\gamma \| [\bar{1}1\bar{1}]_\alpha$	B3	47.1°
23		$[101]_\gamma \| [\bar{1}\bar{1}1]_\alpha$	B2	57.2°
24		$[101]_\gamma \| [\bar{1}1\bar{1}]_\alpha$	B1	21.1°

The matrix $(\alpha M\gamma)$ represents the coordinate transformation of the vector components from the γ to α basis:

$$[\alpha;\mathbf{u}] = (\alpha M\gamma)\,[\gamma;\mathbf{u}]. \tag{4.4}$$

To obtain the position of atoms in the first KS variant, the matrix $(\alpha_1 M\gamma)$ should be calculated, where α_1 designate the variant V1:

$$[111]_\gamma \| [011]_\alpha, \quad [\bar{1}01]_\gamma \| [\bar{1}\bar{1}1]_\alpha, \quad [1\bar{2}1]_\gamma \| [2\bar{1}1]_\alpha. \tag{4.5}$$

The length of the vectors which determine the direction presented in (4.5), should be invariant during fcc-to-bcc transition. Thus it is necessary to equalize the magnitudes of these parallel vectors. For this we will introduce the constants k, g, m as a ratio of lengths of the two parallel vectors:

$$\begin{aligned} k &= \frac{a_0^{fcc}\sqrt{3}}{a_0^{bcc}\sqrt{2}}, \\ g &= \frac{a_0^{fcc}\sqrt{2}}{a_0^{bcc}\sqrt{3}}, \\ m &= \frac{a_0^{fcc}\sqrt{6}}{a_0^{bcc}\sqrt{6}} = \frac{a_0^{fcc}}{a_0^{bcc}}. \end{aligned} \tag{4.6}$$

Substituting relations (4.6), (4.5) in (4.3) we get

$$\begin{aligned} [0kk] &= (\alpha_1 M\gamma)\,[111], \\ [\bar{g}\bar{g}g] &= (\alpha_1 M\gamma)\,[\bar{1}01]\,, \\ [2m\bar{m}m] &= (\alpha_1 M\gamma)\,[1\bar{2}1]\,. \end{aligned} \tag{4.7}$$

Then we can rewrite these equations as

$$\begin{pmatrix} 0 & \bar{g} & 2m \\ k & \bar{g} & \bar{m} \\ k & g & m \end{pmatrix} = \begin{pmatrix} M_{11} & M_{12} & M_{13} \\ M_{21} & M_{22} & M_{23} \\ M_{31} & M_{32} & M_{33} \end{pmatrix} \begin{pmatrix} 1 & \bar{1} & 1 \\ 1 & 0 & \bar{2} \\ 1 & 1 & 1 \end{pmatrix}.$$

Finally the orientation transformation matrix is

TABLE 4.2: The rotational matrices for the 24 variants of KS ORs [11].

$\hat{J}_1 = \begin{pmatrix} 0.742 & -0.667 & -0.075 \\ 0.650 & 0.742 & -0.167 \\ 0.167 & 0.075 & 0.983 \end{pmatrix}$	$\hat{J}_{13} = \begin{pmatrix} 0.667 & 0.742 & -0.075 \\ -0.742 & 0.650 & -0.167 \\ -0.075 & 0.167 & 0.983 \end{pmatrix}$
$\hat{J}_2 = \begin{pmatrix} 0.075 & 0.667 & -0.742 \\ -0.167 & 0.742 & 0.650 \\ 0.983 & 0.075 & 0.167 \end{pmatrix}$	$\hat{J}_{14} = \begin{pmatrix} -0.667 & 0.075 & -0.742 \\ -0.742 & -0.167 & 0.650 \\ -0.075 & 0.983 & 0.167 \end{pmatrix}$
$\hat{J}_3 = \begin{pmatrix} -0.667 & -0.075 & 0.742 \\ 0.742 & -0.167 & 0.650 \\ 0.075 & 0.983 & 0.167 \end{pmatrix}$	$\hat{J}_{15} = \begin{pmatrix} 0.075 & -0.667 & 0.742 \\ 0.167 & 0.742 & 0.650 \\ -0.983 & 0.075 & 0.167 \end{pmatrix}$
$\hat{J}_4 = \begin{pmatrix} 0.667 & -0.742 & 0.075 \\ 0.742 & 0.650 & -0.167 \\ 0.075 & 0.167 & 0.983 \end{pmatrix}$	$\hat{J}_{16} = \begin{pmatrix} 0.742 & 0.667 & 0.075 \\ -0.650 & 0.742 & -0.167 \\ -0.167 & 0.075 & 0.983 \end{pmatrix}$
$\hat{J}_5 = \begin{pmatrix} -0.075 & 0.742 & -0.667 \\ -0.167 & 0.650 & 0.742 \\ 0.983 & 0.167 & 0.075 \end{pmatrix}$	$\hat{J}_{17} = \begin{pmatrix} -0.742 & -0.075 & -0.667 \\ -0.650 & -0.167 & 0.742 \\ -0.167 & 0.983 & 0.075 \end{pmatrix}$
$\hat{J}_6 = \begin{pmatrix} -0.742 & 0.075 & 0.667 \\ 0.650 & -0.167 & 0.742 \\ 0.167 & 0.983 & 0.075 \end{pmatrix}$	$\hat{J}_{18} = \begin{pmatrix} -0.075 & -0.742 & 0.667 \\ 0.167 & 0.650 & 0.742 \\ -0.983 & 0.167 & 0.075 \end{pmatrix}$
$\hat{J}_7 = \begin{pmatrix} -0.075 & 0.667 & 0.742 \\ -0.167 & -0.742 & 0.650 \\ 0.983 & -0.075 & 0.167 \end{pmatrix}$	$\hat{J}_{19} = \begin{pmatrix} 0.742 & -0.075 & 0.667 \\ 0.650 & -0.167 & -0.742 \\ 0.167 & 0.983 & -0.075 \end{pmatrix}$
$\hat{J}_8 = \begin{pmatrix} -0.742 & -0.667 & 0.075 \\ 0.650 & -0.742 & -0.167 \\ 0.167 & -0.075 & 0.983 \end{pmatrix}$	$\hat{J}_{20} = \begin{pmatrix} 0.075 & -0.742 & -0.667 \\ -0.167 & 0.650 & -0.742 \\ 0.983 & 0.167 & -0.075 \end{pmatrix}$
$\hat{J}_9 = \begin{pmatrix} 0.742 & 0.075 & -0.667 \\ 0.650 & 0.167 & 0.742 \\ 0.167 & -0.983 & 0.075 \end{pmatrix}$	$\hat{J}_{21} = \begin{pmatrix} -0.667 & 0.742 & 0.075 \\ 0.742 & 0.650 & 0.167 \\ 0.075 & 0.167 & -0.983 \end{pmatrix}$
$\hat{J}_{10} = \begin{pmatrix} 0.075 & 0.742 & 0.667 \\ -0.167 & -0.650 & 0.742 \\ 0.983 & -0.167 & 0.075 \end{pmatrix}$	$\hat{J}_{22} = \begin{pmatrix} 0.667 & 0.075 & 0.742 \\ 0.742 & -0.167 & -0.650 \\ 0.075 & 0.983 & -0.167 \end{pmatrix}$
$\hat{J}_{11} = \begin{pmatrix} -0.667 & -0.742 & -0.075 \\ 0.742 & -0.650 & -0.167 \\ 0.075 & -0.167 & 0.983 \end{pmatrix}$	$\hat{J}_{23} = \begin{pmatrix} -0.075 & -0.667 & -0.742 \\ -0.167 & 0.742 & -0.650 \\ 0.983 & 0.075 & -0.167 \end{pmatrix}$
$\hat{J}_{12} = \begin{pmatrix} 0.667 & -0.075 & -0.742 \\ 0.742 & 0.167 & 0.650 \\ 0.075 & -0.983 & 0.167 \end{pmatrix}$	$\hat{J}_{24} = \begin{pmatrix} -0.742 & 0.667 & -0.075 \\ 0.650 & 0.742 & 0.167 \\ 0.167 & 0.075 & -0.983 \end{pmatrix}$

$$
\begin{aligned}
(\alpha_1 M \gamma) &= \frac{1}{6} \begin{pmatrix} 3g+2m & -4m & -3g+2m \\ 2k+3g-m & 2k+2m & 2k-3g-m \\ 2k-3g+m & 2k-2m & 2k+3g+m \end{pmatrix} \\
&= \frac{a_0^{fcc}}{a_0^{bcc}} \begin{pmatrix} 0.742 & -0.667 & -0.075 \\ 0.650 & 0.742 & -0.167 \\ 0.167 & 0.075 & 0.983 \end{pmatrix}. \qquad (4.8)
\end{aligned}
$$

Then it is convenient to introduce the rotational matrix $(\alpha_1 J\gamma)$ that transform the coordinates of atoms in the fcc lattice to their position in the V1 KS variant of martensite

$$(\alpha_1 J\gamma) = \hat{J}_1 = \begin{pmatrix} 0.742 & -0.667 & -0.075 \\ 0.650 & 0.742 & -0.167 \\ 0.167 & 0.075 & 0.983 \end{pmatrix}. \tag{4.9}$$

Using this procedure all other rotational matrix can be obtained for all 23 variants presented in Table 4.2.

4.1.1.3 Deformation twinning

As was mentioned before, there are two main deformation modes, which reduce the strain in material during martensite transformation: slip and twinning. Both mechanisms can be involved in MT. In binary alloys, such as Fe-C, Fe-Ni, Fe-N binary alloys with high content of carbon, nickel, nitrogen, respectively, the twinned microstructure is found [88, 89]. Also, twins are observed in iron-carbon [89, 90] alloys with low carbon quenching at temperatures lower then M_s temperature. In general case, twinning mechanism coexists with slip mechanism. However, the decrease of the temperature of martensite transformation or application of the external strain lead to domination of the twinning mechanism [20].

A detailed overview of twinning mechanism of martensite transformation can be found, for example, in [20]. In this paragraph we will focus only on twinning crystallography. According to definition, deformation twinning is a kind of diffusionless transformation in which a new phase has the same crystal structure as a parent phase and corresponds to its mirror image. In the Fig.4.3(a) a twinned crystal is shown. The red part corresponds to the parent undeformed crystal and the green part represents its twin. In our case we will consider the centrosymetrical crystals. In this case, the twins can be obtained from the parent crystal using one of two operations: (1) by a reflection in some plane, which is called twinning plane, or (2) by a rotation by π about some axis, which is called twinning direction. Twins obtained by the first operation are called type I twins and obtained by the second one are called type II twins [91]. For the high symmetry lattices, such as fcc and bcc, these two operations are equivalent and the resulting twins are called compound twins.

The deformation process, which induces twins formation, requires coordinated individual atom displacements, that are achieved by a homogeneous simple shear. In general, deformation twinning can be described by twinning elements: K_1, K_2, η_1, η_2, shear magnitude s and plane of shear P. These elements define a twinning mode. In Fig.4.3(b-c) twinning elements are shown. Twinning shear of magnitude s occurs in the plane K_1. Plane K_1 is the invariant of this shear and is called twinning plane. The direction of the shear is called twinning direction and is denoted as η_1. The conjugate twinning plane, K_2, is undistorted, but due to the shear is rotated. In Fig.4.3(b) the plane K_2 is marked in red and the plane formed by twinning and belonged to

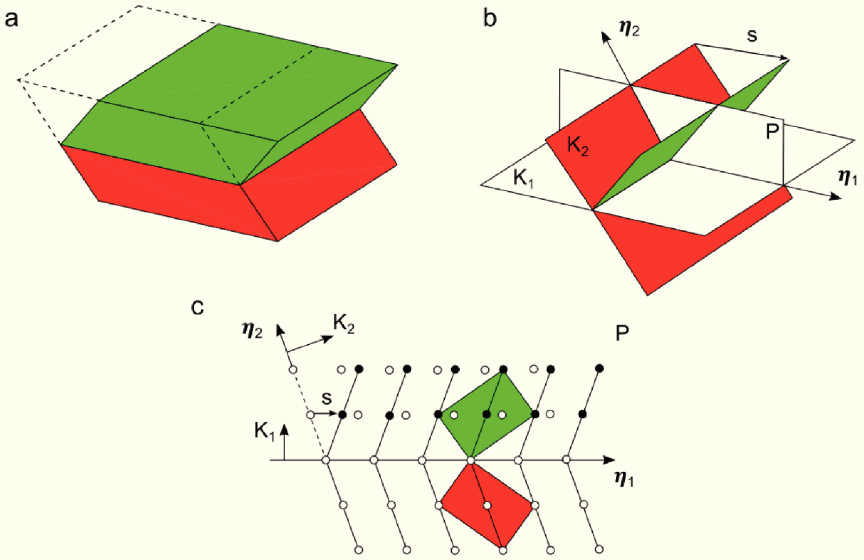

FIGURE 4.3: Schematic representation of deformation twinning. (a) Twins (solid lines) formed from an undistorted single crystal (dashed lines) by shear, parent part of a crystal is in red and its twin in green. (b) The twinning elements: K_1 is the twinning plane, K_2 is the conjugate twinning plane, η_1 and η_2 are the twinning direction and the conjugate twinning direction, respectively, P is the plane of shear, s is the magnitude of the shear. (c) Projection of the atomic positions on plane P. The open circles are the lattice points before the shear, while, the filled black circles are the lattice points after the shear.

twin is marked in green. The plane of shear, P, is defined as a plane containing η_1 and normals to K_1 and K_2. The conjugate twinning direction, η_2, can be found as an intersection of planes P and K_2. Then magnitude of shear, s, can be found as:

$$s = 2\tan\varphi, \tag{4.10}$$

here φ is the angle between η_2 and normal to K_1.

To explain the mechanism of twins formation and their growth, the dislocation-based models are used. The theory based on interfacial line defects has been developed by Pond and Hirth [92–94], this approach describes the mechanical aspects of the diffusionless transformations. These interfacial line defects, which they called disconnections, are elementary agents of the deformation. In the case of deformation twinning, the motion of disconnections on the twinning plane induces the twin growth.

To illustrate the structure of a disconnection we will use Fig.4.4 [92, 95]. In this figure two crystals labeled as λ and μ and indicated in green and red are separated along their interface. In general case, each surface contains a surface step characterized by translation vector (or step vector) $\mathbf{t}_\lambda$ and $\mathbf{t}_\mu$. The overlap of step vectors in the direction normal to interface gives step height h. If we bring together the surfaces of two crystals λ and μ, the resulting bicrystal will be distorted in the vicinity of the interface step. Thus, a line defect is created. The corresponding

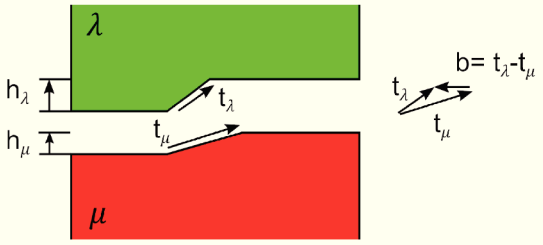

FIGURE 4.4: Schematic representation of a disconnection. Step vectors $\mathbf{t}_\lambda$ and $\mathbf{t}_\mu$ characterize steps on surfaces λ and μ, respectively. $\mathbf{h}_\lambda$ and $\mathbf{h}_\mu$ their step heights. $\mathbf{b}$ is the Burgers vector.

Burgers vector is:

$$\mathbf{b} = \mathbf{t}_\lambda - \mathbf{t}_\mu. \tag{4.11}$$

Its component, which is parallel to the interface, induces a shear and the component perpendicular to the interface induces compression or dilatation. Thus, disconnection is a interfacial defect with Burgers vector $\mathbf{b}$ and step height h.

In the case of twinning, when perpendicular components to the interface, h_λ and h_μ, of step vectors $\mathbf{t}_\lambda$ and $\mathbf{t}_\mu$ are equal, then the disconnection is a twinning dislocation. Due to the fact the Burgers vector is parallel to the interface in twinning dislocation, the deformation twinning is a simple shear and moving of these defects doesn't induce any volume change. Gliding of the twinning dislocations involve the atomic displacements and, therefore, growth of the twin plate.

4.2 Modeling of a FCC to BCC transformation

4.2.1 Simulated details

To model the MT the AFT presented in Chapter 2 has been used. Solving Eq.(2.51) the temporal evolution of the density function $\rho(\mathbf{r})$ can be calculated. This equation was solved using the semi-implicit Fourier spectral method.

The initial state is fcc phase with nucleus of one of KS variants. Therefore, some prior preparations of the initial state of the system is required. The first step is consist of the constructing the fcc and bcc phases at equilibrium. Then the cubic nucleus with bcc structure oriented with respect to one of the KS ORs is introduced into fcc matrix. The initial size of the nucleus should be large enough to overcome the kinetic barrier existing in the MT.

To model the equilibrium state of fcc and bcc crystal we will consider only a monoatomic system representing the iron atoms. In this case the FT of the interaction potential (2.13) can be written:

$$\widetilde{w}(\mathbf{k}) = \lambda_1 \tilde{\theta}(\mathbf{k}) + \lambda_2 \widetilde{w}_{LR}(\mathbf{k}). \tag{4.12}$$

In Eq.(4.12) λ_1 and λ_2 are the fitting parameters determining strength of the short range and long range interactions, respectively, the short range part of the potential $\tilde{\theta}(\mathbf{k})$ is the same as in Eq.(2.14). The long-range part of the interactional potential should be isotropic to allow the formation of any martensite variants. In our case, for long-range interaction we used a Gaussian function:

$$f(x) = \exp\left(-\frac{(x-x_0)^2}{2\sigma^2}\right). \tag{4.13}$$

Here σ is a constant. The function (4.13) has an extremum at x_0 and to provide a minimum at this point the constant λ_2 should be negative. The position of the minimum of the Gaussian function corresponds to the distance between the first neighbors in the reciprocal space.

Using (2.12) the anisotropic long-range potential for the fcc lattice is

$$\widetilde{w}^{\mathrm{fcc}}_{LR}(\mathbf{k}) = \lambda_2 \widetilde{\Omega}_{\mathrm{fcc}}(\mathbf{k}) = \lambda_2 \left|\Psi^{\mathrm{fcc}}(\mathbf{k})\right|^2 = \lambda_2 \times \left(4 + 4\left(\cos(\tfrac{k_x a^{\mathrm{fcc}}}{2})\cos(\tfrac{k_y a^{\mathrm{fcc}}}{2}) + \cos(\tfrac{k_x a^{\mathrm{fcc}}}{2})\cos(\tfrac{k_z a^{\mathrm{fcc}}}{2}) + \cos(\tfrac{k_y a^{\mathrm{fcc}}}{2})\cos(\tfrac{k_z a^{\mathrm{fcc}}}{2})\right)\right). \tag{4.14}$$

This potential reaches the minima at the points $\{\mathbf{k}_{01}\} = \frac{2\pi}{a^{\mathrm{fcc}}}\{111\}$ and $\{\mathbf{k}_{02}\} = \frac{2\pi}{a^{\mathrm{fcc}}}\{200\}$. The distances to these minima respectively are $k^{\mathrm{fcc}}_{01} = \frac{2\pi}{a^{\mathrm{fcc}}}\sqrt{3}$ and $k^{\mathrm{fcc}}_{02} = \frac{2\pi}{a^{\mathrm{fcc}}}2$. Therefore the long-range isotropic potential for the fcc structure can be written as

$$\widetilde{w}^{\mathrm{fcc}}_{LR}(k) = \lambda_2\left(\exp\left(-\frac{(k-k^{\mathrm{fcc}}_{01})^2}{2\sigma^2}\right) + \exp\left(-\frac{(k-k^{\mathrm{fcc}}_{02})^2}{2\sigma^2}\right)\right). \tag{4.15}$$

Similarly for a bcc structure the position of the minimum can be found from an anisotropic potential

$$\widetilde{w}^{\mathrm{bcc}}_{LR}(\mathbf{k}) = \lambda_2 \widetilde{\Omega}_{\mathrm{bcc}}(\mathbf{k}) = \lambda_2 \left|\Psi^{\mathrm{bcc}}(\mathbf{k})\right|^2 = \lambda_2\left(8 + 8\cos(\tfrac{k_x a^{\mathrm{bcc}}}{2})\cos(\tfrac{k_y a^{\mathrm{bcc}}}{2})\cos(\tfrac{k_z a^{\mathrm{bcc}}}{2})\right). \tag{4.16}$$

The potential (4.16) reaches the minima at the points $\{\mathbf{k}_{01}\} = \frac{2\pi}{a^{\mathrm{bcc}}}\{110\}$. Hence the distance to this minimum can be written as: $k^{\mathrm{bcc}}_{01} = \frac{2\pi}{a^{\mathrm{bcc}}}\sqrt{2}$ and the isotropic potential in this case is

$$\widetilde{w}^{\mathrm{bcc}}_{LR}(k) = \lambda_2 \exp\left(-\frac{(k-k^{\mathrm{bcc}}_{01})^2}{2\sigma^2}\right). \tag{4.17}$$

All modeling have been performed at the constant volume. To satisfy this condition we imposed that the distance between first neighbors atoms in both structures (fcc and bcc) are the same (Fig.4.5). In this case the ratio between the lattice constants of the fcc and the bcc structures is

$$\frac{a^{fcc}}{a^{bcc}} = \sqrt{\frac{3}{2}} \approx 1.225. \tag{4.18}$$

The ratio (4.18) is close to that observed in experiment: $a^{fcc}/a^{bcc} = 3.562\,\mathring{A}/2.860\,\mathring{A} \approx 1.245$

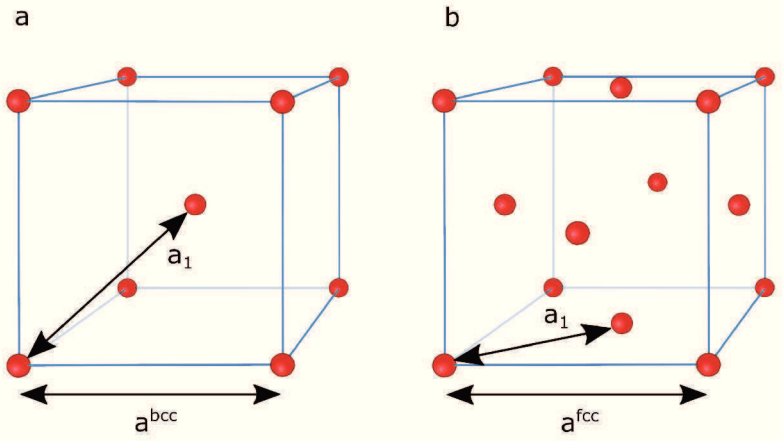

FIGURE 4.5: Schematic representation of the distance a_1 to the nearest neighbors in (a) bcc and (b) fcc lattices with lattice parameters a^{bcc} and a^{fcc}, respectively.

[96]. To generate the fcc and bcc structures the next set of parameters has been used: $\bar{\rho} = 0.13$, $R = 2.75$, $\Delta x = \pi$, $\lambda_1 = 1.0$, $\lambda_2 = -0.2$, $\Delta t = 1 \cdot 10^{-3}$, $L = 80.0$, $\xi = 4$, $\frac{\Delta r}{R} = 0.17$, $\sigma = 0.01$, $k_B T = 5.0 \cdot 10^{-2}$. The values of k were: $k_{01}^{\text{bcc}} = k_{01}^{\text{fcc}} = k_{01} = 0.433$ and $k_{02}^{\text{fcc}} = k_{02} = 0.5$ which correspond to the lattice parameters of the fcc lattice $a^{\text{fcc}} = 8$ and the bcc lattice $a^{\text{bcc}} = 6.5$. It should be noted, that the two radii of the atoms correspond approximately to the distance between the nearest neighbors atoms. In the case of the fcc matrix the simulation box 512^3 has been used. The V1 KS variant of the bcc structure was simulated with the simulation box 128^3. The initial nucleus was rotated with respect to x y, z axes using the rotation matrix defined by equation (4.2).

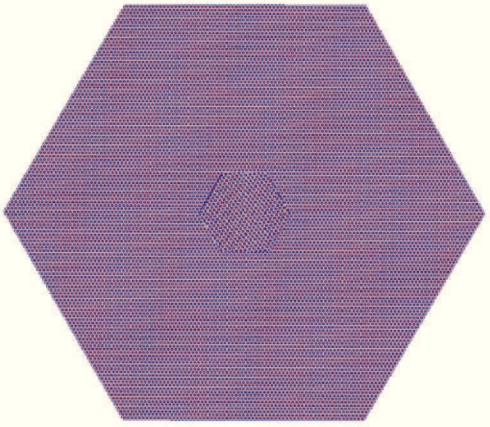

FIGURE 4.6: The initial state of the simulated system. Only the $(111)_{\text{fcc}}$ plane of the 3D simulation box is presented.

Once the equilibrium bcc and fcc phases have been obtained, the initial state to model MT has been constructed. Then the initial state shown in Fig.4.6 contains two phases: the fcc matrix and the cube with a size 48^3 of simulation grids in the center of the simulation box of bcc phase. In this case, the orientation of the bcc nucleus corresponds to the $V1$ variant of KS orientation relationships between austenite and martensite phases. To better visualise the

initial state, the $(111)_{\text{fcc}}$ plane of the fcc matrix that is parallel to the $(011)_{\text{bcc}}$ plane of the bcc nucleus is shown in Fig.4.6.

To stabilize the bcc structure we decreased the amplitude of the second peak in the long-range potential (4.15) for the fcc structure. The first peak in (4.15) is the same as in (4.17) according to (4.18). To model the fcc-to-bcc transition we used the following long-range potential:

$$\widetilde{w}_{LR}(k) = \lambda_2 \left(\exp\left(-\frac{(k-k_{01})^2}{2\sigma^2} \right) + 0.1 \exp\left(-\frac{(k-k_{02})^2}{2\sigma^2} \right) \right). \tag{4.19}$$

The elastic constants for the fcc and bcc lattices with potentials (2.14) and (4.19) which are considered in (4.12) can be calculated using the method specified in Appendix A. Their values in adimensional units are: $C_{11} = 0.233$, $C_{12} = 0.101$, $C_{44} = 0.086$ for bcc lattice and $C_{11} = 0.139$, $C_{12} = 0.081$, $C_{44} = 0.090$ for the fcc lattice. These values were obtained using σ equal 0.05 in potential (4.19). All simulations were done with simulation box 512^3.

For comparison the experimental constants for the iron are: $C_{11} = 246$ GPa, $C_{12} = 140$ GPa, $C_{44} = 116$ GPa for the bbc lattice [97] and $C_{11} = 154$ GPa, $C_{12} = 122$ GPa, $C_{44} = 77$ GPa for fcc lattice [98].

4.2.2 Simulation results

The different steps of the fcc-to-bcc transition in direct space are presented in figures 4.7 and 4.8. For convenience, only $(001)_\gamma$ (Fig.4.7) and $(100)_\gamma$ (Fig.4.8) planes are shown. On the first images (Fig. 4.7(a) and 4.8(a)) the initial state with the fcc matrix and bcc nucleus are shown. At Figs 4.7b-48b 4.7(b-c) and 4.8(b-c) the second variant can be observed. In these figures the system of dislocations on astenite/martensite interface are visible (see white arrows in Figs. 4.7(c) and 4.8(c)). During growth (see Figs. 4.7(c) and 4.8(c)) these two variant structure growth and bcc nucleus transforms in multidomain structure. At the final stage of transformation two variant structure can be clearly distinguished.

To analyze the obtained multidomain structure: the crystallographic orientations of their components with respect to the fcc phase and the misorientation angle between variants of the resulting martensite, the pole figures can be used.

4.2.2.1 Simulations of pole figures

After complete martensite transformation the orientation of each crystallographic variant can be determined by using a pole figure representation (see Appendix B). To recognize the orientation of variants of the multidomain structure it is enough to build only (001) pole figure. In Fig. 4.9(a) are shown (001) pole figures of the ideal KS relations. Each KS variant is marked by a number from 1 to 24. For comparison the experimental pole figure for the prior austenite grain with all 24 variants is also given (Fig.4.9(b)). Pole figures in Fig. 4.9 are given relatively to the (001)[100] orientation of the austenite grain.

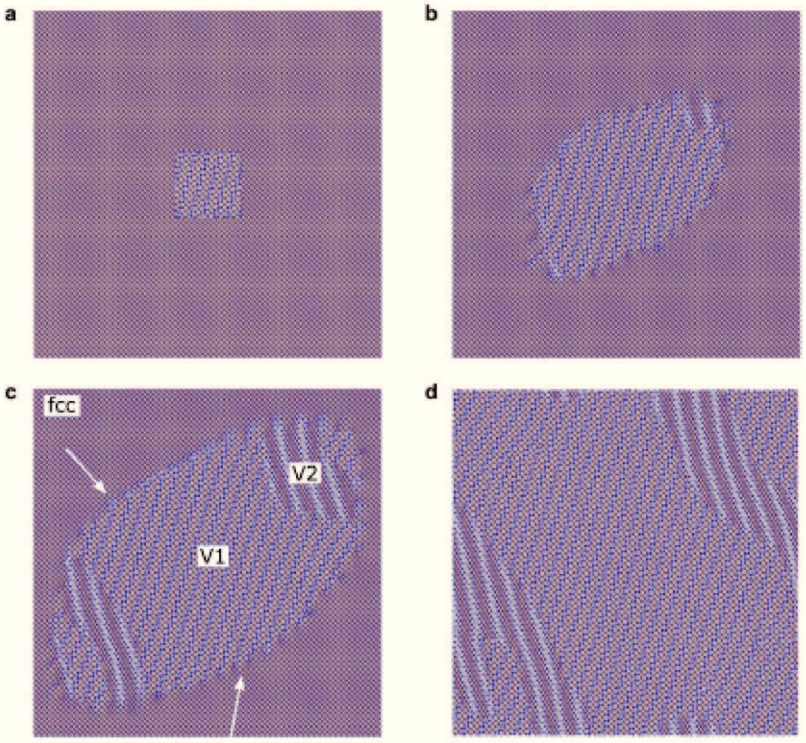

FIGURE 4.7: The atomic density profile at simulation times (a)$\hat{t} = 0$, (b)$\hat{t} = 320000$, (c)$\hat{t} = 520000$, (d)$\hat{t} = 950000$ in $(001)_\gamma$ plane. Different phases (fcc, V1 and V2) are shown in (c), austenite/martensite dislocations are shown by white arrows.

To identify the orientation of the variants obtained in our simulation, the (001) pole figures of 24 KS variants were built. These pole figures and the pole figure obtained from our simulation are shown in Fig.4.10. In Fig.4.10(a) KS variants corresponding to the different close-packed planes are denoted by red, green, blue and black colors. Each crystallographic variant is characterized by three poles in (001) pole figure. Since the pole figure in Fig.4.10(b) contains six spots, there are two different crystallographic variants on the final step of MT in the simulation box. As shown in figure 4.10(c) the superposition of Figs.4.10(a) and 4.10(b) gives the nature of two variants obtained in simulation. In our case V1 and V2 KS variants coexist.

4.2.2.2 Calculation of misorientation angle

In experimental studies the misorientation between two variants is an important characteristic of morphology of materials. The misorientation angle can be measured, for example, by electron backscatter diffraction (EBSD) technique using the scanning electron microscope (SEM) or by selected area diffraction (SAD) patterns using transmission electron microscopy (TEM).

In our case the misorientaion angle can be directly found from the atomic density profile distribution in the direct space. Since the $(011)_\alpha$ (or $(111)_\gamma$) in direct space is a common plane for both variants it can be used to find the misorientation angle between these two variants.

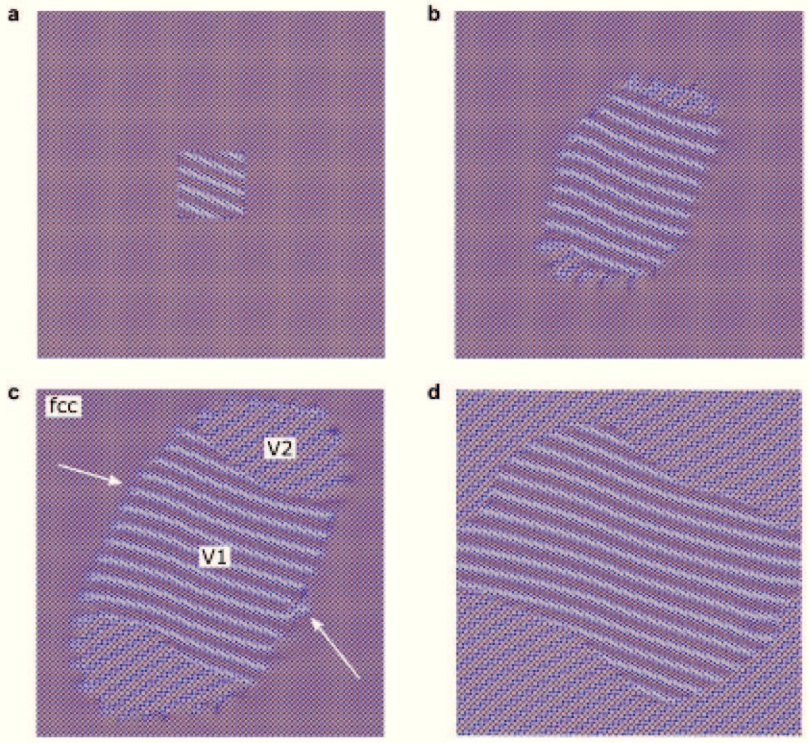

FIGURE 4.8: The atomic density profile at simulation times (a)$\hat{t} = 0$, (b)$\hat{t} = 320000$, (c)$\hat{t} = 520000$, (d)$\hat{t} = 950000$ in $(100)_\gamma$ plane. Different phases (fcc, V1 and V2) are shown in (c), austenite/martensite dislocations are shown by white arrows.

Fig.4.11(a) shows the atomic density profile in $(111)_\gamma$ plane on the last step of modeling. The region, where two variants are connected, is highlighted by the orange rectangle and magnified (Fig.4.11(b)). In Fig.4.11(b) it is possible to recognize crystal structures of both variants. The $(011)_\alpha$ sections of V1 and V2 variants are denoted by red and green colors, respectively. Then using the software ImageJ 1.49v we found the misorientation angle $\theta = 70.1°$.

To compare the obtained angle between two variants with an angle θ_{id} between ideal V1 and V2 variants of KS relations the method described in [25] can be used. First, we can find the orientation relation matrix of V1 and V2 KS variants:

$$(\alpha_2 J \alpha_1) = (\alpha_2 J \gamma)\,(\gamma J \alpha_1) = \frac{1}{3}\begin{pmatrix} \bar{1} & 2 & \bar{2} \\ \bar{2} & 1 & 2 \\ 2 & 2 & 1 \end{pmatrix}. \tag{4.20}$$

Here $(\alpha_2 J \gamma)$ corresponds to the matrix $\hat{J}_2$ from the table 4.2, $(\gamma J \alpha_1)$ is the inverse matrix of $\hat{J}_1$. The $(\alpha_2 J \alpha_1)$ matrix transforms the components of vectors referred to the basis of V1 variant to vectors referred to the V2 variant.

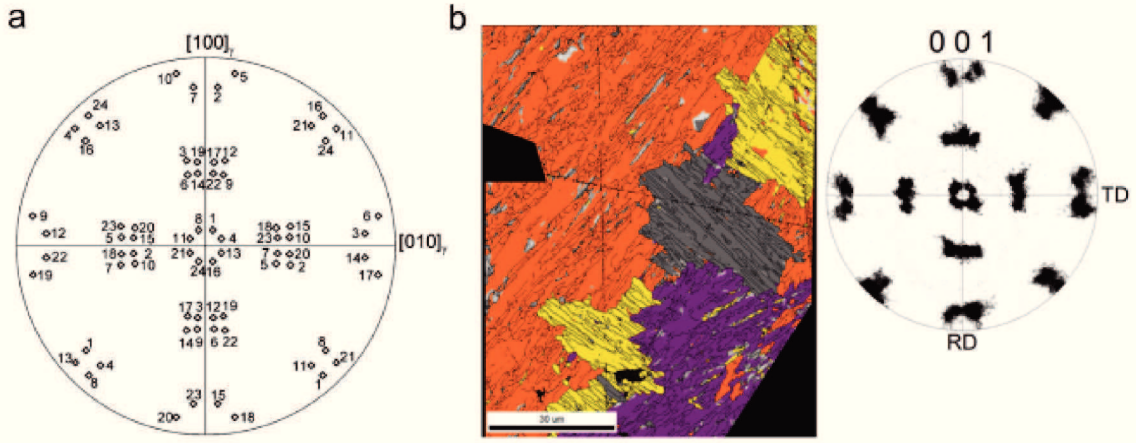

FIGURE 4.9: (a) The theoretically obtained (001) pole figure of 24 K-S variants (numbered from 1 to 24). The orientation of the martensite variants is given relatively to the (001)[100] orientation of the austenite grain [11]. (b) The measured EBSD map and corresponding 001 pole figure [12].

Since both variants V1 and V2 have the same bcc structure, the matrix $(\alpha_2 J \alpha_1)$ can be represented as:

$$(\alpha_2 J \alpha_1) = \begin{pmatrix} u_1^2(1-m)+m & u_1u_2(1-m)-u_3n & u_1u_3(1-m)+u_2n \\ u_1u_2(1-m)+u_3n & u_2^2(1-m)+m & u_2u_3(1-m)-u_1n \\ u_1u_3(1-m)-u_2n & u_2u_3(1-m)+u_1n & u_3^2(1-m)+m \end{pmatrix}, \qquad (4.21)$$

where $m = \cos\theta_{id}$, $n = \sin\theta_{id}$. The rotational matrix $(\alpha_2 J \alpha_1)$ in Eq.(4.21) describes a counter-clockwise rotation by an angle of θ_{id} about an axis in the direction of unit vector $\mathbf{u} = (u_1, u_2, u_3)$ (the components of the vector $\mathbf{u}$ are written in the α_1 basis).

The sum of the main diagonal elements of matrices (4.20) and (4.21) gives:

$$J_{11} + J_{22} + J_{33} = -1 + 1 + 1 = 1 + 2\cos\theta_{id} \;\Rightarrow\; \theta_{id} \approx 109.5^\circ. \qquad (4.22)$$

We also can find the rotation axes:

$$\begin{aligned} u_1 &= (J_{32} - J_{23})/2\sin\theta, \\ u_2 &= (J_{13} - J_{31})/2\sin\theta, \;\Rightarrow\; \mathbf{u} = (0, -0.707, -0.707). \\ u_3 &= (J_{21} - J_{12})/2\sin\theta \end{aligned} \qquad (4.23)$$

This rotation is equivalent to the rotation by an angle $\theta_{id} \approx 70.5^\circ$ with vector $\mathbf{u} = (0, 0.707, 0.707)$. So the rotational angle θ found from our simulation results is very close to the calculated one: $\theta \approx \theta_{id}$.

It should be noted, that the misorientation angle and rotational axis can also be presented in another way. If the bcc lattice will be rotated by an angle 90° about an axis in the direction

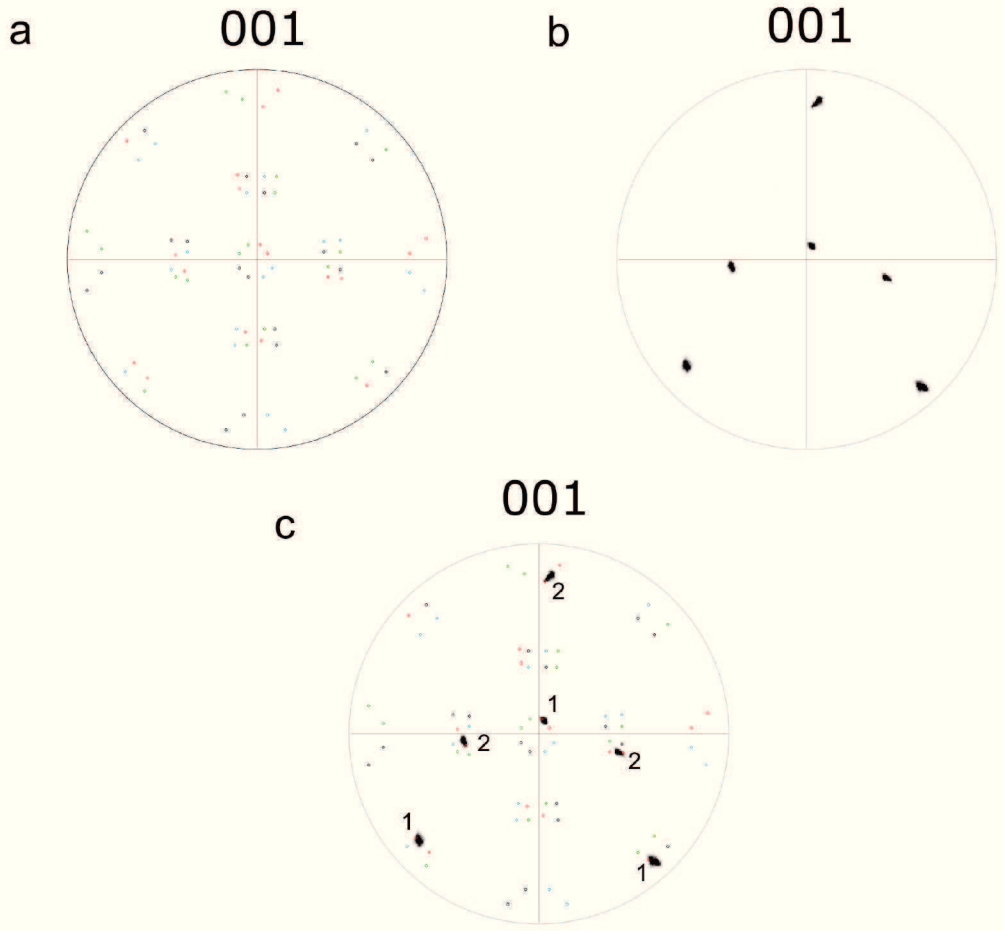

FIGURE 4.10: (a) The map of superposed pole figures for the 24 KS variants. Red, green, blue and black colors denotes the corresponding $(111)_\gamma$, $(1\bar{1}1)_\gamma$, $(\bar{1}11)_\gamma$ and $(11\bar{1})_\gamma$ slip planes. (b) The (001) pole figure for the last step of martensite transformation ($\hat{t} = 9500000$). (c) The map with superposed pole figures (a) and (b). Poles corresponding to the V1 and V2 KS variants are marked as 1 and 2. All pole figures are given relatively to the (001)[100] orientation of the austenite phase.

$\mathbf{u} = (0, 0, 1)$ and by 90° about an axis in the direction $\mathbf{u} = (0, 1, 0)$, the initial crystal will be obtained. Such a new basis $(\alpha_2^{'})$ will be crystallographically equivalent to the unrotated one with basis α_2. The final matrix obtained after such rotation can be written as:

$$\hat{R} = \hat{R}_{[010]}(90°) \times \hat{R}_{[001]}(90°) = \begin{pmatrix} 0 & 0 & 1 \\ 0 & 1 & 0 \\ \bar{1} & 0 & 0 \end{pmatrix} \times \begin{pmatrix} 0 & \bar{1} & 0 \\ 1 & 0 & 0 \\ 0 & 0 & 1 \end{pmatrix} = \begin{pmatrix} 0 & 0 & 1 \\ 1 & 0 & 0 \\ 0 & 1 & 0 \end{pmatrix}. \tag{4.24}$$

The rotation matrix in the new basis is

$$\left(\alpha_2^{'} J \alpha_1\right) = \hat{R} \times (\alpha_2 J \alpha_1) = \frac{1}{3} \begin{pmatrix} 2 & 2 & 1 \\ \bar{1} & 2 & \bar{2} \\ \bar{2} & 1 & 2 \end{pmatrix}. \tag{4.25}$$

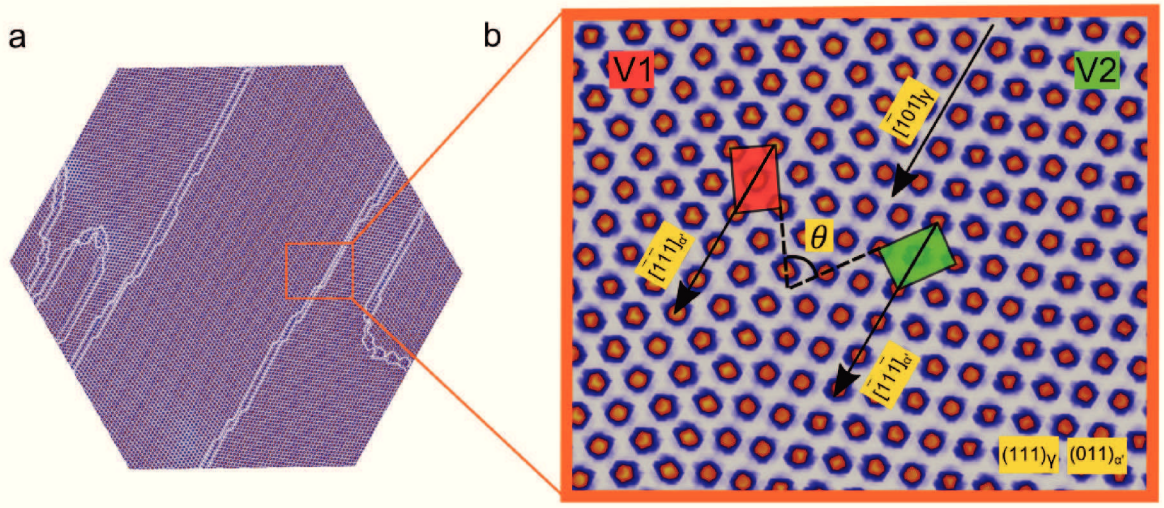

FIGURE 4.11: (a) The atomic density profile at time $\hat{t} = 950000$ in $(111)_\gamma$ plane. (b) The magnification of the region restricted by the orange rectangle from (a). Red and green colors denote V1 and V2 KS variants, respectively. The angle θ is a misorientation angle between two variants. Boundaries of variants are in white.

Using (4.21) and (4.25) we can find the angle and the axis of rotation:

$$\theta_{id} = 60^\circ \text{ and } \mathbf{u} = \frac{1}{\sqrt{3}}(1, 1, -1). \tag{4.26}$$

Thus, V2 variant can be obtained from V1 by a rotation of $\theta_{id} = 60^\circ$ about $[11\bar{1}]_{\alpha_1}$ as well.

4.2.2.3 Simulated diffraction patterns and dark field images

To better determine the form of each variant during growth the diffraction patterns and dark field images have been simulated. To construct the diffraction patterns the next expression for scattered radiation in reciprocal space of the wave vectors, $\mathbf{k} = (k_x\, k_y\, k_z)$, can be used:

$$I(\mathbf{k}) = |\widetilde{\rho}(\mathbf{k})|^2 = \left| \sum_{\mathbf{r}} \rho(\mathbf{r}) e^{-i\mathbf{kr}} \right|^2 . \tag{4.27}$$

Since $(111)_\gamma$ plane of austenite corresponds to the $(001)_\alpha$ plane of V1 and V2 KS variants, then it will be convenient to analyze diffraction patterns in this plane. The Fig.4.12 shows the diffraction intensities in the $(111)_\gamma$ plane for the different steps of our simulation. At the initial stage at $\hat{t} = 0$ (Fig.4.12(a)) the investigated system consists of the fcc phase and a nucleus of the bcc structure (V1 KS variant). Figure 4.12(a) shows the diffraction pattern of this initial configuration where the diffraction spots related to the fcc structure are indicated in yellow: $\{220\}_\gamma$, and that of the bcc one in red: $\{011\}_{\alpha_1}$, $\{200\}_{\alpha_1}$ and $\{211\}_{\alpha_1}$. In the intermediate state $\hat{t} = 400000$ (Fig.4.12(b)) the diffraction spots which correspond to the V2 KS variant (marked in green) appear: $\{011\}_{\alpha_2}$, $\{200\}_{\alpha_2}$ and $\{211\}_{\alpha_2}$. Since the fraction of the fcc phase decreases then the intensity of the diffraction spots of this phase decreases. At the

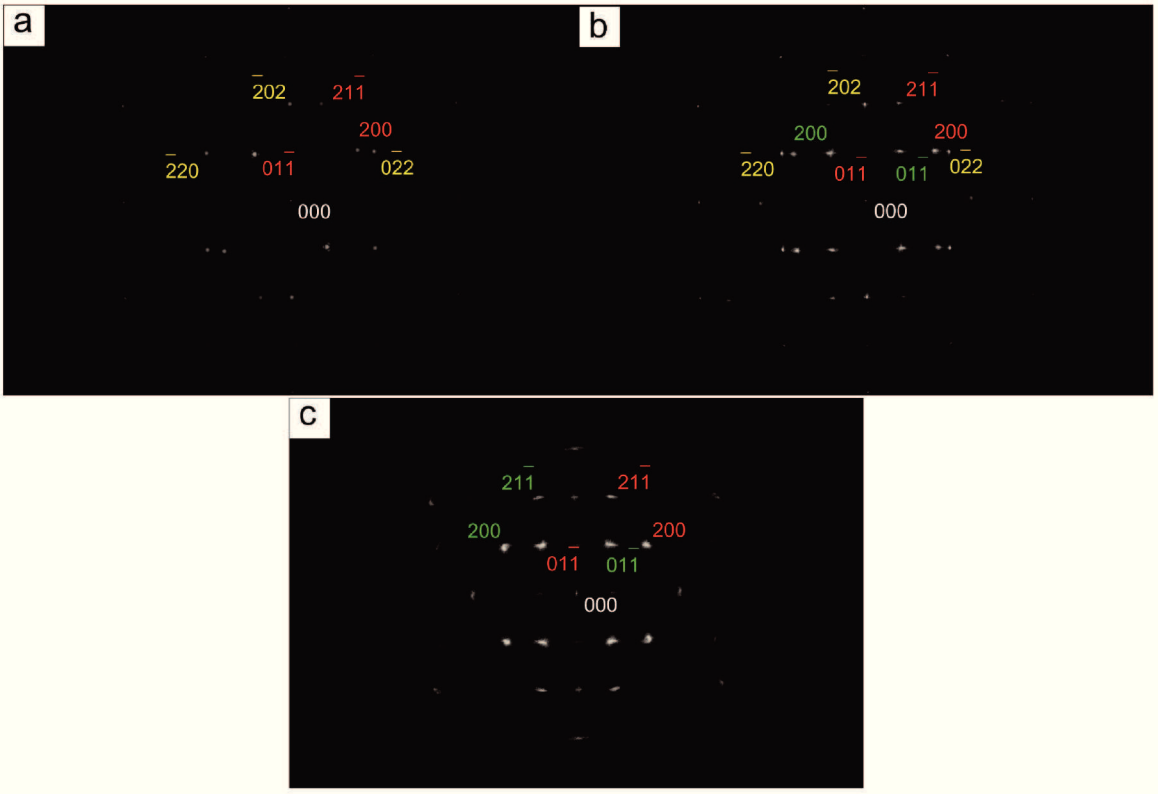

FIGURE 4.12: The slices of diffraction patterns at times (a)$\hat{t} = 0$, (b)$\hat{t} = 400000$, (c)$\hat{t} = 950000$ in $(111)_\gamma$ plane. Yellow, red and green colors denotes reflexes from fcc phase, V1 and V2 KS variants, respectively.

final stage of the simulation at $\hat{t} = 950000$ the system contains two variants V1 and V2 of KS, and the diffraction spots of these two variants can be distinguished on the diffraction pattern, Fig.4.12(c).

Let's proceed to the analysis of the diffraction pattern at this stage (Fig.4.13). Fig.4.13(a)

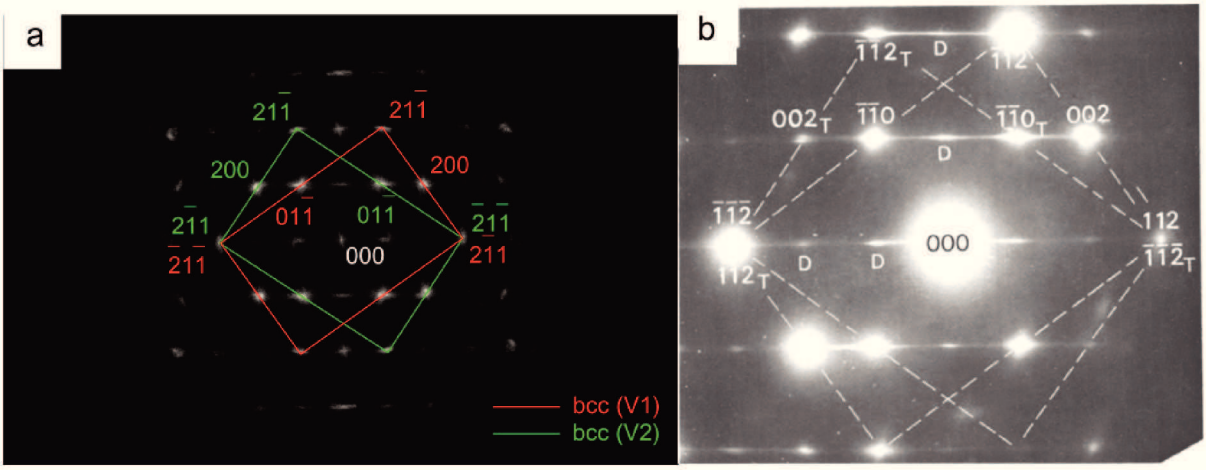

FIGURE 4.13: (a) Diffraction pattern at $\hat{t} = 950000$ in $(011)_{alpha}$ plane. Red and green colors denote spots of the V1 and V2 KS variants, respectively. (b) Diffraction pattern of twinned martensite of Kovar alloy (Fe-27.5 pct Ni-17.2 pct Co) [13].

shows the diffraction pattern in $(011)_\alpha$ plane at time $\hat{t} = 950000$ which contains numbered

diffraction spots. In this plane the spot $2\bar{1}1_{\alpha_1}$ of the V1 variant is superposed with $\bar{2}1\bar{1}_{\alpha_2}$ spot of V2. Consequently, we can conclude that variant V2 is a mirror image of V1 in $(2\bar{1}1)_\alpha$ (or $(1\bar{2}1)_\gamma$) plane and in this case $(2\bar{1}1)_\alpha$ plane is a twinning plane for two variants.

Also, it is important to note, that the lattices of both variants are slightly tetragonal in $[001]_{\alpha_1}$ and $[001]_{\alpha_2}$ directions of V1 and V2 variants, respectively. The axial ratio c/a calculated from diffraction patterns is ≈ 1.025.

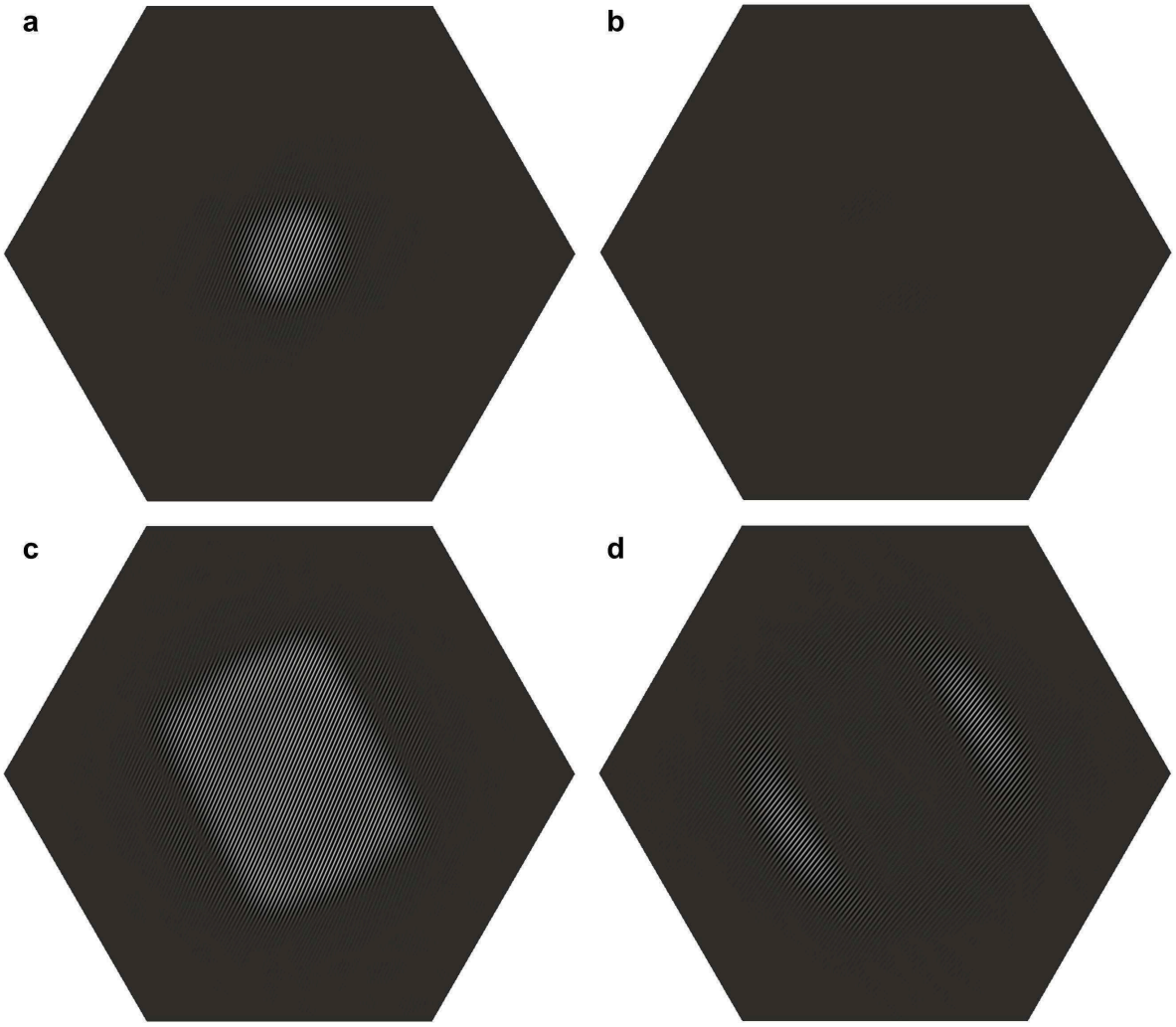

FIGURE 4.14: Dark field images constructed using the 011_α diffraction spot in $(011)_\alpha$ plane at simulation times (a)-(b)$\hat{t} = 0$, (c)-(d)$\hat{t} = 420000$. (a),(c) correspond to V1 variant, (b),(d) correspond to V2.

To investigate the morphology of microstructure it is convenient to use dark field images. Reconstruction of the atomic density field $\rho(\mathbf{r})$ from $\tilde{\rho}(\mathbf{k})$ (by selecting one or several diffraction spots in the plane $k_x = 0$ during the inverse Fourier transformation) leads to a set of atomic lattice fringes or to intersections of several sets. This image we call dark field (DF) image. In a given case, the dark field image was constructed using the next consideration: one of the spot was selected on the diffraction pattern using the function $\phi_{DF}(\mathbf{k})$ which is equal zero in each

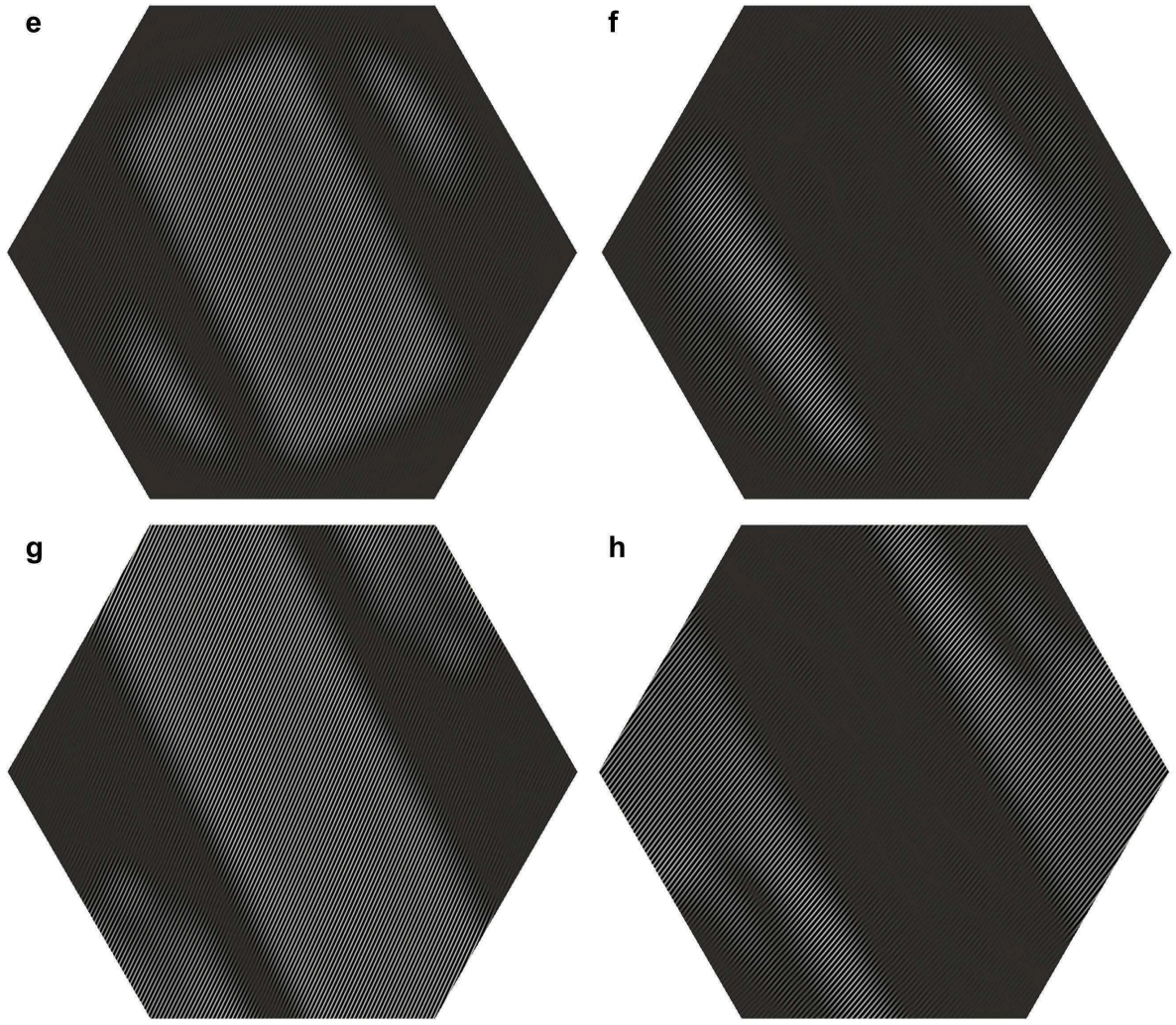

FIGURE 4.15: Dark field images constructed using the 011_α diffraction spot in $(011)_\alpha$ plane at simulation times (a)-(b)$\hat{t} = 620000$, (c)-(d)$\hat{t} = 950000$. (a),(c) correspond to V1 variant, (b),(d) correspond to V2.

point $\mathbf{k}$ of a reciprocal space except selected area of a spot:

$$\begin{cases} \phi_{DF}((k)) = \tilde{\rho}(\mathbf{k}), & \text{if } \mathbf{k} \in \text{ selected area,} \\ \phi_{DF}(\mathbf{k}) = 0, & \text{otherwise.} \end{cases} \tag{4.28}$$

Here $\tilde{\rho}(\mathbf{k})$ is a Fourier transform of the $\rho(\mathbf{r})$. In our case, the dark field image was using the 011_α diffraction spot.

In Figs.4.14-4.15 the $(011)_\alpha$ (or $(011)_\gamma$) section of the 3D DF image at different time are presented. The right images (a,c,e,g) correspond to the DF images built using 011_{α_1} spot of V1 variant and the left-side images (b,d,f,h) correspond to the DF images built using 011_{α_2} diffraction spot of V2. The bright area on the DF images coincides with the position of the variants. At the initial step (Figs.4.14(a-b)) only the first variant V1 is presented in the middle of the simulation box. The next images 4.14(c-d) and 4.15(a-d) show the presence of both variants

and their growth in some particular direction. This growth produced plate-like morphology of KS variants.

The 3D images of DF at different times are shown in Fig.4.16, green color denotes V1 variant and red denotes V2. The growth of V1 variant at the initial stages of modeling is

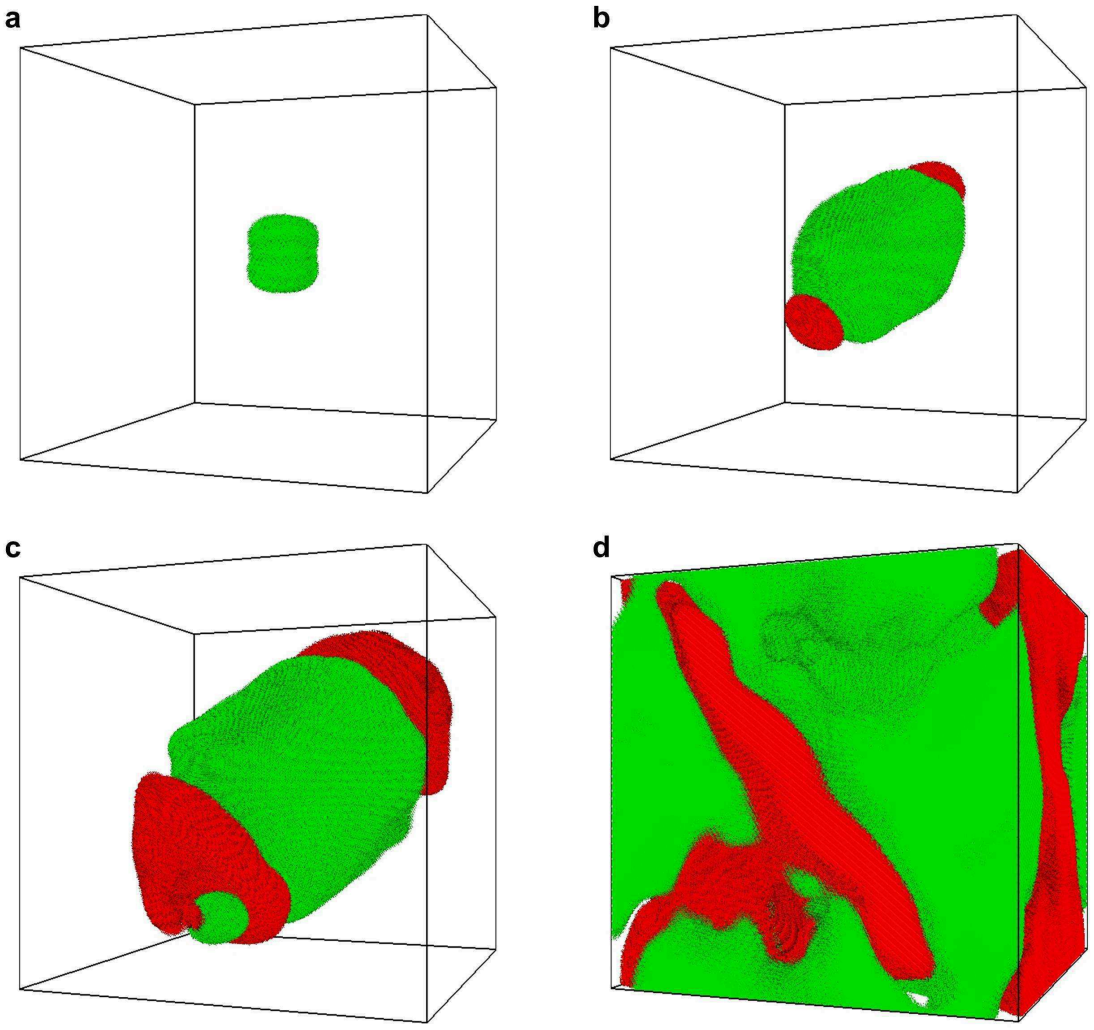

FIGURE 4.16: 3D dark field images calculated using the 011_α diffraction spot at simulation times (a)$\hat{t} = 0$, (b)$\hat{t} = 420000$, (c)$\hat{t} = 620000$, (d)$\hat{t} = 950000$. Red and green colors correspond to the V1 and V2 variants, respectively.

accompanied by emergence of second variant. These two variants form a periodic twin structure of type V2|V1|V2 slightly elongated along $[101]_\alpha$ ($\sim [3\bar{2}3]_\gamma$) direction, Fig.4.16(b). In $[101]_\alpha$ direction the bcc nucleus growth faster, Figs.4.16(b-c). In Figs.4.16(c) the martensite phase has V1|V2|V1|V2|V1 twin structure. The following growth of martensite phase does not have such a clear alternation of variants. This is probably due to the limitation of our simulation box and periodic boundary conditions used in our simulations.

4.2.2.4 Twinning structure

Since variants of martensite are twin related, then we can characterize this twinning structure. As it was found previously, the twinning plane, K_1, is $(2\bar{1}1)_\alpha$, the twinning direction, η_1, is $[\bar{1}\bar{1}1]_\alpha$ and the plane of shear, P, is $(011)_\alpha$ (or $(111)_\gamma$). Using Fig.4.11(b), it is possible to find the conjugate twinning plane, K_2, and the conjugate twinning direction, η_2. They are $(\bar{2}\bar{1}1)_\alpha$ and $[\bar{1}1\bar{1}]_\alpha$, respectively. Then, using Eq.(4.10) the shear magnitude, s is $1/\sqrt{2}$. Fig.4.17(a) shows the twinning structure in $(011)_\alpha$ projection with reflection twin boundary. It should

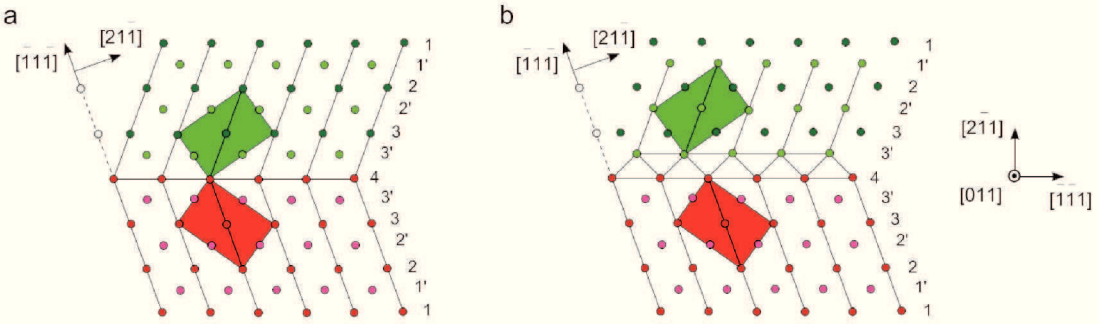

FIGURE 4.17: Schematic representation of two possible twins boundaries in bcc crystal. (a) Reflection twin boundary and (b) isosceles twin boundary are projected on the $(011)_\alpha$ plane. Filled circles in dark green and red represent the atoms on the (011) plane, circles in green and pink indicate the atoms on $(011)_\alpha$ planes under and below this plane on distance $a^{bcc}/\sqrt{2}$. Successive $\{2\bar{1}1\}_\alpha$ planes are numbered as indicated.

be noted, that the shear strain of deformation twinning is lower in bct structure then in bcc. The twinning shear magnitude for the $\{112\} < 111 >$ twinning mode is given by the following equation:

$$s = \frac{1-\gamma^2}{\sqrt{2}\gamma}, \tag{4.29}$$

where $\gamma = c/a$ [99]. In the case of twinning in bcc crystal: $c/a = 1$ and $s = 1/\sqrt{2} \approx 0.707$. In bct structures the value of s decreases, and for $c/a = 1.025$ the shear magnitude is ≈ 0.655.

In the case of reflection twin boundary, the twin structure can be obtained by reflection in the $(2\bar{1}1)_\alpha$ plane. In Fig.4.17, the parallel $\{2\bar{1}1\}_\alpha$ planes are numbered as 1, 1', 2, 2', 3, 3', 4. Here prime symbol denotes the planes with atoms are situated at the distance $a^{bcc}/\sqrt{2}$ below or above of the considered plane. The step vectors of the interfacial defect of reflection twin boundary are $\mathbf{t}_\mu = \frac{1}{2}a^{bcc}[\bar{1}11]_{\alpha_1}$ and $\mathbf{t}_\lambda = a^{bcc}[010]_{\alpha_2}$ (or $\mathbf{t}_\lambda = \frac{1}{3}a^{bcc}[\bar{2}12]_{\alpha_1}$). λ and μ denotes two twins. Using Eq.(4.11) the Burgers vector of this disconnection can be calculated: $\mathbf{b}_{refl} = \frac{1}{6}a^{bcc}[\bar{1}\bar{1}1]_{\alpha_1}$. The spacing between the plane of type$(2\bar{1}1)_\alpha$ gives the step height: $h = a^{bcc}/\sqrt{6}$.

Thus, twinning occurs by the glide of twinning dislocations on $\{2\bar{1}1\}$ successive planes with $\frac{1}{6}a^{bcc}[\bar{1}\bar{1}1]_{\alpha_1}$ Burgers vector. Fig.4.18 shows the schematic illustration of this process. The stacking sequence of $\{2\bar{1}1\}$ planes in the body-centered cubic structure is $ABCDEFABCDEF\ldots$ It is shown in Fig.4.18(a). To provide a twinning deformation, the atoms of each $\{2\bar{1}1\}$ planes above F layer are translated by $\frac{1}{6}a^{bcc}[\bar{1}\bar{1}1]_{\alpha_1}$. Then A layer shifts to E, B to F, etc. Thus after

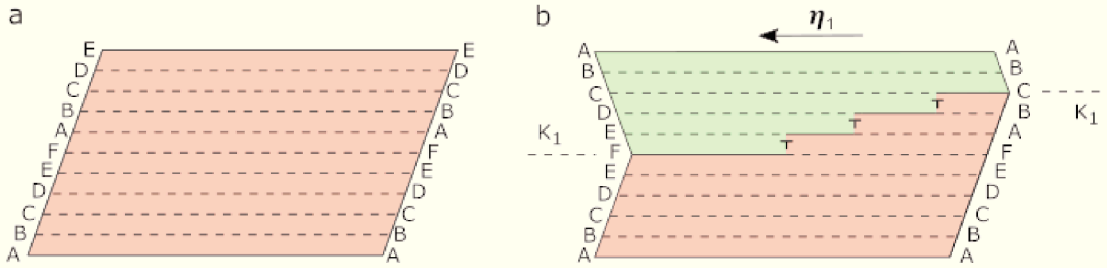

FIGURE 4.18: Schematic representation of $\{2\bar{1}1\} < \bar{1}\bar{1}1 >$ twinning in bcc crystal. The projection of the crystal is in (011) plane. Dashed lines represent $\{2\bar{1}1\}$ planes. (a) Untwinned crystal shows the stacking sequence $ABCDEFABCDEF$. (b) Formation of twin structure through the glide the twinning dislocations from left to right on successive $\{2\bar{1}1\}$ planes. The parent crystal is in red, and its twin in green.

the first translation the new sequence of planes is $ABCDEFEFABCD\ldots$. The next translations of $FABCD\ldots$ planes gives $ABCDEFEDEFAB\ldots$. Following translations on $\{2\bar{1}1\}$ planes give $ABCDEFEDCDEF\ldots \rightarrow ABCDEFEDCBCD\ldots \rightarrow ABCDEFEDCBAB\ldots \rightarrow ABCDEFEDCBAE\ldots$. The resulting twinned crystal is shown on Fig.4.18(b).

Another type of twin boundary, which can be realized in the bcc twins, is isosceles twin boundary. In such boundary, the mirror symmetry is violated. In this case the structure of the interface between parent and twin crystals consists of isosceles triangles shown in Fig.4.17(b). The step height of these interfacial defect is the same as in reflection twin boundary, $h = a^{bcc}/\sqrt{6}$, but Burgers vector is smaller: $\mathbf{b}_{iso} = \frac{1}{12}a^{bcc}[\bar{1}\bar{1}1]_{\alpha_1}$. Then the twins growth occurs by the same mechanism illustrated in Fig.4.18.

Fig.4.19 shows the interface between twins obtained in simulations. Such interface between twins does not give the equivalence with the reflection twin boundary (see Fig. 4.17(a))and corresponds to the isosceles type of interface. Also, several twinning dislocations can be seen on twin boundary, their step heights and Burgers vectors are the same as for the isosceles interfacial defect.

4.2.3 Discussion

Using our simulation we can conclude that martensite nucleus growth as a multi-variants structure, which consists of two twin-related KS variants. This conclusion was also done in [14] using Phase field modeling. In particular, it was shown that the pre-existing martensitic nucleus always has multi-domain structure. Let's describe this simulation in more details. In this simulation the initial state was a homogeneous parent phase were an dislocation loop was introduced (see Fig.4.20(a)). The transformation driving force was determined by the undercooling $\Delta T = T - T_0$, here T_0 is the equilibrium temperature between austenite and martensite phases and T is undercooling temperature. Figs.4.20(b-d) show the formation of the martensite embryo from parent phase around the dislocation loop and its growth at different undercooling temperatures. In all cases an embryo has multidomain structure. The final state, see Fig.4.20(d),

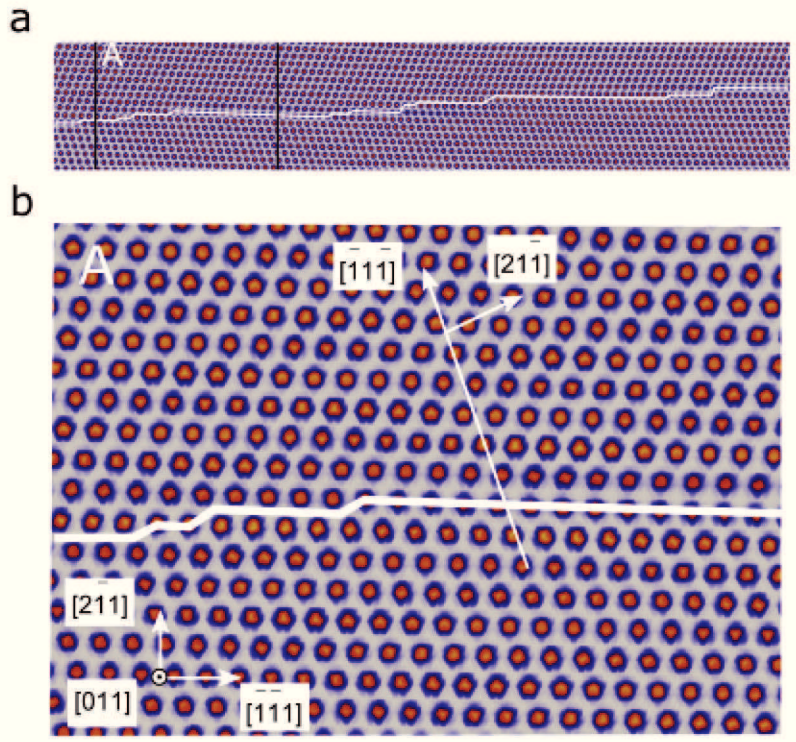

FIGURE 4.19: (a) Twin boundary projected onto the $(011)_\alpha$ plane at $\hat{t} = 950000$, marked in white.(b) The area denoted as "A" have been increased.

contains a big particle of martensite consisting of twin-related domains. This structure is energetically favorable because it minimizes strain and interfacial energies. It is worth noting that the plates of final twin related domain are formed in some preferential direction. In the modeling presented in this work the preferential direction was $[101]_\alpha$.

For the as quenched low carbon steels a lath martensite is a characteristic structure. The orientation relationships between laths and austenite are near KS OR. Usually, virgin martensite consists of many variants with different misorientation. The misorientation angle has a bimodal distribution with two peaks at low ($\sim 10-15°$) and high ($\sim 50-60°$) angle ranges [5, 33, 100]. Combinations of V1/V4, V3/V6, V2/V5 of KS variants correspond to the low misorientation angle ($\theta = 10.5°$) and V1/V2, V1/V3 etc. to the high misorientation angle ($\theta = 60°$). For the IF steels the appearance of combinations of KS variants with low angle are more frequently observed ($\sim$ 60.1%) than with high angle ($\sim$ 20.8%) [33]. This is due to the fact that the combination of V1/V4 variants reduces the total shape strain more than in the case of V1/V2 combination. With increasing of carbon content in steels pairing of V1/V2 variants becomes more favorable [5]. For the steels with a high carbon content ($>$ 0.6 wt.%), twin-related variants prevails in the system. This is because the lattice of martensite becomes tetragonal.

As was discussed previously the twinning mechanism can be characterized by different twinning modes. These modes for the fcc-to-bcc or fcc-to-bct transitions are presented in Table4.3. The result obtained in present work (with V1/V2 variant pairing and $(2\bar{1}1)_\alpha[\bar{1}\bar{1}1]_\alpha$ twinning

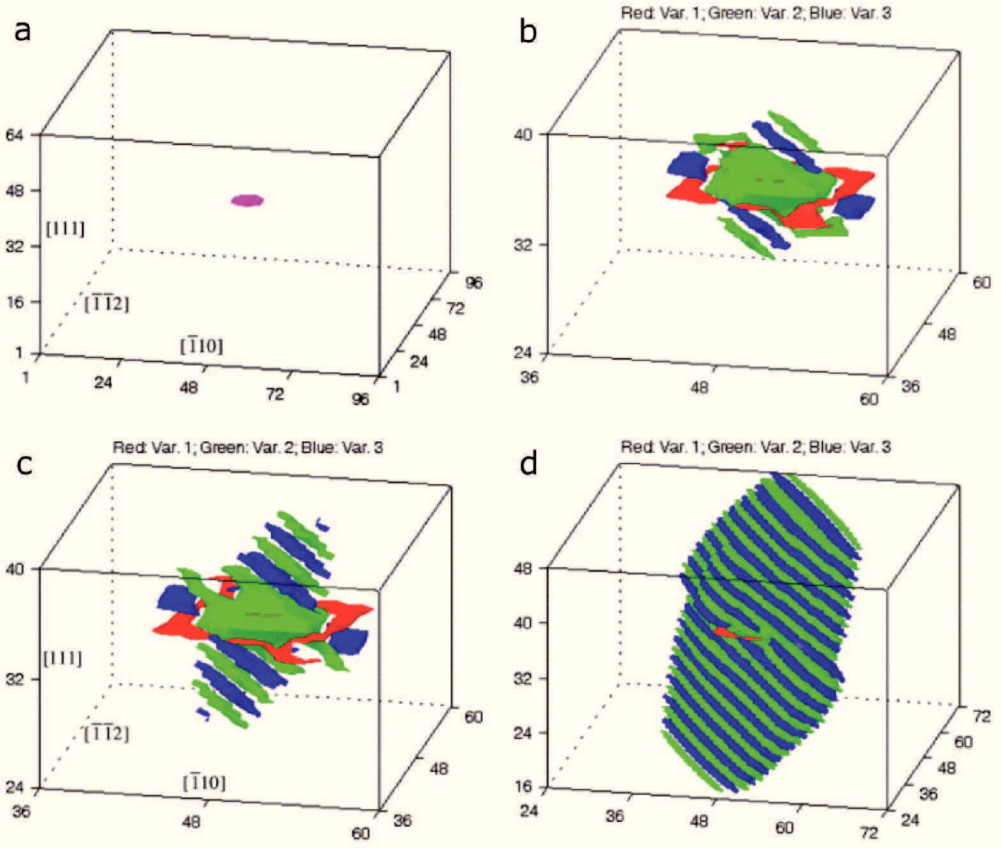

FIGURE 4.20: The microstructure of martensite obtained from the 3D Phase Field modeling. A dislocation loop is placed in the center of the box (in magenta). The results of martensitic structure evolution [14] with undercooling to (b) $\Delta T \approx 207$ at the time $\tau = 2000$, and to $\Delta T \approx 214$ at times (c) $\tau = 1000$, (d) $\tau = 2000$. Different variants are presented in green, blue and red. Parent phase is transparent. Coordinates are aligned with $[\bar{1}10]$, $[\bar{1}\bar{1}2]$ and [111] axes.

TABLE 4.3: Twining modes in martensite [19, 20]. γ is the same as axial ratio c/a.

Structure	K_1	K_2	η_1	η_2	s	P	Alloys
bcc (fcc→bcc)	{112}	$\{\bar{1}\bar{1}2\}$	$<\bar{1}\bar{1}1>$	$<111>$	$1/\sqrt{2}$	$\{1\bar{1}0\}$	Fe-Ni, Fe-Pt
bct (fcc→bct)	{112}	$\{\bar{1}\bar{1}2\}$	$<\bar{1}\bar{1}1>$	$<111>$	$(2-\gamma^2)/\sqrt{2}\gamma$	$\{1\bar{1}0\}$	Fe-C, Fe-Ni-C Fe-Cr-C
	{011}	$\{01\bar{1}\}$	$<01\bar{1}>$	$<011>$	$\gamma - 1/\gamma$	$\{1\bar{1}0\}$	Fe-C

mode) is fully consistent with observed variant pairing. For example, the twin-related variants are observed in Kovar alloy (Fe-27.5 pct Ni-17.2 pct Co) [13] and in Fe-0.58wt.%C steel [15]. The diffraction patterns for the Kovar alloy shown in Fig.4.13(b) and for Fe-0.58wt.%C steel shown in Fig.4.21(a), coincide with diffraction patterns obtained in this work (see Fig.4.13(a)). Figs.4.21(b-c) shows dark-field TEM image and high-resolution TEM lattice image of the $\{112\} < 111 >$ twins. The lattice invariant shear occurs on the $(112)_\alpha$ plane in both examples.

As it was mentioned above, in the bcc crystals two types of the {112} twin boundaries are

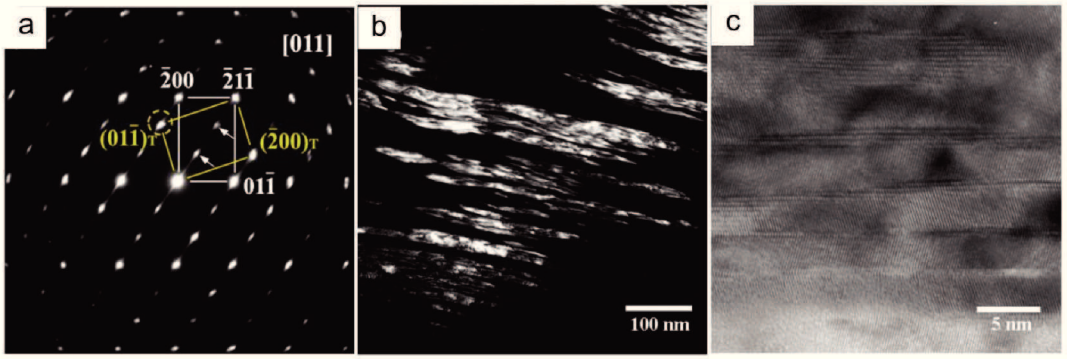

FIGURE 4.21: TEM results from as-quenched Fe-0.58wt [15].%C. (a) SAD pattern with $\{112\} < 111 >$ twining structure, (b) the dark-field images built from the spot in the dashed circle in (a), (c) the high-resolution TEM image of the $\{112\} < 111 >$ twins.

observed: reflection and isosceles. First, the isosceles twin boundary with $\frac{1}{12}a^{bcc}[\bar{1}\bar{1}1]$ Burgers vector was predicted by Vitek [101] in bcc structures. This structure was observed in tantalum [102].

In general case, the stability of the twin structures is controlled by the stable twinning fault energy γ^{stf}. The ratio between these two interface energies for two type of twinning, $\gamma^{stf}_{iso}/\gamma^{stf}_{coh}$, characterizes the relative stability of the two types of twinning. Here γ^{stf}_{iso} and γ^{stf}_{coh} correspond to the stable twinning fault energy of isosceles and coherent interfaces, respectively. These energies can be found, for example, using MD or DFT calculations. Thus, isosceles boundary is more stable in Ta, Nb and Fe, but in Mo and W reflection twin boundaries are realized [103].

4.3 Conclusions

In this chapter the AFT was used to model fcc-to-bcc transition. The choosing potential fits quite well the elastic properties of fcc and bcc iron. It was shown that initially bcc nucleus growth as a multi-domain aggregates. This is typical for the as quenched martensite phase and is consistent with previous Phase Field modeling. The atomistic mechanism of the appearance of second KS variant can be understood from our modeling. It was shown that the growth of KS variant pass through the twinning dislocation moving that produces the steps in the interface between two variants. The Burger vector of this dislocations was found to be equal $\frac{1}{12}a^{bcc}[\bar{1}\bar{1}1]$. The final structure can be characterise by $\{2\bar{1}1\} < \bar{1}\bar{1}1 >$ twinning mode. The diffraction patterns obtained in our simulation are in excellent agreement with experimental diffraction patterns observed in Fe-0.58wt.% C and in Kovar alloys. It should be underlined that unfortunately, the size of our simulation box was not enough to determine the period of two variant structure. The real size of the simulation box used in this modeling was $(22.848\,\mathrm{nm})^3$. Therefore, to model the blocks ($\sim 15\,\mu$m) or packets ($\sim 130\,\mu$m) observed in martensite the Phase Field modeling should be applied.

To identify the variants that appear in our modeling during martensite growth the pole figures have been constructed. It was shown that second variant appear immediately during first

stage of growth and correspond to V2 KS variant. In the case when we started our simulation with bcc nucleus with V3 KS variant the V4 KS variant was appeared. It corresponds to the frequently observed structure in high carbon steels. However, this structure is also observed in low carbon steels.

To conclude, the proposed method based on the AFT can be used to understand the atomistic mechanism of the MT.

Chapter 5

Carbon Diffusion in Steel

In this chapter the kinetics of carbon atoms during aging processes in Fe-C system will be considered. In this chapter we will be interested on the diffusion of carbon atoms in martensite phase.

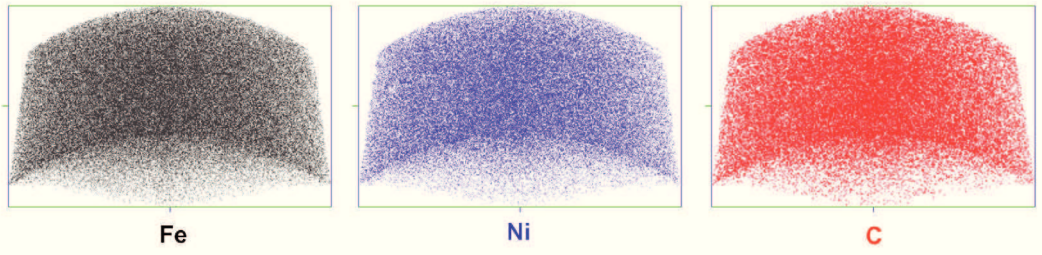

FIGURE 5.1: APT reconstruction of 3D distribution of iron, nickel and carbon atoms in the alloy of composition Fe-25.3 wt% Ni-0.37 wt% C in the virgin martensite. The analyzed volume is $75 \times 75 \times 50$ nm^3. This result was obtained by Frédéric Danoix (GPM).

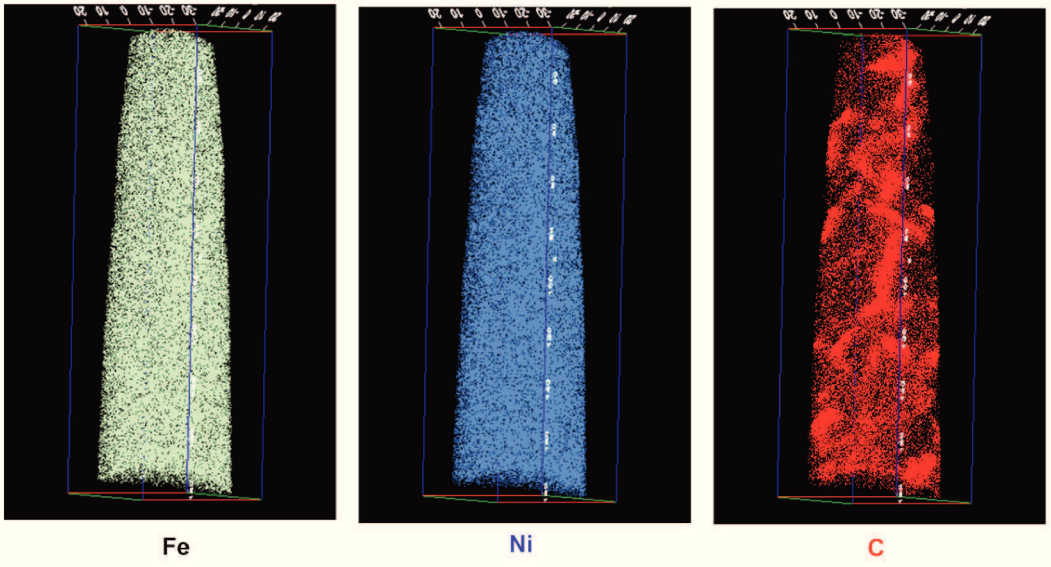

FIGURE 5.2: APT reconstruction of 3D distribution of iron, nickel and carbon in the martensite aged 7 days at room temperature. The volume analyzed is $45 \times 45 \times 180$ nm^3 for the alloy of composition Fe-25.3 wt% Ni-0.37 wt% C. This result was obtained by Frédéric Danoix (GPM).

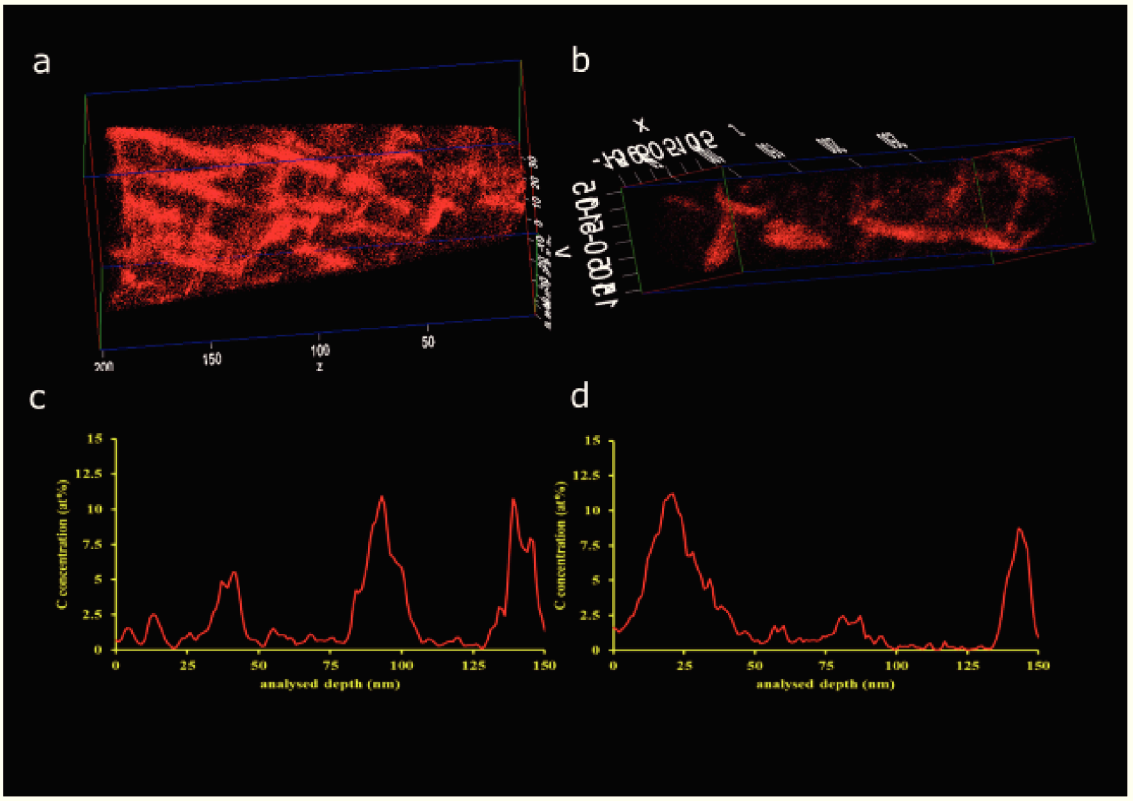

FIGURE 5.3: (a) APT reconstruction of 3D distribution of carbon in the martensite aged during 40000 hours in Fe-25.3 wt% Ni-0.37 wt% C at room temperature. The volume analyzed is $80 \times 80 \times 200$ nm^3. (c) The concentration profile across the carbon rich zone. (b) APT reconstruction of 3D distribution of carbon in Fe-25.3 wt% Ni-0.37 wt% C in the martensite aged during 16 hours at 75° C. The analyzed volume is $35 \times 35 \times 285$ nm^3. (d) The concentration profile across the carbon rich zone. These results were obtained by Frédéric Danoix (GPM).

The redistribution of carbon in martensite phase during aging at room temperature was studied by Frédéric Danoix (GPM) using 3D atom-probe analyzes. Here we will present the result obtained in this study in Fe-25.3 wt% Ni-0.37 wt% C alloy. The temperature of martensite transformation, M_s for this system is around $-10°$ C. First, the investigated sample was heated to 850° to obtain the austenite phase. Then, in order to obtain a martensite phase, the sample was rapidly cooled to 77 K. Such a low temperature is needed to realize martensite transformation, because the alloy contains nickel, which stabilize austenite phase. The distribution of iron, nickel and carbon just after quenching is shown in Fig.5.1. It can be see that the distribution of carbon atoms in virgin martensite is homogeneous.

Then a sample was aged during 7 days at room temperature. The APT reconstruction of 3D distribution of three types of atoms in the aged martensite is presented in Fig.5.2. We can see that there are the significant carbon concentration fluctuations with the characteristic length scale 10-30 nm and the amplitude of concentration fluctuations about 11 at.%. The increasing of ageing time to 40000 hours at room temperature increases the characteristic length scale to $\approx$ 40 nm, but the phase composition remained unchanged $\approx$ 11 at.%. It was shown in Fig.5.3(a,c). The morphology of these carbon rich zones are entirely consistent with the "tweed

like" structure previously observed by TEM. Also, if the ageing temperature is higher, namely 75° C, the characteristic lengthscale increases up to 100 nm, Fig.5.3(b,d), but the concentration in the carbon rich zones is the same as in low temperature treatment, around 11% . This suggests, that in carbon rich zones the metastable phase forms. Thus, the aim of this study is to determine the internal structure of the carbon rich zones and to understand the mechanism responsible for formation and stability of this phase.

5.1 Model

In the virgin martensite carbon atoms occupy the octahedral interstices of the bcc iron lattice. There are three octahedral sublattices in bcc structure. Each sublattice has also bcc structure and it is shifted relative to the host lattice on the vector $\mathbf{h}_p$. The sublattice described by the shift $\mathbf{h}_1 = (a_0/2, 0, 0)$ we will call O_x sublattice, by $\mathbf{h}_2 = (0, a_0/2, 0)$ O_y sublattice and by $\mathbf{h}_3 = (0, 0, a_0/2)$ O_z sublattice. Fig.5.4 shows all possible octahedral interstitial positions in the bcc lattice. Since the size of octahedral interstices in α-iron is smaller than the radius of

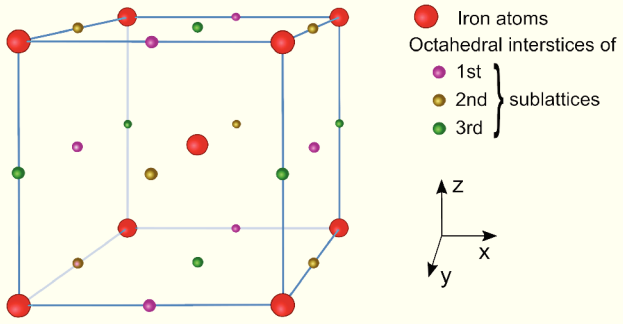

FIGURE 5.4: The schematic representation of the possible octahedral interstices in the bcc lattice. The positions of iron atoms are marked in red, they form the host bcc lattice. The octahedral positions marked in violet, yellow and green and correspond to the O_x, O_y and O_z sublattices, respectively.

carbon atoms, in martensite phase the carbon atoms distributed at these interstices will induce the internal stress in system. Then to describe the diffusion of carbon atoms in martensite the three octahedral sublattices should be included in the model. As well as the carbon atom stay on the octahedral sublattice of the bcc lattice and we want to describe only the redistribution of carbon atoms on this positions the ADF theory on constrain Ising lattice can be used.

In this approach, the configuration of the carbon atoms is described by the probability function $n_p(\mathbf{r}, t)$. Index p specifies a sublattice of octahedral interstices in the iron (host) bcc lattice. $p = \{1, 2, 3\}$ correspond to the O_x, O_y and O_z sublattices, respectively, see Fig.5.4. The evolution of occupation probability functions can be evaluated using the microscopic kinetic equation

$$\frac{dn_p(\mathbf{r}, t)}{dt} = \frac{1}{k_B T} \sum_{q=1}^{3} \sum_{\mathbf{r}'} L_{pq}(\mathbf{r} - \mathbf{r}') \frac{\delta F}{\delta n_q(\mathbf{r}', t)}. \tag{5.1}$$

Here F is the free energy functional of the function $n_p(\mathbf{r},t)$, $L_{pq}(\mathbf{r}-\mathbf{r}')$ is the matrix of kinetic coefficients that characterize the elementary diffusion jumps from the site $(p,\mathbf{r})$ to the site $(q,\mathbf{r}')$. In Eq.(5.1) the summation is carried out over all points, $\mathbf{r}'$, of the computational grid.

The total number of carbon atoms N_C is

$$N_C = \sum_p \sum_{\mathbf{r}} n_p(\mathbf{r},t) = (\bar{n}_1 + \bar{n}_2 + \bar{n}_3)N_0 = \bar{n}_C N_0. \tag{5.2}$$

Here N_0 is a number of all grids in the simulation box, $\bar{n}_1$, $\bar{n}_2$, $\bar{n}_3$ and $\bar{n}_C$ correspond to the average concentrations of carbon atoms in 1-st, 2-nd, 3-rd sublattices and in the whole simulation box, respectively. Since, the total number of carbon atoms N_C is fixed, it is possible to obtain the conservation condition by summing both sides of the Eq.(5.1) and using definition (5.2):

$$\sum_p \sum_{\mathbf{r}} \frac{dn_p(\mathbf{r},t)}{dt} = \frac{1}{k_B T} \sum_{q=1}^{3} \sum_{\mathbf{r}'} \frac{dF}{\delta n_q(\mathbf{r}',t)} \sum_p \sum_{\mathbf{r}} L_{pq}(\mathbf{r}) = 0.$$

Finally it can be rewritten as

$$\sum_p \sum_{\mathbf{r}} L_{pq}(\mathbf{r}) = 0. \tag{5.3}$$

For the conveniens we will use the Fourier transform of the kinetic coefficients matrix:

$$\widetilde{L}_{pq}(\mathbf{k}) \;=\; \sum_{\mathbf{r}} L_{pq}(\mathbf{r}) e^{-i\mathbf{kr}}. \tag{5.4}$$

Fig.5.5 shows the positions of the neighboring octahedral interstitial positions (numbers 1, 2, 3, 4 correspond to the distances of the 1st, 2nd, 3rd, 4th coordination spheres of the carbon atom) in the host iron bcc lattice. Assuming that atomic jumps take place only between the nearest neighbor positions, $L_{pq}(\mathbf{r}) = 0$ for the distance bigger then $a_0/2$. The Fourier transform of coefficients $\widetilde{L}_{pp}(\mathbf{k})$ which describe atomic jumps inside the octahedral sublattice p is

$$\widetilde{L}_{pp}(\mathbf{k}) = L_{pp}(\mathbf{r}=0)e^{-i\mathbf{k0}} + {\sum_{\mathbf{r}}}' L_{pp}(\mathbf{r}) e^{-i\mathbf{kr}} = L(0). \tag{5.5}$$

Here the sum with prime symbol means that the term $\mathbf{r} = 0$ is omitted. Kinetic coefficients which describe the exchange between sublattices are

$$\begin{aligned}
\widetilde{L}_{12}(\mathbf{k}) &= {\sum_{\mathbf{r}}}' L_{12}(\mathbf{r}) e^{-i\mathbf{kr}} = L(a_0/2) 2\cos\frac{k_z a_0}{2}, \\
\widetilde{L}_{13}(\mathbf{k}) &= L(a_0/2) 2\cos\frac{k_y a_0}{2}, \\
\widetilde{L}_{23}(\mathbf{k}) &= L(a_0/2) 2\cos\frac{k_x a_0}{2}.
\end{aligned} \tag{5.6}$$

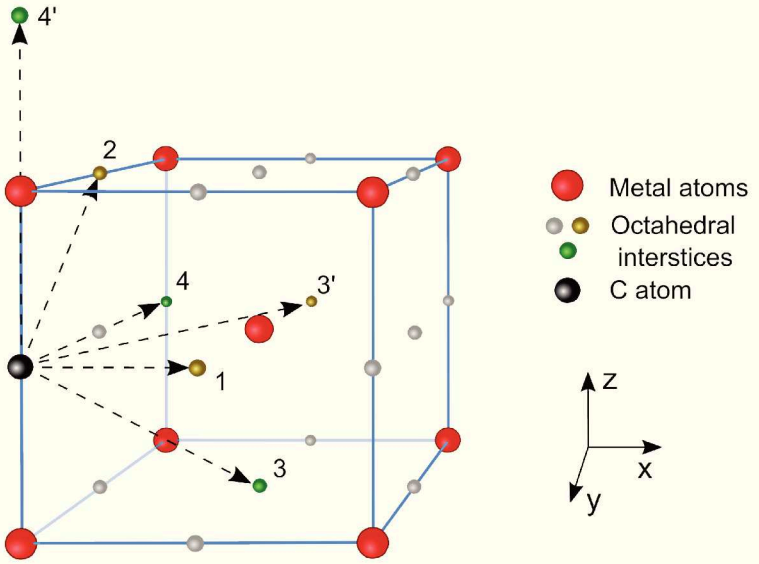

FIGURE 5.5: The neighboring octahedral interstitial positions of the carbon atom in the bcc host lattice. Four different coordination shells of the possible carbon atoms positions marked as 1, 2, 3, 4 are shown. The yellow and green sites correspond to the O_y and O_z octahedral sites, respectively.

Here $L(a_0/2) \equiv L_0 = 1/\tau$ is elementary diffusion jump probability between the nearest neighbors carbon atoms, τ is a characteristic time of an elementary jump. Since

$$\sum_p \sum_{\mathbf{r}} L_{pq}(\mathbf{r}) = \sum_p \widetilde{L}_{pq}(\mathbf{k}=0) = 0,$$

the conservation condition in reciprocal space is

$$\widetilde{L}_{11}(0) + \widetilde{L}_{12}(0) + \widetilde{L}_{13}(0) = L(0) + 2L_0 + 2L_0 = 0.$$

Using this condition the coefficient $\widetilde{L}_{pp}(\mathbf{k})$ can be written as:

$$\widetilde{L}_{pp}(\mathbf{k}) = L(0) = -4L_0. \tag{5.7}$$

Finally, the kinetic coefficients matrix in Fourier space is

$$\widetilde{L}_{pq}(\mathbf{k}) = 4L_0 \begin{pmatrix} -1 & 0.5\cos\left(k_z \frac{a_0}{2}\right) & 0.5\cos\left(k_y \frac{a_0}{2}\right) \\ 0.5\cos\left(k_z \frac{a_0}{2}\right) & -1 & 0.5\cos\left(k_x \frac{a_0}{2}\right) \\ 0.5\cos\left(k_y \frac{a_0}{2}\right) & 0.5\cos\left(k_x \frac{a_0}{2}\right) & -1 \end{pmatrix}. \tag{5.8}$$

The free energy functional in the Fe-C system with three octahedral sublattices in mean-field approximation is

$$F = \frac{1}{2}\sum_{p,q}\sum_{\mathbf{r},\mathbf{r}'} w_{pq}(\mathbf{r}-\mathbf{r}')n_p(\mathbf{r})n_q(\mathbf{r}')+ \\ k_BT\sum_{\mathbf{r}}\sum_{p}\left[n_p(\mathbf{r})\ln n_p(\mathbf{r}) + (1-n_p(\mathbf{r}))\ln\left(1-n_p(\mathbf{r})\right)\right], \tag{5.9}$$

where k_B is the Boltzmann constant, T is the temperature, $w_{pq}(\mathbf{r}-\mathbf{r}')$ is the effective pairwise energy between carbon atoms in $(p,\mathbf{r})$ and $(q,\mathbf{r}')$ sites. The Fourier transform of the potential $w_{pq}(\mathbf{r})$ is

$$\widetilde{w}_{pq}(\mathbf{k}) = \sum_{\mathbf{r}} w_{pq}(\mathbf{r})e^{-i\mathbf{kr}}. \tag{5.10}$$

In the subsection the interaction potential $w_{pq}(\mathbf{r})$ will be presented in details.

5.1.1 Interaction potential

The interaction between two carbon atoms can be divided in the two contributions: the elastic interactions ${w_{pq}}^{elas}(\mathbf{r})$ and chemical ${w_{pq}}^{chem}(\mathbf{r})$ one. In our model we will use the Fourier representation of these potentials. Then the total interaction potential is:

$$\widetilde{w}_{pq}(\mathbf{k}) = {\widetilde{w}_{pq}}^{elas}(\mathbf{k}) + {\widetilde{w}_{pq}}^{chem}(\mathbf{k}). \tag{5.11}$$

5.1.1.1 Effective elastic interactions

First, we will consider the elastic part of the interaction potential. As it was mentioned above, the carbon atoms occupy octahedral interstitial positions in the iron host lattice (Fig.5.4). In the bcc lattice the interstitial atom has two nearest neighbor iron atoms. The octahedral voids are smaller then the radius of carbon (Fig.5.6). Therefore, the carbon atoms induce a tetragonal distortion in the host bcc lattice. Then the lattice expansion $\bar{\varepsilon}_{ij}$ related to this distortion is

$$\bar{\varepsilon}_{ij} = u_{ij}(p)\bar{n}_p, \tag{5.12}$$

where $u_{ij}(p)$ are the concentration expansion coefficients and $\bar{n}_p$ is the mean concentration of carbon atoms in p-sublattice. The expansion coefficient $u_{ij}(p)$ is defined by the next expression:

$$u_{ij}(p) = \frac{da_p}{ad\bar{n}_p}\delta_{ij}. \tag{5.13}$$

Here $\{a_p\} = a_1, a_2, a_3$ are the lattice translations along [100], [010] and [001] directions. The concentration expansion coefficients describe the deformation induced by carbon atom situated in p octahedral sublattice. If carbon atoms occupy, for example, 1st sublattice there is

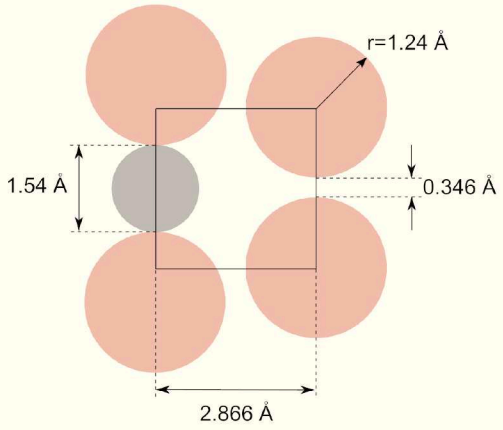

FIGURE 5.6: Schematic representation of the bcc iron lattice in (100) plane. Iron atoms are marked in red and the carbon atom situated in the octahedral interstitial site is marked in grey. The octahedral void ($0.346\mathring{A}$) is not enough big to accommodate the carbon atom ($d_C = 1.54\mathring{A}$) therefore a tetragonal deformation occurs [4].

dilatation u_{33} of the bcc host lattice in [100] direction and compression u_{11} in [010] and [001] directions. However, the total volume before and after deformation is conserved. Thus, tensors of concentration expansion coefficients for three sublattices are

$$\hat{u}(1) = \begin{pmatrix} u_{33} & 0 & 0 \\ 0 & u_{11} & 0 \\ 0 & 0 & u_{11} \end{pmatrix}, \quad \hat{u}(2) = \begin{pmatrix} u_{11} & 0 & 0 \\ 0 & u_{33} & 0 \\ 0 & 0 & u_{11} \end{pmatrix}, \quad \hat{u}(3) = \begin{pmatrix} u_{11} & 0 & 0 \\ 0 & u_{11} & 0 \\ 0 & 0 & u_{33} \end{pmatrix}. \tag{5.14}$$

To describe the elastic interaction between the carbon atoms in the bcc host lattice of iron we will use the notion of Kanzaki forces $\mathbf{f}(p, \mathbf{r})$ [17, 53]. Generally, the Kanzaki forces are forces in which the lattice defect acts on atoms of the host lattice. In our case, the impurity atoms are located in the octahedral interstices of the bcc host lattice. Detailed description of the Kanzaki forces as well as calculation of the expressions for their components in reciprocal space $\mathbf{F}(p, \mathbf{k})$ are given in Appendix C. The final expressions for Kanzaki forces $\mathbf{F}(p, \mathbf{k})$ for three octahedral sublattices $p = \overline{1.3}$ are

$$\mathbf{F}(1, \mathbf{k}) = \begin{pmatrix} -ia_0^2\sigma_{33}\sin(k_x a_0/2) \\ -ia_0^2\sigma_{11}\sin(k_y a_0/2)\cos(k_z a_0/2) \\ -ia_0^2\sigma_{11}\sin(k_z a_0/2)\cos(k_y a_0/2) \end{pmatrix}, \tag{5.15a}$$

$$\mathbf{F}(2, \mathbf{k}) = \begin{pmatrix} -ia_0^2\sigma_{11}\sin(k_x a_0/2)\cos(k_z a_0/2) \\ -ia_0^2\sigma_{33}\sin(k_y a_0/2) \\ -ia_0^2\sigma_{11}\sin(k_z a_0/2)\cos(k_x a_0/2) \end{pmatrix}, \tag{5.15b}$$

$$\mathbf{F}(3, \mathbf{k}) = \begin{pmatrix} -ia_0^2\sigma_{11}\sin(k_x a_0/2)\cos(k_y a_0/2) \\ -ia_0^2\sigma_{11}\sin(k_y a_0/2)\cos(k_x a_0/2) \\ -ia_0^2\sigma_{33}\sin(k_z a_0/2) \end{pmatrix}. \tag{5.15c}$$

The strain-induced interaction potential obtained using the Kanzaki forces by Krivoglaz [53] and by Khachaturyan [17] reads:

$$\widetilde{w}_{pq}{}^{elas}(\mathbf{k}) = \begin{cases} -v_0\lambda_{ijkl}u_{ij}(p)u_{kl}(q) + Q\delta_{pq} & \text{at} \quad \mathbf{k}=0, \\ -F_i(p,\mathbf{k})G_{ij}(\mathbf{k})F_j^*(q,\mathbf{k}) + Q\delta_{pq} & \text{at} \quad \mathbf{k}\neq 0. \end{cases} \tag{5.16}$$

Here the interaction potential is written for the atoms situated in $(p,0)$ and $(q,\mathbf{r})$ interstices, v_0 is atomic volume and for the bcc lattice $v_0 = \frac{a_0^3}{2}$, λ_{ijkl} is a tensor of elastic constants and for cubic lattice it can be written in next form:

$$\lambda_{ijkl} = \begin{pmatrix} C_{11} & C_{12} & C_{12} & 0 & 0 & 0 \\ C_{12} & C_{11} & C_{12} & 0 & 0 & 0 \\ C_{12} & C_{12} & C_{11} & 0 & 0 & 0 \\ 0 & 0 & 0 & C_{44} & 0 & 0 \\ 0 & 0 & 0 & 0 & C_{44} & 0 \\ 0 & 0 & 0 & 0 & 0 & C_{44} \end{pmatrix}. \tag{5.17}$$

To exclude a self-interaction of interstitial atoms the constant Q is introduced. It can be obtained by the averaging of the expression $\mathbf{F}(p,\mathbf{k})\hat{\mathbf{G}}(\mathbf{k})\mathbf{F}^*(q,\mathbf{k})$ over the first Brillouin zone of the bcc lattice:

$$Q = \frac{1}{N_0}\sum_{\mathbf{k}} F_i(p,\mathbf{k})G_{ij}(\mathbf{k})F_j^*(p,\mathbf{k}) = \langle F_i(p,\mathbf{k})G_{ij}(\mathbf{k})F_j^*(p,\mathbf{k})\rangle. \tag{5.18}$$

The Green function $\hat{\mathbf{G}}(\mathbf{k})$ in (5.16) is the inverse matrix of the dynamical matrix $\widetilde{\hat{\mathbf{A}}}(\mathbf{k})$:

$$G_{ij}(\mathbf{k}) = \left[\widetilde{A}_{ij}(\mathbf{k})\right]^{-1} \quad (\mathbf{k}\neq 0)\,. \tag{5.19}$$

The dynamical matrix is a function of the elastic constants λ_{ijkl} and lattice parameter a_0. The analytical form of its components $\widetilde{A}_{ij}(\mathbf{k})$ can be expressed in terms of the Born-Karman constants and in two coordination shells approximation for bcc lattice (see Appendix D):

$$\begin{aligned} \widetilde{A}_{xx}(\mathbf{k}) &= 8\alpha_1\left[1-\cos(k_x\frac{a_0}{2})\cos(k_y\frac{a_0}{2})\cos(k_z\frac{a_0}{2})\right] + \\ &\quad \left[4\alpha_2\sin^2(k_x\frac{a_0}{2}) + 4\beta_2(\sin^2(k_y\frac{a_0}{2})+\sin^2(k_z\frac{a_0}{2}))\right], \\ \widetilde{A}_{xy}(\mathbf{k}) &= 8\gamma_1\sin(k_x\frac{a_0}{2})\sin(k_y\frac{a_0}{2})\sin(k_z\frac{a_0}{2}). \end{aligned} \tag{5.20}$$

The force constants α_1, α_2, γ_1 and β_2 are [53]

$$\alpha_1 = \frac{C_{44}}{2}a_0, \qquad \alpha_2 = \frac{C_{11}-C_{44}}{2}a_0, \qquad \gamma_1 = \frac{C_{12}+C_{44}}{4}a_0, \qquad \beta_2 = 0. \tag{5.21}$$

The expressions for the other components $\widetilde{A}_{ij}(\mathbf{k})$ can be obtained by cyclic permutations:

$$x \to y,$$
$$y \to z,$$
$$z \to x.$$

Using (5.14) and (5.17) we can obtain the potential (5.16) at the point $\mathbf{k} = 0$:

$$\begin{aligned}
\widetilde{w}_{pp}{}^{elas}(\mathbf{k}=0) &= -\frac{a_0^3}{2}\left[2(C_{11}+C_{12}){u_{11}}^2 + C_{11}{u_{33}}^2 + 4C_{12}u_{11}u_{33}\right] + Q, \\
\widetilde{w}_{pq}{}^{elas}(\mathbf{k}=0) &= -\frac{a_0^3}{2}\left[(C_{11}+3C_{12}){u_{11}}^2 + C_{12}{u_{33}}^2 + 2(C_{11}+C_{12})u_{11}u_{33}\right].
\end{aligned}$$

We will use the energy unit $C_{44}a_0^3{u_{33}}^2$ to rewrite the potential (5.16) in the dimensionless form:

$$\frac{\widetilde{w}_{pq}{}^{elas}(\mathbf{k}\neq 0)}{C_{44}a_0^3{u_{33}}^2} = \frac{-F_i(p,\mathbf{k})G_{ij}(\mathbf{k})F_j^*(q,\mathbf{k}) + Q\delta_{pq}}{C_{44}a_0^3{u_{33}}^2}. \tag{5.22}$$

And at $\mathbf{k} = 0$:

$$\begin{aligned}
\frac{\widetilde{w}_{pp}{}^{elas}(\mathbf{k}=0)}{C_{44}a_0^3{u_{33}}^2} &= -\frac{1}{2}\left[2(C_{11}+C_{12}){t_1}^2 + C_{11} + 4C_{12}t_1\right]/C_{44} + \frac{Q}{C_{44}a_0^3{u_{33}}^2}, \\
\frac{\widetilde{w}_{pq}{}^{elas}(\mathbf{k}=0)}{C_{44}a_0^3{u_{33}}^2} &= -\frac{1}{2}\left[(C_{11}+3C_{12}){t_1}^2 + C_{12} + 2(C_{11}+C_{12})t_1\right]/C_{44}.
\end{aligned} \tag{5.23}$$

Here $t_1 = u_{11}/u_{33}$ is a tetragonality factor.

5.1.1.2 Effective chemical interactions

Due to the fact that the distance between the nearest neighbor octahedral interstitial atoms ($a_0/2 = 1.433\mathring{A}$) is smaller then the effective diameter of carbon atom ($d_C = 1.54\mathring{A}$) there is a strong repulsion between the neighboring carbon atoms. Therefore, in chemical part of the effective potential $w_{pq}(\mathbf{r})$ we took into account the contact repulsion between carbon atoms from the first coordination shell. The repulsion between diluted carbon ions caused by a screened Coulomb interaction will be also taken into account. The energies of these interactions can be calculated using *ab initio* methods. Such calculations have been done for the carbon-carbon interactions in various papers [21–23, 104, 105]. In particular, it has been shown that the energy of chemical carbon-carbon interactions decreases rapidly with distance. In this work we consider the chemical interactions between carbon atoms from the first four coordination shells. In Table 5.1 the pairwise interaction energies W_i between carbon atoms placed in octahedral interstices of the host iron lattice are presented. Index $i = \overline{1,4}$ in energies W_i marks the number of coordination shell, the prime symbol is used to distinguish the interactions between two atoms located at the same distance, but situated in one or different sublattices. The positions of neighbor octahedral interstitial sites of carbon atoms are shown in Fig.5.5. The 1st, 2nd,

TABLE 5.1: Pairwise interaction energies W_i obtained in first-principles calculations [21–23] and used in this work.

	Udyansky *et al.* [22], eV	Johnson *et al.* [21], eV	Ruban [23], eV	This work, eV
W_1	3.13	-	3.12	6.26
W_2	0.87	-	1.0	1.74
W_3	0.27	0.13	0.38	0.54
$W_3^{'}$	0.27	0.08	0.38	0.54
W_4	1.4	0.11	1.45	2.8
$W_4^{'}$	0.23	0.11	0.33	0.46

3rd and 4th neighbors are situated at distances $a_0/2$, $a_0\sqrt{2}/2$, $a_0\sqrt{3}/2$ and a_0, respectively. To adapt the *ab initio* calculations to mean field modeling we kept the same energy as in the work of Udyansky *et al.* [22] but results of the mean-field theory (the second column in Table5.1) are multiplied by two. Using this set of parameters the contribution of the elastic and chemical energy to free energy becomes approximately the same. It also help us to obtain the carbon rich zones with large thickness.

For the following calculations it is convenient to write the potential $w_{pq}(\mathbf{r})$ in Fourier space. In the case when the carbon atoms occupy only one sublattice ($p = q$) there are eight possible neighbors in 3rd coordination shell and six in 4th one. Using (5.10) the Fourier transform of $w_{pp}(\mathbf{r})$ is

$$\begin{aligned}
\widetilde{w}_{11}^{chem}(\mathbf{k}) &= 8W_3 \cos(\frac{k_x a_0}{2}) \cos(\frac{k_y a_0}{2}) \cos(\frac{k_z a_0}{2}) + \\
&+ 2W_4 \left(\cos(k_y a_0) + \cos(k_z a_0)\right) + 2W_4^{'} \cos(k_x a_0), \\
\widetilde{w}_{22}^{chem}(\mathbf{k}) &= 8W_3 \cos(\frac{k_x a_0}{2}) \cos(\frac{k_y a_0}{2}) \cos(\frac{k_z a_0}{2}) + \\
&+ 2W_4 \left(\cos(k_x a_0) + \cos(k_z a_0)\right) + 2W_4^{'} \cos(k_y a_0), \\
\widetilde{w}_{33}^{chem}(\mathbf{k}) &= 8W_3 \cos(\frac{k_x a_0}{2}) \cos(\frac{k_y a_0}{2}) \cos(\frac{k_z a_0}{2}) + \\
&+ 2W_4 \left(\cos(k_x a_0) + \cos(k_y a_0)\right) + 2W_4^{'} \cos(k_z a_0).
\end{aligned} \tag{5.24}$$

Here W_3 and W_4 are the chemical interaction energy in third and forth coordination shell. In the case when the carbon atoms are situated in two sublattices ($p \neq q$), there are two neighbors in 1st coordination shell with pairwise interaction energy W_1, four in the 2nd and eight in the 3rd with interaction energies W_2 and $W_3^{'}$, respectively. Thus, the Fourier representation of the

interaction potentials $w_{pq}(\mathbf{r})$ for $p \neq q$ is

$$\begin{aligned}
\widetilde{w}_{12}^{chem}(\mathbf{k}) &= 2W_1 \cos(\frac{k_z a_0}{2}) + 4W_2 \cos(\frac{k_x a_0}{2}) \cos(\frac{k_y a_0}{2}) + \\
&+ 4W_3' \cos(\frac{k_z a_0}{2}) \left(\cos(k_x a_0) + \cos(k_y a_0)\right), \\
\widetilde{w}_{13}^{chem}(\mathbf{k}) &= 2W_1 \cos(\frac{k_y a_0}{2}) + 4W_2 \cos(\frac{k_x a_0}{2}) \cos(\frac{k_z a_0}{2}) + \\
&+ 4W_3' \cos(\frac{k_y a_0}{2}) \left(\cos(k_z a_0) + \cos(k_x a_0)\right), \\
\widetilde{w}_{23}^{chem}(\mathbf{k}) &= 2W_1 \cos(\frac{k_z a_0}{2}) + 4W_2 \cos(\frac{k_y a_0}{2}) \cos(\frac{k_z a_0}{2}) + \\
&+ 4W_3' \cos(\frac{k_x a_0}{2}) \left(\cos(k_y a_0) + \cos(k_z a_0)\right).
\end{aligned} \tag{5.25}$$

Using the expression (5.9) with (5.10) the kinetic equation (5.1) can be written as:

$$\frac{d\widetilde{n}_p(\mathbf{k},t)}{dt} = \frac{1}{k_B T} \sum_{q=1}^{3} \widetilde{L}_{pq}(\mathbf{k}) \left[\widetilde{w}_{sq}(\mathbf{k}) \widetilde{n}_s(\mathbf{k},t) + k_B T \left(\ln \frac{n_q(\mathbf{r},t)}{1 - n_q(\mathbf{r})} \right)_{\mathbf{k}} \right]. \tag{5.26}$$

Numerical solution of this equation allows to follow the kinetics of carbon diffusion in martensite.

5.1.2 Scattering intensities of the imperfect crystal lattice structure

To characterise the obtained microstructure the diffraction pattern should be also simulated. Since we use in our simulation the ADF theory on constrained Ising lattice the displacement of carbon atoms cannot be visualized in the real space. However it can be taken into account in calculation of diffraction patterns.

Then the positions of iron atoms are described by the radius vector $\mathbf{r} + \sum_p \mathbf{u}(p,\mathbf{r})$, where $\mathbf{r}$ corresponds to positions in a perfect crystal lattice and $\mathbf{u}(p,\mathbf{r})$ is a displacement caused by a diluted atom in p octahedral sublattice. The carbon atoms positions are determined by the vector $\mathbf{r} + \mathbf{h}_p$, where vector $\mathbf{h}_p$ determines the position of the p sublattice. In the case of the bcc host lattice these vectors are

$$\begin{aligned}
\mathbf{h}_1 &= (a_0/2, 0, 0), \\
\mathbf{h}_2 &= (0, a_0/2, 0), \\
\mathbf{h}_3 &= (0, 0, a_0/2).
\end{aligned}$$

According to the mentioned above the scattered wave amplitude of the Fe-C system can be written as:

$$A(\mathbf{q}) = \sum_{\mathbf{r}} \left[f_{\mathrm{Fe}} e^{-i\mathbf{q}(\mathbf{r} + \sum_p \mathbf{u}(p,\mathbf{r}))} + f_{\mathrm{C}} \sum_p e^{-i\mathbf{q}(\mathbf{r}+\mathbf{h}_p)} n_p(\mathbf{r}) \right]. \tag{5.27}$$

Here $f_{\mathrm{Fe}} = 26$ and $f_{\mathrm{C}} = 6$ are atomic factors of iron and carbon atoms. It is convenient to represent a point in reciprocal space as

$$\mathbf{q} = 2\pi\mathbf{H} + \mathbf{k},$$

where $\mathbf{H}$ is a reciprocal lattice vector closest to the point $\mathbf{q}$, $\mathbf{k}$ is a distance between the observation point $\mathbf{q}$ and vector $2\pi\mathbf{H}$. According to this representation it can be written:

$$e^{-i\mathbf{qr}} = e^{-i(2\pi\mathbf{H}+\mathbf{k})\mathbf{r}} = e^{-i\mathbf{kr}}. \tag{5.28}$$

Therefore expression (5.27) may be rewritten as

$$A(\mathbf{q}) = \sum_{\mathbf{r}} e^{-i\mathbf{kr}} \left[f_{\mathrm{Fe}} e^{-i\mathbf{q}\sum_p \mathbf{u}(p,\mathbf{r})} + \sum_p f_{\mathrm{C}} e^{-i\mathbf{q}\mathbf{h}_p} n_p(\mathbf{r}) \right]. \tag{5.29}$$

For the small displacements $\mathbf{u}(p,\mathbf{r})$ Eq. (5.29) can be simplified:

$$A(\mathbf{q}) \approx \sum_{\mathbf{r}} e^{-i\mathbf{kr}} \left[f_{\mathrm{Fe}} - i f_{\mathrm{Fe}} \mathbf{q} \sum_p \mathbf{u}(p,\mathbf{r}) + f_{\mathrm{C}} \sum_p e^{-i\mathbf{q}\mathbf{h}_p} n_p(\mathbf{r}) \right]. \tag{5.30}$$

In (5.30) we used

$$e^{-i\mathbf{q}\sum_p \mathbf{u}(p,\mathbf{r})} \approx 1 - i\mathbf{q}\sum_p \mathbf{u}(p,\mathbf{r}).$$

The Fourier transform of atomic displacements is

$$\widetilde{\mathbf{u}}(p,\mathbf{k}) = \sum_{\mathbf{r}} \mathbf{u}(p,\mathbf{r}) e^{-i\mathbf{kr}}. \tag{5.31}$$

The displacement $\widetilde{\mathbf{u}}(p,\mathbf{k})$ can be calculated using the Kanzaki forces:

$$\widetilde{\mathbf{u}}(p,\mathbf{k}) = \hat{\mathbf{G}}(\mathbf{k})\mathbf{F}(p,\mathbf{k})\widetilde{n}_p(\mathbf{k}) = \widetilde{\mathbf{u}}_0(p,\mathbf{k})\widetilde{n}_p(\mathbf{k}), \tag{5.32}$$

where the vector $\widetilde{\mathbf{u}}_0(p,\mathbf{k}) = \hat{\mathbf{G}}(\mathbf{k})\mathbf{F}(p,\mathbf{k})$.

Substituting Eqs.(5.31) and (5.32) into Eq.(5.30) gives

$$A(\mathbf{q}) = f_{\mathrm{Fe}} \sum_{\mathbf{r}} e^{-i\mathbf{kr}} + \sum_{p=1}^{3} \left[-i f_{\mathrm{Fe}} \mathbf{q} \widetilde{\mathbf{u}}_0(p,\mathbf{k}) + f_{\mathrm{C}} e^{-i\mathbf{q}\mathbf{h}_p} \right] \widetilde{n}_p(\mathbf{k}). \tag{5.33}$$

The diffraction intensities are proportional to the square of absolute value of scattered amplitude:

$$I(\mathbf{q}) = |A(\mathbf{q})|^2. \tag{5.34}$$

Using (5.33) in (5.34) gives finally the expression for the scattered intensity:

$$I(\mathbf{q}) = \left| f_{\mathrm{Fe}} \sum_{\mathbf{r}} e^{-i\mathbf{kr}} + \sum_{p=1}^{3} \left[-i f_{\mathrm{Fe}} \mathbf{q} \widetilde{\mathbf{u}}_0(p, \mathbf{k}) + f_{\mathrm{C}} e^{-i\mathbf{q}\mathbf{h}_p} \right] \widetilde{n}_p(\mathbf{k}) \right|^2 . \tag{5.35}$$

In Eq.(5.35) the first term is equal 0 for each point $\mathbf{k} \neq 0$, so $\sum_{\mathbf{r}=1}^{N} e^{-i\mathbf{kr}} = N\delta(\mathbf{k})$. The second term gives zero at points $2\pi\mathbf{H}$. Therefore we can present diffraction intensity as a sum of the scattering intensity of the perfect crystal $I_0(\mathbf{q})$ and the scattering intensity $I_C(\mathbf{q})$ associated with a carbon influence:

$$I(\mathbf{q}) = I_0(\mathbf{q}) + I_C(\mathbf{q}), \tag{5.36}$$

where

$$I_0(\mathbf{q}) = f_{\mathrm{Fe}}^2 N^2 \delta(\mathbf{k}) \tag{5.37}$$

and

$$I_C(\mathbf{q}) = \left| \sum_{p=1}^{3} \left[-i f_{\mathrm{Fe}} \mathbf{q} \widetilde{\mathbf{u}}_0(p, \mathbf{k}) + f_{\mathrm{C}} e^{-i\mathbf{q}\mathbf{h}_p} \right] \widetilde{n}_p(\mathbf{k}) \right|^2 . \tag{5.38}$$

This is the final formula which gives the possibility to calculate the scattering intensity in the iron-carbon system.

5.2 Simulation results

To perform the computer modeling of atomic diffusion kinetics during aging of martensite phase, the atomic density function kinetic equation (Eq.(5.26)) for occupation density, $n_p(\mathbf{r}, t)$ should be numerically solved. Typically, in the freshly formed martensite the carbon atoms are randomly distributed only in one octahedral sublattice of the bcc iron lattice [106]. This kind of distribution corresponds to the α' phase of martensite.

In our simulation the initial state was a random distribution of the carbon atoms in the three iron octahedral sublattices with average concentrations $\bar{n}_1 = 0.02$ and $\bar{n}_2 = \bar{n}_3 = 0.002$. This distribution reflects the preferential occupation of the sublattices by carbon atoms. At each point of sublattice p the values of occupation densities $n_p(\mathbf{r}, t)$ are given as $\bar{n}_p \pm \Delta n_p$, where Δn_p varies randomly within a range of 0 to $0.5\bar{n}_p$. The iron host lattice was occupied with probability 1 by iron atoms. In this case we can calculate the average concentration of carbon atoms which in our case equal $\bar{n}_C = 0.024$. It corresponds to 2.34 at.% or 0.51 wt.%.

Let us remember that the value of Kanzaki forces is proportional to the tetragonality of the system. The interaction parameters used in modeling are given in Table5.2. In this study

TABLE 5.2: Experimental elastic constants C_{ij} and lattice constant a_0 of Fe in α phase.

a_0, $\mathring{A}$	C_{11}, GPa	C_{12}, GPa	C_{44}, GPa
2.865[17]	242[96]	146[96]	112[96]

we considered Kanzaki forces that correspond to two kinds of alloys: Fe-C and Fe-Ni-C. In the case of Fe-C system the concentration expansion coefficients, that are used for the calculation of Kanzaki forces, are $u_{11} = -0.09$, $u_{33} = 0.86$ and the corresponding tetragonality factor is $t_1 = -0.1$ [17]. For the other type of alloy, Fe-Ni-C, we used parameters proposed in [107] by Taylor *et al.*: $u_{11} = -0.275$, $u_{33} = 1.016$ and $t_1 = -0.27$. Thus, it will allow us to investigate the effect of tetragonality on high-carbon regions formation.

The pairwise chemical interaction energies W_i used in modeling are presented in the fifth column of Table5.1.

In our modeling all energetic parameters are expressed in the energetic unit $C_{44}a_0^3{u_{33}}^2$. In this unit the energy k_BT is $1.5 \cdot 10^{-3}$. The time, t, is measured in units of typical atomic migration time, τ_0, and is proportional to $L_0\Delta f$, where Δf is a driving force. Adimensional kinetic coefficient, L_0, equal 1/12 was used. In computations the simulation box 128^3 has been used.

5.2.1 Modeling with $t_1 = -0.1$

For the α-Fe-C alloy the concentration expansion coefficients are $u_{11} = -0.09$, $u_{33} = 0.86$ [17]. Then the tetragonal factor is $t_1 = -0.1$.

First, using the concentration wave method [17] we will analyze the conditions under which the system looses stability and the ordered phase phase forms from a disordered solution. To this end, we will find the eigenvalues $\lambda_s(\mathbf{k})$ of the matrix of potential $\widetilde{w}_{pq}(\mathbf{k})$ which are determined from the equation:

$$\begin{vmatrix} \widetilde{w}_{11}(\mathbf{k}) - \lambda & \widetilde{w}_{12}(\mathbf{k}) & \widetilde{w}_{13}(\mathbf{k}) \\ \widetilde{w}_{12}(\mathbf{k}) & \widetilde{w}_{22}(\mathbf{k}) - \lambda & \widetilde{w}_{23}(\mathbf{k}) \\ \widetilde{w}_{13}(\mathbf{k}) & \widetilde{w}_{23}(\mathbf{k}) & \widetilde{w}_{33}(\mathbf{k}) - \lambda \end{vmatrix} = 0. \tag{5.39}$$

Cubic equation (5.39) has three solutions $\lambda_1(\mathbf{k})$, $\lambda_2(\mathbf{k})$ and $\lambda_3(\mathbf{k})$. The minimal value of eigenvalues $\lambda_s(\mathbf{k})$ ($s = \overline{1,3}$) determines the temperature of the order-disorder phase transition, T_c:

$$T_c = -\frac{\bar{n}_C(1-\bar{n}_C)\lambda_{s0}(\mathbf{k}_{s0})}{k_B}, \tag{5.40}$$

where index $s0$ denotes the lowest branch of the eigenvalues spectrum $\lambda_s(\mathbf{k})$, the star of the vector $\mathbf{k}_{s0}$ corresponds to the global minimum of $\lambda_s(\mathbf{k})$. If $\mathbf{k}_{s0} = 0$ the aging kinetics will be determined by the spinodal decomposition. However if the global minima takes place at $\mathbf{k}_{s0}$

not equal 0 the ordering structure with period $\mathbf{k}_{s0}$ will appear. The corresponding eigenvector $\mathbf{v}_{s0}(p, \mathbf{k}_{s0})$ gives a dominant concentration mode. Thus the occupation probabilities, $n(p, \mathbf{r})$, can be presented as superposition of the static concentration waves, $v_{s0}(p, \mathbf{k}_{s0})e^{-i\mathbf{k}_{s0}\mathbf{r}}$:

$$n(p, \mathbf{r}) = \frac{\bar{n}_C}{3} + \frac{1}{2}\sum_{s0}\left(Q_{s0}(\mathbf{k}_{s0})v_{s0}(p, \mathbf{k}_{s0})e^{-i\mathbf{k}_{s0}\mathbf{r}} + Q^*_{s0}(\mathbf{k}_{s0})v^*_{s0}(p, \mathbf{k}_{s0})e^{i\mathbf{k}_{s0}\mathbf{r}}\right). \qquad (5.41)$$

Here the concentration amplitudes $Q_{s0}(\mathbf{k}_{s0}) = \eta_{s0}\gamma_s$ are proportional to the long-range order parameters η_{s0} and the normalization coefficients γ_s. The coefficients γ_s provide all parameters η_{s0} to be equal to unity in the completely ordered state. The dominant mode $v_{s0}(p, \mathbf{k}_{s0})e^{-i\mathbf{k}_{s0}\mathbf{r}}$ generates the distribution of carbon between three octahedral interstitial sublattices.

In Figs.5.7 and 5.8 the eigenvalue $\lambda_s(\mathbf{k})$ of spectrum was presented which is called also dispersion curves. This spectrum was calculated in the directions of the high symmetry points of the first Brillouin zone of the bcc lattice. The eigenvalue spectrum in Fig.5.7 corresponds to the case where only strain-induced interactions ($\widetilde{w}_{pq}(\mathbf{k}) = \widetilde{w}_{pq}{}^{elas}(\mathbf{k})$) have been considered. In this case we can conclude that the minima of eigenvalue fells at $\mathbf{k} = 0$. In this case the redistribution of carbon should undergo through spinodal decomposition. In Fig. 5.8 the eigenvalues spectrum, where both chemical and elastic interaction were taking into account, is presented. In this case the minimum values are situated at points close to $\frac{2\pi}{a_0}\left(\frac{1}{2}\frac{1}{2}\frac{1}{2}\right)$ and $\frac{2\pi}{a_0}\left(\frac{1}{2}0\frac{1}{2}\right)$. Comparison of these two figures indicates that elastic interaction is responsible to the spinodal decomposition as well as chemical interaction induces the ordering kinetics in Fe-C system.

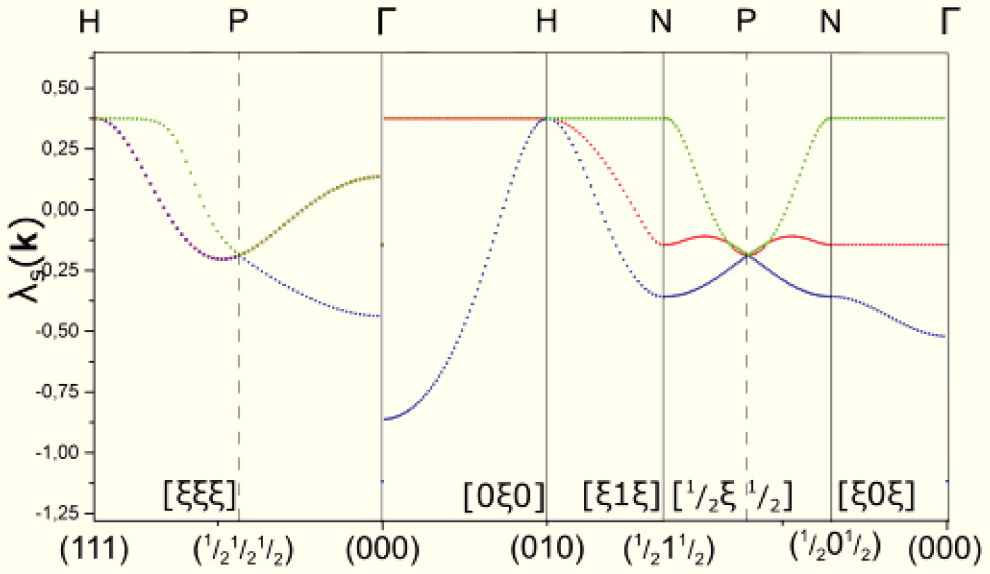

FIGURE 5.7: The eigenvalue spectrum of the strain-induced interaction matrix $\widetilde{w}_{pq}{}^{elas}(\mathbf{k})$ of the Fe-C system. The blue curve corresponds to the eigenvalue $\lambda_1(\mathbf{k})$, red and green curves correspond to the $\lambda_2(\mathbf{k})$ and $\lambda_3(\mathbf{k})$, respectively. Eigenvalues are presented in dimensionless form in units $C_{44}a_0^3{u_{33}}^2$. The dispersion curves are built for the several directions in reciprocal space, the wave vector ξ is written in units $\frac{2\pi}{a_0}$.

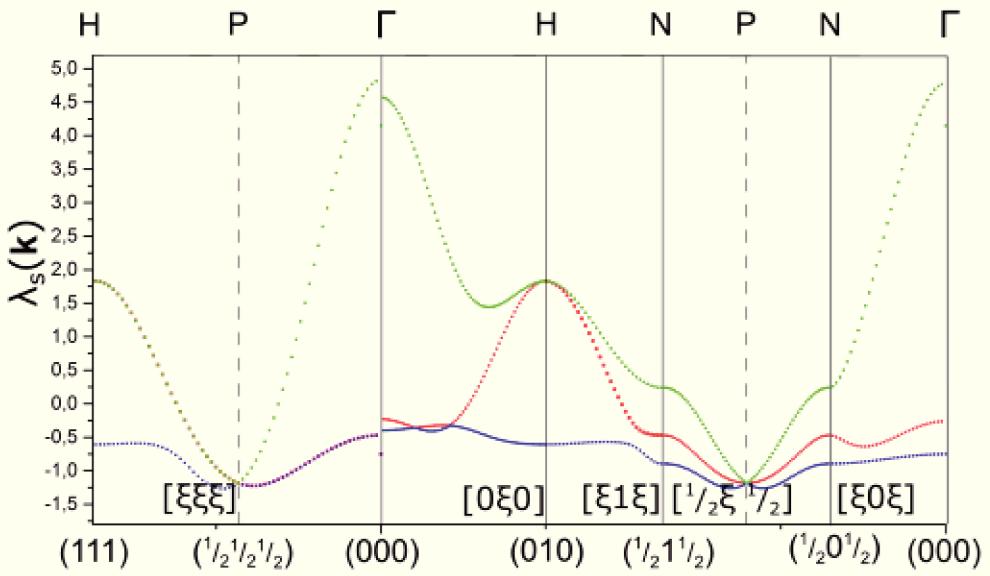

FIGURE 5.8: The eigenvalue spectrum of the total interaction matrix $\widetilde{w}_{pq}(\mathbf{k})$ of the Fe-C system. Blue and red curves correspond to the eigenvalues $\lambda_1(\mathbf{k})$ and $\lambda_2(\mathbf{k})$, respectively, green curve corresponds to $\lambda_3(\mathbf{k})$. Eigenvalues are presented in dimensionless form in units $C_{44}a_0^3{u_{33}}^2$. The dispersion curves are built for the several directions in reciprocal space, the wave vector ξ is written in units $\frac{2\pi}{a_0}$.

Let us consider the solution of the interaction matrix at $\mathbf{k}_0 = 0$. This wave vector corresponds to the minima on the dispersion curve Fig.5.7. In this case equation (5.39) simplifies to:

$$\begin{vmatrix} \widetilde{w}_{11}(0) - \lambda_s & \widetilde{w}_{12}(0) & \widetilde{w}_{12}(0) \\ \widetilde{w}_{12}(0) & \widetilde{w}_{11}(0) - \lambda_s & \widetilde{w}_{12}(0) \\ \widetilde{w}_{12}(0) & \widetilde{w}_{12}(0) & \widetilde{w}_{11}(0) - \lambda_s \end{vmatrix} = 0. \tag{5.42}$$

The cubic equation (5.42) has two different solutions: $\lambda_1(0) = \widetilde{w}_{11}(0) + 2\widetilde{w}_{12}(0)$ and $\lambda_2(0) = \lambda_3(0) = \widetilde{w}_{11}(0) - \widetilde{w}_{12}(0)$.

To obtain the corresponding eigenvectors $\mathbf{v}_{s0}(p,0)$ we have to solve the system of linear equations:

$$\begin{pmatrix} \widetilde{w}_{11}(0) & \widetilde{w}_{12}(0) & \widetilde{w}_{12}(0) \\ \widetilde{w}_{12}(0) & \widetilde{w}_{11}(0) & \widetilde{w}_{12}(0) \\ \widetilde{w}_{12}(0) & \widetilde{w}_{12}(0) & \widetilde{w}_{11}(0) \end{pmatrix} \begin{pmatrix} v_{s0}(1,0) \\ v_{s0}(2,0) \\ v_{s0}(3,0) \end{pmatrix} = \lambda_{s0} \begin{pmatrix} v_{s0}(1,0) \\ v_{s0}(2,0) \\ v_{s0}(3,0) \end{pmatrix}. \tag{5.43}$$

Since eigenvector $\mathbf{v}_{s0}(p,0)$ is a unit vector, the components $v_{s0}(p,0)$ should satisfy the equation:

$$v_{s0}^2(1,0) + v_{s0}^2(2,0) + v_{s0}^2(3,0) = 1. \tag{5.44}$$

Equations (5.43) and (5.44) have only one solution corresponding to the eigenvalue $\lambda_1(0)$:

$$\mathbf{v}_1(p,0) = \frac{1}{\sqrt{3}} \begin{pmatrix} v_1(1,0) \\ v_1(2,0) \\ v_1(3,0) \end{pmatrix} = \begin{pmatrix} 1 \\ 1 \\ 1 \end{pmatrix}. \tag{5.45}$$

The eigenvectors which correspond to eigenvalue $\lambda_2(0)$ are

$$\mathbf{v}_2(p,0) = \frac{1}{\sqrt{6}} \begin{Bmatrix} 2 \\ \bar{1} \\ \bar{1} \end{Bmatrix} \quad \text{and} \quad \frac{1}{\sqrt{2}} \begin{Bmatrix} 1 \\ \bar{1} \\ 0 \end{Bmatrix}. \tag{5.46}$$

If the dominant mode is $v_1(p,0)e^{-i0\mathbf{r}}$, using (5.41), then the carbon distribution for the first eigenvalue is

$$n(p,\mathbf{r}) = \begin{pmatrix} n(1,\mathbf{r}) \\ n(2,\mathbf{r}) \\ n(3,\mathbf{r}) \end{pmatrix} = \frac{\bar{n}_C}{3} \begin{pmatrix} 1 \\ 1 \\ 1 \end{pmatrix} + \eta_1 \begin{pmatrix} 1 \\ 1 \\ 1 \end{pmatrix}. \tag{5.47}$$

Since the occupation probabilities $n(p,\mathbf{r}) = \frac{\bar{n}_C}{3} + \eta_1$ for different sublattices are equal, the mode $v_1(p,0)$ corresponds to the disordered phase of carbon. Here we defined: $\eta_1 = \eta_{10}\gamma_1/\sqrt{3}$. For the second eigenvalues (5.46) there are two wave vectors and the probability function can be written as

$$n(p,\mathbf{r}) = \begin{pmatrix} n(1,\mathbf{r}) \\ n(2,\mathbf{r}) \\ n(3,\mathbf{r}) \end{pmatrix} = \frac{\bar{n}_C}{3} \begin{pmatrix} 1 \\ 1 \\ 1 \end{pmatrix} + \eta_2 \begin{pmatrix} 2 \\ \bar{1} \\ \bar{1} \end{pmatrix} + \eta_2' \begin{pmatrix} 1 \\ \bar{1} \\ 0 \end{pmatrix}. \tag{5.48}$$

Here $\eta_2 = \eta_{20}\gamma_2/\sqrt{6}$ and $\eta_2' = \eta_{20}'\gamma_2'/\sqrt{2}$. The long-range parameters, η_{s0}, depend of the eigenvalues $\lambda_s(\mathbf{k}_s)$, tetragonality, t_1, temperature, T, and the average concentration of carbon, $\bar{n}_C$. Since the distribution (5.48) is determined by weights η_2 and η_2' of the vectors (5.46), all these factors will affect the final distribution of carbon between octahedral sublattices.

To summarize, the kinetics during aging will be determined by the lowest eigenvalue (5.47) or (5.48).

In the case of Fe-C system with the tetragonality $t_1 = -0.1$, without taking into account the chemical interactions (case when $\widetilde{w}_{pq}(\mathbf{k}) = \widetilde{w}_{pq}{}^{elas}(\mathbf{k})$, see Fig.5.7), the eigenvalues are

$$\begin{aligned} \lambda_1(\mathbf{k_0} = 0) &= -1.123, \\ \lambda_2(\mathbf{k_0} = 0) &= -0.15. \end{aligned} \tag{5.49}$$

Since the $\lambda_1(0) < \lambda_2(0)$ the carbon atoms will undergo the spinodal decomposition and in the final structure will occupy all three octahedral sublattices with equal probabilities.

In the case when both elastic and chemical interactions are taken into account the eigenvalues spectrum has minima at two wave vectors $\frac{2\pi}{a_0}\left(\frac{1}{2}\frac{1}{2}\frac{1}{2}\right)$ and $\frac{2\pi}{a_0}\left(\frac{1}{2}0\frac{1}{2}\right)$. Then ordering structure is expected.

5.2.1.1 Simulation results in the direct space

The results of simulations of the carbon ordering in FeC alloy in direct space at different time steps is presented on Fig.5.9.

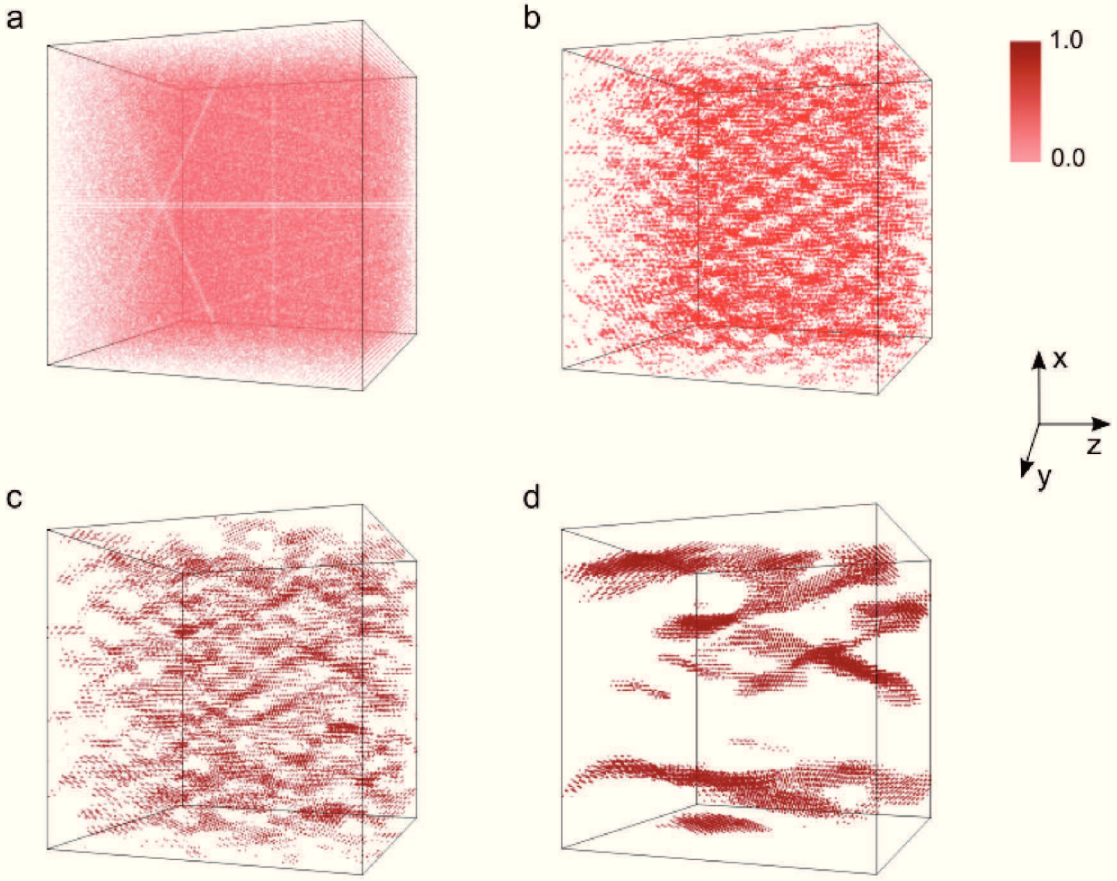

FIGURE 5.9: The results of simulations for FeC system in 3D at times (a)$\hat{t} = 0$, (b)$\hat{t} = 2500$, (c)$\hat{t} = 10000$, (d)$\hat{t} = 148000$. The isosurfaces for the occupation probability $n_1(\mathbf{r}, t)$ are shown in red.

In the first image Fig.5.9(a) the initial state is shown. As it was mentioned above, at the initial step most of the atoms are located in O_x octahedral sublattice ($\bar{n}_1 = 0.02$ and $\bar{n}_2 = \bar{n}_3 = 0.002$). The red color on Fig.5.9 denotes the probability function $n_1(\mathbf{r}, t)$.

The kinetics of carbon diffusion can be divided into two stages (Fig.5.9(b-d)). At the beginning, there is decomposition of carbon atoms and their vacancies of the first sublattices. Then the carbon rich zones aligned to the some particular direction appear and coarsening begins. The final configuration consist only of carbon atoms situated in the O_x octahedral sublattice ($\bar{n}_1 = 0.024$ and $\bar{n}_2 = \bar{n}_3 = 0$).

To compare our results with 3D APT images we will use the density map representation to identify the average impurity atoms concentration $c_{ch}(\mathbf{r}, t)$ in the carbon rich zones. Then we will determine the carbon superstructure using simulated diffraction pattern images.

To determine the density map representation the average carbon concentration in the small characteristic volume v_{ch} for each point of the simulation box has been calculated. For this a cubic characteristic volume $v_{ch} = a_{ch}^3$ with a characteristic length a_{ch} was considered. The size of the length a_{ch} should be commensurate with a thickness of carbon rich regions or smaller. In our investigation the characteristic length a_{ch} was chosen $2a_0$. Then the mean concentration of carbon was calculated in the cubic region $2a_0^3$ at each point of simulation box $\mathbf{r}(x, y, z)$ as shown in Fig.5.10. For the points with a characteristic volume that goes beyond the simulation

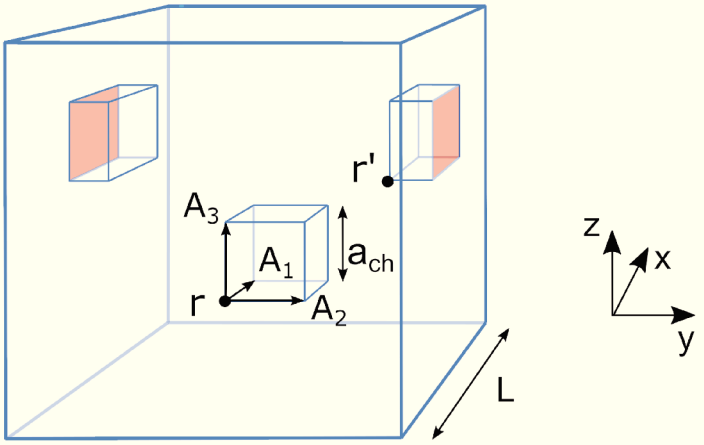

FIGURE 5.10: The schematic representation of a characteristic volume. The big cube corresponds to the simulation box. The characteristic volume is built on the basis $\mathbf{A}_1 = (a_{ch}, 0, 0)$, $\mathbf{A}_2 = (0, a_{ch}, 0)$ and $\mathbf{A}_3 = (0, 0, a_{ch})$.

box the periodic conditions have been used:

$$x_i = \begin{cases} x_i, & \text{if} \quad x_i \leq L, \\ x_i - L, & \text{if} \quad x_i > L, \end{cases} \quad \{x_i\} = \{x, y, z\}. \tag{5.50}$$

Here $\{x_i\}$ are coordinates of the points within the characteristic volume v_{ch}, L is a edge length of the simulation box.

Then the concentration of carbon was calculated using the next expression: $\sum_{v_{ch}} B_i n_C(\mathbf{r}) = \sum_{v_{ch}} B_i \left(n_1(\mathbf{r}) + n_2(\mathbf{r}) + n_3(\mathbf{r})\right)$ at each point within the volume v_{ch}. Weights B_i are $1, \frac{1}{2}, \frac{1}{4}$ and $\frac{1}{8}$ for the points inside, on faces, on edges and on vertices of the characteristic volume, respectively. The number of iron atoms in v_{ch} is $N_{Fe} = 2\left(\frac{a_{ch}}{a_0}\right) = 16$. Finally the average concentration in each point is determined by the formula:

$$c_{ch}(\mathbf{r}, t) = \frac{\sum_{v_{ch}} B_i n_C(\mathbf{r}, t)}{N_{Fe}}. \tag{5.51}$$

We find that the concentration in carbon rich zones is $c_{ch}(\mathbf{r}, t) = 0.25$, see Fig.5.11, and corresponds to the stoichiometric formula Fe_4C. On the edges of these zones the concentration

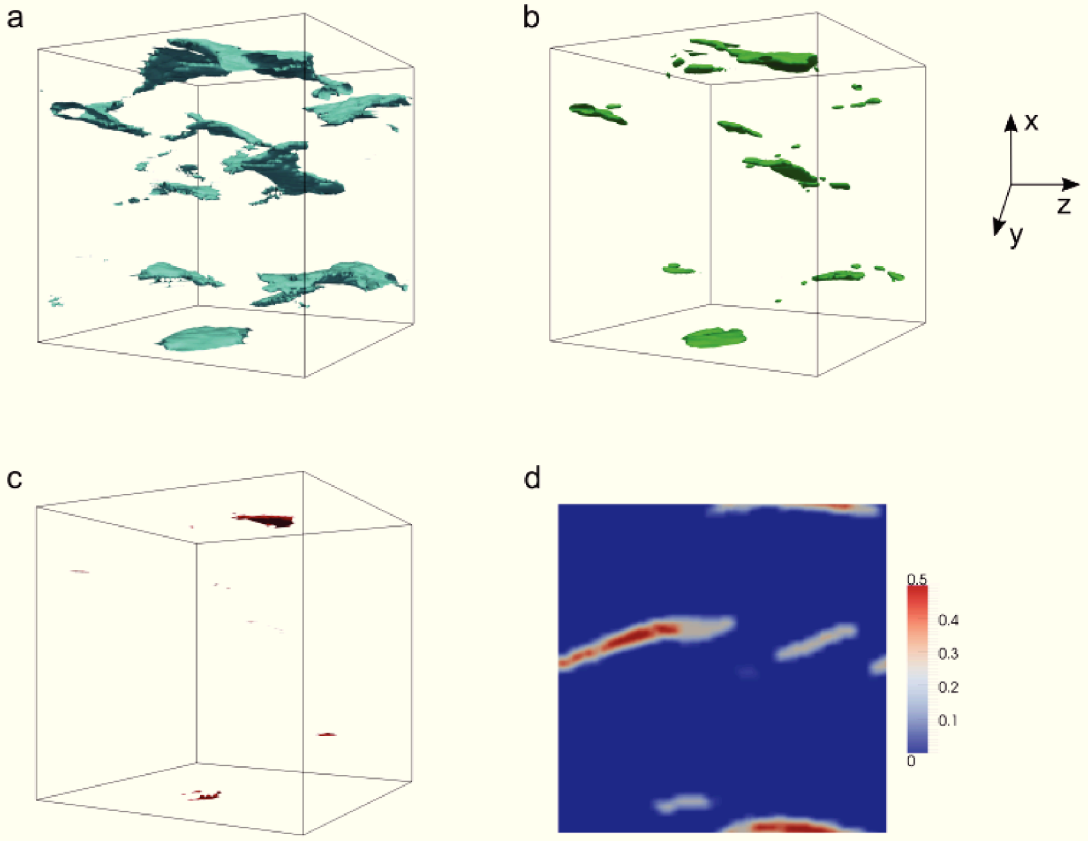

FIGURE 5.11: The density map representation of the carbon distribution for the last step of simulation. Isosurfaces were built for the average concentrations (a) $c_{ch}(\mathbf{r}) = 0.25$, (b) $c_{ch}(\mathbf{r}) = 0.40625$, (c) $c_{ch}(\mathbf{r}) = 0.4875$. (d) 2D slice of $c_{ch}(\mathbf{r})$ in (001) plane.

$c_{ch}(\mathbf{r}, t)$, is slightly smaller. At the stage of coarsening the region with stoichiometric concentration Fe_2C also appear. The change of the concentration in carbon-rich zones can be see in Fig.5.12. First, the concentration grows quickly and achieves the value 0.25, Fe_4C, and after coarsening becomes equal 0.5, Fe_2C (blue curve on Fig.5.12). With increasing of carbon concentration $\bar{n}_C$ in all of the simulation box the total weight of regions with Fe_2C increases.

The analysis of the carbon rich regions with concentration Fe_4C and Fe_2C allows to understand their superstructures. In Fe_4C zones, the carbon atoms are distributed on the fcc lattice with lattice parameter $2a_0$. This structure is presented in Fig. 5.13(a). In the carbon rich zones with stoichiometric concentration Fe_2C the carbon atoms form the diamond structure with the lattice parameter $2a_0$. This structure is presented in Fig.5.13(b).

Using a density map representation it is possible to determine approximatively the orientation of the carbon rich regions. It is convenient to use 2D slice of the concentration $c_{ch}(\mathbf{r})$ in (001) plane to find the orientation of carbon-rich clusters, see Fig.5.11(d). Finally, it gives the direction of the carbon-rich regions elongation: $\mathbf{n}(2 \ -0.79 \ 0)$. A more accurate result can be

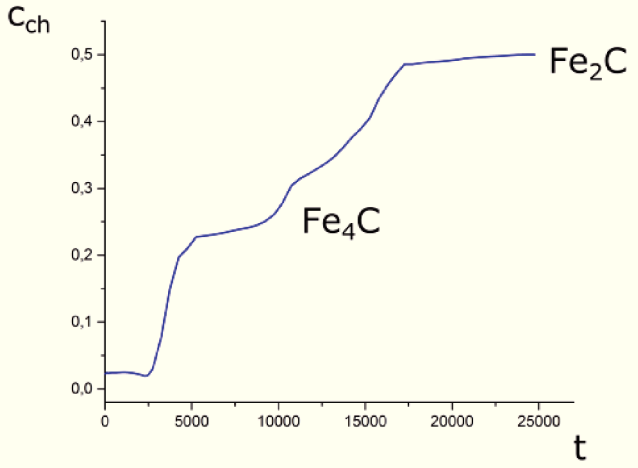

FIGURE 5.12: Dependence of the concentration $c_{ch}(\mathbf{r}, t)$ on time at the point $\mathbf{r}(x, y, z)$ with coordinates $(52, 31, 61)$. The final stoichiometric formula for the blue curve is Fe_2C with an intermediate Fe_4C concentration. The time units are in $\hat{t}$.

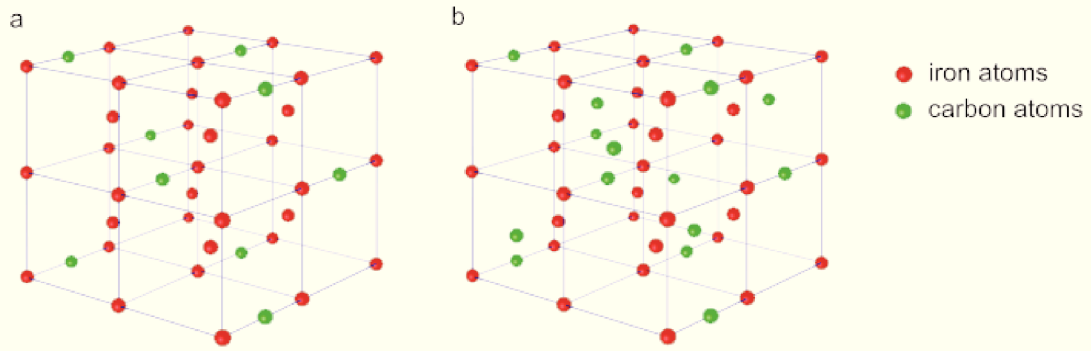

FIGURE 5.13: Schematic representation of atomic structure in (a) Fe_4C zones, (b) Fe_2C zones.

obtained from the analysis of diffusion spikes around the fundamental spots on the diffraction patterns.

5.2.1.2 The diffraction patterns analysis

To analyze more precisely the structure obtained in previously presented modeling the scattering intensities $I_C(\mathbf{q})$ using Eq. (5.38) were calculated. The diffraction patterns for the configuration presented in Fig. 5.9(d) are shown in Fig.5.14. In these figures we presented only two planes, (011) and (001), from 3D diffraction pattern. The fundamental spots 000, {110} and {200} correspond to the iron host lattice. Other scattering maxima correspond to the superstructure produced by carbon atoms.

In the previous subsection we identified two kinds of superstructures at the final step of simulation: Fe_4C and Fe_2C, Fig.5.13. The superstructures spots for the Fe_4C structure are $\{\frac{1}{2}\frac{1}{2}\frac{1}{2}\}$ and {100}. The Fe_2C superstructure is characterized by maxima at $\{\frac{1}{2}\frac{1}{2}\frac{1}{2}\}$, {110} and

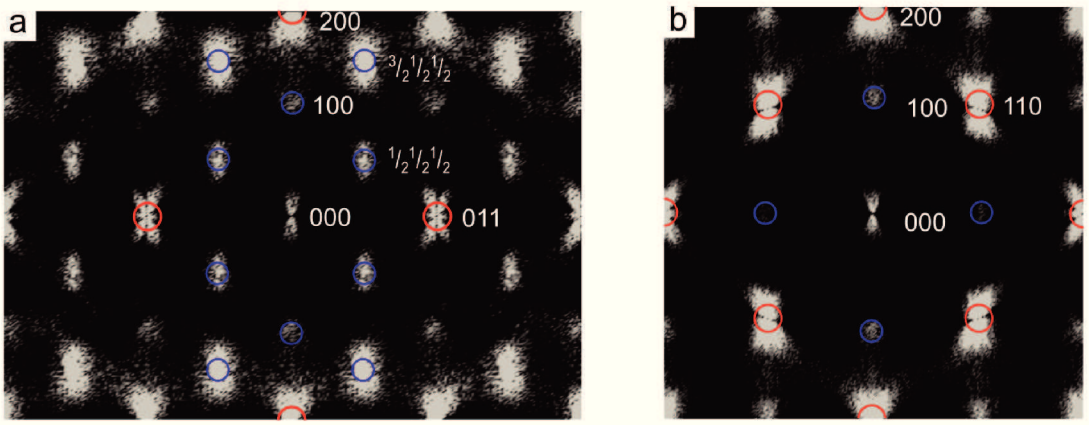

FIGURE 5.14: Diffraction pattern of the configuration presented in Fig.[5.9(d)] stage of simulation in (a) (011) and (b) (001) planes. The fundamental intensity maxima are denoted by red circles, the superstructure spots denoted by blue circles.

$\{\frac{3}{2}\frac{1}{2}\frac{1}{2}\}$ points of reciprocal space. The observed superstructure spots in Fig.5.14 are consistent with identified structures Fe_4C and Fe_2C.

The fundamental intensity maxima 000, {110} and {200} have a special form which is characterized by the diffusion spikes elongated to some special directions. Since carbon occupy only O_x sublattice in the iron matrix, the elongation of fundamental spots is along [100] direction in reciprocal space. The angle θ between diffusion spike and [100] (see Fig.5.15(a)) axis determines the direction of the orientation of carbon rich zones in the system.

Fig.5.15(a) shows the diffraction scattering around 000 spot in (001) plane. In this case θ is angle between the [100] direction and the direction of diffusion spike. This angle equals 23.4°. Then the corresponding direction in real space is along the vector $\mathbf{n}(2\ -0.87\ 0)$.

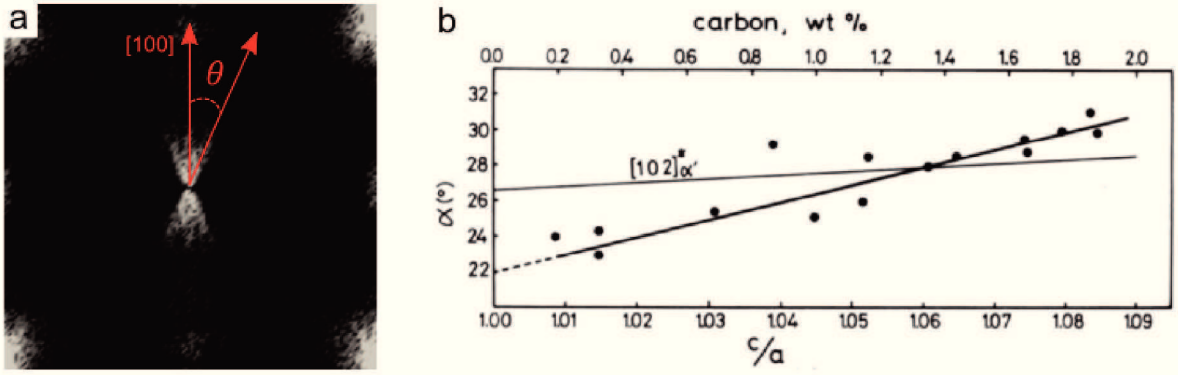

FIGURE 5.15: (a) The diffraction pattern of the 000 spot in (001) plane. (b) Dependence of the angle θ between the direction of the spike of diffraction spot and the direction of lattice tetragonality, [001], as function of the axial ratio $\frac{c}{a}$ [6]. Thin line corresponds the angle between $[102]_{\alpha'}$ and [001] directions.

As was shown by Khachaturyan [17] this special form of diffraction scattering around fundamental spots can be explained by the presence the spinodal decomposition in the system.

Following this approach the intensity of diffusion scattering maxima around each fundamental reciprocal lattice can be calculated using the next equality:

$$-F_i(3,\mathbf{k})G_{ij}(\mathbf{k})F_j^*(3,\mathbf{k}) + Q + 8W_3 + k_BT/\left(\bar{n}_C(1-\bar{n}_C)\right) = 0. \tag{5.52}$$

Where function $F_i(3,\mathbf{k})G_{ij}(\mathbf{k})F_j^*(3,\mathbf{k})$ describes the shape of the surface around fundamental reciprocal lattice points. The calculated diffusion scattering intensity for different axial ratio, c/a, is presented in Fig.5.16. It can be clearly seen that the form of this diffusion scattering is

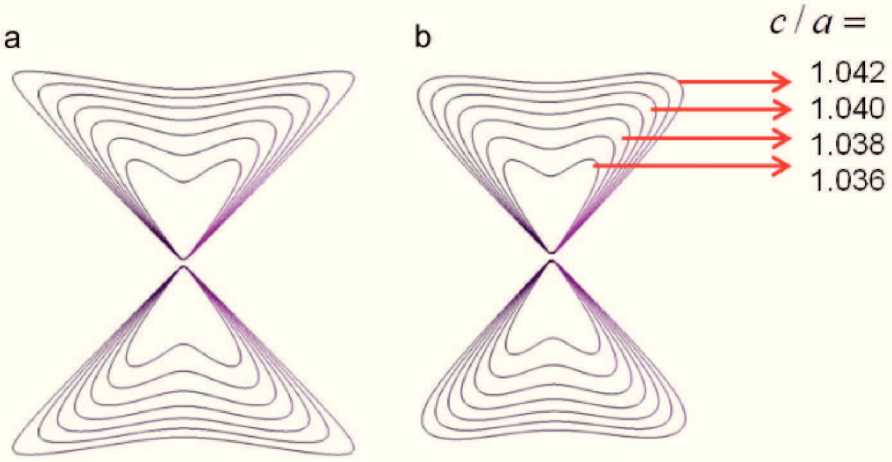

FIGURE 5.16: The plot of the intensity of diffusion scattering maxima near the reciprocal lattice site described by the surface (5.52) for a different axial ratio c/a in (a) (100) and (b) (110) planes of the bcc lattice.

in perfect agreement with a form of spots obtained in our calculations. Let us note that the amplitude of the spikes in this case is proportional to the tetragonality of the martensite. Then the diffraction scattering patterns can be used to determine the variation of tetragonality during spinodal decomposition.

5.2.2 Modeling with $t_1 = -0.27$

In Fe-Ni-C alloys, that form platelike martensite, the martensite lattice can have the orthorhombic distortion. In Taylor *et al.* [107] using [108] concluded that the twinned martensite can be regarded as a displacement of carbon atoms from O_z octahedral sublattice into O_x or O_y sublattices. Thus, the lattice parameters of orthorhombic martensite a, b and c can be expressed in the form [108]:

$$\begin{aligned} a &= a_0\left[1 + u_{11}(\bar{n}_2 + \bar{n}_3) + u_{33}\bar{n}_1\right], \\ b &= a_0\left[1 + u_{11}(\bar{n}_3 + \bar{n}_1) + u_{33}\bar{n}_2\right], \\ c &= a_0\left[1 + u_{11}(\bar{n}_1 + \bar{n}_2) + u_{33}\bar{n}_3\right]. \end{aligned} \tag{5.53}$$

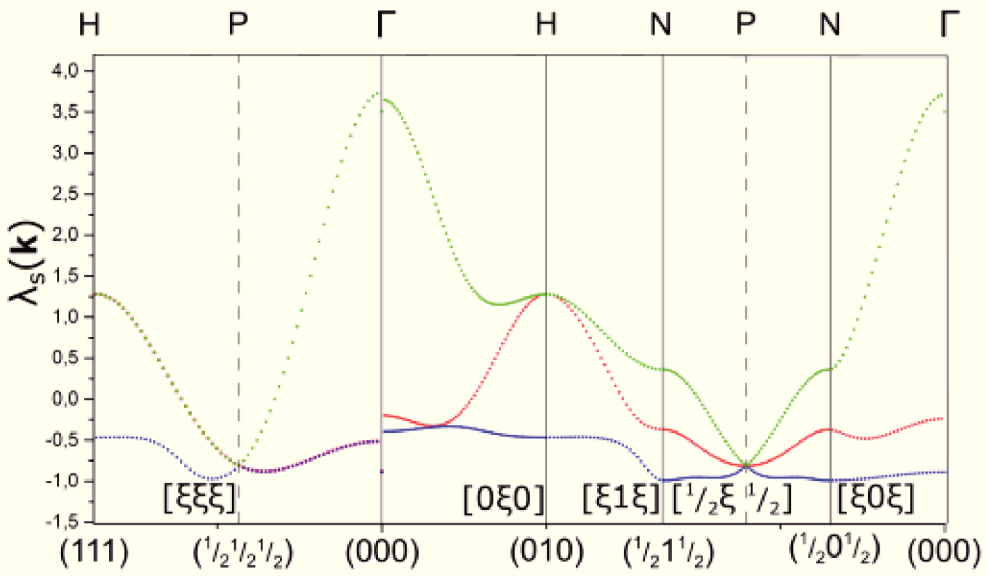

FIGURE 5.17: The eigenvalue spectrum of the total interaction matrix $\widetilde{w}_{pq}(\mathbf{k})$ of the Fe-C system with tetragonality $t_1 = -0.27$. Blue and red curves correspond to the eigenvalues $\lambda_1(\mathbf{k})$ and $\lambda_2(\mathbf{k})$, respectively, green curve corresponds to the $\lambda_3\mathbf{k}$). Eigenvalues are presented in dimensionless form in units $C_{44}a_0^3{u_{33}}^2$. The dispersion curves are built for the several directions in reciprocal space, the wave vector ξ is written in units $\frac{2\pi}{a_0}$.

Considering the case when only a single twinning variant appears in a martensitic crystal, only two octahedral sublattices in martensite are occupied by carbon atoms (for example, $\bar{n}_1 = 0$). Then the lattice parameters for the virgin Fe-18Ni-1C martensite are $a = 0.28314$ nm, $b = 0.28433$ nm and $c = 0.29913$ nm [109]. Using (5.53) with condition $\bar{n}_1 = 0$ and given parameters, a, b and c for Fe-18Ni-1C martensite, the concentration expansion coefficients were obtained

$$u_{11} = -0.275, \quad u_{33} = 1.016 \quad \rightarrow \quad t_1 = -0.27. \tag{5.54}$$

It is important to note that in the case of twinning there are two different interstitial domains within the martensite phase and each martensite domain is Zener-ordered.

The following analysis will be provided in the same way as for the previous case.

The dispersion curves for the case with $t_1 = -0.27$ with chemical interactions are shown in Figs.5.17. The distribution of carbon atoms between sublattices is determined by the minimum at $\mathbf{k} = 0$. In contrast to the case with tetragonality factor $t_1 = -0.1$, the system with $t_1 = -0.27$ will have an Zener ordering distribution even without chemical interactions (case when $\widetilde{w}_{pq}(\mathbf{k}) = \widetilde{w}_{pq}{}^{elas}(\mathbf{k})$), because $\lambda_2(0) < \lambda_1(0)$ ($\lambda_1(0) = -0.27$ and $\lambda_2(0) = \lambda_3(0) = -0.46$). The eigenvalue spectrum where the total interaction matrix was considered has the minima at $\mathbf{k}_1 = \frac{2\pi}{a_0}\left\{\frac{1}{2}\frac{1}{2}0\right\}$, $\lambda_2(\mathbf{k}_1) = -0.989$, and at $\mathbf{k}_2$ which is close to $\frac{2\pi}{a_0}\left\{\frac{1}{2}\frac{1}{2}\frac{1}{2}\right\}$, $\lambda_2(\mathbf{k}_2) = -0.97$ (the energy unit is $C_{44}a_0^3{u_{33}}^2 = 16.97$eV).

5.2.2.1 Simulation results in the direct space

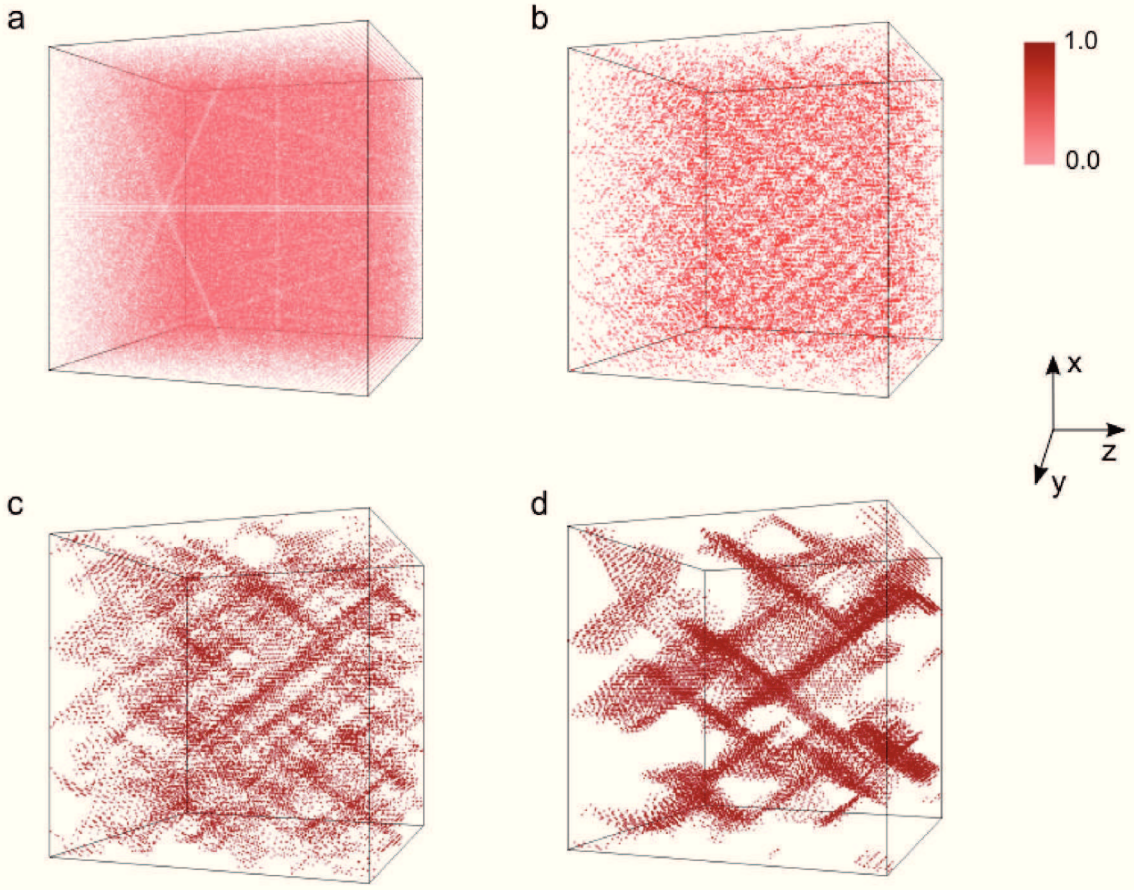

FIGURE 5.18: The results of simulations for the system with $t_1 = -0.27$ in 3D at times (a)$\hat{t} = 0$, (b)$\hat{t} = 1000$, (c)$\hat{t} = 17500$, (d)$\hat{t} = 150000$. The isosurfaces for the occupation probability $n_1(\mathbf{r}, t)$ are shown in red.

The result of simulations of the carbon redistribution in Fe-C system with the tetragonality factor $t_1 = -0.27$ in direct space at different time steps is presented on Fig. 5.18.

The time-evolution of the system is similar to the case with $t_1 = -0.1$ described in subsection (5.2.1.1). Starting from the same initial state, Fig. 5.18(a), the system undergo the spinodal decomposition and grows, Fig. 5.18(b-c). However, strong alinement to some preferential directions are observed from earlier stage of decomposition. In Fig. 5.18(c) the tweed structure can be observed. To minimize an interfacial energies between iron matrix and ordered phase the coalescence of neighbor carbon-rich particles occurs until the system reaches an equilibrium, Fig. 5.18(c-d). At the final step of simulation due to the Zener-ordering all carbon atoms occupy only O_x octahedral sublattice ($\bar{n}_1 = 0.024$ and $\bar{n}_2 = \bar{n}_3 = 0$).

The stoichiometric composition of the carbon-rich regions can be found from the density map representation. Fig. 5.19 shows that the concentration of carbon in carbon rich zones is $c_{ch}(\mathbf{r}, t) = 0.25$ with corresponding stoichiometric formula Fe_4C. Also, there are regions with

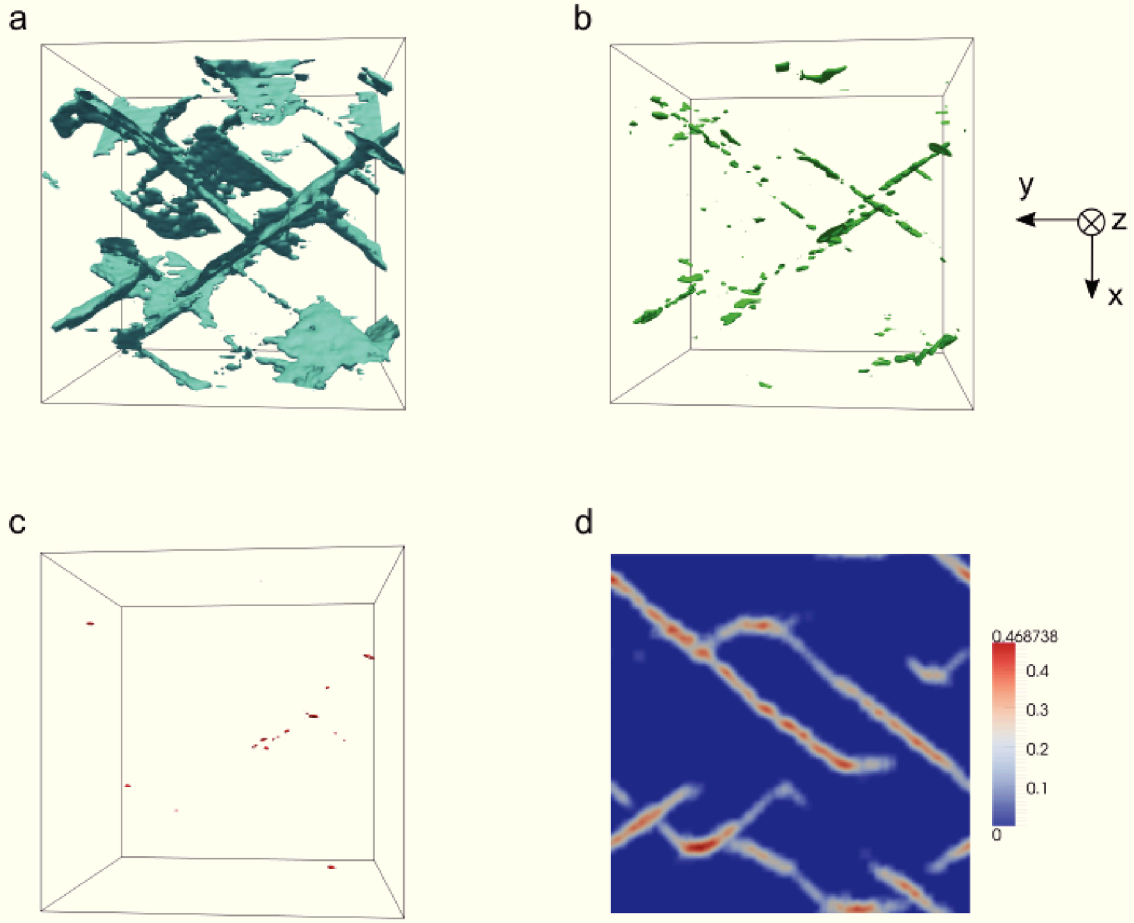

FIGURE 5.19: The density map representation of the carbon distribution for the last step of simulation with $t_1 = -0.27$. Isosurfaces were built for the average concentrations (a) $c_{ch}(\mathbf{r}) = 0.25$, (b) $c_{ch}(\mathbf{r}) = 0.4$, (c) $c_{ch}(\mathbf{r}) = 0.47$. (d) 2D slice of $c_{ch}(\mathbf{r})$ in (001) plane.

stoichiometry close to Fe_2C. In the Fe_4C zones carbon atoms have fcc structure with lattice parameter $2a_0$, see Fig. 5.13(a), in the Fe_2C zones carbon atoms have diamond structure with lattice parameter $2a_0$ as shown in Fig. 5.13(b).

The orientation of carbon-rich regions can be easily obtained from 2D slice of concentration $c_{ch}(\mathbf{r})$ in (001) plane: $\mathbf{n}(-2.45\ 3\ 0)$.

5.2.2.2 The diffraction patterns analysis

Fig.5.20 shows the calculated diffraction patterns in (011) and (001) planes for the final step of simulation. The scattering maxima at 000, {110} and {200} points of reciprocal space correspond to the iron host lattice. These spots are marked by red circles. The superstructure of carbon with stoichiometry Fe_4C is described by diffraction spots $\{\frac{1}{2}\frac{1}{2}\frac{1}{2}\}$ and {100}, and with stoichiometry Fe_2C by spots $\{\frac{1}{2}\frac{1}{2}\frac{1}{2}\}$, {110} and $\{\frac{3}{2}\frac{1}{2}\frac{1}{2}\}$.

The diffraction scattering around 000 spot in (001) plane is shown in Fig.5.21. The angle between [100] direction and the direction of diffusion spike, θ, is 37.7°. It gives the direction

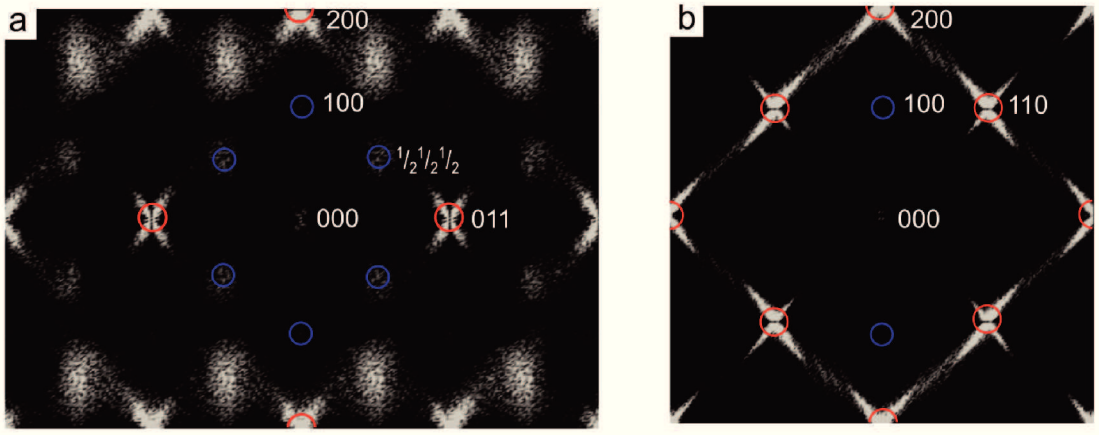

FIGURE 5.20: Diffraction patterns of the configuration presented in (a) (011) and (b) (001) planes. The fundamental intensity maxima are denoted by red circles, the superstructure spots denoted by blue circles.

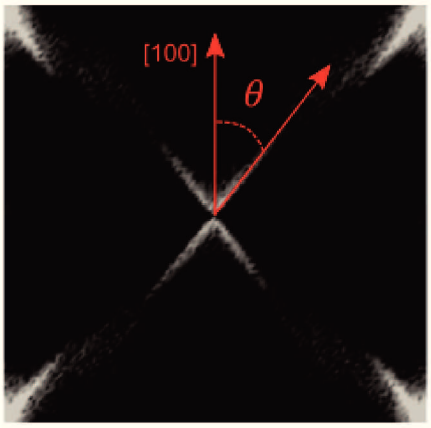

FIGURE 5.21: The diffraction pattern of the 000 spot in (001) plane. The angle θ between the direction of the spike of diffraction spot and the direction of lattice tetragonality, [001], is shown.

of the carbon-rich zones orientation along $\mathbf{n}(-2.32\ 3\ 0)$ vector. The special form of the diffusion scattering on the (001) plane of the diffraction pattern can be related to the directional displacement of carbon atoms in carbon rich zones.

5.2.3 Modeling of carbon redistribution in martensite without Zener-ordering

Previously, we suggested that the elastic interaction induced by carbon atoms in martensite is infinitely long. Such interaction is responsible to Zener-ordering in martensite. However it is true only in the case of monocrystal. In general case, where the martensite is a polycrystal the grain boundaries or other defects can cancel or modify this interaction. That is why we decided to consider the carbon kinetics without Zener-ordering. As was shown previously in our model Zener-ordering is related to the minima of eigenvalue at $\mathbf{k}_0 = 0$. To remove this ordering we

removed the point $\mathbf{k}_0 = 0$ in the FT in interaction energy. Further, we will present modeling without Zener-ordering for two cases with $t_1 = -0.1$ and $t_1 = -0.275$.

5.2.3.1 Modeling with $t_1 = -0.1$

Fig. 5.22 shows the result of simulation for the system with $t_1 = -0.1$ and without Zener-ordering in the direct space at different time steps. For convenience, carbon atoms which

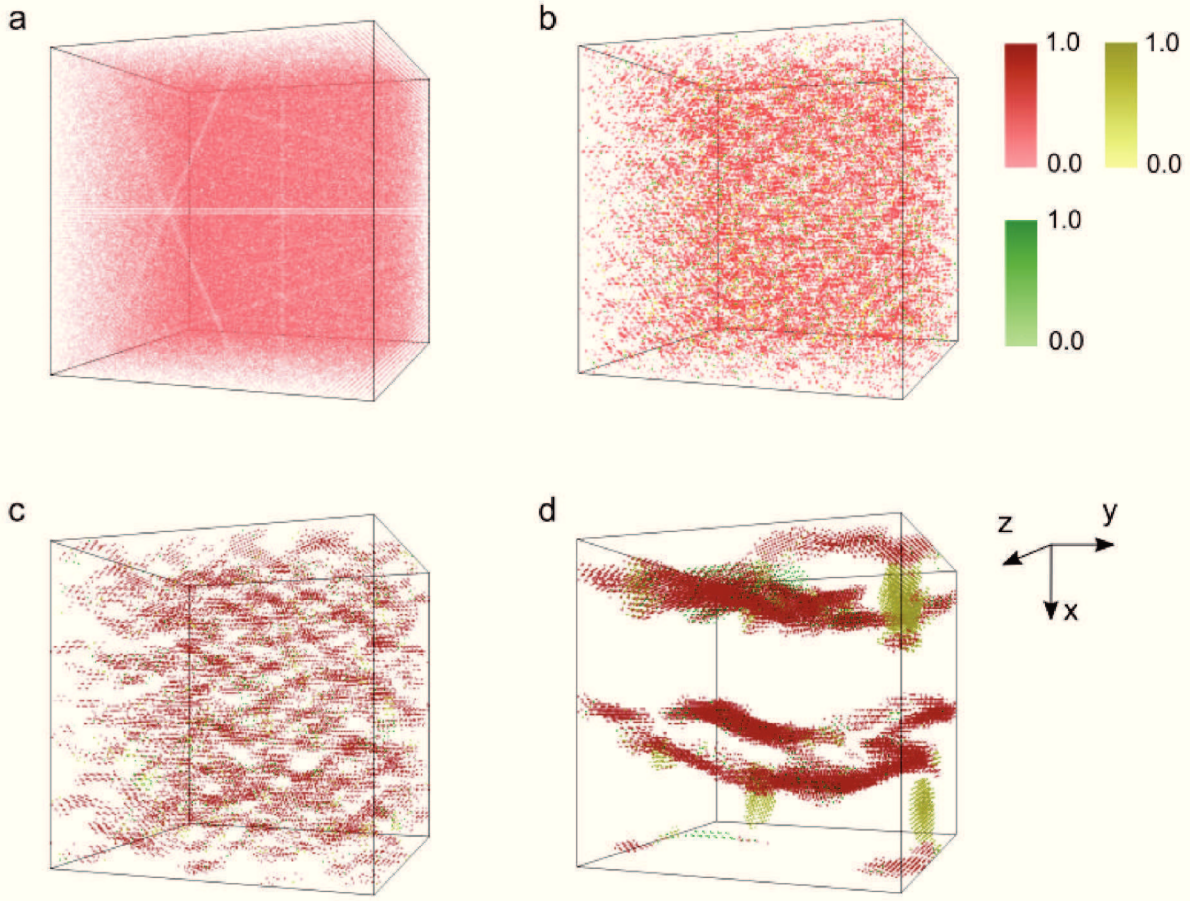

FIGURE 5.22: The results of simulations for FeC ($t_1 = -0.1$) system without Zener-ordering in 3D at times (a)$\hat{t} = 0$, (b)$\hat{t} = 1000$, (c)$\hat{t} = 10000$, (d)$\hat{t} = 150000$. The isosurfaces for the occupation probabilities $n_1(\mathbf{r}, t)$, $n_2(\mathbf{r}, t)$ and $n_3(\mathbf{r}, t)$ are shown in red, yellow and green, respectively.

correspond to the different octahedral sublattices are marked in different colors. Red color corresponds to the $n_1(\mathbf{r}, t)$, yellow to $n_2(\mathbf{r}, t)$ and green to $n_3(\mathbf{r}, t)$. The time-evolution of the system is similar to the previous cases. At the first stage the carbon-rich clusters appear and grow, Fig.5.22(b-c). Then the coarsening of carbon-rich zones occurs, Fig.5.22(c-d). The difference is that the carbon atoms now are distributed on the three octahedral sublattices. The carbon rich zones formed by carbon atoms from different sublattices can be identified on the final state of simulation, Fig.5.22(d). The coarsening of clusters occurs for the different

sublattices separately. The average concentrations at the final step of simulations are $\bar{n}_1 = 0.01908$, $\bar{n}_2 = 0.00344$ and $\bar{n}_3 = 0.00148$. We can conclude that in spite of all three sublattices are occupied by carbon atoms, however the concentration in the first sublattice is thirteen times larger then in the third one and five times larger then in the second one.

The isoconcentration surfaces are shown in Fig.5.23. The concentration of carbon in carbon-rich zones corresponds to the stoichiometric formula Fe_4C. The fraction of zones with higher

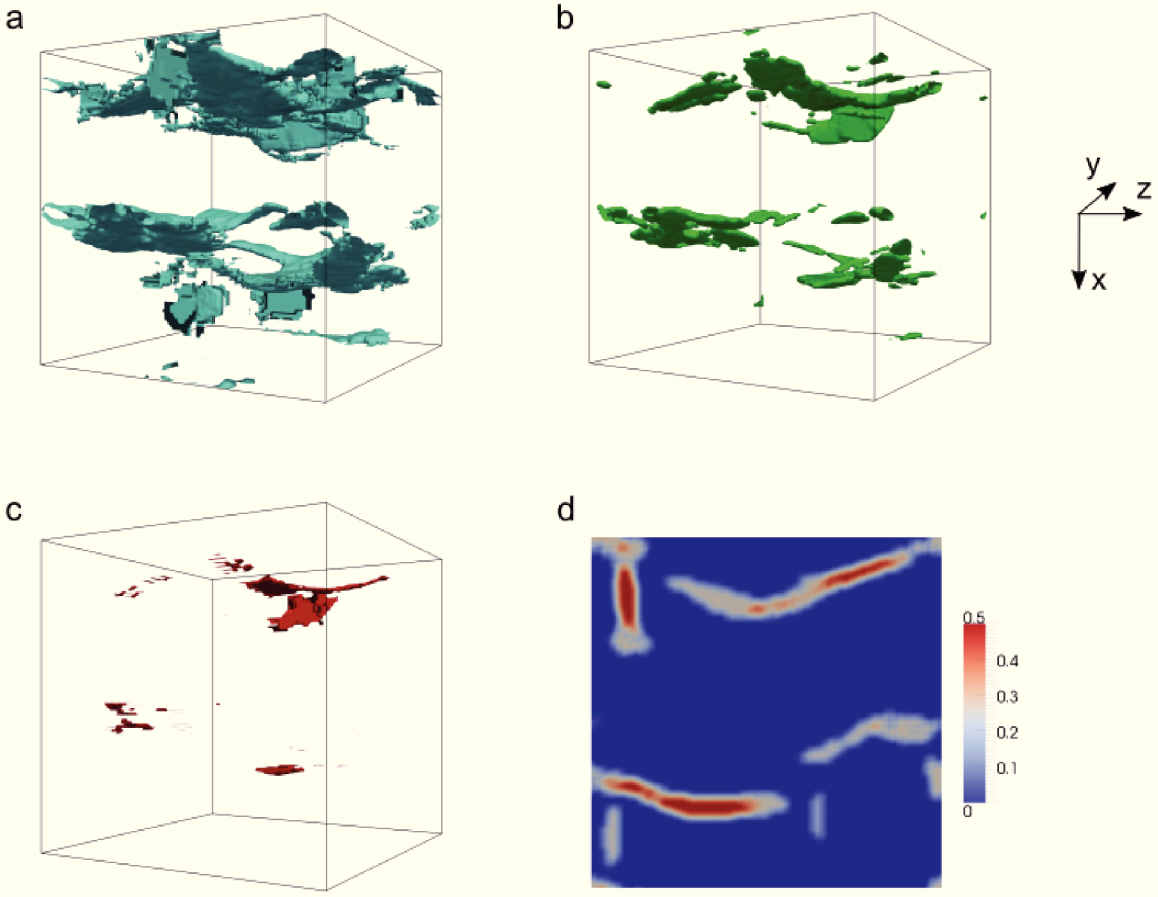

FIGURE 5.23: The density map representation of the carbon distribution for the last step of simulation. Isosurfaces were built for the average concentrations (a) $c_{ch}(\mathbf{r}) = 0.25$, (b) $c_{ch}(\mathbf{r}) = 0.4$, (c) $c_{ch}(\mathbf{r}) = 0.5$. (d) 2D slice of $c_{ch}(\mathbf{r})$ in (010) plane.

concentration of carbon, Fe_2C, is much lower than in modeling with Zener-ordering. The internal structure of Fe_4C zones corresponds to the fcc lattice with lattice parameter $2a_0$, Fig.5.13(a). In Fe_2C zones carbon atoms have diamond structure with lattice parameter $2a_0$, Fig.5.13(b).

Clusters consisting of atoms from O_x sublattice are elongated along vector $\mathbf{n}(2\ -0.8\ 0)$, O_y clusters along $\mathbf{n}(0\ 0\ 1)$ vector and O_z clusters along $\mathbf{n}(0\ 1\ 0)$ vector, Fig.5.23(d).

(011) and (001) planes of the diffraction patterns calculated for the final step of simulation are shown in Fig.5.24. The scattering maxima at 000, {110} and {200} points of reciprocal space correspond to the iron bcc lattice. Spots $\{\frac{1}{2}\frac{1}{2}\frac{1}{2}\}$ and {100} correspond to the superstructure

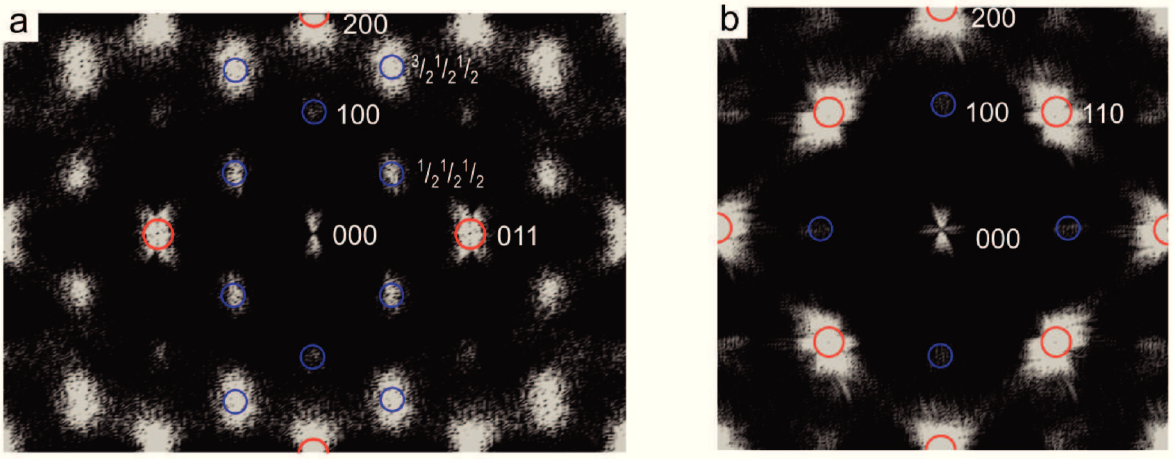

FIGURE 5.24: Diffraction pattern of the final stage of simulation in (a) (011) and (b) (001) planes. The fundamental intensity maxima are denoted by red circles, the superstructure reflexes denoted by blue circles.

with stoichiometry Fe_4C, the superstructure of Fe_2C regions is described by $\{\frac{1}{2}\frac{1}{2}\frac{1}{2}\}$, $\{110\}$ and $\{\frac{3}{2}\frac{1}{2}\frac{1}{2}\}$ diffraction spots.

More accurate orientation of carbon-rich clusters can be found from the angle θ obtained from the scattering maxima around 000 point of reciprocal space, Fig.5.25. For O_x clusters

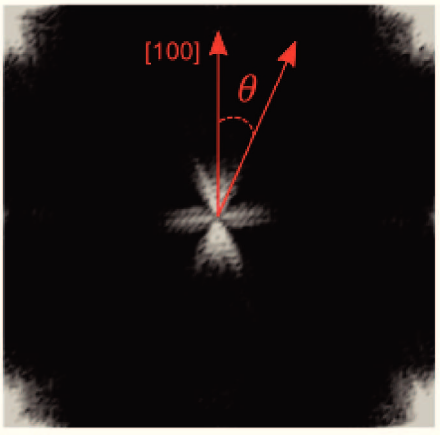

FIGURE 5.25: The diffraction pattern of the 000 spot in (001) plane. The angle θ between the direction of the spike of diffraction spot and the direction of lattice tetragonality, [001], is shown.

angle θ is equal 23.6°, which corresponds to the direction along vector $\mathbf{n}(2 \ -0.87 \ 0)$. The diffusion spikes corresponding to the O_y clusters laying approximately in (010) plane, $\theta \approx 0°$.

It should be noted that the volume fraction of O_y and O_z clusters is low comparing to O_x clusters. Thereby the result of modeling without Zener-ordering is very similar to the modeling with Zener-ordering.

5.2.3.2 Modeling with $t_1 = -0.27$

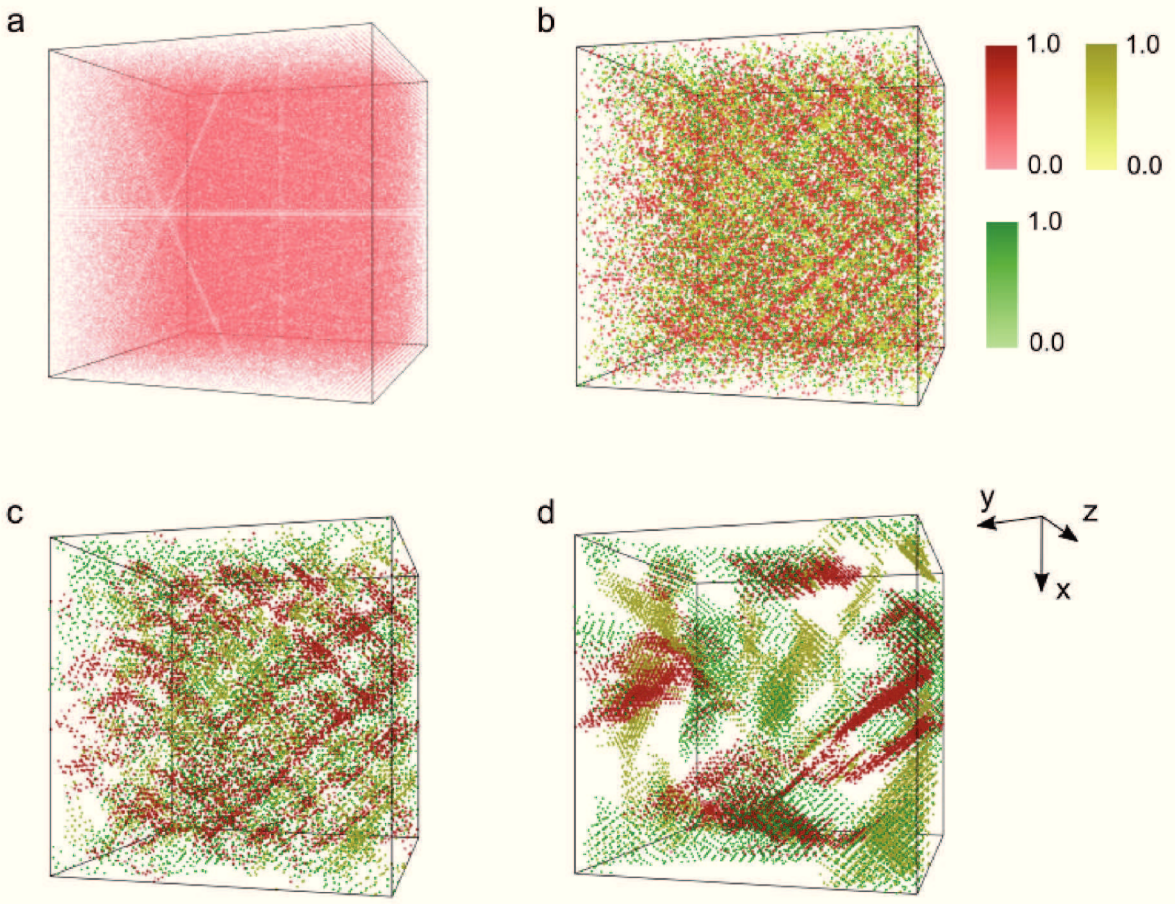

FIGURE 5.26: The results of simulations for FeC ($t_1 = -0.27$) system without Zener-ordering in 3D at times (a)$\hat{t} = 0$, (b)$\hat{t} = 1000$, (c)$\hat{t} = 10000$, (d)$\hat{t} = 530000$. The isosurfaces for the occupation probabilities $n_1(\mathbf{r}, t)$, $n_2(\mathbf{r}, t)$ and $n_3(\mathbf{r}, t)$ are shown in red, yellow and green, respectively.

The redistribution of carbon atoms during aging with $t_1 = -0.27$ is shown in Fig.5.26. At final step of simulation the average concentrations of carbon atoms within O_x, O_y and O_z sublattices are 0.0084, 0.0086 and 0.007. In this case the concentration of carbon in all three sublattices is approximately the same. The time-evolution of the system is similar to the previous cases. The difference is that the some clusters of different sublattices are mixed and form new superstructure. Then the density map representation will be used to determine the details of carbon-rich zones. The density map is shown in Fig. 5.27.

In this case, the concentration, $c_{ch}(\mathbf{r}, t)$, in carbon rich zones is in vicinity of 0.125 with the stoichiometric concentration Fe_8C. The regions with stoichiometry Fe_4C are also presented in the center of carbon rich zones. We can distinguish two different types of internal structure of carbon rich zones. One is formed by carbon atoms belonging to the same octahedral sublattice,

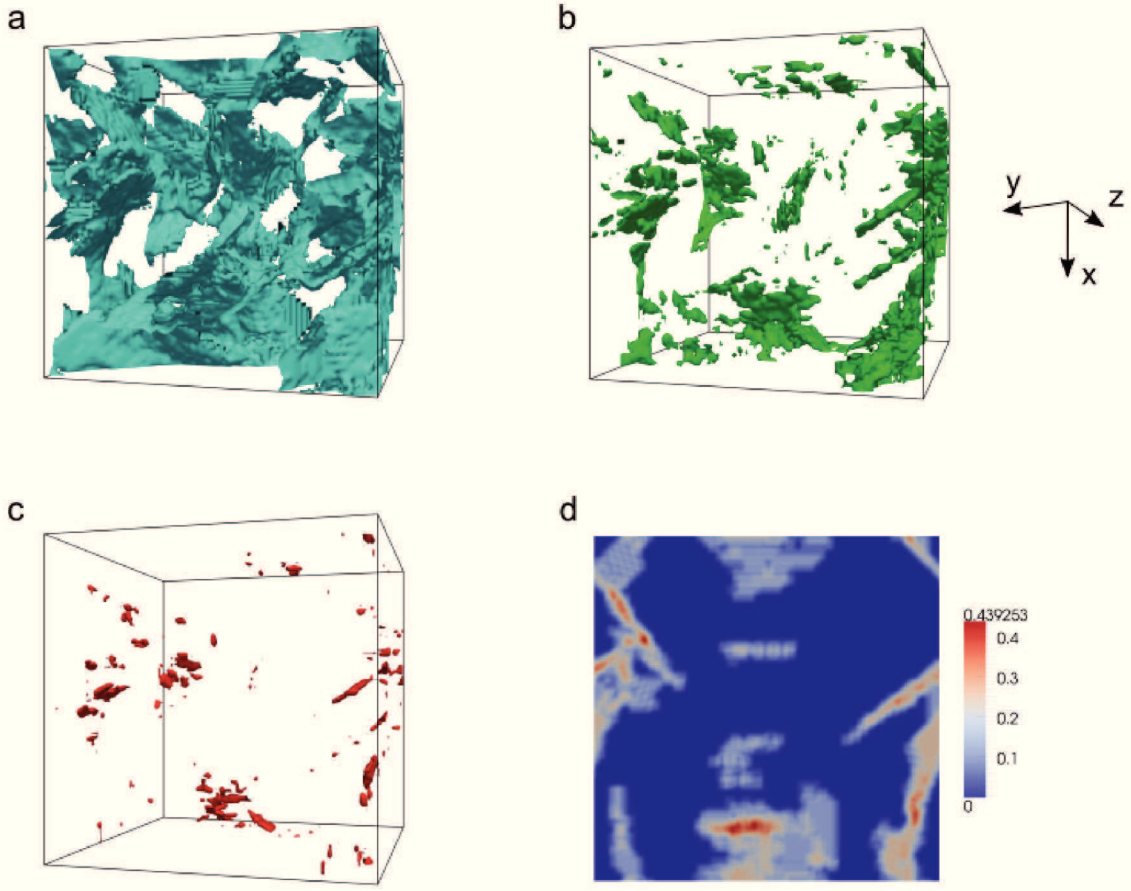

FIGURE 5.27: The density map representation of the carbon distribution for the final step of simulation. Isoconcentration surfaces were built for the average concentrations (a) $c_{ch}(\mathbf{r}) = 0.125$, (b) $c_{ch}(\mathbf{r}) = 0.35$, (c) $c_{ch}(\mathbf{r}) = 0.25$. (d) 2D slice of $c_{ch}(\mathbf{r})$ in (010) plane.

and another formed by atoms from two different sublattices. However, the ordered phase mostly consists of the first type of structure.

In Fig.5.28(a) the dependence of concentration of carbon atoms situated in the same sublattices on time in carbon rich zone is presented. Its crystal structure is shown in Fig.5.28(b). The corresponding superstructure for this zone is the bcc structure with lattice parameter $2a_0$, Fig.5.28(b). Such a structure is called α'' phase and corresponds to the stoichiometric formula $Fe_{16}C_2$.

Identification the superstructure formed by carbon atoms situated in two different sublattices is more complicated, because the volume fraction of such zones is small. These zones can be presented by alternating planes of different sublattices elongated in one of the direction $\{110\}$. One of the possible atomic structure of such zones formed by atoms of O_x and O_y sublattices is shown in Fig.5.28(c). It corresponds to the stoichiometric concentration $Fe_{80}C_9$.

The diffraction patterns of the final step of simulation on Fig.5.29 clearly show the presence of the α'' phase. The superstructure spots, marked by blue circles, $\{\frac{1}{2}\frac{1}{2}0\}$ and $\{100\}$, correspond to the bcc structure with lattice parameter $2a_0$. Since the volume fraction of zones, which consist

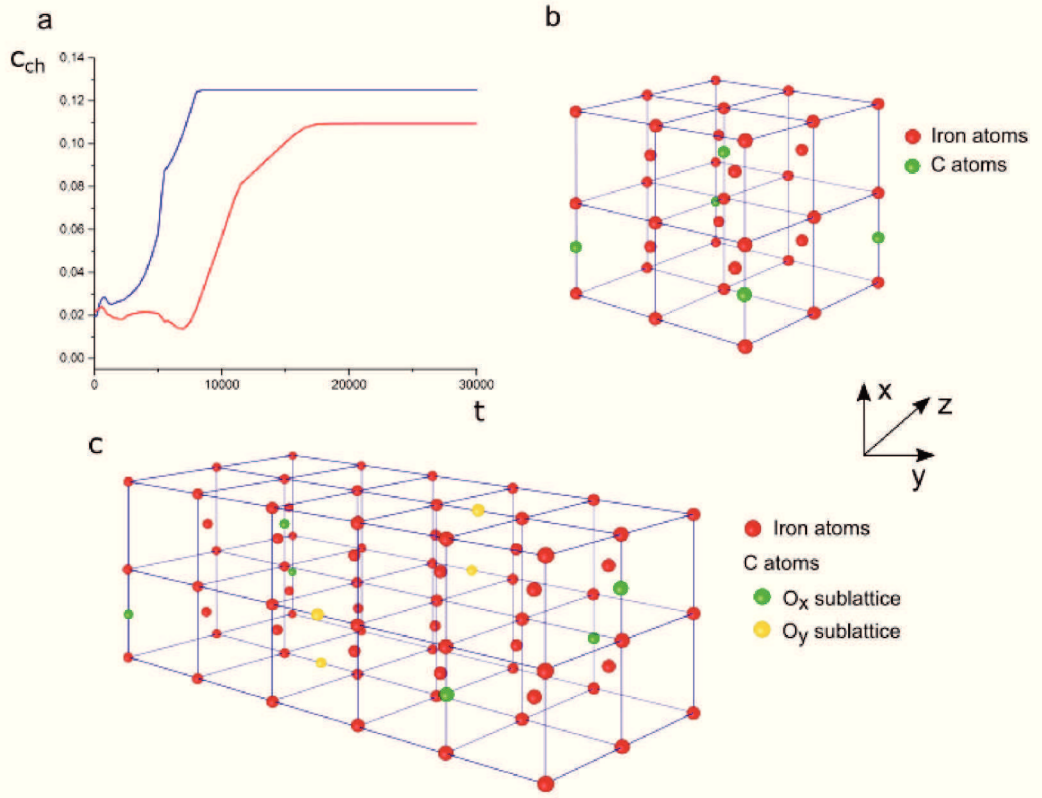

FIGURE 5.28: (a) Dependence of the concentration $c_{ch}(\mathbf{r}, t)$ on time at the carbon rich zones where the carbon atoms are distributed in one (blue) and in two (red) octahedral sublattices. Schematic representation of atomic structure in (b) Fe_8C zone, (c) $Fe_{80}C_9$ zone.

of different sublattices, is too small it is not possible to detect this phase from diffraction pattern.

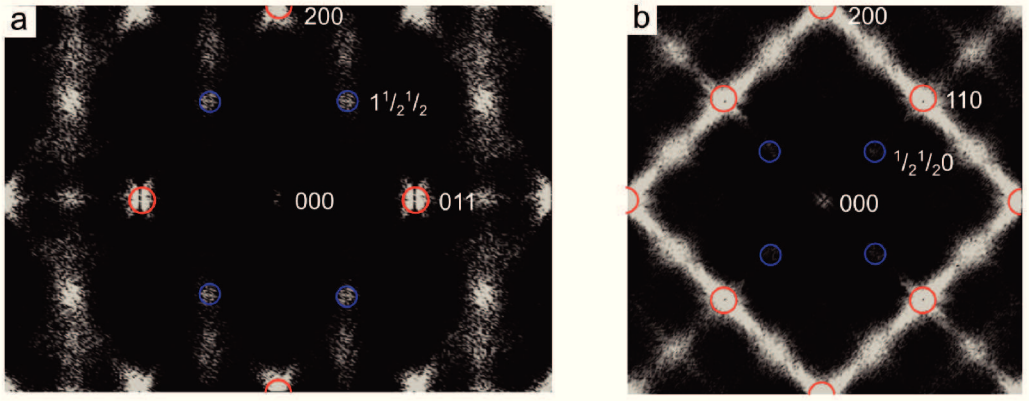

FIGURE 5.29: Diffraction pattern of the final stage of simulation in (a) (011) and (b) (001) planes. The fundamental intensity maxima are denoted by red circles, the superstructure reflexes denoted by blue circles.

5.2.4 Discussion

Now we will compare the obtained results with experimental data.

First, we consider the thermodynamics of carbon ordering (within the meaning of Zener-ordering). In the approach proposed by Khachatuyan [17] and used in present work it is possible to define the composition-dependent critical temperature for carbon ordering. As it was shown above, the ordered state is stable when $\lambda_2(\mathbf{k}=0) < \lambda_1(\mathbf{k}=0)$. Then the atomic density function probability is described by Eq.(5.48). Within the mean-field approximation the free energy of this ordering structure can be expressed as

$$\begin{aligned} F(\bar{n}_C,\eta) = U - TS = \frac{1}{2}3N\lambda_1(0)\left(\frac{\bar{n}_C}{3}\right)^2 + 3N\lambda_2(0)\left(\frac{\bar{n}_C}{3}\right)^2\eta^2 \\ + k_BTN\left\{2\frac{\bar{n}_C}{3}(1-\eta)\ln\left[\frac{\bar{n}_C}{3}(1-\eta)\right] + \frac{\bar{n}_C}{3}(1+2\eta)\ln\left[\frac{\bar{n}_C}{3}(1+2\eta)\right]\right. \\ + 2\left[1-\frac{\bar{n}_C}{3}(1-\eta)\right]\ln\left[1-\frac{\bar{n}_C}{3}(1-\eta)\right] \\ \left. + \left[1-\frac{\bar{n}_C}{3}(1+2\eta)\right]\ln\left[1-\frac{\bar{n}_C}{3}(1+2\eta)\right]\right\}. \end{aligned} \tag{5.55}$$

Here the first two terms describe the internal energy U and the other terms correspond to the entropy S in mean-field approximation. η is the long-range order parameter, N is a number of all atoms of the system. The temperature dependence of the long-range order parameter η can be found by minimization of free energy Eq.(5.55):

$$\frac{k_BT}{\lambda_2(0)\bar{n}_C} = -\frac{\eta}{\ln\left[(1+2\eta)/(1-\eta)\right]}. \tag{5.56}$$

Eq.(5.56) was obtained for small concentrations of carbon, $\bar{n}_C \ll 1$.

The temperature of order-disorder transition, T_0, can be found from the equilibrium condition

$$F(\bar{n}_C,\eta_0) = F(\bar{n}_C,0). \tag{5.57}$$

Here η_0 is the equilibrium long-range-order parameter, the case when $\eta = 0$ corresponds to the disordered state.

The solution of transcendental equations (5.56) and (5.57) gives the expression for the critical temperature T_c

$$T_c = -1.08\,\frac{\lambda_2(0)\bar{n}_C}{3k_B}. \tag{5.58}$$

The phase diagram of Fe-C with ordered and disordered phases is presented in Fig.5.30. The temperatures of order-disorder transformation obtained for parameters used in our model are presented by blue (for $t_1 = -0.1$) and red (for $t_1 = -0.27$) lines. For the comparison, it is also given critical temperatures obtained within Khachaturyan [17] and Zener [16] models.

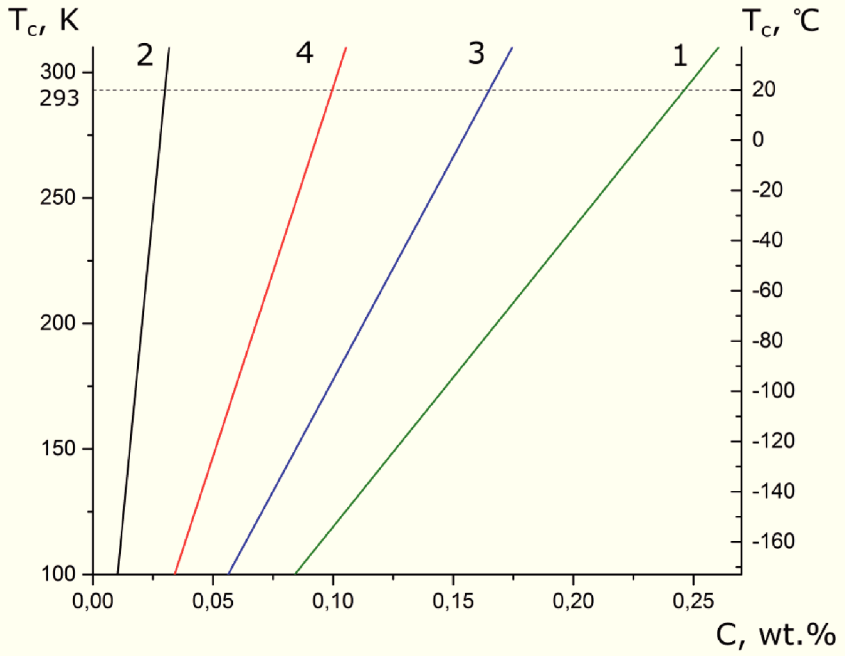

FIGURE 5.30: Critical temperature for Zener-ordering as a function of the carbon content in wt.% according to models proposed by (1) Zener [16], in green, (2) Khachaturyan [17], in black, and according to model used in present work with (3) $t_1 = -0.1$, is shown in blue, and (4) $t_1 = -0.27$, is shown in red.

Temperature of order-disorder transformation for Zener model is

$$T_c = 1190\, C. \tag{5.59}$$

Here C is the carbon concentration in wt.%.

Eq.(5.58) also gives the critical concentration of order-disorder transition at a given temperature. At room temperature the critical concentration for the Fe-C solid solution obtained by Zener [16] is 0.25 wt.%. The critical carbon content according to model proposed by Khachaturyan [17] is much smaller: 0.03 wt.%. At room temperature ($T_c = 293$ K) our model gives the critical concentrations equal to 0.1 wt.% and 0.17 wt.% for Fe-Ni-C system with $t_1 = -0.27$ and for Fe-C system with $t_1 = -0.1$, respectively. The last result is in good agreement with experimental study [42] where the critical concentration of carbon in Fe-C martensite was found 0.18 wt.% at room temperature.

For the further analysis all data obtained in our simulations related to the morphology and internal structure of carbon-rich zones are summarized in Table 5.3.

The performed simulations show that the used model describes well the orientation of carbon-rich zones. It was found experimentaly that in Fe-C alloys carbon-rich regions are aligned along to [102] direction [6]. This is consistent with the simulation results for the system obtained with $t_1 = -0.1$. As was shown in Fig.5.15(b) the experimentally observed angle θ, which determine

TABLE 5.3: Modeling results for systems with tetragonality factors $t_1 = -0.1$ and $t_1 = -0.27$ with and without Zener-ordering. Vector $\mathbf{n}$ characterizes the direction of carbon-rich zones elongation. Wave vectors $\mathbf{k}_i$ describe the superstructure formed by carbon atoms. Average concentrations $\bar{n}_c(p)$ represents the occupancy of octahedral sublattices.

t_1	$\mathbf{n}$	Zener-ordering	$\mathbf{k}_i$	$\bar{n}_c(p)$
-0.1	$\sim [2\ \bar{1}\ 0]$	yes	$\{\frac{1}{2}\frac{1}{2}\frac{1}{2}\}$, $\{100\}$	$\bar{n}_1 = 2.4\%$ $\bar{n}_2 = 0.0\%$ $\bar{n}_3 = 0.0\%$
-0.1	$\sim [2\ \bar{1}\ 0]$	no	$\{\frac{1}{2}\frac{1}{2}\frac{1}{2}\}$, $\{100\}$	$\bar{n}_1 = 1.91\%$ $\bar{n}_2 = 0.34\%$ $\bar{n}_3 = 0.15\%$
-0.27	$\sim [\bar{2}\ 3\ 0]$	yes	$\{\frac{1}{2}\frac{1}{2}\frac{1}{2}\}$, $\{100\}$	$\bar{n}_1 = 2.4\%$ $\bar{n}_2 = 0.0\%$ $\bar{n}_3 = 0.0\%$
-0.27	–	no	$\{\frac{1}{2}\frac{1}{2}0\}$, $\{100\}$	$\bar{n}_1 = 0.84\%$ $\bar{n}_2 = 0.86\%$ $\bar{n}_3 = 0.70\%$

the direction of spikes, is slightly deviated from the angle between the [100] axis and $[201]_{\alpha'}$ direction. In our simulation with the average carbon concentration $\bar{n}_C = 0.51$ wt.% the angle θ is equal 23.4° which is very close to the experimentally observed angle of $\sim 24°$ obtained in [6] in the Fe-C system with the same average concentration of carbon. For the system with higher tetragonality $t_1 = -0.27$, which describes the Fe-Ni-C system, there is also good concordance with experimental data of diffuse spikes elongation close to [023] direction [7].

In spite of good description of a morphology of carbon in carbon-rich zones, the model does not give the expected concentration of carbon in carbon rich zones. The observed concentration at room temperature in these zones during earlier stages of aging is lower then that obtained in our simulation. In the most of cases in our simulations the carbon rich zones reach the value 20 at.% of carbon. It was shown experimentally in Fe-Ni-C alloys with low carbon content [45–47] at the earlier stages of aging at room temperature that carbon concentration does not exceed the value of 11 at.%. Such carbon content (11 at.%) has been obtained with the tetragonality factor $t_1 = -0.27$ without Zener-ordering.

Also, it is very important to note that the α'' phase, which is obtained in the case of the system with $t_1 = -0.27$ without Zener-ordering, does not observed in experimental studies. It should be noted that in experimental data the long-period ordered metastable phases has been proposed [9] to explain the experimentally observed diffraction patterns. Some of them based on the fcc lattice. To model these long-periodic structures the ADF method should be improved.

5.3 Conclusions

In this chapter the ADF theory on constrained Ising lattice to describe carbon diffusion in Fe-C alloys has been used. In considered model the carbon-carbon interatomic interaction was

divided in two parts: elastic and chemical part. The elastic part of interaction potential was calculated using the microscopic elasticity theory developed by Kurdjumov and Khachaturyan. The chemical pairwise interaction energies were fitted on the *ab initio* calculations.

The numerical resolution of the kinetic microscopic equation gave a possibility to reproduce the kinetics of the redistribution of carbon atoms on the three octahedral sublattices in bcc Fe-C and Fe-Ni-C alloys.

It was shown that at the beginning the carbon kinetics is governed by the spinodal decomposition and small carbon rich zones appear. During growth these zones elongated to some special crystallographic directions to minimize the free energy of system. Simulation results are in good agreement with experimental data and reproduce quite well the direction of the alignment of these zones. These directions for the Fe-C and Fe-Ni-C systems are $[2\bar{1}0]$ and $[\bar{2}31]$, respectively. To understand the influence of Zener-ordering on carbon rich zones two kinds of modeling has been done, with and without of point $\mathbf{k} = 0$ of the FT in the interaction energy. The simulations with Zener-ordering tetragonality gives Fe_4C and Fe_2C stoichiometric compositions, which are too high in comparison with experimentally observed concentrations in the carbon-rich zones. Modeling without Zener-ordering with $t_1 = -0.27$ gives the concentration in carbon-rich zones close to 11at.% observed in experience in the carbon-rich zones in the Fe-Ni-C alloys during aging at room temperature. The simulation and experimental results show that the carbon-rich phase with such concentration is quite stable during kinetics at low temperature.

Conclusions and future prospects

The aim of this work was to develop and to apply the atomistic model to describe the growth of martensite in austenite phase and low temperature diffusion kinetics of carbon atoms in martensite phase.

To achieve this goal the new atomistic method, Atomic Fraton Theory, has been developed. The proposed theory rests on two novel conceptual premises: (a) the introduction of interacting pseudoparticles that we call fratons that described two configurational states of each point of continuum space. One of them is an event in which the point is inside the atomic sphere of any atom and the other is an event in which the point is outside of atomic sphere; the fratons are considered as a non-ideal gas whose "condensation" describes a diffusional self-assembling of atomic system, and (b) a concept of a structural cluster function describing the directions, length and strength of interatomic bonds. The latter allows us to formulate a new and simple model Hamiltonian that is proportional to a bilinear expansion in these cluster functions. This model Hamiltonian provides the formation of a predetermined atomic structure and has a sufficient flexibility to describe the desired mechanic and thermodynamic properties of this structure. It should be noted that the proposed cluster formulation of the model Hamiltonian has its own more general intrinsic value: in principle, it can be used not only in our theory but in other methods as well.

The modeling based on the proposed theory is at atomic resolution, and addresses the time scale commensurate with a typical diffusion time, which may range from a fraction of a second to years. To demonstrate a potentiality and versatility of our approach, we tested its application to a self-assembling of disordered systems to three groups of systems of increasing topological complexity, viz., single component crystals (fcc and diamond structures), two component crystals (zinc-blend structure), and polymers (self-assembly of the randomly distributed monomers into single-strand and double-stranded helixes, which may mimics the DNA structure formation from nucleotides).

To describe the martensite transformation from austenite phase the AFT theory was used. Since this transformation is undergo by the displacements of atoms, a given method was a natural choice to model this kind of transition in order to understand at atomic scale how martensite transformation proceeds. It was shown that a martensite nucleus cannot growth

as monovariant particle in austenite matrix and during its growth is transformed to a multivariant aggregate. This multivariant structure consists from two twin related KS variants. Using our simulation results in direct and reciprocal spaces we identified the orientation relations between two martensite variants and calculated the angle between them. In particular, the pole figures have been used to identify the nature of coexisting variants and the calculated diffraction pattern allowed to determine the angle between these two variants. It was fond that the misorientation angle between these two variants is 70.1°. Our simulation results are in good agreements with experience. AFT modelling has also allowed to establish the mechanism of formation of second KS variants and to reproduce the periodic dislocation structure at the interface austenite/martensite. It was shown that twin formed by the twinning dislocations gliding on the successive $\{2\bar{1}1\}$ planes.

The Atomic Density Function (ADF) approach on the constrained Ising lattice, that is a particular case of the AFT theory, was applied to model the carbon diffusion in martensite phase. The input parameters of the model for the chemical interaction between carbon atoms were derived from *ab initio* simulation. The elastic interaction induced of interstitial carbon atoms was calculated using Kanzaki forces. Two systems with the tetragonality factors $t_1 = -0.1$ and $t_1 = -0.27$ was studied. First one can be associated with Fe-C and second one with Fe-Ni-C compound. To simulate the diffusion of carbon atoms in these two compounds during low temperature aging the microscopic diffusion equation for a three-component system has been solved. In this modelling the iron, carbon and carbon vacancies were considered. It was shown that during first stage of aging the carbon atoms undergo a spinodal decomposition on the octahedral subsystem in the bcc lattice and form the carbon-rich zones. These zones growth and carbon-rich domains becomes ordered with stoichiometric composition Fe_4C or Fe_2C. The simulated "tweed-like" morphology of carbon-rich zones is in a good agreement with experience. However, the concentration inside of these domain is higher than the concentrations measured in experience. Concentration in the core of areas rich in carbon reported in literature and obtained by 3D atom probe analyses is between 10 and 16 at.% C. To explain this disagreement we proposed to consider the case where kinetics of carbon atoms is governed by the thermodynamic driving force where Zener ordering was excluded. It corresponds to the situation where the point k=0 in the Fourier transform of interatomic interaction is excluded from consideration. This particular point is responsible to appearance of Zener-ordering. This idea was put forward from the fact that a long range elastic interaction, which is the origin of Zener ordering, can be cancelled if studied system contains grain boundaries or other structural defects. Using this hypothesis we show that during spinodal decomposition in Fe-Ni-C system with $t_1 = -0.27$ the carbon-rich zones with the concentration 11 at.% are formed. Then these domains are growing but the concentration did not differ during aging kinetics, indicating that this phase is metastable. The crystal structure of the carbon-rich zone in this case corresponds to the α'' ordered phase. However, as these simulations were done without Zener ordering, the carbon

atoms are distributed on the three octahedral sublattices and α'' phase is formed at each of them. Then the final structure can be seen as an interposition of the three α'' structures.

As perspective the AFT theory can be applied to large game of self-assembly phenomena or phase transformations where crystallographic structure is changing. In the further studies it will be interesting to apply this approach to model martensite transformation with taking into account the carbon atoms. The follow studies of Zener ordering and its influence on the redistribution of carbon atoms during low temperature aging in Fe-C and Fe-Ni-C systems can be also done. It will be very interesting and challenging to apply the AFT approach to reproduce whole chain of metastables phases appearing during aging from virgin martensite to coexisting of ferrite and carbide. All these metastables phases could be the member of adaptive phase predicted by Khachaturyan in the previous theoretical work.

The AFT is a phenomenological approach and the quasiparticles using in this approach can be interpreted at different scales. In principle, this approach can be even used for the description of three-dimensional pattern formation by any macroscopic objects and optimisation of their properties. The "fratons" in this case being fragments of these objects are also macroscopic.

It will be also very challenging to continue develop this approach to model a self-assembly in biological system. Our first results shown that this approach can reproduce the formation of helix and double helix structures. Next developing of this method can open a way to model a real structure of DNA molecule with four structural units.

Appendix A

Calculation of the elastic properties of the potential

In this appendix, a method of calculation of the elastic constants of the bcc and fcc structures is given.

Cubic systems have three independent elastic constants: C_{11}, C_{12} and C_{44}. To find them three characteristic deformations [110] were used.

1) Uniform compression or expansion, $\mathbf{r} \to (\hat{I} + \hat{\delta}_{bulk})\mathbf{r}$, with symmetric strain tensor

$$\widehat{\delta}_{bulk} = \begin{pmatrix} \delta & 0 & 0 \\ 0 & \delta & 0 \\ 0 & 0 & \delta \end{pmatrix}. \tag{A.1}$$

Here δ is a magnitude of the strain.

2) Equal contraction and expansion along two cube edges: O_x and O_y, $\mathbf{r} \to (\hat{I} + \hat{\delta}_{dev})\mathbf{r}$, with symmetric strain tensor

$$\widehat{\delta}_{dev} = \begin{pmatrix} \delta & 0 & 0 \\ 0 & -\delta & 0 \\ 0 & 0 & 0 \end{pmatrix}. \tag{A.2}$$

3) Simple shear, $\mathbf{r} \to (\hat{I} + \hat{\delta}_{shear})\mathbf{r}$, with symmetric strain tensor

$$\widehat{\delta}_{shear} = \begin{pmatrix} 0 & \delta & 0 \\ 0 & 0 & 0 \\ 0 & 0 & 0 \end{pmatrix}. \tag{A.3}$$

The change in the energy per unit volume with respect to these deformations can be written as

$$\begin{aligned} \Delta F^{bulk} &\approx \frac{9}{2} B\delta^2 + O\left(\delta^4\right), \\ \Delta F^{dev} &\approx \left(C_{11} - C_{12}\right)\delta^2 + O\left(\delta^4\right), \\ \Delta F^{shear} &\approx \frac{1}{2} C_{44}\delta^2 + O\left(\delta^4\right). \end{aligned} \tag{A.4}$$

In (A.4) bulk modulus, B, is equal $\left(C_{11} + 2C_{12}\right)/3$.

Therefore, the elastic constants can be found from the second derivative of the free energy change with respect to δ. The free energy for the one component system used in Chapter4 is

$$F(\{\rho(\mathbf{r})\}, T) = \frac{1}{2}\sum_{\mathbf{r},\mathbf{r}'} w(\mathbf{r}-\mathbf{r}')\rho(\mathbf{r})\rho^*(\mathbf{r}') + \sum_{\mathbf{r}} f(\{\rho_\alpha(\mathbf{r})\}, T). \tag{A.5}$$

Second term in Eq.(A.5) does not change with respect to deformations. Thus, only change of internal energy, the first term in Eq.(A.5), contributes in the strain energy.

The deformation of the system can be provided by replacement $\mathbf{r} \to (\hat{I} + \hat{\delta}_{def})\mathbf{r}$ in interaction potential $w(\mathbf{r})$:

$$w(\mathbf{r}) \to w\left((\hat{I} + \hat{\delta}_{def})\mathbf{r}\right), \tag{A.6}$$

where $(\hat{I} + \hat{\delta}_{def})$ is the matrix described deformation, $\hat{\delta}_{def}$ is the symmetric strain tensor.

Using Eq.(A.5) with replacement (A.6) the change in free energy is

$$\Delta F = \frac{1}{2}\sum_{\mathbf{r},\mathbf{r}'} w\left((\hat{I} + \hat{\delta}_{def})(\mathbf{r}-\mathbf{r}')\right)\rho(\mathbf{r})\rho^*(\mathbf{r}') - \frac{1}{2}\sum_{\mathbf{r},\mathbf{r}'} w(\mathbf{r}-\mathbf{r}')\rho(\mathbf{r})\rho^*(\mathbf{r}'). \tag{A.7}$$

Since in our simulations the FT of interaction potential is used, then the reciprocal lattice transformation should be determined. For this it can be used the fact that the product of vector $\mathbf{r}$ and corresponding vector of reciprocal space $\mathbf{k}$ is always equal 2π. Therefore, the product of vectors $\mathbf{r}$ and $\mathbf{k}$ of not deformed system and product of vectors $\mathbf{r}'$ and $\mathbf{k}'$ of deformed system are equal:

$$\mathbf{k}\mathbf{r} = \mathbf{k}'\mathbf{r}'. \tag{A.8}$$

Substituting the relation $\mathbf{r}' = \hat{A}\mathbf{r}$ between initial and transformed lattices and Eq.(A.8):

$$\mathbf{k}\mathbf{r} = \mathbf{k}\left(\hat{A}^{-1}\hat{A}\right)\mathbf{r} = \left(\mathbf{k}\hat{A}^{-1}\right)\left(\hat{A}\mathbf{r}\right) = \mathbf{k}'\mathbf{r}', \tag{A.9}$$

where $\hat{A} = \hat{I} + \hat{\delta}_{def}$. Thus, vector $\mathbf{k}'$ of deformed system is

$$\mathbf{k}' = \mathbf{k}\hat{A}^{-1} = \left(\hat{A}^{-1}\right)^T\mathbf{k} = \left((\hat{I} + \hat{\delta}_{def})^{-1}\right)^T\mathbf{k}. \tag{A.10}$$

For the considered deformations the vector $\mathbf{k}'$ is

1) for uniform compression or expansion:

$$\mathbf{k}' = \begin{pmatrix} k_x/(1+\delta) & k_y/(1+\delta) & k_z/(1+\delta) \end{pmatrix}; \tag{A.11}$$

2) for equal contraction and expansion along two cube edges: O_x and O_y:

$$\mathbf{k}' = \begin{pmatrix} k_x/(1+\delta) & k_y/(1-\delta) & k_z \end{pmatrix}; \tag{A.12}$$

3) for simple shear:

$$\mathbf{k}' = \begin{pmatrix} k_x & k_y - \delta k_x & k_z \end{pmatrix}. \tag{A.13}$$

The FT of change of free energy (A.7) using Eq.(A.10):

$$\Delta F = \frac{1}{2}\sum_{\mathbf{k}} \left\{ \widetilde{w}\left(\left((\hat{I} + \hat{\delta}_{def})^{-1} \right)^T \mathbf{k} \right) - \widetilde{w}(\mathbf{k}) \right\} |\rho(\mathbf{k})|^2 . \tag{A.14}$$

The change of free energy (A.14) could be found using potentials (4.12) and (4.19) with density functions of fcc and bcc phases at equilibrium. The free energy of deformed crystal was calculated with $\delta = \delta_0 n$, where n is integer and $\delta_0 = 0.002$. To approximate the derivative of the change in free energy a centered difference formula was used:

$$f'(x_i) \approx \frac{f(x_{i+1}) - f(x_{i-1})}{2\delta}. \tag{A.15}$$

Finally, using the same approach the second derivative of free energy in $\delta = 0$ with respect to δ for the three characteristic deformations can be also evaluated. These derivatives are equal to the coefficients at δ^2 in Eqs.(A.4). Calculated elastic constants for the fcc and bcc phases are given in TableA.1.

TABLE A.1: Elastic constants C_{ij} for the bcc and fcc lattice structures. Elastic constants used in this work are presented in dimensionless form.

Structure	C_{11}	C_{12}	C_{44}
bcc	0.233	0.101	0.086
fcc	0.139	0.081	0.090

Appendix B

Pole figures

Usually for graphical representation of a crystallographic texture pole figures are used. A pole figure is provided in the form of stereographic projection. On this projection the poles which correspond to the directions of the (hkl) crystallographic plane normals of each grain of the investigated polycrystal structure [111] are presented.

The pole figure construction going on in two stages. The first is to build the spherical projection of poles and the second one is to obtain a two-dimensional stereographic projection of poles on a selected plane.

To illustrate the process of a pole figure construction the unit cubic cell has been taken and placed into the center of the sphere with some given radius (Fig.B.1). In Fig.B.1(a) three mutually perpendicular normals to the planes (100), (010) and (001) of the unit cell are shown. Then these normals extend till they cross the sphere. The intersection of the extended normal and a sphere called "pole" (on Fig.B.1(a) marked in red). The position of the pole on a sphere is characterized by two spherical coordinates: polar angle θ and azimuthal angle φ.

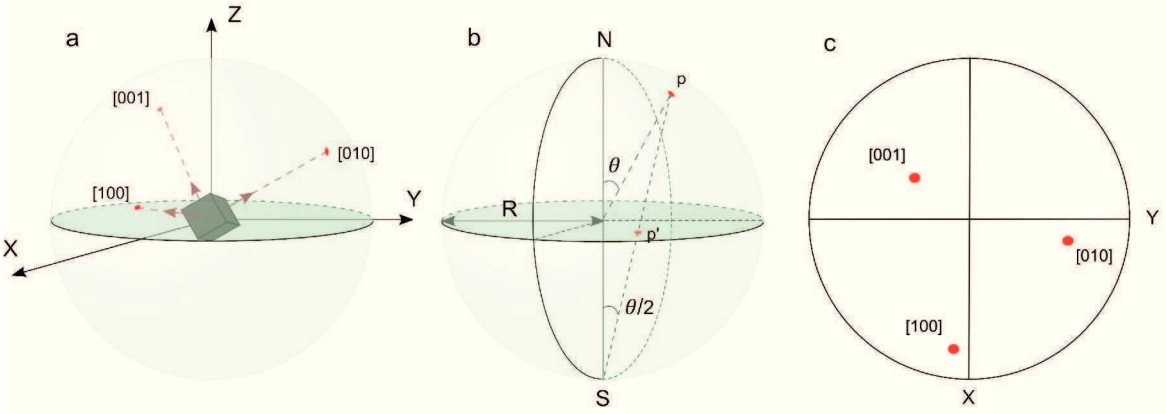

FIGURE B.1: Schematic representation of (001) pole figure construction. (a) Spherical projection of {100} poles (in red) of the crystal cube in the origin; (b) the construction of pole p' on stereographic projection from p pole of spherical projection; (c) {100} poles on (001) pole figure.

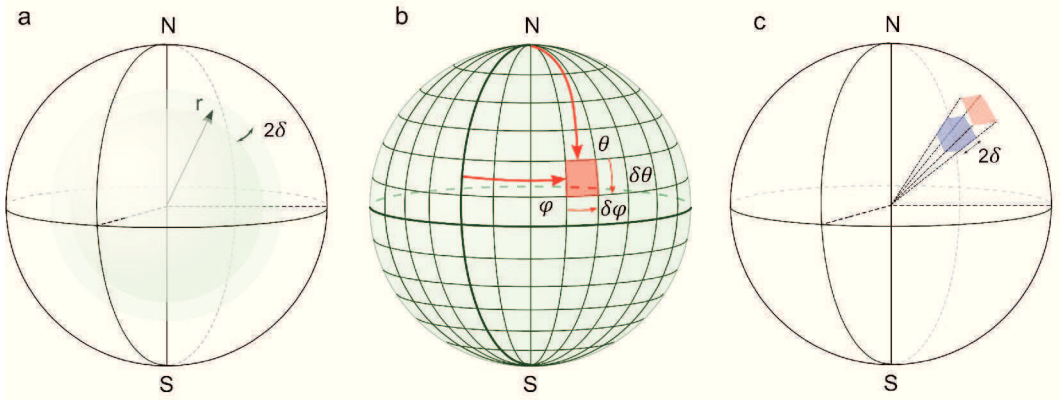

FIGURE B.2: Schematic representation of the spherical projection construction.

One of more common types of projections in crystallography is a stereographic projection. In the Fig.B.1(b) the construction of a stereographic projection is schematically shown. First we must connect the pole on the sphere with a South pole S by a line. The projection point is defined by the intersection of this line with the equatorial plane, which is the projection plane. The coordinates of the projected point on the plane are

$$\begin{pmatrix} x \\ y \end{pmatrix} = R\tan(\theta/2)\begin{pmatrix} \cos(\varphi) \\ \sin(\varphi) \end{pmatrix}. \tag{B.1}$$

In Fig.B.1(c) the stereographic projection of (100), (010) and (001) poles of the unit cell which corresponds to the certain grain is shown. Usually in crystallography it is enough to consider the poles on half of the sphere.

To practical construction of the pole figure the diffraction pattern in 3D is used. As example, the scheme for the grains with bcc structure (fcc in reciprocal space) and build the (001) pole figure is described. First we choose a sphere with a radius bigger then our simulation box, Fig.B.2. Then we take a spherical shell of the diffraction with radii $r+\delta$ and $r-\delta$ where r is a distance from 000 to 002 diffraction spots in reciprocal space, this distance is $r = \frac{2\pi}{a^{\text{bcc}}}2$. The direction from 000 to 002 corresponds to the direction of the normal to (001) plane. Then we build a grid on the sphere as it is shown on Fig.B.2. Each cell of the grid with coordinates of the center of the cell φ and θ is restricted by the angles $\varphi \pm \frac{1}{2}\delta\varphi$ and $\theta \pm \frac{1}{2}\delta\theta$. Here $\delta\varphi = 360°/n$ $\delta\theta = 180°/m$. The number of the cells in the grid is $n \times m$, it determines precision of the position of poles on the pole figure. Then a unit element of sphere from 000 to the grid cell on the sphere is builded. During next step the value of intensity at each point of such a section in spherical shell (the area of summation in the Fig.B.2 is in red) should be added and should be divided this value on the number of grids N_s in section of spherical shell. After, the value of intensity $I(\varphi,\theta)$ for each cell of the grid can be calculated using the same procedure:

$$I(\varphi,\theta) = \frac{1}{N_s}\sum_{N_s} I\left(\mathbf{k}(\varphi \pm \frac{1}{2}\delta\varphi, \theta \pm \frac{1}{2}\delta\theta)\right). \tag{B.2}$$

Then at the end, the value $I(\varphi, \theta)$ of each cell are projected on the projected plane using the scheme described above.

Appendix C

Kanzaki forces

Here we obtain the way to find expressions for Kanzaki forces $\mathbf{f}(p, \mathbf{r})$ and its Fourier transforms $\mathbf{F}(p, \mathbf{k})$. We will follow the method of Kanzaki forces calculations presented in [17].

The Kanzaki forces describe the action of the lattice defect on atoms of the host lattice. In our case the lattice defect is the diluted interstitial carbon atom. If carbon atoms occupy 3rd sublattice (O_z sublattice) of octahedral interstices in the bcc lattice then the position of the the nearest neighbor iron atoms in the host lattice relative to the diluted atom are $(0, 0, \pm a_0/2)$, here a_0 is the lattice parameter of the bcc host lattice. The vectors of Kanzaki forces $\mathbf{f}(p, \mathbf{r})$ are forwarded along the directions to these points, Fig.C.1. In the second coordination shell there

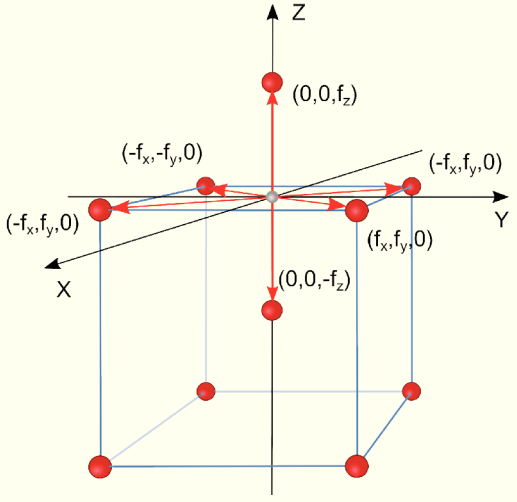

FIGURE C.1: The schematic representation of the Kanzaki forces. The iron atoms of the host bcc lattice are marked in red and the diluted carbon atom situated in the O_z octahedral interstitial site is marked in grey. The directions of Kanzaki forces are shown by the red arrows.

are four iron atoms at the points $(\pm a_0/2, \pm a_0/2, 0)$. Thus, if we take into account interactions

with iron atoms from the first two coordination shells, the Kanzaki forces have a form:

$$\mathbf{f}(3,\mathbf{r}) = \begin{cases} (0,0,\pm f_z(3)), & \text{if } \mathbf{r} = (0,0,\pm a_0/2), \\ (\pm f_x(3), \pm f_y(3), 0), & \text{if } \mathbf{r} = (\pm a_0/2, \pm a_0/2, 0), \\ 0, & \text{otherwise.} \end{cases} \tag{C.1}$$

The Kanzaki forces components $f_i(p)$ can be found from

$$\sigma^0_{ij}(p) = \frac{1}{2v_0} \sum_{\mathbf{r}} \left(f_i(p) r_j + f_j(p) r_i \right), \tag{C.2}$$

where $v_0 = \frac{a_0^3}{2}$ is a volume per atom in the bcc lattice, $\sigma^0_{ij}(p)$ are the components of the tensor which describes the transformation stress:

$$\sigma^0_{ij}(p) = \lambda_{ijkl} u_{kl}(p). \tag{C.3}$$

Using the expansion coefficients (5.14) and tensor of elastic constants (5.17) the tensors $\sigma^0_{ij}(p)$ can be written as

$$\sigma^0_{ij}(1) = \begin{pmatrix} \sigma^0_{33} & 0 & 0 \\ 0 & \sigma^0_{11} & 0 \\ 0 & 0 & \sigma^0_{11} \end{pmatrix}, \quad \sigma^0_{ij}(2) = \begin{pmatrix} \sigma^0_{11} & 0 & 0 \\ 0 & \sigma^0_{33} & 0 \\ 0 & 0 & \sigma^0_{11} \end{pmatrix}, \quad \sigma^0_{ij}(3) = \begin{pmatrix} \sigma^0_{11} & 0 & 0 \\ 0 & \sigma^0_{11} & 0 \\ 0 & 0 & \sigma^0_{33} \end{pmatrix}, \tag{C.4}$$

here

$$\begin{aligned} \sigma^0_{11} &= (C_{11} + C_{12}) u_{11} + C_{12} u_{33}, \\ \sigma^0_{33} &= 2C_{12} u_{11} + C_{11} u_{33}. \end{aligned} \tag{C.5}$$

Then to obtain the components of Kanzaki forces then three independent equations from equation (C.2) using (C.1) can be done:

$$\sigma^0_{ij}(p) = \frac{1}{2v_0} \sum_{\mathbf{r}} 2 f_i(p) r_i \delta_{ij}, \tag{C.6}$$

or for the carbon situated in the O_z octahedral sublattice

$$\begin{aligned} \sigma^0_{xx}(3) &= \tfrac{1}{2v_0} 2 \left[f_x(3) \tfrac{a_0}{2} + f_x(3) \tfrac{a_0}{2} - f_x(3) \left(-\tfrac{a_0}{2}\right) - f_x(3) \left(-\tfrac{a_0}{2}\right) \right] = \tfrac{2}{v_0} f_x(3) a_0, \\ \sigma^0_{yy}(3) &= \tfrac{1}{2v_0} 2 \left[f_y(3) \tfrac{a_0}{2} - f_y(3) \left(-\tfrac{a_0}{2}\right) + f_y(3) \tfrac{a_0}{2} - f_y(3) \left(-\tfrac{a_0}{2}\right) \right] = \tfrac{2}{v_0} f_y(3) a_0, \\ \sigma^0_{zz}(3) &= \tfrac{1}{2v_0} 2 \left[f_z(3) \tfrac{a_0}{2} - f_z(3) \left(-\tfrac{a_0}{2}\right) \right] = \tfrac{1}{v_0} f_z(3) a_0. \end{aligned} \tag{C.7}$$

The equations (C.8) give the forces components $f_i(3)$:

$$\begin{aligned} f_x(3) &= \frac{a_0^2}{4}\sigma_{11}^0(3), \\ f_y(3) &= \frac{a_0^2}{4}\sigma_{11}^0(3), \\ f_z(3) &= \frac{a_0^2}{2}\sigma_{33}^0(3). \end{aligned} \tag{C.8}$$

The elastic interaction potential representation (5.16) needs to introduce the Fourier transform of the Kanzaki forces:

$$\mathbf{F}(p,\mathbf{k}) = \sum_{\mathbf{r}} \mathbf{f}(p,\mathbf{r}) e^{-i\mathbf{kr}}. \tag{C.9}$$

Considering the expressions for the Kanzaki forces (C.1) and its components (C.9) the Fourier transform $\mathbf{F}(p,\mathbf{k})$ is

$$\begin{aligned} \mathbf{F}(3,\mathbf{k}) = &\begin{pmatrix} 0 \\ 0 \\ f_z(3) \end{pmatrix} e^{-ik_z a_0/2} + \begin{pmatrix} 0 \\ 0 \\ -f_z(3) \end{pmatrix} e^{ik_z a_0/2} + \begin{pmatrix} f_x(3) \\ f_y(3) \\ 0 \end{pmatrix} e^{-i(k_x+k_y)a_0/2} \\ &+ \begin{pmatrix} f_x(3) \\ -f_y(3) \\ 0 \end{pmatrix} e^{-i(k_x-k_y)a_0/2} + \begin{pmatrix} -f_x(3) \\ f_y(3) \\ 0 \end{pmatrix} e^{-i(-k_x+k_y)a_0/2} + \begin{pmatrix} -f_x(3) \\ -f_y(3) \\ 0 \end{pmatrix} e^{-i(-k_x-k_y)a_0/2}, \end{aligned}$$

or

$$\mathbf{F}(3,\mathbf{k}) = \begin{pmatrix} f_x(3)\,(-4i\sin(k_x a_0/2)\cos(k_y a_0/2)) \\ f_y(3)\,(-4i\sin(k_y a_0/2)\cos(k_x a_0/2)) \\ f_z(3)\,(-2i\sin(k_z a_0/2)) \end{pmatrix}.$$

Finally

$$\mathbf{F}(3,\mathbf{k}) = \begin{pmatrix} -ia_0^2\sigma_{11}\sin(k_x a_0/2)\cos(k_y a_0/2) \\ -ia_0^2\sigma_{11}\sin(k_y a_0/2)\cos(k_x a_0/2) \\ -ia_0^2\sigma_{33}\sin(k_z a_0/2) \end{pmatrix}. \tag{C.10}$$

Kanzaki forces for atoms placed in the other octahedral sublattices can be obtained using cyclic permutations:

$$\begin{aligned} x &\to y, \\ y &\to z, \\ z &\to x. \end{aligned}$$

Thus the Fourier transform of the Kanzaki forces which are caused by the atoms diluted in the O_x octahedral sublattice($p = 1$) of the bcc lattice is

$$\mathbf{F}(1,\mathbf{k}) = \begin{pmatrix} -ia_0^2\sigma_{33}\sin(k_x a_0/2) \\ -ia_0^2\sigma_{11}\sin(k_y a_0/2)\cos(k_z a_0/2) \\ -ia_0^2\sigma_{11}\sin(k_z a_0/2)\cos(k_y a_0/2) \end{pmatrix}. \tag{C.11}$$

And for the case when $p = 2$:

$$\mathbf{F}(2,\mathbf{k}) = \begin{pmatrix} -ia_0^2\sigma_{11}\sin(k_x a_0/2)\cos(k_z a_0/2) \\ -ia_0^2\sigma_{33}\sin(k_y a_0/2) \\ -ia_0^2\sigma_{11}\sin(k_z a_0/2)\cos(k_x a_0/2) \end{pmatrix}. \tag{C.12}$$

The expressions (C.11), (C.12) and (C.10) can be used for all kinds of point defects placed in octahedral interstices of the bcc host lattice.

Appendix D

Calculation of dynamical matrix for bcc lattice structure

In this appendix, the dynamical matrix for bcc lattice structure are obtained and Born-von Karman constants through elastic constants are expressed.

For the description of dynamical properties of a crystal it is convenient to use the theory of lattice vibrations. The basic theory of this phenomena has been described in detail, for example, in [112],[113] and [114].

In the next consideration it assumed that the mean equilibrium positions of each atom, s, is a Bravais lattice site, $\mathbf{R}_s$. Therefore, the position of an atom in crystal, $\mathbf{r}_s$, can be described by the displacement $\mathbf{u}(\mathbf{R}_s)$ from the nearest equilibrium position $\mathbf{R}_s$ of atom s:

$$\mathbf{r}(\mathbf{R}_s) = \mathbf{R}_s + \mathbf{u}(\mathbf{R}_s).$$

The free energy E can be presented as a function of the static displacements $E = E(\mathbf{u}(\mathbf{R}_s))$. If the amplitude of atomic deviations is smaller then the interatomic distance, then we can expand the free energy in Taylor series near equilibrium positions $\mathbf{R}_s$:

$$E = E_0 + \sum_s \frac{\partial E}{\partial u_i(\mathbf{R}_s)}\bigg|_{\mathbf{u}\equiv 0} u_i(\mathbf{R}_s) + \frac{1}{2}\sum_{ss'} \frac{\partial^2 E}{\partial u_i(\mathbf{R}_s)\partial u_j(\mathbf{R}_{s'})}\bigg|_{\mathbf{u}\equiv 0} u_i(\mathbf{R}_s)u_i(\mathbf{R}_{s'}) + O(\mathbf{u}^3). \quad \text{(D.1)}$$

Here $u_i(\mathbf{R}_s)$ $(i = x, \bar{y}, z)$ are components of a displacement vector $\mathbf{u}(\mathbf{R}_s)$, E_0 is an energy of the system at equilibrium. The second term in (D.1) is vanished because the free energy reaches a minimum ($\frac{\partial E}{\partial \mathbf{u}(\mathbf{R}_s)}\Big|_{\mathbf{u}\equiv 0} = 0$) when the positions of all atoms correspond to sites of perfect crystal. This leads to a *harmonic approximation* which is sufficiently accurate to describe most of the lattice dynamical effect of interest. In the harmonic approximation the free energy has sense of the potential energy of the imperfect crystal. It should be noted that in the case of a crystal with defects the equilibrium positions don't correspond to the minimum of free energy and derivatives $\frac{\partial E}{\partial u(\mathbf{R}_s)}$ don't vanish.

The second non-vanishing term in (D.1) is

$$E_{harm} = \frac{1}{2}\sum_{ss'} A_{ij}(\mathbf{R}_s - \mathbf{R}_{s'})u_i(\mathbf{R}_s)u_j(\mathbf{R}_{s'}),$$
$$\text{or} \tag{D.2}$$
$$E_{harm} = \frac{1}{2}\sum_{ss'} \mathbf{u}^T(\mathbf{R}_s)\hat{\mathbf{A}}(\mathbf{R}_s - \mathbf{R}_{s'})\mathbf{u}(\mathbf{R}_{s'}).$$

Here $A_{ij}(\mathbf{R}_s - \mathbf{R}_{s'})$ is a force constants tensor (Born-von Karman tensor), that determines the force acting on atom s' in j-direction when atom s is displaced in i-direction:

$$A_{ij}(\mathbf{R}_s - \mathbf{R}_{s'}) = \left.\frac{\partial^2 E}{\partial u_i(\mathbf{R}_s)\partial u_j(\mathbf{R}_{s'})}\right|_{\mathbf{u}\equiv 0}. \tag{D.3}$$

The set of interatomic force constants $A_{ij}(\mathbf{R}_s - \mathbf{R}_{s'})$ characterizes the rigidity of the lattice against displacements. The lattice symmetry determines the number of unique Born-von Karman constants.

Using Born-von Karman constants we can express a force on atom s, $\mathbf{F}$, by the relative displacements of all other atoms:

$$\begin{aligned} F_i(\mathbf{R}_s) &= -\frac{\partial E_{harm}}{\partial u_i(\mathbf{R}_s)} = -\sum_{s'} A_{ij}(\mathbf{R}_s - \mathbf{R}_{s'})u_j(\mathbf{R}_{s'}) = \\ &= -\sum_{s'} \left[A_{ix}(\mathbf{R}_s - \mathbf{R}_{s'})u_x(\mathbf{R}_{s'}) + A_{iy}(\mathbf{R}_s - \mathbf{R}_{s'})u_y(\mathbf{R}_{s'}) + A_{iz}(\mathbf{R}_s - \mathbf{R}_{s'})u_z(\mathbf{R}_{s'})\right]. \end{aligned} \tag{D.4}$$

Before the determination of the Born-von Karman constants value we consider some symmetry properties of the tensor $\hat{\mathbf{A}}(\mathbf{R})$.

The first property follows from the fact that the differentiation order in (D.3) is not important:

$$A_{ij}(\mathbf{R}_s - \mathbf{R}_{s'}) = A_{ji}(\mathbf{R}_s - \mathbf{R}_{s'}). \tag{D.5}$$

Also, due to the inversion symmetry of the Bravais lattice the configurational energy (D.2) does not change with change of the displacement $\mathbf{u}(\mathbf{R}_s)$ to the opposite direction $-\mathbf{u}(-\mathbf{R}_s)$:

$$A_{ij}(\mathbf{R}_s - \mathbf{R}_{s'}) = A_{ij}(\mathbf{R}_{s'} - \mathbf{R}_s), \quad \text{or} \quad \hat{\mathbf{A}}(\mathbf{R}) = \hat{\mathbf{A}}(-\mathbf{R}). \tag{D.6}$$

If we give the same displacement for all atoms ($\mathbf{u}(\mathbf{R}) \equiv \mathbf{a}$) in crystal, it will lead only to the displacement of whole crystal without internal distortion. The potential energy E will not change due to this operation ($E = E_0$). Thus,

$$E_{harm} = \frac{1}{2}\sum_{ss'} A_{ij}(\mathbf{R}_s - \mathbf{R}_{s'})a_i a_j = \frac{1}{2}\sum_{ij} a_i a_j N\left(\sum_s A_{ij}(\mathbf{R}_s)\right) = 0. \tag{D.7}$$

Since the displacement **a** is an arbitrarily chosen vector, Eq.(D.7) reduces to the condition:

$$\sum_s A_{ij}(\mathbf{R}_s) = 0. \tag{D.8}$$

Now, we will consider the symmetry relations between components of tensor $\hat{\mathbf{A}}(\mathbf{R})$ in the bcc lattice. Since we regard perfect crystal containing atoms of one kind, force constants $A_{ij}(\mathbf{R}_s - \mathbf{R}_{s'})$ depend only of vector $\mathbf{R} = \mathbf{R}_s - \mathbf{R}_{s'}$. We assume that interatomic forces strongly decrease with increasing distance between atoms. Therefore, we will take into account only first two coordination shells in the bcc lattice. In the bcc lattice each atom s has eight nearest neighbors and six neighbors from the second coordination shell. All neighbors of atom s, that we took into consideration, are listed in Table D.1. For convenience, we placed atom s in the origin.

TABLE D.1: Tensor of Born-von Karman constants $\hat{\mathbf{A}}(\mathbf{R})$ for the bcc lattice. Constants $A_i j^{(1)}(\mathbf{R})$ and $A_i j^{(2)}(\mathbf{R})$ correspond to the interatomic interactions with atoms from the first and second coordination shells. a_0 is lattice constant.

$\mathbf{R}$, $\frac{1}{2}a_0$	$\hat{\mathbf{A}}^{(1)}(\mathbf{R})$	$\mathbf{R}$, $\frac{1}{2}a_0$	$\hat{\mathbf{A}}^{(2)}(\mathbf{R})$
(111)	$\begin{pmatrix} -\alpha_1 & -\gamma_1 & -\gamma_1 \\ -\gamma_1 & -\alpha_1 & -\gamma_1 \\ -\gamma_1 & -\gamma_1 & -\alpha_1 \end{pmatrix}$	(200)	$\begin{pmatrix} -\alpha_2 & 0 & 0 \\ 0 & -\beta_2 & 0 \\ 0 & 0 & -\beta_2 \end{pmatrix}$
$(\bar{1}11)$	$\begin{pmatrix} -\alpha_1 & \gamma_1 & \gamma_1 \\ \gamma_1 & -\alpha_1 & -\gamma_1 \\ \gamma_1 & -\gamma_1 & -\alpha_1 \end{pmatrix}$	$(\bar{2}00)$	$\begin{pmatrix} -\alpha_2 & 0 & 0 \\ 0 & -\beta_2 & 0 \\ 0 & 0 & -\beta_2 \end{pmatrix}$
$(1\bar{1}1)$	$\begin{pmatrix} -\alpha_1 & \gamma_1 & -\gamma_1 \\ \gamma_1 & -\alpha_1 & \gamma_1 \\ -\gamma_1 & \gamma_1 & -\alpha_1 \end{pmatrix}$	(020)	$\begin{pmatrix} -\beta_2 & 0 & 0 \\ 0 & -\alpha_2 & 0 \\ 0 & 0 & -\beta_2 \end{pmatrix}$
$(11\bar{1})$	$\begin{pmatrix} -\alpha_1 & -\gamma_1 & \gamma_1 \\ -\gamma_1 & -\alpha_1 & \gamma_1 \\ \gamma_1 & \gamma_1 & -\alpha_1 \end{pmatrix}$	$(0\bar{2}0)$	$\begin{pmatrix} -\beta_2 & 0 & 0 \\ 0 & -\alpha_2 & 0 \\ 0 & 0 & -\beta_2 \end{pmatrix}$
$(\bar{1}\bar{1}1)$	$\begin{pmatrix} -\alpha_1 & -\gamma_1 & \gamma_1 \\ -\gamma_1 & -\alpha_1 & \gamma_1 \\ \gamma_1 & \gamma_1 & -\alpha_1 \end{pmatrix}$	(002)	$\begin{pmatrix} -\beta_2 & 0 & 0 \\ 0 & -\beta_2 & 0 \\ 0 & 0 & -\alpha_2 \end{pmatrix}$
$(\bar{1}1\bar{1})$	$\begin{pmatrix} -\alpha_1 & \gamma_1 & -\gamma_1 \\ \gamma_1 & -\alpha_1 & \gamma_1 \\ -\gamma_1 & \gamma_1 & -\alpha_1 \end{pmatrix}$	$(00\bar{2})$	$\begin{pmatrix} -\beta_2 & 0 & 0 \\ 0 & -\beta_2 & 0 \\ 0 & 0 & -\alpha_2 \end{pmatrix}$
$(1\bar{1}\bar{1})$	$\begin{pmatrix} -\alpha_1 & \gamma_1 & \gamma_1 \\ \gamma_1 & -\alpha_1 & -\gamma_1 \\ \gamma_1 & -\gamma_1 & -\alpha_1 \end{pmatrix}$		
$(\bar{1}\bar{1}\bar{1})$	$\begin{pmatrix} -\alpha_1 & -\gamma_1 & -\gamma_1 \\ -\gamma_1 & -\alpha_1 & -\gamma_1 \\ -\gamma_1 & -\gamma_1 & -\alpha_1 \end{pmatrix}$		

The force constants tensor for interactions with first coordinate shell are denoted as $\hat{\mathbf{A}}^{(1)}(\mathbf{R})$, and for the interactions with second coordinate shell as $\hat{\mathbf{A}}^{(2)}(\mathbf{R})$.

Symmetry operations of the lattice can be expressed as a transformation matrix $\hat{\mathbf{T}}$:

$$\mathbf{R}' = \hat{\mathbf{T}}\mathbf{R}. \tag{D.9}$$

The harmonic energy after transformation (D.9) is

$$\begin{aligned} E'_{harm} &= \frac{1}{2}\sum_{ss'}\left(\hat{\mathbf{T}}\mathbf{u}(\mathbf{R}_s)\right)^T \hat{\mathbf{A}}(\mathbf{R}'_s-\mathbf{R}'_{s'})\left(\hat{\mathbf{T}}\mathbf{u}(\mathbf{R}_{s'})\right) = \\ &= \frac{1}{2}\sum_{ss'}\mathbf{u}^T(\mathbf{R}_s)\left(\hat{\mathbf{T}}^T\hat{\mathbf{A}}(\mathbf{R}'_s-\mathbf{R}'_{s'})\hat{\mathbf{T}}\right)\mathbf{u}(\mathbf{R}_{s'}), \end{aligned} \tag{D.10}$$

where $\hat{\mathbf{T}}^T$ is the transpose of matrix $\hat{\mathbf{T}}$. Since energy is invariant under the symmetry operations of the lattice ($E'_{harm} = E_{harm}$), then combining (D.2) with (D.10) we have the transformation law for a tensor $\hat{\mathbf{A}}$:

$$\hat{\mathbf{A}}(\mathbf{R}_s-\mathbf{R}_{s'}) = \hat{\mathbf{T}}^T\hat{\mathbf{A}}(\mathbf{R}'_s-\mathbf{R}'_{s'})\hat{\mathbf{T}}. \tag{D.11}$$

If one of the atom in (D.11) is situated in the origin of coordinates then the transformation law can be simplified:

$$\hat{\mathbf{A}}(\mathbf{R}) = \hat{\mathbf{T}}^T\hat{\mathbf{A}}(\mathbf{R}')\hat{\mathbf{T}}. \tag{D.12}$$

The body-centered cubic lattice belongs to the O_h point group, and therefore has three 4-fold axes of rotation: O_x, O_y and O_z. Rotations by 90° about the O_x, O_y and O_z axes provide movements of the vectors $\frac{1}{2}a_0(111) \to \frac{1}{2}a_0(1\bar{1}1)$, $\frac{1}{2}a_0(111) \to \frac{1}{2}a_0(11\bar{1})$ and $\frac{1}{2}a_0(111) \to \frac{1}{2}a_0(\bar{1}11)$, respectively, a_0 is lattice constant of the bcc lattice. The corresponding rotational matrices, using the right-hand rule, are

$$\hat{\mathbf{T}}_x = \begin{pmatrix} 1 & 0 & 0 \\ 0 & 0 & -1 \\ 0 & 1 & 0 \end{pmatrix}, \quad \hat{\mathbf{T}}_y = \begin{pmatrix} 0 & 0 & 1 \\ 0 & 1 & 0 \\ -1 & 0 & 0 \end{pmatrix}, \quad \hat{\mathbf{T}}_z = \begin{pmatrix} 0 & -1 & 0 \\ 1 & 0 & 0 \\ 0 & 0 & 1 \end{pmatrix}. \tag{D.13}$$

Substituting the matrices (D.13) into the transformation law (D.12) gives following relations between force constants:

$$\begin{aligned} &A^{(1)}_{xx}\left(\frac{a_0}{2}(111)\right) = A^{(1)}_{xx}\left(\frac{a_0}{2}(1\bar{1}1)\right) = A^{(1)}_{zz}\left(\frac{a_0}{2}(11\bar{1})\right) = A^{(1)}_{yy}\left(\frac{a_0}{2}(\bar{1}11)\right), \\ &A^{(1)}_{yy}\left(\frac{a_0}{2}(111)\right) = A^{(1)}_{zz}\left(\frac{a_0}{2}(1\bar{1}1)\right) = A^{(1)}_{yy}\left(\frac{a_0}{2}(11\bar{1})\right) = A^{(1)}_{xx}\left(\frac{a_0}{2}(\bar{1}11)\right), \\ &A^{(1)}_{zz}\left(\frac{a_0}{2}(111)\right) = A^{(1)}_{yy}\left(\frac{a_0}{2}(1\bar{1}1)\right) = A^{(1)}_{xx}\left(\frac{a_0}{2}(11\bar{1})\right) = A^{(1)}_{zz}\left(\frac{a_0}{2}(\bar{1}11)\right), \\ &A^{(1)}_{xy}\left(\frac{a_0}{2}(111)\right) = A^{(1)}_{xz}\left(\frac{a_0}{2}(1\bar{1}1)\right) = -A^{(1)}_{yz}\left(\frac{a_0}{2}(11\bar{1})\right) = -A^{(1)}_{xy}\left(\frac{a_0}{2}(\bar{1}11)\right), \\ &A^{(1)}_{xz}\left(\frac{a_0}{2}(111)\right) = -A^{(1)}_{xy}\left(\frac{a_0}{2}(1\bar{1}1)\right) = -A^{(1)}_{xz}\left(\frac{a_0}{2}(11\bar{1})\right) = A^{(1)}_{yz}\left(\frac{a_0}{2}(\bar{1}11)\right), \\ &A^{(1)}_{yz}\left(\frac{a_0}{2}(111)\right) = -A^{(1)}_{yz}\left(\frac{a_0}{2}(1\bar{1}1)\right) = A^{(1)}_{xy}\left(\frac{a_0}{2}(11\bar{1})\right) = -A^{(1)}_{xz}\left(\frac{a_0}{2}(\bar{1}11)\right). \end{aligned}$$

Atoms with vectors (000), $\frac{1}{2}a_0(111)$ and $\frac{1}{2}a_0(11\bar{1})$ are in the reflection plane $(\bar{1}10)$. Since, the reflection about plane does not change positions of atoms in this plane, it follows that

$$A_{xx}^{(1)}\left(\frac{a_0}{2}(111)\right) = A_{yy}^{(1)}\left(\frac{a_0}{2}(111)\right), \qquad A_{yz}^{(1)}\left(\frac{a_0}{2}(111)\right) = A_{xz}^{(1)}\left(\frac{a_0}{2}(111)\right),$$
$$A_{xx}^{(1)}\left(\frac{a_0}{2}(11\bar{1})\right) = A_{yy}^{(1)}\left(\frac{a_0}{2}(11\bar{1})\right), \qquad A_{yz}^{(1)}\left(\frac{a_0}{2}(11\bar{1})\right) = A_{xz}^{(1)}\left(\frac{a_0}{2}(11\bar{1})\right).$$

The transformation matrix for the reflection about $(\bar{1}10)$ plane is

$$\hat{\mathbf{T}}_{(\bar{1}10)} = \begin{pmatrix} 0 & 1 & 0 \\ 1 & 0 & 0 \\ 0 & 0 & 1 \end{pmatrix}. \tag{D.14}$$

Finally, there are two independent constants in the tensor $\hat{\mathbf{A}}^{(1)}(\mathbf{R})$:

$$\begin{aligned} A_{xx}^{(1)}\left(\frac{a_0}{2}(111)\right) &= -\alpha_1, \\ A_{xy}^{(1)}\left(\frac{a_0}{2}(111)\right) &= -\gamma_1. \end{aligned} \tag{D.15}$$

Matrices for $\hat{\mathbf{A}}^{(1)}(\mathbf{R})$ are given in the Table D.1. We used symmetry property (D.6) to obtain force constants for interactions with atoms on $\frac{1}{2}a_0(\bar{1}\bar{1}1)$, $\frac{1}{2}a_0(\bar{1}1\bar{1})$, $\frac{1}{2}a_0(1\bar{1}\bar{1})$ and $\frac{1}{2}a_0(\bar{1}\bar{1}\bar{1})$ lattice positions.

The force constants for the second neighbors can be found using the same symmetry properties as for the first neighbor atoms. First, we will use the reflections about (100), (010), (001) planes. The corresponding transformation matrices are

$$\hat{\mathbf{T}}_{(100)} = \begin{pmatrix} -1 & 0 & 0 \\ 0 & 1 & 0 \\ 0 & 0 & 1 \end{pmatrix}, \quad \hat{\mathbf{T}}_{(010)} = \begin{pmatrix} 0 & 0 & 0 \\ 0 & -1 & 0 \\ 0 & 0 & 1 \end{pmatrix}, \quad \hat{\mathbf{T}}_{(001)} = \begin{pmatrix} 1 & 0 & 0 \\ 0 & 1 & 0 \\ 0 & 0 & -1 \end{pmatrix}. \tag{D.16}$$

Substituting (D.16) in (D.12) gives the vanishing of all elements of matrices $\hat{\mathbf{A}}^{(2)}(\mathbf{R})$ except the main diagonal:

$$\begin{aligned} A_{xy}^{(2)}(\mathbf{R}) &= -A_{xy}^{(2)}(\mathbf{R}) = 0, \\ A_{xz}^{(2)}(\mathbf{R}) &= -A_{xz}^{(2)}(\mathbf{R}) = 0, \\ A_{yz}^{(2)}(\mathbf{R}) &= -A_{yz}^{(2)}(\mathbf{R}) = 0. \end{aligned}$$

The next relations of force constants can be obtain using the rotations by 90° about the O_x, O_y and O_z axes:

$$\begin{aligned} A_{xx}^{(2)}\left(\frac{a_0}{2}(200)\right) &= A_{yy}^{(2)}\left(\frac{a_0}{2}(020)\right) = A_{zz}^{(2)}\left(\frac{a_0}{2}(002)\right), \\ A_{yy}^{(2)}\left(\frac{a_0}{2}(200)\right) &= A_{xx}^{(2)}\left(\frac{a_0}{2}(020)\right) = A_{yy}^{(2)}\left(\frac{a_0}{2}(002)\right), \\ A_{zz}^{(2)}\left(\frac{a_0}{2}(200)\right) &= A_{zz}^{(2)}\left(\frac{a_0}{2}(020)\right) = A_{xx}^{(2)}\left(\frac{a_0}{2}(002)\right). \end{aligned}$$

Reflection about $(\bar{1}10)$ gives:

$$A_{yy}^{(2)}\left(\frac{a_0}{2}(002)\right) = A_{zz}^{(2)}\left(\frac{a_0}{2}(002)\right).$$

As follows, the forces between an atom and its second neighbors expressed by the two coefficients:

$$\begin{aligned} A_{xx}^{(2)}\left(\frac{a_0}{2}(200)\right) &= -\alpha_2, \\ A_{yy}^{(2)}\left(\frac{a_0}{2}(200)\right) &= -\beta_2. \end{aligned} \tag{D.17}$$

Matrices for $\hat{\mathbf{A}}^{(1)}(\mathbf{R})$ are given in the Table D.1.

If interatomic forces act along a line connecting the centers of atoms and depend only of distance between atoms (the case of central forces) then a number of force matrix coefficients reduced:

$$\beta_2 = 0. \tag{D.18}$$

Other coefficients α_1, γ_1 and α_2 can be expressed by elastic properties of the crystal.

The Fourier transform of the force constants matrix $\hat{\mathbf{A}}(\mathbf{R})$ is commonly referred to as the dynamical matrix:

$$\widetilde{A}_{ij}(\mathbf{k}) = \sum_s A_{ij}(\mathbf{R}_s) e^{-i\mathbf{k}\mathbf{R}_s}. \tag{D.19}$$

Using symmetry properties (D.8), the dynamical matrix can be written in the form:

$$\begin{aligned} \widetilde{A}_{ij}(\mathbf{k}) &= A_{ij}(0)e^{-i\mathbf{k}0} + \sum_s{}' A_{ij}(\mathbf{R}_s) e^{-i\mathbf{k}\mathbf{R}_s} = \\ &= -\sum_s{}' A_{ij}(\mathbf{R}_s) + \sum_s{}' A_{ij}(\mathbf{R}_s) e^{-i\mathbf{k}\mathbf{R}_s} = \sum_s{}' A_{ij}(\mathbf{R}_s)\left(e^{-i\mathbf{k}\mathbf{R}_s} - 1\right). \end{aligned} \tag{D.20}$$

Here the sum with prime symbol means that the term $\mathbf{r} = 0$ is omitted. Substituting (D.8) into (D.20) gives:

$$\widetilde{A}_{ij}(\mathbf{k}) = \frac{1}{2}\sum_s{}' A_{ij}(\mathbf{R}_s)\left(e^{-i\mathbf{k}\mathbf{R}_s} + e^{i\mathbf{k}\mathbf{R}_s} - 2\right) = \sum_s{}' A_{ij}(\mathbf{R}_s)\left(\cos\mathbf{k}\mathbf{R}_s - 1\right). \tag{D.21}$$

The components of the dynamical matrix, $\widetilde{A}_{ij}(\mathbf{k})$, can be expressed using Eq.(D.21) and tensor of Born-von Karman constants, Table D.1:

$$\begin{aligned}\widetilde{A}_{xx}(\mathbf{k}) = 2\alpha_1 \Big[4 - \cos\frac{a_0}{2}(k_x + k_y + k_z) - \cos\frac{a_0}{2}(-k_x + k_y + k_z) - \cos\frac{a_0}{2}(k_x - k_y + k_z) - \\ - \cos\frac{a_0}{2}(k_x + k_y - k_z)\Big] + 2\alpha_2\left[1 - \cos a_0 k_x\right] + 2\beta_2\left[2 - \cos a_0 k_y - \cos a_0 k_z\right] = \\ = 8\alpha_1\left[1 - \cos\frac{a_0}{2}k_x \cos\frac{a_0}{2}k_y \cos\frac{a_0}{2}k_z\right] + 2\alpha_2\left[1 - \cos a_0 k_x\right], \quad \text{(D.22)}\end{aligned}$$

$$\begin{aligned}\widetilde{A}_{xy}(\mathbf{k}) = 2\gamma_1 \Big[1 - \cos\frac{a_0}{2}(k_x + k_y + k_z) - (1 - \cos\frac{a_0}{2}(-k_x + k_y + k_z)) - \\ -(1 - \cos\frac{a_0}{2}(k_x - k_y + k_z)) + 1 - \cos\frac{a_0}{2}(k_x + k_y - k_z)\Big] = \\ = 8\gamma_1 \sin\frac{a_0}{2}k_x \sin\frac{a_0}{2}k_y \cos\frac{a_0}{2}k_z. \quad \text{(D.23)}\end{aligned}$$

Other components of dynamical matrix can be obtained from (D.22) and (D.23) using cyclic permutations:

$$\begin{aligned} x &\to y, \\ y &\to z, \\ z &\to x. \end{aligned}$$

The expressions for the remaining components of matrix $\widetilde{\hat{\mathbf{A}}}(\mathbf{k})$ are

$$\begin{aligned}\widetilde{A}_{yy}(\mathbf{k}) &= 8\alpha_1\left[1 - \cos\frac{a_0}{2}k_x \cos\frac{a_0}{2}k_y \cos\frac{a_0}{2}k_z\right] + 2\alpha_2\left[1 - \cos a_0 k_y\right], \\ \widetilde{A}_{zz}(\mathbf{k}) &= 8\alpha_1\left[1 - \cos\frac{a_0}{2}k_x \cos\frac{a_0}{2}k_y \cos\frac{a_0}{2}k_z\right] + 2\alpha_2\left[1 - \cos a_0 k_z\right], \\ \widetilde{A}_{xz}(\mathbf{k}) &= 8\gamma_1 \sin\frac{a_0}{2}k_x \cos\frac{a_0}{2}k_y \sin\frac{a_0}{2}k_z, \\ \widetilde{A}_{yz}(\mathbf{k}) &= 8\gamma_1 \cos\frac{a_0}{2}k_x \sin\frac{a_0}{2}k_y \sin\frac{a_0}{2}k_z. \end{aligned} \quad \text{(D.24)}$$

In the long-wave approximation ,$\mathbf{k} \to 0$, the dynamical matrix can be expressed through the elastic modulus tensor, λ_{iklj}:

$$\lim_{\mathbf{k}\to 0} \widetilde{A}_{ij}(\mathbf{k}) = v_0 k^2 \lambda_{iklj} n_k n_l, \quad \text{(D.25)}$$

where $\mathbf{n} = \frac{\mathbf{k}}{k}$ is a unit vector, $v_0 = \frac{a_0^3}{2}$ is a volume per atom in the bcc lattice. The approximation (D.25) allows to find Born-von Karman constants in terms of elastic constants. We will use

Taylor series about $\mathbf{k}$ to find limit of functions (D.22),(D.23):

$$\widetilde{A}_{xx}(\mathbf{k})\Big|_{\mathbf{k}\to 0} = 8\alpha_1\left[1-\left(1-\frac{1}{2}\left(\frac{a_0}{2}k_x\right)^2\right)\left(1-\frac{1}{2}\left(\frac{a_0}{2}k_y\right)^2\right)\left(1-\frac{1}{2}\left(\frac{a_0}{2}k_z\right)^2\right)\right]+$$
$$+2\alpha_2\left[1-\left(1-\frac{1}{2}\left(a_0k_x\right)^2\right)\right]=\alpha_1a_0^2k^2\left[n_x^2+n_y^2+n_z^2\right]+\alpha_2a_0^2k^2n_x^2=$$
$$=a_0^2k^2\left[\alpha_1+\alpha_2n_x^2\right], \quad \text{(D.26)}$$

$$\widetilde{A}_{xy}(\mathbf{k})\Big|_{\mathbf{k}\to 0} = 8\gamma_1\left(\frac{a_0}{2}k_x\right)\left(\frac{a_0}{2}k_y\right)\left(1-\frac{1}{2}(\frac{a_0}{2}k_z)^2\right)=2a_0^2k^2\left[\gamma_1n_xn_y\right]. \quad \text{(D.27)}$$

Here the unit vector $\mathbf{n}^2=n_x^2+n_y^2+n_z^2=1$ was used. Functions $\widetilde{A}_{ij}(\mathbf{k})$ are restricted by the second-order Taylor expansion with respect to $\mathbf{k}$. On the other hand, substituting (5.17) in (D.25) gives components $\widetilde{A}_{xx}(\mathbf{k})$ and $\widetilde{A}_{xy}(\mathbf{k})$:

$$\begin{aligned}\widetilde{A}_{xx}(\mathbf{k})\Big|_{\mathbf{k}\to 0} &= v_0k^2\left[C_{11}n_1^2+C_{44}(n_2^2+n_3^2)\right]=v_0k^2\left[(C_{11}-C_{44})n_x^2+C_{44}\right],\\ \widetilde{A}_{xy}(\mathbf{k})\Big|_{\mathbf{k}\to 0} &= v_0k^2\left[(C_{12}+C_{44})n_xn_y\right].\end{aligned} \quad \text{(D.28)}$$

Combining (D.26) and (D.27) with (D.28) gives final expressions for Born-von Karman constants:

$$\alpha_1=\frac{C_{44}}{2}a_0, \quad \alpha_2=\frac{C_{11}-C_{44}}{2}a_0, \quad \gamma_1=\frac{C_{12}+C_{44}}{4}a_0. \quad \text{(D.29)}$$

Bibliography

[1] Z. Nishiyama (Auth.). *Martensitic Transformation*. Academic Press Inc, 1978.

[2] G. Krauss. *Steels: Processing, Structure, and Performance*. ASM International, 2005.

[3] S. Morito, H. Tanaka, R. Konishi, T. Furuhara, and T. Maki. The morphology and crystallography of lath martensite in Fe-C alloys. *Acta Materialia*, 51(6):1789 – 1799, 2003.

[4] G. Krauss. Martensite in steel: strength and structure. *Materials Science and Engineering: A*, 273-275(0):40 – 57, 1999.

[5] A. Stormvinter, G. Miyamoto, T. Furuhara, P. Hedström, and A. Borgenstam. Effect of carbon content on variant pairing of martensite in Fe-C alloys. *Acta Materialia*, 60(20): 7265 – 7274, 2012.

[6] M. Kusunoki and S. Nagakura. Modulated structure of iron–carbon martensite studied by electron microscopy and diffraction. *Journal of Applied Crystallography*, 14(5):329–336, 1981.

[7] K. A. Taylor, L. Chang, G. B. Olson, G. D. W. Smith, M. Cohen, and J. B. V. Sande. Spinodal decomposition during aging of Fe-Ni-C martensites. *Metallurgical Transactions A*, 20(12):2717–2737, 1989.

[8] S. Nagakura, Y. Hirotsu, M. Kusunoki, T. Suzuki, and Y. Nakamura. Crystallographic study of the tempering of martensitic carbon steel by electron microscopy and diffraction. *Metallurgical Transactions A*, 14(5):1025–1031, 1983.

[9] S. Nagakura and M. Toyoshima. Crystal structure and morphology of the ordered phase in iron-carbon martensite. *Trans. JIM*, 20(3):100–110, 1979.

[10] A. A. Lucas and P. Lambin. Diffraction by DNA, carbon nanotubes and other helical nanostructures. *Reports on Progress in Physics*, 68(5):1181, 2005.

[11] H. Kitahara, R. Ueji, N. Tsuji, and Y. Minamino. Crystallographic features of lath martensite in low-carbon steel. *Acta Materialia*, 54(5):1279 – 1288, 2006.

[12] C.C. Kinney, K.R. Pytlewski, A.G. Khachaturyan, and J.W. Morris Jr. The microstructure of lath martensite in quenched 9Ni steel. *Acta Materialia*, 69:372 – 385, 2014.

[13] K. Shimizu and Z. Nishiyama. Electron microscopic studies of martensitic transformations in iron alloys and steels. *Metallurgical Transactions*, 3(5):1055–1068, 1972.

[14] W. Zhang, Y.M. Jin, and A.G. Khachaturyan. Phase field microelasticity modeling of heterogeneous nucleation and growth in martensitic alloys. *Acta Materialia*, 55(2):565 – 574, 2007.

[15] T Liu, D Zhang, Q Liu, Y Zheng, Y Su, X Zhao, J Yin, M Song, and D Ping. A new nanoscale metastable iron phase in carbon steels. *Scientific Reports*, 5:15331, 2015.

[16] C. Zener. Theory of strain interaction of solute atoms. *Physical Review*, 74:639–647, Sep 1948.

[17] A.G. Khachaturyan. *Theory of structural transformations in solids*. New York, Wiley, 1983.

[18] E. V. Pereloma, F. Al-Harbi, and A. A. Gazder. The crystallography of carbide-free bainites in thermo-mechanically processed low Si transformation-induced plasticity steels. *Journal of Alloys and Compounds*, 615(0):96 – 110, 2014.

[19] C. M. Wayman K. Otsuka. *Shape Memory Materials*. Cambridge University Press, 1998.

[20] J.W. Christian and S. Mahajan. Deformation twinning. *Progress in Materials Science*, 39 (1):1 – 157, 1995.

[21] R.A Johnson, G.J Dienes, and A.C Damask. Calculations of the energy and migration characteristics of carbon and nitrogen in α-iron and vanadium. *Acta Metallurgica*, 12(11): 1215 – 1224, 1964.

[22] A. Udyansky, J. von Pezold, A. Dick, and J. Neugebauer. Orientational ordering of interstitial atoms and martensite formation in dilute Fe-based solid solutions. *Physical Review B*, 83:184112, 2011.

[23] A. V. Ruban. Self-trapping of carbon atoms in α'-Fe during the martensitic transformation: A qualitative picture from *ab initio* calculations. *Physical Review B*, 90:144106, 2014.

[24] E. Pereloma and D.V. Edmonds. *Phase Transformations in Steels*. Elsevier Science Limited, 2012.

[25] H.K.D.H. Bhadeshia. *Worked examples in the geometry of crystals*. Institute of Materials, 1987.

[26] G.V.Kurdjumov. Martensite crystal lattice, mechanism of austenite-martensite transformation and behavior of carbon atoms in martensite. *Metallurgical Transactions A*, 7(7): 999–1011, 1976.

[27] V. A. Lobodyuk and E. I. Estrin. Isothermal martensitic transformations. *Physics-Uspekhi*, 48(7):713–732, 2005.

[28] J.S Bowles and J.K Mackenzie. The crystallography of martensite transformations I. *Acta Metallurgica*, 2(1):129 – 137, 1954.

[29] J.W. Christian. *The Theory of Transformations in Metals and Alloys*. Pergamon, Oxford, third edition, 2002.

[30] J.W. Morris Jr. The Khachaturyan theory of elastic inclusions: Recollections and results. *Philosophical Magazine*, 90(1-4):3–35, 2010.

[31] M. Umemoto, E. Yoshitake, and I. Tamura. The morphology of martensite in Fe-C, Fe-Ni-C and Fe-Cr-C alloys. *Journal of Materials Science*, 18(10):2893–2904, 1983.

[32] M. Umemoto, T. Hyodo, T. Maeda, and I. Tamura. Electron microscopy studies of butterfly martensite. *Acta Metallurgica*, 32(8):1191–1203, 1984.

[33] S. Morito, X. Huang, T. Furuhara, T. Maki, and N. Hansen. The morphology and crystallography of lath martensite in alloy steels. *Acta Materialia*, 54(19):5323 – 5331, 2006.

[34] L. Qi, A.G. Khachaturyan, and J.W. Morris Jr. The microstructure of dislocated martensitic steel: Theory. *Acta Materialia*, 76:23 – 39, 2014.

[35] G. B. Olson and M. Cohen. A general mechanism of martensitic nucleation: Part I. General concepts and the FCC $\rightarrow$ HCP transformation. *Metallurgical Transactions A*, 7 (12):1897–1904, 1976.

[36] G. B. Olson and M. Cohen. A general mechanism of martensitic nucleation: Part II. FCC $\rightarrow$ BCC and other martensitic transformations. *Metallurgical Transactions A*, 7(12): 1905–1914, 1976.

[37] G. B. Olson and M. Cohen. A general mechanism of martensitic nucleation: Part III. Kinetics of martensitic nucleation. *Metallurgical Transactions A*, 7(12):1915–1923, 1976.

[38] S. Kartha, J. A. Krumhansl, J. P. Sethna, and L. K. Wickham. Disorder-driven pretransitional tweed pattern in martensitic transformations. *Physical Review B*, 52:803–822, Jul 1995.

[39] Y. Shao, P. C. Clapp, and J. A. Rifkin. Molecular dynamics simulation of martensitic transformations in NiAl. *Metallurgical and Materials Transactions A*, 27(6):1477–1489, 1996.

[40] Y. Wang and A.G. Khachaturyan. Three-dimensional field model and computer modeling of martensitic transformations. *Acta Materialia*, 45(2):759 – 773, 1997.

[41] G. T. Eldis and M. Cohen. Strength of initially virgin martensites at $-196°C$ after aging and tempering. *Metallurgical Transactions A*, 14(5):1007–1012, 1983.

[42] L. Xiao, Z. Fan, Z. Jinxiu, Z. Mingxing, K. Mokuang, and G. Zhenqi. Lattice-parameter variation with carbon content of martensite. i. X-ray-diffraction experimental study. *Physical Review B*, 52:9970–9978, 1995.

[43] O. N. C. Uwakweh, J. M. R. Génin, and J. F. Silvain. Electron microscopy study of the aging and first stage of tempering of high-carbon Fe-C martensite. *Metallurgical Transactions A*, 22(4):797–806, 1991.

[44] Y. Ohmori and I. Tamura. An interpretation of the carbon redistribution. *Metallurgical Transactions A*, 23(8):2147–2158, 1992.

[45] M. K. Miller, P. A. Beaven, S. S. Brenner, and G. D. W. Smith. An atom probe study of the aging of iron-nickel-carbon martensite. *Metallurgical Transactions A*, 14(6):1021–1024, 1983.

[46] L. Chang, A. Cerezo, G. D.W. Smith, M. K. Miller, M. G. Burke, S. S. Brenner, K. A. Taylor, T. Abe, and G. B. Olson. Ageing of Fe-Ni-C martensite. *Journal de Physique Colloques*, 45(C9):C9–409–C9–416, 1984.

[47] C. Zhu, A. Cerezo, and G. D. W. Smith. Carbide characterization in low-temperature tempered steels. *Ultramicroscopy*, 109(5):545 – 552, 2009.

[48] K. A. Taylor and M. Cohen. Aging of ferrous martensites. *Progress in Materials Science*, 36:151 – 272, 1992.

[49] G. B. Olson and M. Cohen. Early stages of aging and tempering of ferrous martensites. *Metallurgical Transactions A*, 14(5):1057–1065, 1983.

[50] G. V. Kurdjumov and A. G. Khachaturyan. Phenomena of carbon atom redistribution in martensite. *Metallurgical Transactions*, 3(5):1069–1076, 1972.

[51] H.E Cook and D de Fontaine. On the elastic free energy of solid solutions—I. microscopic theory. *Acta Metallurgica*, 17(7):915 – 924, 1969.

[52] D.W Hoffman. Concerning the elastic free energy of dilute interstitial alloys. *Acta Metallurgica*, 18(7):819 – 833, 1970.

[53] M.A. Krivoglaz. *X-ray and neutron diffraction in nonideal crystals*. Springer, 1996.

[54] S. B. Ren, T. Tadaki, K. Shimizu, X. T. Wang, H. M. Shen, and Y. N. Wang. Electron diffraction study of long-period ordered phase formed in Fe − 1.83 mass%C martensite during aging at room temperature. *Materials Transactions, JIM*, 36(12):1440–1446, 1995.

[55] S. B. Ren and S. T. Wang. A theoretical analysis of the spinodal decomposition in Fe- C martensite during aging stage of tempering. *Metallurgical Transactions A*, 19(10):2427–2432, 1988.

[56] C. W. Sinclair, M. Perez, R. G. A. Veiga, and A. Weck. Molecular dynamics study of the ordering of carbon in highly supersaturated α-Fe. *Physical Review B*, 81:224204, 2010.

[57] L.-Q. Chen and A.G. Khachaturyan. Computer simulation of structural transformations during precipitation of an ordered intermetallic phase. *Acta Metallurgica et Materialia*, 39(11):2533 – 2551, 1991.

[58] Y. Wang, L.-Q. Chen, and A.G. Khachaturyan. Kinetics of strain-induced morphological transformation in cubic alloys with a miscibility gap. *Acta Metallurgica et Materialia*, 41 (1):279 – 296, 1993.

[59] K. R. Elder, M. Katakowski, M. Haataja, and M. Grant. Modeling elasticity in crystal growth. *Physical Review Letters*, 88:245701, 2002.

[60] K. R. Elder and M. Grant. Modeling elastic and plastic deformations in nonequilibrium processing using phase field crystals. *Physical Review E*, 70:051605, 2004.

[61] Y. M. Jin and A. G. Khachaturyan. Atomic density function theory and modeling of microstructure evolution at the atomic scale. *Journal of Applied Physics*, 100(1):013519, 2006.

[62] M. Lavrskyi, H. Zapolsky, and A.G. Khachaturyan. Fraton theory and modelling of self-assembling of complex structures. *ArXiv e-prints*, 2014.

[63] M. Lavrskyi, H. Zapolsky, and A.G. Khachaturyan. Quasiparticle approach to diffusional atomic scale self-assembly of complex structures: from disorder to complex crystals and double-helix polymers. *Npj Computational Materials*, 2, 2016.

[64] L.-Q. Chen and A. G. Khachaturyan. Kinetics of virtual phase formation during precipitation of ordered intermetallics. *Physical Review B*, 46:5899–5905, 1992.

[65] L. D. Landau and E. M. Lifshitz. *Statistical Physics Part 1.* Pergamon, Oxford, third edition, 1989.

[66] J. W. D. Connolly and A. R. Williams. Density-functional theory applied to phase transformations in transition-metal alloys. *Physical Review B*, 27:5169–5172, Apr 1983.

[67] K. Ohno, K. Esfarjani, and Y. Kawazoe. *Computational materials science : from ab initio to Monte Carlo methods*. Springer, Berlin, 1999.

[68] L.Q. Chen and J. Shen. Applications of semi-implicit fourier-spectral method to phase field equations. *Computer Physics Communications*, 108(2):147 – 158, 1998.

[69] H. M. J. Smith. The theory of the vibrations and the raman spectrum of the diamond lattice. *Philosophical Transactions of the Royal Society of London A: Mathematical, Physical and Engineering Sciences*, 241(829):105–145, 1948.

[70] J. S. Reid. Debye–Waller factors of zinc-blende-structure materials – a lattice dynamical comparison. *Acta Crystallographica Section A*, 39(1):1–13, 1983.

[71] J. A. Czaban, D. A. Thompson, and R. R. LaPierre. Gaas core–shell nanowires for photovoltaic applications. *Nano Letters*, 9(1):148–154, 2009.

[72] A. H. Chin, S. Vaddiraju, A. V. Maslov, C. Z. Ning, M. K. Sunkara, and M. Meyyappan. Near-infrared semiconductor subwavelength-wire lasers. *Applied Physics Letters*, 88(16), 2006.

[73] J. Wang, M. S. Gudiksen, X. Duan, Y. Cui, and C. M. Lieber. Highly polarized photoluminescence and photodetection from single indium phosphide nanowires. *Science*, 293 (5534):1455–1457, 2001.

[74] V. Percec, M. Glodde, T. K. Bera, Y. Miura, I. Shiyanovskaya, K.D. Singer, V. S. K. Balagurusamy, P. A. Heiney, I. Schnell, A. Rapp, H.-W. Spiess, S. D. Hudson, and H. Duan. Self-organization of supramolecular helical dendrimers into complex electronic materials. *Nature*, 417:384 – 387, 2002.

[75] A. J. Steckl. DNA - a new material for photonics? *Nature Photonics*, 1:3 – 5, 2007.

[76] J. J. Storhoff, , and C. A. Mirkin. Programmed Materials Synthesis with DNA. *Chemical Reviews*, 99(7):1849–1862, 1999.

[77] S. Iijima. Helical microtubules of graphitic carbon. *Nature*, 354:56 – 58, 1991.

[78] P. M. Ajayan. Nanotubes from Carbon. *Chemical Reviews*, 99(7):1787–1800, 1999.

[79] I. Dierking. *Textures of Liquid Crystals*. Wiley-VCH Verlag GmbH & Co. KGaA, 2004.

[80] S. Singh. Phase transitions in liquid crystals. *Physics Reports*, 324(2–4):107 – 269, 2000.

[81] J. D. Watson and F. H. C. Crick. Molecular structure of nucleic acids: A structure for deoxyribose nucleic acid. *Nature*, 171:737 – 738, 1953.

[82] N. C. Seeman. DNA in a material world. *Nature*, 421:727 – 731, 2003.

[83] J. H. K. K. Hirschberg, L. Brunsveld, A. Ramzi, J. A. J. M. Vekemans, R. P. Sijbesma, and E. W. Meijer. Helical self-assembled polymers from cooperative stacking of hydrogen-bonded pairs. *Nature*, 407:167 – 170, 2000.

[84] A. Klug, F. H. C. Crick, and H. W. Wyckoff. Diffraction by helical structures. *Acta Crystallographica*, 11(3):199–213, 1958.

[85] C. Kittel. X-Ray diffraction from helices: Structure of DNA. *American Journal of Physics*, 36(7):610–616, 1968.

[86] J.S. Bowles and C.M. Wayman. The bain strain, lattice correspondences, and deformations related to martensitic transformations. *Metallurgical Transactions*, 3(5), 1972.

[87] T.J. Headley and J.A. Brooks. A new BCC-FCC orientation relationship observed between ferrite and austenite in solidification structures of steels. *Metallurgical and Materials Transactions A*, 33(1):5–15, 2002.

[88] G. Krauss and A. R. Marder. The morphology of martensite in iron alloys. *Metallurgical Transactions*, 2(9):2343, 1971.

[89] P. M. Kelly and J. Nutting. The martensite transformation in carbon steels. *Proceedings of the Royal Society of London A: Mathematical, Physical and Engineering Sciences*, 259 (1296):45–58, 1960.

[90] S. K. Das and G. Thomas. On the morphology and substructure of martensite. *Metallurgical Transactions*, 1(1):325–327, 1970.

[91] B. A. Bilby and A. G. Crocker. The theory of the crystallography of deformation twinning. *Proceedings of the Royal Society of London A: Mathematical, Physical and Engineering Sciences*, 288(1413):240–255, 1965.

[92] J. P. Hirth and J. Lothe. *Theory of dislocations*. Krieger Pub. Co, 2nd ed edition, 1982.

[93] R. C. Pond and S. Celotto. Special interfaces: military transformations. *International Materials Reviews*, 48(4):225–245, 2003.

[94] R.C. Pond, S. Celotto, and J.P. Hirth. A comparison of the phenomenological theory of martensitic transformations with a model based on interfacial defects. *Acta Materialia*, 51(18):5385 – 5398, 2003.

[95] P. Müllner and A.H. King. Deformation of hierarchically twinned martensite. *Acta Materialia*, 58(16):5242 – 5261, 2010.

[96] M. Müller, P. Erhart, and K. Albe. Analytic bond-order potential for BCC and FCC iron – comparison with established embedded-atom method potentials. *Journal of Physics: Condensed Matter*, 19(32):326220, 2007.

[97] D. R. Lide. *CRC Handbook of chemistry and physics*. CRC Press, 84th edition, 2003.

[98] J. Zarestky and C. Stassis. Lattice dynamics of γ -Fe. *Physical Review B*, 35:4500–4502, 1987.

[99] A.G Crocker. Twinned martensite. *Acta Metallurgica*, 10(2):113 – 122, 1962.

[100] H. Beladi, G. S. Rohrer, A. D. Rollett, V. Tari, and P. D. Hodgson. The distribution of intervariant crystallographic planes in a lath martensite using five macroscopic parameters. *Acta Materialia*, 63:86 – 98, 2014.

[101] V. Vítek. Multilayer stacking faults and twins on {211} planes in B.C.C. metals. *Scripta Metallurgica*, 4(9):725 – 732, 1970.

[102] L.M. Hsiung and D.H. Lassila. Shock-induced displacive transformations in tantalum and tantalum-tungsten alloys. *Scripta Materialia*, 39(4–5):603 – 609, 1998.

[103] Z. Shi and C. V. Singh. Competing twinning mechanisms in body-centered cubic metallic nanowires. *Scripta Materialia*, 113:214 – 217, 2016.

[104] C. Domain, C. S. Becquart, and J. Foct. *Ab initio* study of foreign interstitial atom (C, N) interactions with intrinsic point defects in α-Fe. *Physical Review B*, 69:144112, 2004.

[105] C.S. Becquart, J.M. Raulot, G. Bencteux, C. Domain, M. Perez, S. Garruchet, and H. Nguyen. Atomistic modeling of an Fe system with a small concentration of C. *Computational Materials Science*, 40(1):119 – 129, 2007.

[106] G. V. Kurdjumov and A. G. Khachaturyan. Phenomena of carbon atom redistribution in martensite. *Metallurgical Transactions*, 3(5):1069–1076, 1972.

[107] K.A. Taylor, G.B. Olson, M. Cohen, and J. B. V. Sande. {011} Twinning in Fe-Ni-C martensites. *Metallurgical Transactions A*, 20(12):2739–2747, 1989.

[108] G.V Kurdjumov and A.G Khachaturyan. Nature of axial ratio anomalies of the martensite lattice and mechanism of diffusionless $\gamma \rightarrow \alpha$ transformation. *Acta Metallurgica*, 23(9): 1077 – 1088, 1975.

[109] P. C. Chen and P. G. Winchell. Martensite lattice changes during tempering. *Metallurgical Transactions A*, 11(8):1333–1339, 1980.

[110] Seitz F. *The Modern Theory of Solids*. McGraw-Hill, 1940.

[111] S. Suwas and R. K. Ray (auth.). *Crystallographic Texture of Materials*. Engineering Materials and Processes. Springer-Verlag London, 1 edition, 2014.

[112] K. Huang M. Born. *Dynamical Theory of Crystal Lattices*. Clarendon Press Oxford, 1998.

[113] N.W. Ashcroft and N.D. Mermin. *Solid State Physics*. Saunders College, Philadelphia, 1976.

[114] B.E. Warren. *X-ray Diffraction*. Addison-Wesley series in metallurgy and materials engineering. Dover Publications, 1969.

Résumé:

Cette thèse a été centrée sur l'étude de la formation d'une phase martensitique dans les aciers Fe-Ni-C et sur la diffusion des atomes de carbone dans cette phase à basse température. La modélisation à l'échelle atomique a été utilisée. Pour décrire ces phénomènes, deux approches ont été développées: un modèle discret basé sur la théorie de la fonction de densité atomique (ADF) et une approche quasiparticulaire basée sur la théorie atomique de Fratons (AFT). Dans un premier temps, pour montrer l'universalité de notre approche, nous avons appliqué l'AFT pour modéliser la cinétique d'auto-assemblage des atomes initialement désordonnés à des structures ordonnées complexes. Cette approche a ensuite été appliquée à l'étude de transformation austénite/martensite. Il a été montré que le germe de martensite se développe comme agrégat multivariant dans la matrice austénitique. En utilisant des figures de pôles et des diagrammes de diffraction simulés, ces variants ont été identifiés et comparés aux données expérimentales. La diffusion du carbone dans la phase de martensite a été étudiée en utilisant la théorie ADF. Deux systèmes avec différentes propriétés élastiques, Fe-C et Fe-Ni-C, ont été considérés. Il a été montré qu'au cours du premier stade de vieillissement, les atomes de carbone subissent une décomposition spinodale sur les interstices octaédriques du réseau tétragonal centré de martensite et forment les zones riches en carbone. Ensuite, la morphologie «tweed-like» des zones riches en carbone est développée. Les résultats des simulations sont un bon accord avec les images expérimentales obtenues par sonde atomique tomographique. La relation entre une mise en ordre de Zener et la concentration des zones riches en carbone a été discutée.

Abstract:

This thesis examines the formation of martensite in Fe-Ni-C steels and the diffusion of carbon atoms in this phase at low temperatures. To achieve this goal the atomistic modeling have been used. To describe these phenomena two different approaches were developed: a discrete model based on the Atomic Density Function (ADF) theory and the quasiparticle approaches based on the Atomic Fraton Theory (AFT). First, the AFT was tested to model a self-assembly kinetics of initially disordered systems to three different classes of ordered one: single component crystals with fcc and diamond structures, two component crystals with zinc-blend structure, and polymers with single-strand and double-stranded helixes structures. Then this approach was applied to model austenite/martensite transformation. It was shown that martensite nucleus grows as multivariant aggregate in austenite matrix. Using pole figures and simulated diffraction patterns these variants were identified and compared with the experimental data. The carbon diffusion in martensite phase was studied using ADF theory. Two systems with the different elastic properties corresponding to the Fe-C and Fe-Ni-C systems were considered. It was shown that during a first stage of aging the carbon atoms undergo a spinodal decomposition on the octahedral interstices of bcc lattice and form the carbon-rich zones. Then "tweed-like" morphology of carbon-rich zones is developed. The simulations results are a good agreement with experimental images obtained by atom probe tomography. The relation between Zener ordering and the concentration of carbon reach zones is discussed.